

Syracuse University

SURFACE

Dissertations - ALL

SURFACE

August 2020

DIRECT DETERMINATION OF THE WEAK CHARGE OF THE PROTON VIA PARITY-VIOLATING ELECTRON SCATTERING

Peng Zang
Syracuse University

Follow this and additional works at: <https://surface.syr.edu/etd>



Part of the [Physical Sciences and Mathematics Commons](#)

Recommended Citation

Zang, Peng, "DIRECT DETERMINATION OF THE WEAK CHARGE OF THE PROTON VIA PARITY-VIOLATING ELECTRON SCATTERING" (2020). *Dissertations - ALL*. 1293.
<https://surface.syr.edu/etd/1293>

This Dissertation is brought to you for free and open access by the SURFACE at SURFACE. It has been accepted for inclusion in Dissertations - ALL by an authorized administrator of SURFACE. For more information, please contact surface@syr.edu.

Abstract

The weak charge of the proton is determined via Q_{weak} experiment at Thomas Jefferson Laboratory in Newport News, VA. A longitudinally polarized electron beam was scattered by a liquid hydrogen target. The spin direction of the electron beam was switched between left and right helicity states. The cross section under both of the electron states were measured to form the parity-violating asymmetry. An asymmetry of $-226.5 \pm 7.3(\text{stat}) \pm 5.8(\text{syst})$ was measured, corresponding to a weak charge of 0.0719 ± 0.0045 for the proton, which agrees with the value of 0.0708 ± 0.0003 from the Standard Model.

During the spin reversion of the electrons, other unwanted changes of the electron beam can be introduced as well to cause false cross section changes, also known as the "false" asymmetry. Successful evaluation and removal of these false asymmetries are crucial to the accuracy of the final measured results. In this thesis, the methods of beam correction, including regression, are discussed in detail about how the false asymmetry removal is done and how the results of the experiment can be more robust under such corrections. Other asymmetry corrections terms are discussed as well, including beam current asymmetry correction.

DIRECT DETERMINATION OF THE WEAK CHARGE OF THE
PROTON VIA PARITY-VIOLATING ELECTRON SCATTERING

by

Peng Zang

B.S., Shandong University, 2008

M.S., Syracuse University, 2015

Dissertation

Submitted in partial fulfillment of the requirements for the degree of
Doctor of Philosophy in Physics.

Syracuse University

August 2020

Copyright © Peng Zang 2020
All Rights Reserved

Acknowledgments

I would like to thank my mentor, Prof. Paul Souder. Paul has been a wonderful advisor during my PhD years. Not only I have learned a lot from him, also he gave me freedom to perform research on my own. It has been a marvelous experience working with him.

I would also like to thank Prof. Kent Paschke. We had been working in the beam correction team for the experiment. Kent was the group leader and his great instincts and skills made us this far.

I'd also like to thank Mark Pitt, who was also in the beam correction group and provided lots of advice and support, and Greg Smith, who was the project manager for the experiment and gave great support and useful discussions for various aspects of the experiment.

I'd also like to thank David Armstrong, Paul King, Wim van Oers, Wade Duvall and other collaborators from the collaboration for various supports of my work.

I thank my family for supporting me during my study abroad.

This work is funded in part by the Department of Energy (DOE) under grant DE-FG02-84ER40146.

Contents

Abstract	1
Acknowledgments	iv
1 Introduction	1
1.1 Symmetries and the Standard Model	2
1.1.1 Symmetries	2
1.1.2 The Standard Model	4
1.1.3 Parity Violation in the Standard Model	6
1.2 Electroweak Unification	7
1.2.1 Local gauge invariance	7
1.2.2 Spontaneous symmetry breaking	8
1.2.3 Neutral weak current	10
1.2.4 Electroweak radiative corrections	11
1.3 PV Scattering Experiment	12
1.3.1 Electron Scattering and Form Factors	12
1.3.2 e + p Scattering Parity-Violating Asymmetry	13
1.3.3 Motivation for Q_{weak}	14
2 The Q_{weak} Experiment	15
2.1 Overview	16

2.2	Polarized Electron Source	18
2.3	Polarimetry	20
2.4	Beamline Measurements	21
2.5	Hydrogen Target	23
2.6	Collimating System	25
2.7	QTOR Spectrometer	27
2.8	Main Detectors	28
2.9	Tracking System	29
2.10	Background Detection	30
2.11	Electronics and Software	31
3	Dithering Correction	33
3.1	Helicity Correlated Beam Asymmetries	33
3.2	Beam Modulation	35
3.3	Signal Ramp Fixing	37
3.3.1	Features of Raw Ramp	38
3.3.2	Ramp Fixing Procedure	39
3.3.3	Comparison between Raw and Fixed Ramp	44
3.4	Dithering Quality Checking	45
3.4.1	Dithering Coefficients	45
3.4.2	Sine and Cosine Dithering Patterns	47
3.4.3	Monitor Coefficient Vector	49
3.4.4	Checking Criteria and Results	55
3.5	Beam Correction Sensitivities	67
3.5.1	Standard Sensitivity Extraction Method	68
3.5.2	Sensitivity Calculation with More Patterns	71
3.5.3	Sensitivity History	74
3.6	Beam Correction with Residual	79

3.6.1	Dithering Residual	79
3.6.2	Residual History	81
3.7	Beam Correction Systematic Error	86
3.7.1	Dithering Schemes	87
3.7.2	Sensitivities with Different Schemes	89
3.7.3	Main Detector Asymmetries with Different Schemes	94
3.7.4	Scheme Selection Criteria	95
3.7.5	Schemes Systematic Error Assignment	100
3.8	Beam Correction Results	102
3.8.1	Beam Correction to Raw Asymmetry	102
3.8.2	Wien and HWP Cancellations	103
4	Regression and Dithering	107
4.1	Natural and Driven Motion	107
4.2	Main Detector Dipole	109
4.2.1	Main Detector Combinations	109
4.2.2	Main Detector Dipole Asymmetries	110
4.3	Correlation between Monitors	111
4.3.1	Partially Uncorrelated Monitors	113
4.3.2	Fully Uncorrelated Monitors	115
4.4	Comparison between Regression and Dithering	123
4.4.1	Monitor Difference Width	123
4.4.2	The Comparison of Regression and Dithering Sensitivities	125
4.4.3	The Comparison of Regression and Dithering Correction	129
5	Beam Current Correction	137
5.1	BCM Choices	137
5.2	Combining Different BCMs	138

5.3	Statistical Error of Renormalized Asymmetry	139
5.4	Systematic Error	142
6	Ditherless Data Recovery	148
6.1	Background	148
6.1.1	Ditherless Data Coverage	148
6.1.2	Regression and Dithering Approaches	149
6.2	Recovery Method	150
6.2.1	Ditherless Sensitivity Definition	150
6.2.2	Further Details of Ditherless Sensitivity Calculation	151
6.2.3	Dithering Sensitivity Slug History	153
6.3	Main Detector Asymmetry with Ditherless Data	156
6.3.1	Null Asymmetry	156
6.3.2	Physics Asymmetry	157
6.3.3	BB Corrected Physics Asymmetry	158
6.4	Dithering Sensitivity Error	160
6.4.1	From Ditherless Slope Error to Main Detector Error	160
6.4.2	Beam Correction Statistical Error	160
7	Conclusion	163
7.1	The Asymmetry	163
7.2	The Weak Charge of the Proton	165
A	MCV Angle History	168
	Bibliography	179

List of Tables

1.1	Electric and weak charges for quarks and leptons.	10
2.1	Typical parameters of the Q_{weak} experiment.	15
2.2	Typical time period definitions for the analysis.	31
3.1	Beam parameters for Helicity Correlated Beam Asymmetries.	34
3.2	Dithering patterns during beam modulation.	36
3.3	Raw and remapped ramp for four different ramp types.	41
3.4	In-phase and out-of-phase dithering coefficients.	46
3.5	Dithering patterns for both in-phase and out-of-phase responses.	48
3.6	Dithering quality checking with MCV angle.	56
3.7	Dithering quality checking with the error of MCV angle.	57
3.8	Dithering quality checking with MCV angle and error.	59
3.9	Runs with special dithering conditions by dithering quality checking [1].	64
3.10	Dithering schemes with select pattern removal	88
3.11	Beam correction at Wien level in Run 1.	103
3.12	Beam correction at Wien level in Run 2.	104
3.13	Beam correction at Wien level in Run 1, weighted.	105
3.14	Beam correction at Wien level in Run 2, weighted	105
4.1	Comparison between beam natural and driven motion.	108
4.2	The detector combinations and relative weights.	110

6.1	Ditherless data coverage summary.	149
6.2	Main detector Physics asymmetries.	158
6.3	Main detector Physics asymmetries + BB correction.	159

List of Figures

1.1	The Standard Model of elementary particles.	5
1.2	Neutral current interactions. Left: Z boson exchange; right: photon γ exchange.	10
1.3	Feynman diagrams for γ exchange at 1st (left) and 2nd (right) orders.	11
1.4	Feynman diagrams for higher order electroweak interactions.	11
2.1	Schematic of the Continuous Electron Beam Accelerator at Thomas Jefferson National Accelerator Facility.	16
2.2	CAD view of the experimental apparatus.	17
2.3	Schematic of the polarized source.	18
2.4	Layout of the Møller polarimeter.	20
2.5	Layout of the Compton polarimeter.	21
2.6	Schematic of the liquid hydrogen target.	24
2.7	Schematic of cross section of the collimator system.	26
2.8	Scattered electron profile defined by the collimators, spectrometer and main detector shielding.	27
2.9	PMT yield versus run number.	28
2.10	Main detector asymmetry RMS vs run number.	29
2.11	Profile of electron flux in the main detector.	30
2.12	DAQ and analysis framework.	32
3.1	Raw ramp vs time.	37

3.2	Ramp histogram before rescaling.	38
3.3	Comparison between raw and fixed ramp.	44
3.4	Example of redundant dithering patterns	60
3.5	Example of weak or missing dithering pattern	61
3.6	Example of moderate pattern pair.	62
3.7	Example of good pattern pair.	63
3.8	Angle slug history.	65
3.9	Main detector energy sensitivity slug history.	76
3.10	Main detector horizontal position and angle sensitivities slug history.	77
3.11	Main detector vertical position and angle sensitivities slug history.	78
3.12	Main detector dithering residual slug history in pattern Y1 and Y2.	82
3.13	Main detector dithering residual slug history in pattern X1 and X2.	84
3.14	Main detector dithering residual slug history in pattern E.	85
3.15	Main detector energy sensitivity slug history from different dithering schemes.	90
3.16	Main detector vertical angle sensitivity slug history from different dithering schemes.	91
3.17	Main detector vertical position sensitivity slug history from different dithering schemes.	91
3.18	Main detector horizontal angle sensitivity slug history from different dithering schemes.	92
3.19	Main detector horizontal position sensitivity slug history from different dithering schemes.	93
3.20	Main detector physics asymmetry in Run 1 with different dithering schemes.	95
3.21	Main detector physics asymmetry in Run 2 with different dithering schemes.	96
3.22	Summary of results for dither schemes in Run 1.	97
3.23	Summary of results for dither schemes in Run 2.	98
3.24	Main detector asymmetries from working dither schemes in Run 1.	102

3.25	Main detector asymmetries from working dither schemes in Run 2.	103
4.1	Different combinations of the main detector array.	109
4.2	Comparison between regressed and dither-corrected main detector dipole D1 asymmetries.	111
4.3	Comparison between regressed and dither-corrected main detector dipole D3 asymmetries.	112
4.4	Correlation factors between monitor differences at slug level before and after correlation removal.	114
4.5	Correlation factors between horizontal detector sensitivities at slug level before and after correlation removal.	116
4.6	Correlation factors between vertical detector sensitivities at slug level before and after correlation removal.	116
4.7	Transformation matrix slug level history.	122
4.8	Monitor differences width slug history.	124
4.9	Detector monopole sensitivity slug history.	126
4.10	Detector dipole 1 sensitivity slug history.	127
4.11	Detector dipole 3 sensitivity slug history.	128
4.12	Monitor differences at Wien level.	130
4.13	Detector monopole beam corrections at Wien level.	131
4.14	Detector dipole 1 beam corrections at Wien level.	134
4.15	Detector dipole 3 beam corrections at Wien level.	135
4.16	Detector monopole asymmetries at Wien level.	136
4.17	Detector dipole asymmetries at Wien level.	136
5.1	Residual correlation between main detector and BCM asymmetries in Run 1.	138
6.1	Ditherless slug with measured sensitivities on both sides.	150
6.2	Main detector dithering sensitivity slug history for energy monitor.	153

6.3	Main detector dithering sensitivity slug history for targetX monitor.	154
6.4	Main detector dithering sensitivity slug history for targetXSlope monitor. . .	154
6.5	Main detector dithering sensitivity slug history for targetY monitor.	155
6.6	Main detector dithering sensitivity slug history for targetYSlope monitor. . .	155
6.7	Main detector IHWP+Spin Null asymmetries.	156
6.8	Main detector IHWP-only Null asymmetries.	157
6.9	Main detector Physics asymmetries.	157
6.10	Main detector Physics asymmetries + BB correction.	159
7.1	Most significant systematic error contributions [2].	164
7.2	Results for the weak charge of the proton.	164
7.3	World PVES data fitting of reduced asymmetry versus Q^2 to determine the weak charge of the proton [2].	165
7.4	Constraints on coupling constants C_{1u} and C_{1d} [2].	166
7.5	Running of weak mixing angle with previous measurements [2].	166
7.6	New physics limits vs quark flavor coupling [2].	167

Chapter 1

Introduction

The Standard Model, together with Einstein's General Relativity, provides the best description of the universe for humankind. Both of the theories were developed in the last century by brilliant minds from all over the world. They describe four known fundamental forces and the particles with which we are made of. Even though there are more sophisticated theoretical structures that are built on them, including GUT (Grand Unified Theory), string theory etc, the Standard Model and General Relativity have stood long-term experimental tests and proven to be on the right track to the ultimate truth of the universe.

Here in this thesis, one of those experiments is described. The Q_{weak} experiment is another strict test for the Standard Model. Q_{weak} aims to measure the weak charge of the proton by scattering longitudinally polarized electrons to a hydrogen target. The change of scattering rates (asymmetry) with respect to the change of the polarization direction gives the weak charge of the proton and also the weak mixing angle for the electroweak sector of the Standard Model. By comparing the experimental results with theoretical prediction, Q_{weak} experiment offers a test of the Standard Model's current framework.

This thesis first gives the background of the Standard Model and formalism of the Q_{weak} experiment. In the next few chapters, the corrections to the asymmetry, including beam

current and beam position, energy corrections, are described in details. One chapter gives the comparison between regression and dithering—two different beam correction techniques—and partial reasons for the difference between them. The last chapter gives final results and conclusion for the experiment.

1.1 Symmetries and the Standard Model

1.1.1 Symmetries

Symmetry is one of the great underlying characteristics of nature. The symmetry we are most familiar with in our daily lives is the symmetry through the mirror. The image in the mirror and ourselves are the same except that the left becomes right and the right becomes left. Symmetry, in a more broad sense, gives the invariance of the system under some operation. Taking the mirror again for example, the operation is the reflection through the mirror and the invariance of the system is simply the same image in the mirror and the person looking at the mirror. Like in a mirror maze, it is hard to tell the actual image in the mirror from a real person, so don't try to run into and hug someone unless you are ready to pay for the broken mirror on top of the ticket.

When we include more operations in the concept of symmetry, we are not limited to mirror symmetry. Other types of symmetries are not very closely related to literal meaning of “symmetry” by first look. Time translation for the conservation of the energy is a symmetry. The irrelevance of momentum with respect to position is also a symmetry. They are all some invariance of something under certain operations. The examples so far sound pretty trivial at first but when we try to include symmetry groups for the system at hand, the concept of symmetry becomes deeper and this is how the Standard Model is formulated.

For the symmetries in the Standard Model, the system at hand is more abstract—the Lagrangian of the system of interest. Physicists of modern days love to work with Lagrangian not only because the equations of motion (like $F = ma$ in Newton's days) can

be easily obtained by applying Euler-Lagrangian equations to the Lagrangian itself, but also the Lagrangian in general is a linear sum of different energy pieces of the system we are studying. Normally the kinetic energy terms have positive sign and the potential or interaction terms have negative signs in the Lagrangian. So with Lagrangian the physics significance of the system is clear and easy to interpret.

Now comes to the operation of the symmetry on the Standard Model. For a specific operation, we have an operator and an object. The object which the operation is operated upon is wave function of particles. The object can be a singlet with which only one particle is involved. Or a doublet, which has two different types of particles in it. And a triplet, with each wave function from three particles. For sure, the multilets are not composed of randomly chosen particles. Normally in a multilet, the particles have almost all in common but one important property of interest. In the Standard Model, that important particle property which distinguishes particles in the multilet is electric charge for doublet, and color charge (source of strong force) for triplet.

$$\Psi \quad \begin{pmatrix} \Psi^{+e} \\ \Psi \end{pmatrix} \quad \begin{pmatrix} \Psi_r \\ \Psi_g \\ \Psi_b \end{pmatrix}$$

Singlet Doublet Triplet

As for the operator of a specific symmetry, we need matrices to manipulate multilets. For a singlet, we use a simple number as the operator. For doublet, we use a matrix of rank 2, and rank 3 for triplet. In the Standard Model, the operator matrices are not completely arbitrary. For the singlet operator, the matrix (a complex number) belongs to U(1) group. The operator of U(1) group follows a simple rule: $U^\dagger U = 1^1$. Since for singlet, the operator is a complex number, this condition limits this number to have only one degree of freedom, which we can take as $e^{i\theta}$.

For doublet, the operator, matrix of rank 2, is required to follow SU(2) in the Standard

¹† means transpose conjugate.

Model. For SU(2) group, the matrix obeys two conditions: a unitary condition $U^\dagger U = I_2^2$ and a “special” condition $|U|=1$. With these conditions, a SU(2) matrix has three degrees of freedom, which can be realized by Pauli matrices³ in the exponent: $e^{i(\tau_1\theta_1+\tau_2\theta_2+\tau_3\theta_3)}$. And for triplet, the operator of a matrix of rank 3 in the Standard Model obeys SU(3), similar to SU(2) with only an increase in the rank. And with unitary condition and special requirement of unit determinant, the SU(3) operator has eight degrees of freedom, which can be expressed using Gell-Mann matrices⁴ as $e^{i(\lambda_1\alpha_1+\lambda_2\alpha_2+\dots+\lambda_8\alpha_8)}$.

Now for symmetry of the Standard Model, the gist is that the Lagrangian is invariant (Lagrangian has a real value, so simply this value is to be kept unchanged) under operations we have described on the particle wave functions (singlet or multilets). There are further procedures, including global or local operations and symmetry breaking, which are to be introduced in later sections.

1.1.2 The Standard Model

The Standard Model was developed in the 1960–70s and it describes the known fundamental particles and three of the four interactions (electromagnetic, weak and strong forces). The Standard Model has stood long and rigorous experimental tests and the last puzzle of the model—Higgs boson—was discovered in 2012. The current framework of Standard Model itself is fairly complete except for a few missing parameters in the lepton section involved with neutrino oscillations. The Standard Model has already been a very successful theory framework even though many parameters (19) have to be provided by experiment. So it is not fair to blame the Standard Model for its exclusion of other

² I_2 is a unit matrix of rank 2.

³The Pauli matrices are $\tau_1 = \begin{bmatrix} 0 & 1 \\ 1 & 0 \end{bmatrix}$, $\tau_2 = \begin{bmatrix} 0 & -i \\ i & 0 \end{bmatrix}$, $\tau_3 = \begin{bmatrix} 1 & 0 \\ 0 & -1 \end{bmatrix}$.

⁴The Gell-Mann matrices are $\lambda_1 = \begin{bmatrix} 0 & 1 & 0 \\ 1 & 0 & 0 \\ 0 & 0 & 0 \end{bmatrix}$, $\lambda_2 = \begin{bmatrix} 0 & -i & 0 \\ i & 0 & 0 \\ 0 & 0 & 0 \end{bmatrix}$, $\lambda_3 = \begin{bmatrix} 1 & 0 & 0 \\ 0 & -1 & 0 \\ 0 & 0 & 0 \end{bmatrix}$, $\lambda_4 = \begin{bmatrix} 0 & 0 & 1 \\ 0 & 0 & 0 \\ 1 & 0 & 0 \end{bmatrix}$, $\lambda_5 = \begin{bmatrix} 0 & 0 & -i \\ 0 & 0 & 0 \\ i & 0 & 0 \end{bmatrix}$, $\lambda_6 = \begin{bmatrix} 0 & 0 & 0 \\ 0 & 0 & 1 \\ 0 & 1 & 0 \end{bmatrix}$, $\lambda_7 = \begin{bmatrix} 0 & 0 & 0 \\ 0 & 0 & -i \\ 0 & i & 0 \end{bmatrix}$, $\lambda_8 = \frac{1}{\sqrt{3}} \begin{bmatrix} 1 & 0 & 0 \\ 0 & 1 & 0 \\ 0 & 0 & -2 \end{bmatrix}$.

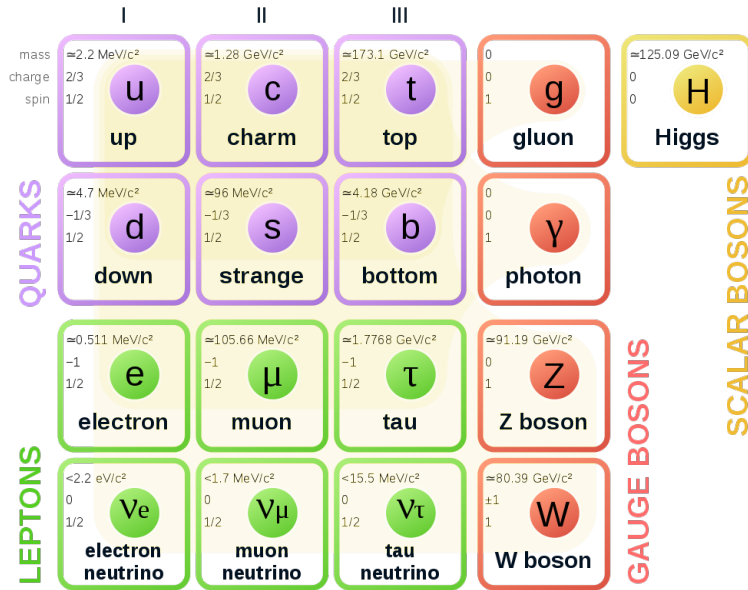


Figure 1.1: Classification of elementary particles in the Standard Model [3].

phenomena in nature. But still, the gravitational force is not incorporated with the Standard Model. Also the Standard Model can not explain well the matter-antimatter asymmetry mystery. And the dark matter and dark energy problems can't find their origins in the current framework of Standard Model. Therefore, there is still room for new physics to be found beyond the Standard Model.

The current Standard Model classifies elementary particles into two main categories: fermions and bosons. Fermions are “matter” particles and have half-integer spin. The bosons are mostly “force” carrier particles and they have integer spin. Fermions can be divided into quarks and leptons. Quarks have fractional (increment of $1/3$) element electric charges while leptons have integer element charges (-1, 0, 1). Quarks and leptons have three generations, with mass increasing from generation to the next generation. The bosons include gluons (eight of them, carriers of strong force), photon (mediator of electromagnetic force), Z and W^\pm bosons (carrier of weak forces). These “force” carrier particles have spin of 1. Also there is newly discovered (theoretically predicted in 1970s) Higgs boson, which has spin of 0, gives fermions and weak force carrier bosons masses via spontaneous symmetry breaking.

1.1.3 Parity Violation in the Standard Model

Of the three fundamental forces described by the Standard Model, the weak force has one feature that the other two forces (electromagnetic and strong forces) don't - weak force violates parity symmetry. Parity violation is unique to weak force. To understand this feature, first we need to know what parity operation is and what it means for particles.

Parity is a concept that is closely related to the spin of a particle. The spin, even though we don't know the exact source or structure of spin, it can be treated as internal angular momentum of a particle. The angular momentum, like orbital angular momentum, is the cross product of two vectors - position and momentum. Under parity operation, $x, y, z \rightarrow -x, -y, -z$, the directions of position and momentum are both changed by 180 degrees while the cross product - the angular momentum - doesn't change its direction. So the spin of a particle, under parity operation, keeps its direction as well.

Now we introduce the handedness for a particle. If the spin of a particle is in the same direction with its momentum, it is a right-handed particle. If the spin and momentum are in opposite directions, the particle is left-handed. Since under parity operation, the direction of spin is kept while the direction of momentum is inverted, the handedness of a particle is changed under parity. A left-handed particle can be changed to a right-handed particle under parity operation and vice versa.

In nature it is surprising that the weak forces in the Standard Model only work on left-handed particles. This means the right-handed particles don't participate in the weak interactions, at all. Since parity operation changes handedness, basically the parity operation turns weak force "on and off"⁵. And this is why we say "weak force violates parity symmetry", and in a maximum way.

⁵This is true for a 100% right-handed particle and 100% left-handed particle in the model. In experiment, we are dealing with particles that are not 100% left-handed or right-handed, normally a mixed state. For example, the Q_{weak} experiment utilized a 89% polarized electron beam.

1.2 Electroweak Unification

Like Maxwell unified electricity and magnetism into a single electromagnetism framework with a set of equations, weak force and electromagnetic force are unified as well in the Standard Model. This is not in the sense that the force carriers can all be generated with different group symmetries we mentioned earlier, but that the SU(2) and U(1) are intimately bound together. There is a mixing between the force carrier bosons through SU(2) and the force boson with U(1), which is known as “weak mixing angle”. There is no mixing between SU(3) and other groups, so strong force is considered to be independent from electromagnetic force and weak forces, even though they all can be formulated with the same principle - local gauge invariance.

1.2.1 Local gauge invariance

The local gauge invariance, or in other words based on what we have introduced so far, the local operation on particle singlet or multiplets, with the Lagrangian conserved. The operators we mentioned earlier all have different numbers of degrees of freedom depending on the group they belong to. For U(1) operator, the degree of freedom is 1 and for SU(2) or SU(3) operators, there are 3 or 8 free parameters, accordingly. These free parameters can be constants in the global gauge invariance scenario or they can depend on position and time for local gauge invariance.

In the Lagrangian of the Standard Model, before the local gauge invariance is applied, there are only kinetic terms from the particles involved, singlet or multiplets. The kinetic terms are in the form of free Dirac particles,

$$\bar{u}\gamma^\mu\partial_\mu u,$$

where \bar{u} is Dirac conjugate of a spinor, it could be a singlet or multiplet.

As we can see, there are partial derivatives in the term shown above. If the operator has constant free parameter(s), the partial derivative has no effects and the operator from

Dirac spinor and adjoint Dirac spinor cancel each other and the resulted Lagrangian is unaffected. This is what “Global Gauge Invariance” means.

For “local” gauge invariance, the free parameters depend on x^μ , or position and time. Therefore the partial derivative can work on the free parameters in the operators and an extra term shows up after the operation on wave functions. This extra term contains partial derivatives of the free parameters from the operator of interest. To make sure the resulted Lagrangian is still conserved, the extra term must be compensated by other things. And at this point, the vector bosons show up to make up for the extra partial derivatives from the operator parameters. For $SU(2) \times U(1)$ symmetry groups, four parameters exist in the $SU(2)$ operator and $U(1)$ operator and therefore four vector boson field are introduced. Effectively speaking we can replace the original partial derivative with “covariant” derivative. The vector boson fields can be integrated in the “covariant” derivative as

$$D_\mu = \partial_\mu + i\frac{g}{2}(\tau^1 W_\mu^1 + \tau^2 W_\mu^2 + \tau^3 W_\mu^3) + i\frac{g'}{2}B_\mu,$$

where W_μ^{1-3} and B_μ are four vector boson fields introduced with “Local Gauge Invariance”.

1.2.2 Spontaneous symmetry breaking

When Maxwell introduced the unified theory of electromagnetism, the key idea was that a changing electric field generates a magnetic field and vice versa. In the Standard Model, the weak force and the electromagnetic force are unified with a mixing between them. The strength of the mixing is represented by the weak mixing angle, θ_W . The vector boson fields W_μ^3 and B_μ are mixed to form the neutral weak boson field Z and the electromagnetic photon field A :

$$\begin{cases} Z_\mu = \cos \theta_W W_\mu^3 - \sin \theta_W B_\mu \\ A_\mu = \sin \theta_W W_\mu^3 + \cos \theta_W B_\mu \end{cases}.$$

The coupling constants from $SU(2)$ and $U(1)$ gauge bosons are related to the element electric charge by

$$g = e/\sin \theta_W, g' = e/\cos \theta_W .$$

The charged W bosons are related to the original W bosons by

$$W_\mu^\pm = \frac{1}{\sqrt{2}}(W_\mu^1 \mp W_\mu^2) .$$

As of now, the fermions and bosons in the Standard Model are still massless. Their mass terms (if there should be any) are not introduced until the Higgs boson (via Higgs mechanism) and Yukawa interactions are added into the framework of the Standard Model.

The Higgs Lagrangian is

$$\mathcal{L} = (D_\mu \Psi)^\dagger (D^\mu \Psi) - \mu^2 \Psi^\dagger \Psi - \lambda (\Psi^\dagger \Psi)^2 ,$$

where the negative terms are the potential energy of the Higgs boson and the Higgs boson is a complex doublet,

$$\Psi = \begin{pmatrix} \psi^+ \\ \psi^0 \end{pmatrix} ,$$

with ψ^+ carrying a positive charge and the neutral ψ^0 . When the SU(2) symmetry is spontaneously broken, the Higgs boson takes the form

$$\Psi \rightarrow \frac{1}{\sqrt{2}} \begin{pmatrix} 0 \\ \nu + H \end{pmatrix} ,$$

in which H is the scalar Higgs boson and ν minimizes Higgs potential energy when $\mu^2 < 0$. Since ν is not zero, mass terms for Z and W bosons show up in the Higgs Lagrangian after spontaneous symmetry breaking, together with the interaction terms between Z , W bosons and the Higgs boson. The masses of Z and W bosons are related to each other by

$$M_Z = M_W / \cos \theta_W .$$

. Further with Yukawa interaction terms between the Higgs boson and the fermions, after spontaneous symmetry breaking, the fermion masses are introduced as well. Since there are no right-handed neutrinos observed in experiments, neutrino masses can't be generated via Yukawa interactions with symmetry breaking in the Standard Model.

1.2.3 Neutral weak current

In the electroweak sector of the Standard Model, there are two neutral interactions - the Z boson and the photon (γ). While the charged W bosons change the flavor of a particle by absorbing or emitting an element charge, Z and γ keep the particle's original flavor (Fig. 1.2).

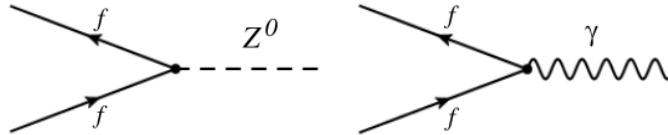


Figure 1.2: Neutral current interactions. Left: Z boson exchange; right: photon γ exchange.

The neutral currents for Z and γ are

$$\begin{aligned} J_\mu^\gamma &= \bar{\psi} Q_f \gamma_\mu \psi, \\ J_\mu^Z &= \bar{\psi} \gamma_\mu (g_V^f - g_A^f \gamma_5) \psi, \end{aligned} \tag{1.1}$$

where Q_f is the electric charge for a lepton or a quark. g_V^f and g_A^f are the weak vector and axial charges, respectively. The values of Q_f , g_V^f , g_A^f for leptons and quarks in the Standard Model are listed in Tab. 1.1.

Table 1.1: Electric and weak charges for quarks and leptons.

f	Q_f	g_V^f	g_A^f
u, c, t	$+2/3$	$1 - 8/3 \sin^2 \theta_W$	1
d, s, b	$-1/3$	$-1 + 4/3 \sin^2 \theta_W$	-1
e, μ, τ	0	1	1
ν_e, ν_μ, ν_τ	-1	$-1 + 4 \sin^2 \theta_W$	-1

For electron-quark scattering, the parity-violating part of the Z exchange Lagrangian is

$$L_{PV} = -\frac{G_F}{\sqrt{2}} \sum_q (C_{1q} \bar{e} \gamma_\mu \gamma_5 e \bar{q} \gamma^\mu q + C_{2q} \bar{e} \gamma_\mu e \bar{q} \gamma^\mu \gamma_5 q), \tag{1.2}$$

where G_F is the Fermi constant, q runs through all quark flavors (actually only light

quarks u, d, s are important in the experiment), C_{1q} and C_{2q} are weak coupling constants for vector and axial quarks. The Q_{weak} experiment can determine a linear combination of C_{1q} 's, $2C_{1u} + C_{1d}$.

1.2.4 Electroweak radiative corrections

The interaction terms in the Lagrangian so far have been at tree level - four point interaction with two vertexes. At higher order levels, loops can be inserted into the diagrams (Fig. 1.3). Due to the loop vacuum effect, the true charge of the coupling is screened, which causes the running of the coupling constant α with the energy scale.



Figure 1.3: Feynman diagrams for γ exchange at 1st (left) and 2nd (right) orders.

There are also higher order diagrams for electroweak interactions, as shown in Fig. 1.4. These higher order diagrams lead to the running of the weak coupling.

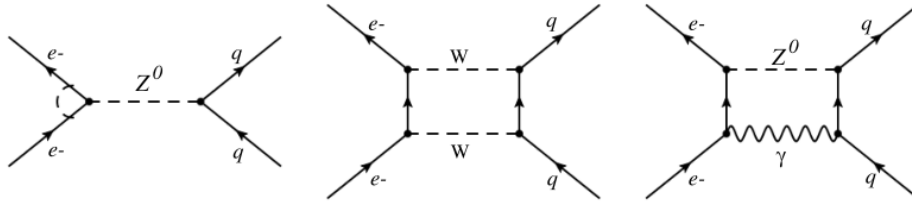


Figure 1.4: Feynman diagrams for higher order electroweak interactions.

With radiative corrections, the proton's weak charge is of the form

$$Q_W^p = [1 + \Delta_\rho + \Delta_e][(1 - 4 \sin^2 \theta_W(0)) + \Delta_{e'}] + \square_{WW} + \square_{ZZ} + \square_{\gamma Z}, \quad (1.3)$$

where Δ_ρ modifies the coupling, Δ_e and $\Delta_{e'}$ are vertex corrections to Z and γ vertexes.

The last three terms are from box diagrams like in Fig. 1.4. \square_{WW} and \square_{ZZ} can be well

calculated due to large masses of W and Z bosons. But $\square_{\gamma Z}$ is hard to calculate because the photon is massless.

1.3 PV Scattering Experiment

1.3.1 Electron Scattering and Form Factors

In the electron-nucleon scattering experiment, due to the structure of proton and neutron, the neutral currents associated with the nucleon vertexes are

$$\begin{aligned} J^{\mu,\gamma} &= \bar{\psi}(F_1^\gamma \gamma^\mu + F_2^\gamma \frac{i\sigma^{\mu\nu} q_\nu}{2M})\psi, \\ J^{\mu,Z} &= \bar{\psi}(F_1^Z \gamma^\mu + F_2^Z \frac{i\sigma^{\mu\nu} q_\nu}{2M} + G_A^Z \gamma^\mu \gamma^5)\psi, \end{aligned} \quad (1.4)$$

where F_1 and F_2 are Dirac and Pauli form factors for photon and Z boson and G_A^Z is the axial form factor for Z boson. In Sachs form factors G_E (electric) and G_M (magnetic) [4], we have

$$\begin{aligned} G_E &= F_1 - \tau F_2, \\ G_M &= F_1 + F_2, \end{aligned} \quad (1.5)$$

in which $\tau = Q^2/4M$ is a kinematic factor.

The electromagnetic form factors G_E^γ and G_M^γ for proton and neutron are well studied over a wide range of Q^2 and can be summarized as

$$\begin{aligned} G_E^{p,\gamma} &= G_D, \\ G_M^{p,\gamma} &= \mu_M^p G_D, \\ G_E^{n,\gamma} &= -\mu_E^n \frac{\tau}{1+5.6\tau} G_D, \\ G_M^{n,\gamma} &= \mu_M^n G_D, \end{aligned} \quad (1.6)$$

where $G_D = 1/(1 + Q^2/0.711)^2$ is a dipole form.

The neutral weak form factors G_E^Z and G_M^Z for proton and neutron are not as well known as the electromagnetic form factors, but they can be written in terms of the

electromagnetic form factors as

$$\begin{aligned} G_{E,M}^{p,Z} &= (1 - 4 \sin^2 \theta_W) G_{E,M}^{p,\gamma} - G_{E,M}^{m,\gamma} - G_{E,M}^s, \\ G_{E,M}^{m,Z} &= (1 - 4 \sin^2 \theta_W) G_{E,M}^{m,\gamma} - G_{E,M}^{p,\gamma} - G_{E,M}^s, \end{aligned} \quad (1.7)$$

where G^s is the form factors for strange quark.

The axial form factor for Z boson follows a dipole form

$$G_A^Z = \frac{G_A^Z(0)}{(1 + \frac{Q^2}{M_A^2})^2}. \quad (1.8)$$

1.3.2 e + p Scattering Parity-Violating Asymmetry

The electron-proton scattering parity-violation asymmetry is [5]

$$A_{PV} = \frac{-G_F Q^2}{4\pi\alpha\sqrt{2}} \frac{\epsilon G_E^\gamma G_E^Z + \tau G_M^\gamma G_M^Z - (1 - 4\sin^2\theta_W)\epsilon' G_M^\gamma G_A^Z}{\epsilon(G_E^\gamma)^2 + \tau(G_M^\gamma)^2}, \quad (1.9)$$

where

$$\epsilon' = \sqrt{\tau(1+\tau)(1-\epsilon^2)}, \quad \epsilon = \frac{1}{1 + 2(1+\tau)\tan^2\frac{\theta}{2}}, \quad (1.10)$$

G_F is the Fermi constant, α the fine structure constant, M the proton mass, θ the electron deflection angle in the laboratory.

The asymmetry can be further reduced to

$$A_{PV} = \frac{-G_F Q^2}{4\pi\alpha\sqrt{2}} [Q_W^p + Q^2 B(Q^2, \theta)], \quad (1.11)$$

where the B term contains hadronic structure contribution to the asymmetry. At the small four-momentum transfer for Q_{weak} experiment, the proton structural contributions can be greatly suppressed.

1.3.3 Motivation for Q_{weak}

Q_{weak} provides strong constraints on weak vector quark coupling combination $2C_{1u} + C_{1d}$.

Together with atomic parity violation (APV) experiments, the coupling C_{1u} and C_{1d} can be determined separately with good precision.

New lepton-quark PV physics at TeV scale can be parameterized in a contact interaction Lagrangian as

$$\mathcal{L}_{eq}^{PV} = \frac{g^2}{4\Lambda^2} \bar{e} \gamma_\mu \gamma_5 e \sum h_V^q \bar{q} \gamma^\mu q, \quad (1.12)$$

in which Λ is the energy scale. The weak charge of proton determined by the Q_{weak} experiment can set bounds on new semi-leptonic PV physics beyond the Standard Model.

Chapter 2

The Q_{weak} Experiment

The goal of the Q_{weak} experiment was to determine the weak charge of the proton via the measurement of parity-violation asymmetry in electron-proton elastic scattering. In order to achieve better precision, the experiment pushed forward on many existing boundaries, including higher beam intensity, faster electron helicity reversal, higher power target, etc. The typical parameters of the experiment are listed in Tab. 2.1.

Table 2.1: Typical parameters of the Q_{weak} experiment.

Quantity	Value
Beam Energy	1.16 GeV
Beam Polarization	$\sim 89\%$
Beam Current (Integrating Mode)	100-180 μA
Beam Current (Event Mode)	50 pA - 200 nA
Target Length	34.4 cm
Target Temperature	20 K
Beam Power in Target	2.1 kW
Luminosity	$1.0 - 1.7 \times 10^{39} \text{ cm}^{-2}\text{s}^{-1}$
θ Acceptance	$5.8^\circ - 11.6^\circ$
Nominal Scattering Angle	7.9°
ϕ Acceptance	49% of 2π
Elastic Solid Angle	43 msr
Acceptance Averaged Q^2	0.025 GeV^2
$\int \vec{B} dl$	0.9 T·m
Total Detector Rate	7 GHz

2.1 Overview

The experiment took place in Hall C at the Thomas Jefferson National Accelerator Facility[6] (see Fig. 2.1) located in Newport News, Virginia. The data taking was divided into three running periods:

- Commissioning Run: February, 2011
- Run 1: February - May, 2011
- Run 2: November 2011 - May 2012

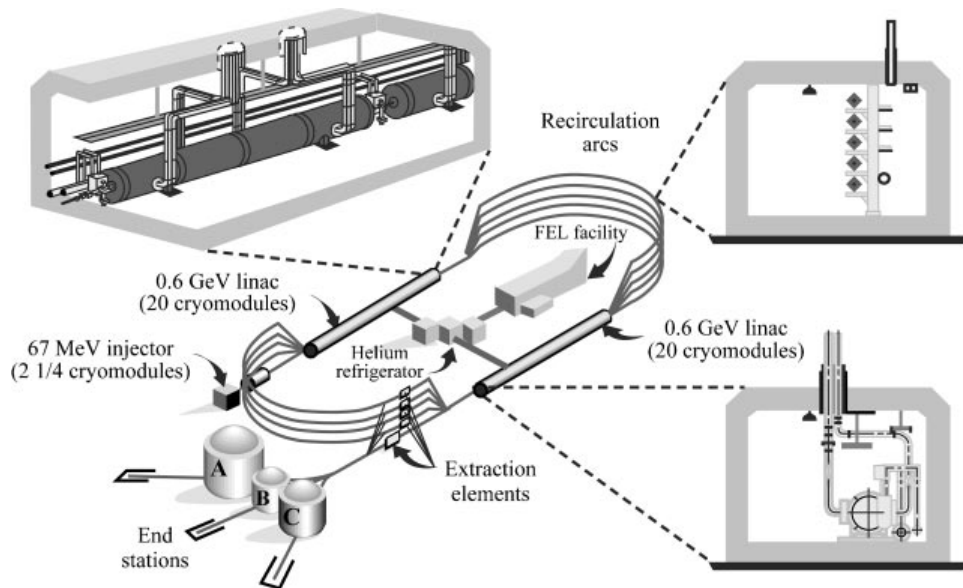


Figure 2.1: Schematic of the Continuous Electron Beam Accelerator at Thomas Jefferson National Accelerator Facility [6].

A $\sim 89\%$ longitudinally polarized electron beam with a current of $180 \mu\text{A}$ and energy of 1.16 GeV was delivered to a 34.4 cm long liquid hydrogen target. Two independent polarimeters, Compton and Møller, were utilized to measure the polarization. Several beam position and current monitors along the beam line were installed to measure the beam position, angle, energy and current. Eight quartz $200 \text{ cm} \times 18 \text{ cm} \times 1.25 \text{ cm}$ Čerenkov detectors were positioned azimuthally in the end of scattering region, with an

azimuthal angle coverage of 49% of 2π . The symmetry of the detector suppresses helicity-correlated beam motion differences and transverse polarization asymmetries.

There are two modes associated with the detector measurement. One is current mode during which the beam was at about $180 \mu\text{A}$. The electron rate for each detector bar was at ~ 800 MHz and the current in the PMTs were integrated every millisecond. The other is event mode with a low beam current of 50-100 pA which allowed for single electrons to be detected by the detector bars for electron momentum transfer determination.

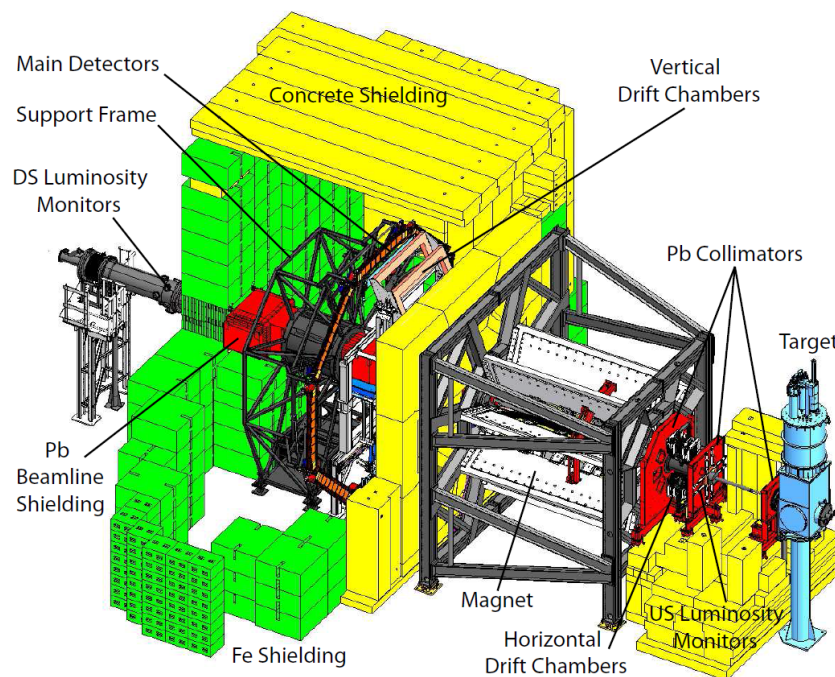


Figure 2.2: CAD view of the experimental apparatus [7].

A triple collimator system, together with a resistive toroidal magnetic spectrometer, allowed elastically scattered electrons within 5.8° to 11.6° to travel onto the main detector array, while keeping inelastic and Møller scattered electrons and neutral events away from the detector. An electron rate of 0.9 GHz was achieved in each of these detectors during the integrating mode (beam current $180 \mu\text{A}$ for asymmetry measurement). A tracking system composed of horizontal and vertical drift chambers before and after the magnet were periodically inserted during the event mode to measure the acceptance-weighted

electron kinematics.

2.2 Polarized Electron Source

The polarized source is illustrated in the schematic of Fig. 2.3. In short, a circularly polarized laser is incident on a photocathode, which produce polarized electrons with corresponding helicity. The electrons are accelerated to ~ 1 GeV in the CEBAF and bent into the experiment Hall for later use.

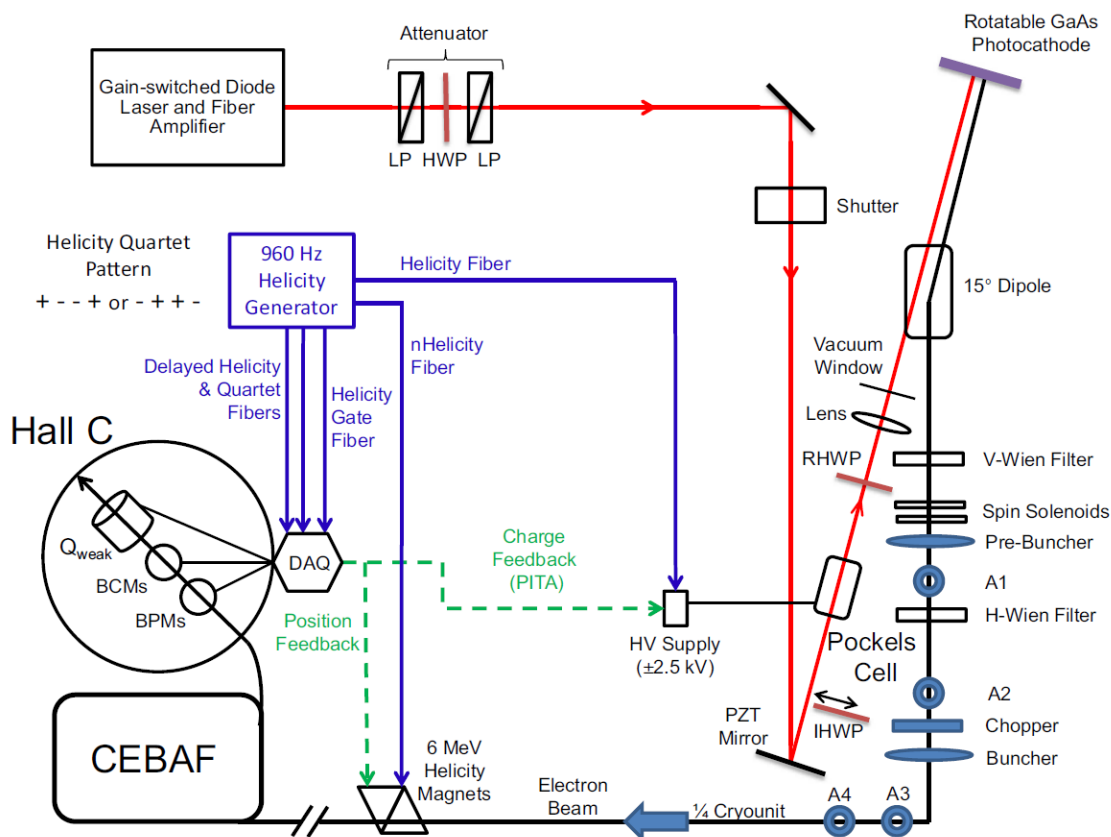


Figure 2.3: Schematic of the polarized source for the experiment [7].

The helicity generator produced a signal of 960 Hz, about period of 1 ms, which was used to flip the high voltage of Pockels cell. The pattern was repeated with a quartet of four helicity states, $-+-$ or $+-+$, with the first helicity state of each quartet determined with a pseudo-random number. The four sequential helicity state windows forms a quartet, at

which we average the detector yield or define detector asymmetry.

The linearly polarized laser delivered to Hall C was incident on the Pockels Cell, which birefringence effect depended on the voltage applied. The Pockels Cell served as a quarter-wave plate that can transform the linearly polarized laser light into circularly polarized light. Switching of the sign of the high voltage, about 2.5 kV, also switched the helicity of the emerging laser light at a rate of 960 Hz.

The flipping of the direction of the spin causes helicity-correlated change in the energy, position and angle of the beam, referred to as a Helicity-Correlated Beam Asymmetry (HCBA). The optical elements, especially the Pockels Cell, were carefully aligned to minimize these false asymmetries. Besides, the Quantum Efficiency (QE) hole generated at the photocathode during use of laser light can change the profile of the generated electron beam, which contributes to the measured beam position differences.

Besides fast helicity reversal at a period of 1 ms, there are also slow reversal techniques. The Insertable Half Wave Plate (IHWP) located in the trajectory of the laser beam before the Pockels Cell changes the helicity of the beam. It was inserted about every 8 hr to alter the polarization of the laser and thus the electron beam. The beam position differences generated by optical elements in the Pockels Cell during fast reversal can have a changed sign from IHWP “IN” state to “OUT” state. The combined beam position differences were suppressed when two data segments with opposite IHWP states were combined, reducing the size of the HCBAs.

The photocathode was a p-doped strained-superlattice GaAs/GaAsP wafer, with a QE anisotropy of about 4%. The yield of photoelectrons depends on the orientation of the incident light. During helicity reversal, the change of laser polarization could cause a false asymmetry, referred to as Polarization Induced Transport Asymmetry (PITA). Charge feedback from the measured electron beam current was utilized to slightly change the high voltage of the Pockels Cell, providing equal amounts of electrons in different helicity states.

A Double-Wien filter system was composed of a horizontal Wien and a vertical Wien

filter (see details in [8]). This could reverse the polarization of the beam, and it was carried out every month during the experiment. The Wien reversal helped reduce the HCBAs, especially the differences in the beam spot size (not like energy, position and angle which were constantly monitored by series of beam position monitors).

2.3 Polarimetry

In order to measure the polarization of the beam, two independent methods were utilized in this experiment, Møller [9] and Compton polarimeters. The former is invasive and performed periodically, 2-3 times per week, and the latter is non-invasive and provided a continuous measurement.

For the Møller polarimeter (see Fig. 2.4), the polarized electron beam is incident on a magnetized Fe film target with an asymmetry that can be precisely analyzed. The valence electrons were polarized while the inner shells resulted in a largest uncertainty due to Levchuk effect [10]. Also since this was performed at a low current $\sim 2 \mu\text{A}$, a conservative uncertainty was assigned to the extrapolation to high current. In Run 1, an additional uncertainty for short in one of the quadrupoles was added, which was absent in Run 2.

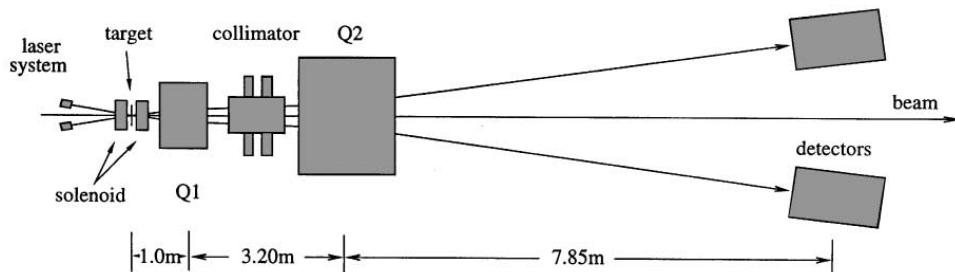


Figure 2.4: Layout of the Møller polarimeter [9].

The Compton polarimeter setup is shown in Fig. 2.5. The optics table was located 57 cm below the beam. A coherent laser was locked to an ~ 80 cm long optical cavity that crossed the electron beam at an angle of 1.3° . Compton scattered photons were measured with photon detector and the recoil electrons were detected by a set of micro-strip detectors to

analyze their momentum. An asymmetry with respect to the helicity state of the electrons as a function of the electron momentum was compared to QED calculation to determine the electron polarization.

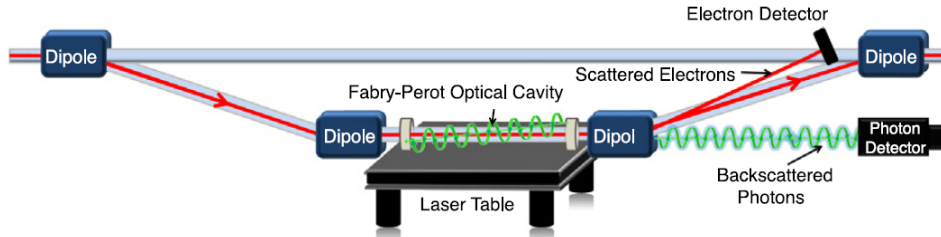


Figure 2.5: Layout of the Compton polarimeter [7].

In the middle of Run 1, the Compton polarimeter was commissioned to take polarization data continuously, with a statistical error of about 1% at run level (in Run 2 this improved to 0.5%). And as mentioned earlier, a broken quad in Møller polarimeter resulted in its larger uncertainty in Run 1. For Run 2, the more productive part of the experiment, both polarimeters functioned properly and the beam polarization obtained from the Compton measurements at a current of $\sim 180 \mu\text{A}$ was consistent with Møller results that ran at a lower current.

2.4 Beamline Measurements

Six beam charge (or current) monitors (BCM) were utilized in this experiment, labeled BCM1-2, 5-8. They were located upstream of the target at distances of 16 m (BCM5, 7, 8), 13.4 m (BCM1, 2) and 2.7 m (BCM6) to perform continuous measurement of the beam current. BCM1 and BCM2 used analog receivers while BCM5-8 used digital receivers. BCM7 and BCM8 were added between Run 1 and Run 2. Because of the nonlinearity of the detector ($\sim 1\%$), detector asymmetry plus charge asymmetry results in a systematic error. Therefore a small charge asymmetry was desired. To achieve this, a charge feedback system was utilized to change the voltage of the Pockels Cell to null the change in beam

current. A small charge asymmetry (IA) was typically averaged to below 40 ppb for both Run 1 and Run 2.

Stripline monitors were unitized to continuously monitor beam positions along the beamline. A linear least square fit of 4 or 5 such monitors 1.5-10 m upstream of the target determined the position and angle of the beam at the target. The typical resolutions are $\sim 1 \mu\text{m}$ and $\sim 150 \mu\text{rad}$ for position and angle, respectively.

In the arc of the Hall C beamline, the BPM readings can reflect the change in the beam energy. In the highest dispersion region, BPM3C12X¹ was utilized to help characterize the energy property of the beam. Since the BPM in the arc is also sensitive to the change of position and angle of the beam at the target, a relative energy difference can be built upon BPM3C12X, targetX, targetX'²:

$$\frac{\Delta E}{E} = \frac{\Delta X_{3C12X}}{411} - \frac{\Delta X_{target}}{596} + \frac{\Delta X'_{target}}{0.443}, \quad (2.1)$$

where in the numerator Δ represents the difference between the BPM readings for two helicity states. The units here are cm for position and radian for angle. The three quantities, readings of a BPM in the arc region, position and angle at the target, are linearly combined with the factors in the denominator in order to remove the non-energy responses in the BPM3C12X and determine the residual response of this BPM to the change in beam energy.

HCBAs are important sources of false asymmetries in our results, and they are already greatly suppressed by careful management at the polarized source and the symmetric layout of the detector array. But still monitoring of the beam parameter differences during the experiment with the BPMs described above provided essential information for us to further remove the HCBAs, including X (horizontal position), X' (horizontal angle), Y (vertical position), Y' (vertical angle) and E (energy). For this purpose, we need to know

¹The postfix X represents the horizontal reading for a specific BPM.

²The targetX' can also be written as targetXSlope.

the sensitivity of the detector signal to the change of these beam parameters to actually calculate the size of the false asymmetries, the sum of which is A_{beam} , defined as³

$$A_{\text{beam}} = - \sum_{i=1}^5 \frac{\partial A}{\partial \chi_i} \Delta \chi_i, \quad (2.2)$$

where $\partial A/\partial \chi_i$ are the measured detector sensitivities and $\Delta \chi_i$ are the corresponding five beam parameter differences.

To measure these sensitivities, natural jitter of the beam can be used via regression of the detector asymmetry to these parameter differences. Also, a more reliable and effective measure was taken during the experiment to help determine these sensitivities in a controlled manner by varying the beam parameters with the beam modulation system. Air-core magnets along the beamline and one of the accelerator cavities modulated the trajectory and energy of the beam at a frequency of 125 Hz. The parameters were modulated in greater amplitude than natural jitter and in a relatively well-separated manner in order that the sensitivities due to different parameters can be better decoupled.

2.5 Hydrogen Target

The liquid hydrogen (LH₂) target (see Fig. 2.6) was mainly composed of a cell with thin aluminum windows that allowed beam to interact with H₂, a centrifugal pump to circulate the liquid in the closed loop, and a heat exchanger to remove the heat deposited by the beam. The energy absorbed by the H₂ target from the beam is 2.1 kW, with an extra 0.7 kW for other the heat load in the components of the loop system.

The LH₂ cell (Fig. 2.6A) had a conical shape with an angle of 14° to allow a safe pass of scattered electrons at the acceptance angle of 5.8°-11.6° (see Table 2.1) required for this experiment. The inner segments of the target cell was simulated with computational fluid

³The negative sign in Eq. 2.2 is for historical reasons, to be consistent with other asymmetry correction terms.

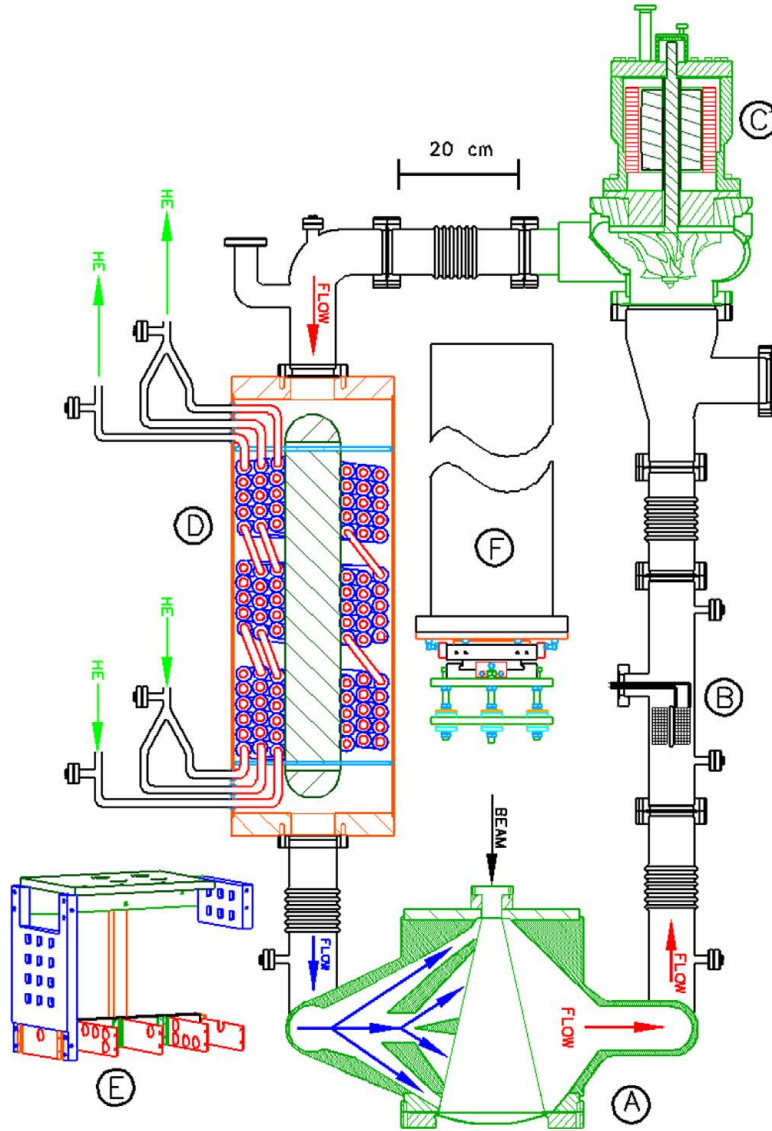


Figure 2.6: Schematic of the liquid hydrogen target used by Q_{weak} experiment [7]. (A) beam cell, (B) heater, (C) centrifugal pump, (D) heat exchanger, (E) solid target ladder, (F) steel pipe support and adjustment.

dynamics. The flow of liquid hydrogen was transverse with respect to the beam axis, with a speed of about several meters per second. The entrance and exit windows of the cell were made of Al alloy, with about 2 cm and 30 cm in diameter, 0.1 mm and 0.6 mm in thickness, respectively. The exit window also had a curvature of about 25 cm with a thinner spot in the center for unscattered electrons.

The temperature of the target was kept at 20.00 ± 0.02 K via the heat exchanger with helium coolant (Fig. 2.6D) and the heater (Fig. 2.6B) with temperature feedback. The head exchanger removed the 2.1 kW from the target. The heater kept the target from freezing when the beam was off. When the intensity of the beam changed, the heat exchanger and the heater were also able to maintain a constant temperature in the target.

The target noise from density fluctuations contributed to the noise of the measured main detector asymmetry. The fast helicity flipping increased the statistical error per window and at the same time was able to suppress those low frequency noises from the target.

2.6 Collimating System

The main components of the collimating system were three lead collimators (see Fig. 2.2 or Fig. 2.7) with eight apertures each, located downstream of the target at 0.7 m, 2.7 m and 3.8 m respectively. With thicknesses of 11-15 cm, they provided cleanup and defined the acceptance of scattered electrons.

A pair of tungsten blocks could be inserted behind two opposing apertures of the first collimator for background studies. Lead lintels were installed between magnet coils to block neutral line-of-sight events from the inner apertures of the defining collimator. To reduce the backgrounds from the aluminum beamline pipes, a water-cooled tungsten-copper beam collimator was installed in the central aperture of the first collimator, which defined a maximum angle of 0.88° for the central beam after the target. Around the beamline at the second collimator, a 5 cm (upstream) and 30 cm (downstream,

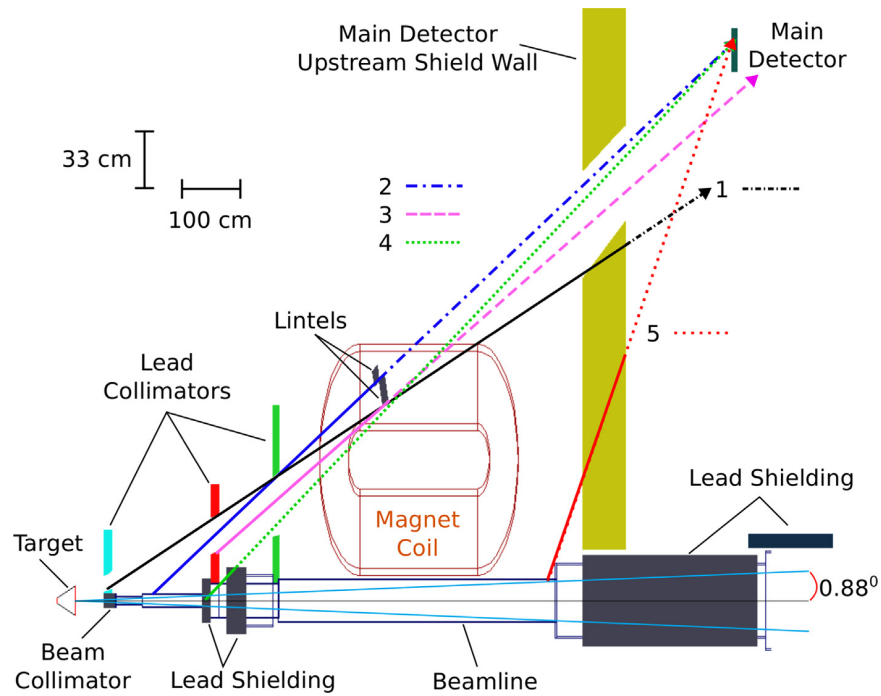


Figure 2.7: Schematic of cross section of the collimator system. Different sources of neutral backgrounds are represented by colorful lines, which are solid until shielded by the collimating system [7]. (1) neutral particles from the target, (2) the first region of the beamline, (3) inner apertures of the defining collimator, (4) upstream face of the defining collimator, (5) third region of the beamline.

after Run 1) lead shielding were installed. Concrete shielding enclosed the region between the first and second collimators and the main detector region. Lead shielding around the beamline was also installed in the enclosed shield hut of the main detector.

2.7 QTOR Spectrometer

The Q_{weak} toroid (QTOR) magnet spectrometer focused the elastically scattered electrons within the acceptance defined by the collimators onto the eight fused silica detectors. It could separate the elastic electrons from the inelastic ones and also prevent the neutral events from reaching the detectors. The QTOR spectrometer consisted of eight resistive coils 6.5 m downstream of the target. The coils were made of copper bar with cooling water flowing in the central hole. The iron-free spectrometer was supported by aluminum frames.

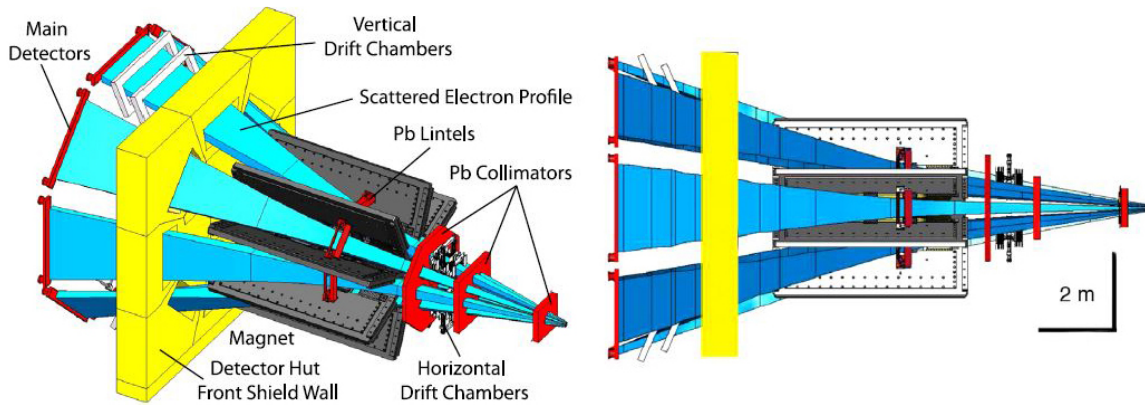


Figure 2.8: Scattered electron profile defined by the collimators, spectrometer and main detector shielding [7].

The QTOR spectrometer, together with the collimator system, is shown in Fig. 2.8. The scattered electrons were defined by the triple collimator system and deflected in the magnetic field generated by the QTOR spectrometer magnets, through the apertures in the upstream shielding wall of main detector hut and then focused onto the detector plane.

2.8 Main Detectors

The main detector array was composed of eight Cherenkov detectors, which were symmetrically located around the central beam. Each of the detector consisted of two $100\text{ cm} \times 18\text{ cm} \times 1.25\text{ cm}$ synthetic quartz bars and two $18\text{ cm} \times 18\text{ cm} \times 1.25\text{ cm}$ light guides glued together. PMTs were installed on downstream sides of the light guides. 2 cm thick lead pre-radiators were installed in front of each detector to suppress neutral backgrounds.

During the integration mode for the main detector, the electrons incident at each detector were at a rate of 850 MHz. The raw current of each PMT was read out and then the pedestal was subtracted and the beam current from BCMs was used for normalization. The gain of the PMT degraded over time and the beam current was increased gradually throughout the experiment. Fig. 2.9 shows the normalized PMT yield vs run number in this experiment.

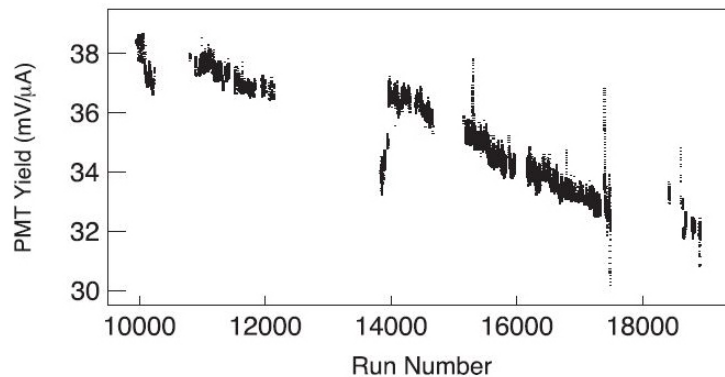


Figure 2.9: PMT yield versus run number [7].

The width of the main detector asymmetry is about 230 ppm, with sources from BCM instrumental noise, target density fluctuation, BCM resolution, target density fluctuation and non-linearities in detector or BCMs. The RMS of the asymmetry over time (see Fig. 2.10) is relatively stable over the experiment, with Run 1 slightly higher than Run 2.

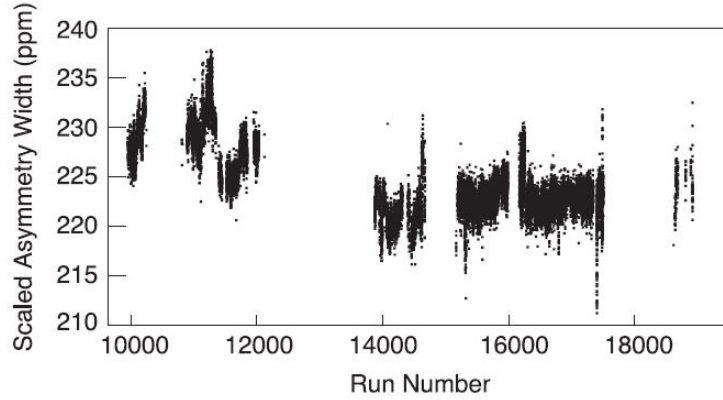


Figure 2.10: Main detector asymmetry RMS (scaled by $\sqrt{\text{beam current}/180 \mu A}$) vs run number [7].

2.9 Tracking System

The tracking system was mainly used to measure the acceptance-weighted average of four-momentum transfer, $\langle Q^2 \rangle$ during the event mode. Under such low current, the tracks of individual scattered particles can be determined. The detector operated at event mode and low-gain was switched to high gain in order to see the individual particles.

The system was composed of four horizontal drift chambers (HDCs) and four vertical drift chambers (VDCs) and two scintillators. The HDCs and VDCs were located upstream and downstream of the QTOR magnets, respectively. The scintillators were positioned between the VDCs and the main detectors. During integration mode, the tracking system was retracted outside of the acceptance.

The HDCs determined the trajectory of the scattered electrons before the QTOR magnet. By tracking the trajectory back to the target, the scattering angle can be determined to derive the value of Q^2 . After deflection in the magnet, the trajectory can be determined by the VDCs. With combination of knowledge of magnet field and both trajectories before entering and after exiting the field, the momentum of the electron can be determined to distinguish elastic events from inelastic ones. The elastic Q^2 distribution within the acceptance can be found this way to provide an acceptance-weighted average.

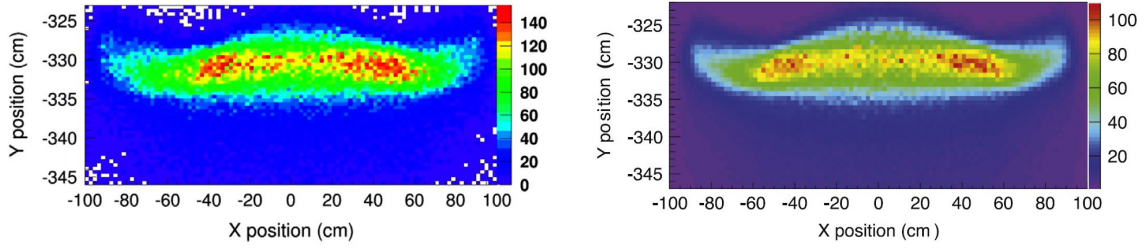


Figure 2.11: Profile of electron flux in the main detector (bottom octant) [7]. *Left*: VDC projection of electron tracks in the main detector. *Right*: electron flux scanned by focal plane scanner. The scale is relative electron flux.

The tracking mode utilized a beam current of <100 pA while the production run with integrating mode was typically under a current of >100 μ A. A focal plane scanner, a small Cherenkov detector ($1\text{ cm} \times 1\text{ cm}$) in the bottom octant, was used to match the tracking results to high current. The scanner can be operated at both event mode and integrating mode and was movable with a 2-D driven system to determine the profile of the electron flux in the focal plane. In Fig. 2.11, the scanned electron flux from focal plane scanner agreed well with the projection of the VDC tracks to the main detector.

2.10 Background Detection

Four luminosity monitors, synthetic quartz bars with a dimension of $27\text{ cm} \times 7\text{ cm} \times 2\text{ cm}$ each, were located on the upstream face of the second collimator, 2.7 m downstream of the target, close to the beam line. They detected electrons with a scattering angle of $\sim 5^\circ$.

Eight downstream luminosity monitors were installed 17m downstream of the target, inside the beam pipe, which detected electrons with a scattering angle of only 0.5° . Each of these had a dimension of $4\text{ cm} \times 3\text{ cm} \times 1.3\text{ cm}$ and was covered in the front with 2 cm lead pre-radiator. Because of the small forward angle and resulting small parity asymmetry, the downstream lumis provided false asymmetry studies related to the main detector.

One complete detector which was identical to each of eight main detectors, the “ninth” detector, was located in the super-elastic region in the main detector hut to measure the

diffuse background. Other background detectors in the hut included PMTs in dark boxes placed in the super elastic region as well. One bare PMT was used to measure “PMT background” and the other PMT had the same lightguide part used in main detectors glued to it to measure background in PMT+lightguide.

2.11 Electronics and Software

The voltage outputs from the detector and beam monitor pre-amplifiers or BCM receivers were collected and sampled by Q_{weak} 18-bit sampling ADCs (VQWKs) at a rate of 500 kHz. With a 960 Hz helicity reversal rate and exclusion of delay & settling time, a total of 464 samples were collected and averaged for the stable time in each helicity state⁴. To digitize all the detectors, beamline and injector instrumentation, a total of 32 VQWK modules with eight input channels each contributed a data rate of 6.5 MB per second. The data was written at file sizes no greater than 1.9 GB. These files were called “runlets”, each of which had about 5 minutes of data. A typical hour-long run included 10-12 runlets. During later analysis, runlet level was usually used to take averages and run asymmetry analysis since the experimental condition was generally stable during the 5 min period. The typical time periods we use for the analysis are listed in Tab. 2.2.

Table 2.2: Typical time period definitions for the analysis.

Name	Approx. Duration	Note
quartet	4 ms	basic unit to form asymmetry etc.
runlet	5 min	for averages and statistical error
run	1 hr	generally stable experiment condition in each run
Slug	1 day	the same Half Wave Plate state in each day
Wien	1 month	beam helicity reversal from Double-Wien filter
Run	several months	experiment intermission and upgrade

The simulation packages included GEANT3 (optimization of acceptance and background studies), GEANT4 (main detector yield optimization and tracking analysis) and

⁴Samples from every quarter of a helicity state was also averaged to “block” level.

GARFIELD (design of the drift chambers).

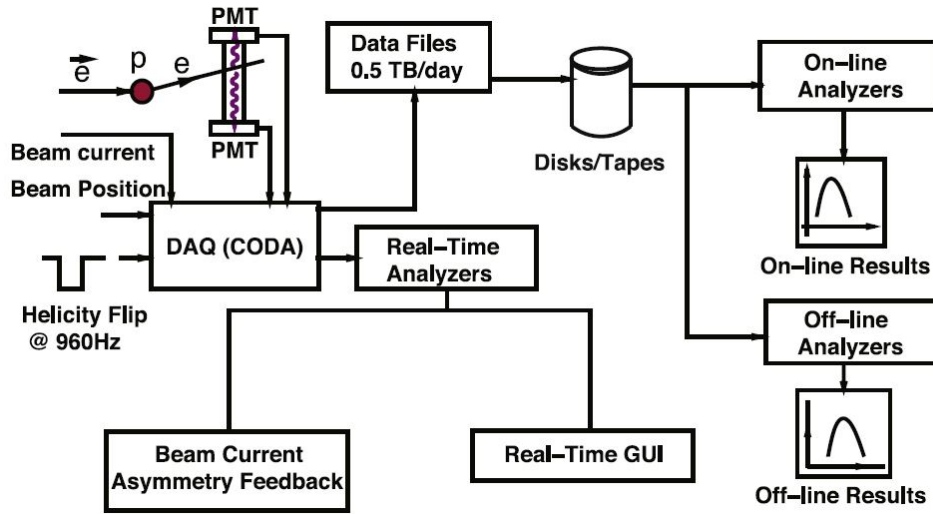


Figure 2.12: DAQ and analysis framework [7].

The analysis framework is shown in Fig. 2.12. For each helicity window, the data acquisition (DAQ) integrated the signals from various detectors and monitors used in this experiment, computed asymmetries, and stored the data on disk. Real-time and on-line analyzers provided information on experimental status and the feedback for beam current control. For off-line analysis, the raw files were processed to form yield and asymmetry from those events that passed basic cuts on beam current & position, signal saturation and hardware faults. The main detector asymmetries were blinded with random factors (different in Run 1 and Run 2) ranging in ± 60 ppb.

Chapter 3

Dithering Correction

Beam corrections were needed to remove false asymmetries in the main detector, which were resulted from helicity correlated beam motion. To connect beam motion with the detector response, beam sensitivities were extracted. The dithering correction utilized the beam modulation method for sensitivity extraction. This chapter gives the description of dithering correction, including beam modulation, beam sensitivity extraction, beam correction calculation and related analysis.

3.1 Helicity Correlated Beam Asymmetries

When the beam helicity state is switched from one state to another, the values of beam parameters from the current helicity window can be slightly different from the previous one. This can be from beam natural motion or a small change of beam trajectory during helicity reversal at the polarized source. These beam parameters include beam energy, position and angle. The beam current parameter change during the helicity reversal was taken out by normalizing main detector yield with beam current measurement, which is in the analysis of Ch. 5.

The beam position and angle are defined and measured at the target, by fitting with several beam position monitors upstream of the target. The beam position and angle at

the target give a convenient visualization of beam trajectory in front of the target before the scattering process. This helps with the analysis and gives a direct physics meaning of the beam sensitivities. The beam energy is measured with the curvature of the beam trajectory along the arc of the beamline, or the dispersion of the beam measured by the beam position monitor located in the middle of the beam arc. The beam energy measurement in this experiment was performed with a linear combination of position and angle at the target, together with a BPM(3C12X) that has the largest dispersion along the beam arc (see Sect. 2.4).

Since the main detector output can be sensitive to beam energy, position and angle, the change of these beam parameters, after being scattered by the target, can result in the change of the main detector yield. Therefore, after forming main detector asymmetry with main detector yields from each helicity state, the variation of these beam parameters during helicity reversal can result in undesired asymmetries in the main detector. These “false” asymmetries from beam energy, position and angle are mixed with main detector parity asymmetry. These asymmetries, related to beam helicity change, are referred to as Helicity Correlated Beam Asymmetries (HCBAs), which are listed in Tab. 3.1.

Table 3.1: Beam parameters for Helicity Correlated Beam Asymmetries.

No.	Parameter	Symbol	Monitor Difference	Sensitivity	HCBA
0	Beam energy	E	dE	S_E	A_E
1	Horizontal position	X	dX	S_X	A_X
2	Horizontal angle	X'	dX'	$S_{X'}$	$A_{X'}$
3	Vertical position	Y	dY	S_Y	A_Y
4	Vertical angle	Y'	dY'	$S_{Y'}$	$A_{Y'}$

To remove these HCBAs from main detector asymmetry, two sets of quantities are required. The first is beam parameter sensitivities (or slopes) that reflect the amount of change in main detector yield due to the changes of beam parameter values. The beam sensitivities provide the quantitative connections between the beam parameters and the main detector yield. The other set of quantities necessary is the beam parameter values

themselves. These were constantly monitored and stored during the experiment via beam position monitors located along the beamline. The change of beam parameters from one helicity to another are beam monitor differences, listed in Tab. 3.1.

$$\begin{aligned} \text{Helicity Correlated Beam Asymmetry} &= \text{Beam Sensitivity} \cdot \text{Monitor Difference} \\ A_x &= S_x \cdot dx \end{aligned} \tag{3.1}$$

With beam parameter sensitivities and beam monitor differences, the HCBA's can be calculated and corrected in the main detector asymmetry. The beam correction term is shown in Eq. 3.2, in which A_{beam} is the beam correction term. The individual A 's from various beam parameters are calculated with the product of beam sensitivity and the corresponding monitor difference (Eq. 3.1). The beam sensitivity is presented by symbol S and the monitor difference is prefixed with d in this thesis. The symbol x in Eq. 3.1 and 3.2 runs through five beam parameters, E , X , X' , Y and Y' . The negative sign introduced in Eq. 3.2 is conventional in this experiment to agree with the signs of other correction terms.

$$A_{\text{beam}} = - \sum_{x=1}^5 A_x = - \sum_{x=1}^5 S_x \cdot dx \quad (x = E, X, X', Y, Y') \tag{3.2}$$

The beam monitor differences were constantly monitored and can be applied to the beam correction term directly. The beam sensitivities must be obtained through some dedicated procedure.

3.2 Beam Modulation

For the beam dithering correction, the modulation system is dedicated to extract detector sensitivities. It was performed during the experiment to provide information for detector and monitor response when the beam was dithered in certain pre-defined ways. The beam modulation system dithers the beam in its five parameters, including energy E , horizontal position&angle, X & X' , and vertical position&angle, Y & Y' . Sine wave signals are provided

by five function generators fge, fgx1, fgx2, fgy1, fgy2. The function generator fge is for beam energy modulation and fgx1 and fgx2 are used to modulate the horizontal position and angle. fgy1 and fgy2 are for vertical position and angle of the beam. The reason we have two function generators in either horizontal or vertical direction is that we have two degrees of freedom in that certain direction.

During the modulation for horizontal position and angle two separate driving patterns were utilized. The function generators fgx1 and fgx2 have the same frequency and are in phase with each other, but the relative amplitude settings for them are different from one modulation pattern to another. Two dithering patterns drive position and angle in different ways, which helps better decouple these two beam parameters for later sensitivity extraction.

Table 3.2: Dithering patterns during beam modulation.

Pattern	Function Generators	Beam Parameters Modulated	Fast Feedback
X1	fgx1, fgx2	Horizontal position and angle	on
Y1	fgy1, fgy2	Vertical position and angle	on
E	fge	Energy	off
X2	fgx1, fgx2	Horizontal position and angle	on
Y2	fgy1, fgy2	Vertical position and angle	on

There are five modulation patterns¹ in total, E, X1, X2, Y1, Y2². Pattern E drives beam energy. Patterns X1 and X2 modulate horizontal position and angle. Y1 and Y2 are for vertical position and angle of the beam. Different driving patterns are listed in Tab. 3.2. The relative amplitude of fgx1:fgx2 changes from pattern X1 to X2 and the same goes for Y1 and Y2. During the energy modulation pattern E, Fast Feedback (FFB) system for locking beam positions was turned off and during other dithering patterns the FFB system was on.

¹“Pattern” is also referred to as “coil” sometimes. For example, coilE represents driving pattern E.

²Pattern numbers documented in file (bm_pattern_number) are mainly 0-4 or 11-15, corresponding to patterns X1, Y1, E, X2, Y2. Pattern groups 0-4 and 11-15 are different sets of modulation amplitude setting for function generators.

3.3 Signal Ramp Fixing

During the modulation of beam parameters, the phase of function generators was recorded as the “ramp” variable at event level. Ideally, the phase increases from 0° to 360° and repeats itself, which forms a ramp-like shape. Since we averaged the phase for the duration of each event (1 ms), the actual phase vs time at the event level looked like Fig. 3.1.

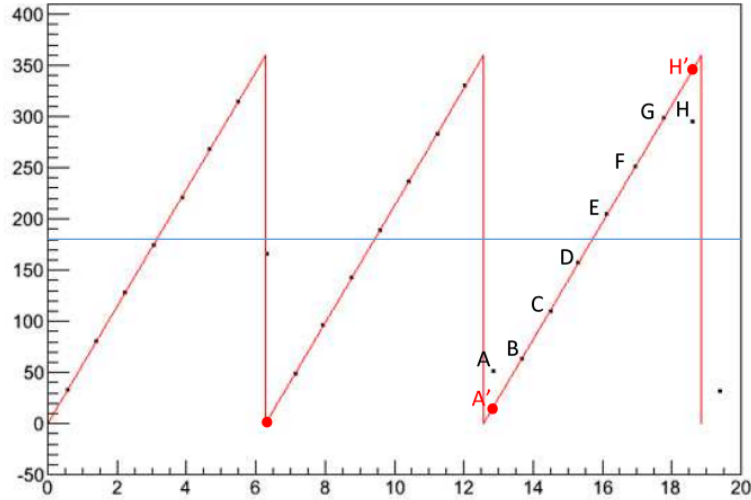


Figure 3.1: Raw ramp vs time. Red line: ideal ramp line. Blue line: average of ramp. Black points: original raw ramp. Red points: corrected ramp from bad ramp points.

In Fig. 3.1, the black points are read from the file at event level. Each ramp cycle contains about 7 consecutive windows. Ideally, the black points should lie on the red line. While most of the ramp points sit on the red line, a few ramp events do not. For the ramp around 180° , the original phase signal increased gradually and the averaging at event level left averaged ramp points on the line. The averaged ramp for these events gives “healthy” average values that can increase linearly with time. But for the events near 0° or 360° , since the phase jumped from 360° to 0° , the averaging at event level gave a value inbetween. These points don’t change linearly with time and can affect the fitting of modulation response vs ramp plots later. Therefore these “bad” ramps should be fixed.

The approach to ramp fixing presented here is to remap and rescale the ramp. Details of the procedure will be described afterwards. To begin with, a few features of the original

raw ramp are listed and discussed below.

3.3.1 Features of Raw Ramp

1. The average and range of raw ramp. The original raw ramp lies approximately within 0-360°. The average of raw ramp is around 180° (shown as the blue line in Fig. 3.1). This is only “generally” true because actually the average might not be exactly 180° and the range of raw ramp, even after initial fixing of the bad ramps, might not take the full range of 0-360°;however, this will be accounted for during complete procedure of ramp fixing. For the moment they are referred to as raw ramp average and range. In the end, the rescaled ramp will have its average as 180° and range from 0° to 360° to allow for accurate fitting of detector or monitor modulation responses to a sine function.

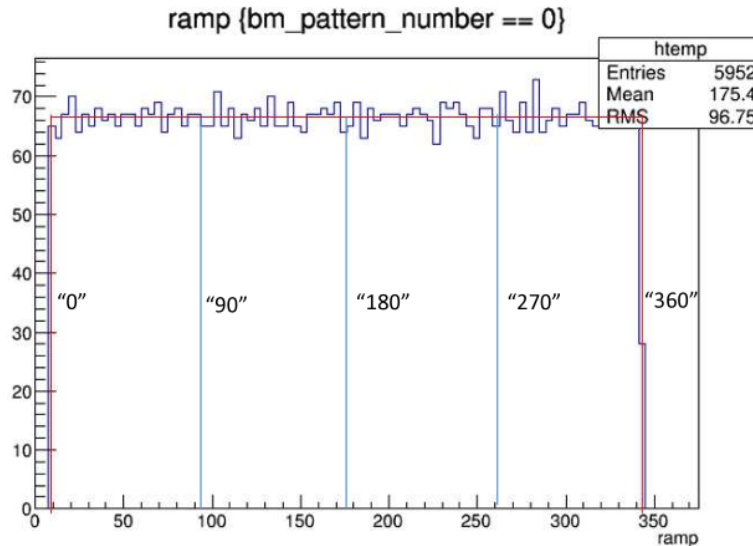


Figure 3.2: Ramp histogram before rescaling. Red rectangle: flat probability distribution. Vertical blue lines: virtual 0°, 90°, 180°, 270°, 360° before rescaling.

Fig. 3.2 shows a ramp distribution for a modulation pattern, in which the central average is about 175° and the range is from 5° to 345°. The vertical lines are “virtual” lines for the phases of interest, which will be rescaled to ensure an actual full range of 360°.

2.Stability of raw ramp average and range. Each modulation period contains thousands of ramp cycles. Fig. 3.1 shows only about three ramp cycles, and for each only the

modulation duration of a specific pattern are shown. The raw ramp average is pretty stable for the modulation period, and the raw range is firm for these ramp cycles as well. But from one modulation period to another, the average and range might change. Therefore ramp fixing is done for each modulation period.

3. Categories of raw ramp points. The original raw ramp could be classified as “healthy” or “bad” points. Each of such main categories could be further divided into two sub-categories: those ramp points that are higher than raw ramp average and those lower than that threshold. All four categories are summarized below.

- “Healthy” ramp, consecutive and linearly increases with time
 - “healthy high” ramp, higher than raw average
 - “healthy low” ramp, lower than raw average
- “Bad” ramp, not falling on the ramp lines
 - “bad high” ramp, higher than raw average
 - “bad low” ramp, lower than raw average

The “healthy” and “bad” classification is largely qualitative, done by eye, but the “high” and “low” criteria can be quantitatively verified against the raw ramp average. The significance of such ramp classification will be discussed in the procedure of ramp fixing.

3.3.2 Ramp Fixing Procedure

Step 1: Take the average of raw ramp.

$$\bar{\theta}^{\text{Raw}} = \frac{\sum_{i=1}^{N^{\text{Raw}}} \theta_i^{\text{Raw}}}{N^{\text{Raw}}}, \quad (3.3)$$

where $\bar{\theta}^{\text{Raw}}$ is the average of the raw ramp θ_i^{Raw} . Index i runs from 1 to N^{Raw} , the number of raw ramp events in the duration of a modulation pattern. Basically, this is to calculate the vertical position of the blue line shown in Fig. 3.1, except that this is done for

thousands of ramp cycles. The average value $\bar{\theta}^{\text{Raw}}$ is close to 180° . As discussed in Sect. 3.3.1, for so many ramp cycles, this raw ramp average is stable and can serve as certain criteria for the procedure afterwards.

Step 2: Remap the raw ramp based on “high” or “low” ramp type.

To remap the ramp, the raw ramp value is compared with the average of raw ramp calculated in the last step. If the raw ramp is higher than average, take the two raw ramp points on its left (two previous raw ramps) to linearly correct it and generate a new remapped ramp. If the current raw ramp is lower than average, take the two raw ramps on its right (two raw ramps afterwards) to calculate the remapped one.

$$\theta_i^{\text{Remap}} = \begin{cases} 2 \cdot \theta_{i-1}^{\text{Raw}} - \theta_{i-2}^{\text{Raw}}, & \text{if “high” } \theta_i^{\text{Raw}} > \bar{\theta}^{\text{Raw}} \\ 2 \cdot \theta_{i+1}^{\text{Raw}} - \theta_{i+2}^{\text{Raw}}, & \text{if “low” } \theta_i^{\text{Raw}} < \bar{\theta}^{\text{Raw}} \end{cases} \quad (3.4)$$

In Eq. 3.4, the criteria is the average of raw ramp, $\bar{\theta}^{\text{Raw}}$. Whether the current raw ramp is higher or lower than this criteria, it is rebuilt and linearly remapped using two adjacent raw ramps. This is done for all the ramps in this modulation pattern period.

The remapping procedure above can be justified by the fact that each ramp cycle contains at least six “healthy” consecutive raw ramp points and only one “bad” isolated raw ramp³. The four categories of ramps listed in the last section can be examined to verify that step 2 can always produce a “healthy” remapped ramp.

If the current raw ramp is “healthy high” (like points E, F, G in Fig. 3.1), the two raw ramps on its left are “healthy” as well; so a remapping of the current ramp gives “healthy” ramp, which almost coincides with the original raw one. The same applies for “healthy low” raw ramp (points B, C, D in Fig. 3.1) remapped using the two “healthy” raw ramps on its right. The remapped and raw ramps for this point also almost coincide with each

³With lower modulation frequency, the number of consecutive ramp points can become more and instead of two points used in this experiment, potentially more adjacent raw ramps can be used to remap ramp.

other because of the linear nature of the good consecutive ramp points. As for the "bad high" raw ramp (point H in Fig. 3.1), since it is isolated, the two raw ramps on its left are "healthy" and can be used to remap it. Only this time the remapped ramp is moved upward to its rightful position, linearly positioned along with other "healthy" ramps in the ramp cycle, which sits right on the ramp line (red line in Fig. 3.1). The same can be reasoned for "bad low" raw ramps (point A in Fig. 3.1), for which the newly remapped one lies below the original and sits linearly with other ramps. Remapping for the four different types of ramps are listed below.

Table 3.3: Raw and remapped ramp for four different ramp types.

Ramp Type	Raw Ramp		After Remapping	
	On Ramp Line	Position	On Ramp Line	Position
"Healthy High"	Yes	above average	Yes	coincide with raw
"Healthy Low"	Yes	below average	Yes	coincide with raw
"Bad High"	No	above average	Yes	above raw
"Bad Low"	No	below average	Yes	below raw

In Tab. 3.3, after remapping, all four categories of ramps sit on ramp line. The "bad" raw ramps were not on the line initially but after remapping the newly obtained points moved onto the line. And "healthy" ramps are basically unmoved and kept along the ramp line all the time. A clean ramp-like shape is generated for each ramp cycle after remapping.

Special care had to be taken for the first and last two ramps of each modulation period. For example, if the first raw ramp is higher than average, according to step 2, it should rely on its previous two ramp points for remapping; however, since it is the first one, this can't be done and this ramp point is discarded. For other ramps in the very beginning and end of the pattern duration, if the condition in Eq. 3.4 can be satisfied, they are remapped along with other tens of thousands ramps in the modulation pattern period. The same situation can happen during the run whenever the event counter is discontinuous or simply when some events are just missing; the one or two ramps near these positions are un-fixable with the procedure above and should be discarded. Fortunately such outliers are

pretty rare out of the large number of events we can recover.

Step 3: Rescale ramp to full range.

As described in Sect. 3.3.1, the remapped ramps don't usually average on 180° and the ramp range does not take $0\text{-}360^\circ$. The remapped ramp should be rescaled to bring its average to 180° and the range to 360° so that the sine function can be fit properly for detector and monitor modulation responses.

From Fig. 3.2, the ramp has a flat probability distribution. Even though the range is not full 360° , the ramps still distribute evenly from the minimum to the maximum within its original range. The rescaling step here tries to bring the “virtual” 90° and 270° lines to their rightful places so that the new flat distribution can center on 180° and range between 0° and 360° . The procedure of ramp rescaling is shown below.

First, take the average of remapped ramp by

$$\bar{\theta}^{\text{Remap}} = \frac{\sum_{i=1}^{N^{\text{Remap}}} \theta_i^{\text{Remap}}}{N^{\text{Remap}}}. \quad (3.5)$$

Here $\bar{\theta}^{\text{Remap}}$ is the average of remapped ramp, which is very close to the average of raw ramp, $\bar{\theta}^{\text{Raw}}$, provided by Eq. 3.5 in step 1. The index i runs through the number of remapped ramp, N^{Remap} , which has fewer events than N^{Raw} because of the special treatment of a few events mentioned in step 2.

Second, calculate the flat width of remapped ramp distribution:

$$\sigma^{\text{Remap}} = \frac{\sum_{i=1}^{N^{\text{Remap}}} \left| \theta_i^{\text{Remap}} - \bar{\theta}^{\text{Remap}} \right|}{N^{\text{Remap}}}, \quad (3.6)$$

where σ^{Remap} is the width of flat distribution for the remapped ramp. It has a “virtual” size of 90° for the ramp before rescaling, which will serve as calibration next.

Third, we need to establish the connection between ramps before and after rescaling:

$$\theta_i^{\text{Rescaled}} = a \cdot \theta_i^{\text{Remap}} + b, \quad (3.7)$$

in which $\theta_i^{\text{Rescaled}}$ is the rescaled ramp. Free parameters a and b are to be solved based on certain conditions. Assume the “virtual” 90° and 270° lines from the original flat distribution (Fig. 3.2) are relocated to actual 90° and 270° positions after rescaling; we then have an equation set for solving free parameters a and b :

$$\begin{cases} 90^\circ &= a \cdot (\bar{\theta}^{\text{Remap}} - \sigma^{\text{Remap}}) + b \\ 270^\circ &= a \cdot (\bar{\theta}^{\text{Remap}} + \sigma^{\text{Remap}}) + b \end{cases}. \quad (3.8)$$

In the equations above, since the average of remapped ramp $\bar{\theta}^{\text{Remap}}$ effectively represents the “virtual” 180° line (Fig. 3.2), and the remapped ramp width σ^{Remap} has a size of “ 90° ”, the quantities $\bar{\theta}^{\text{Remap}} - \sigma^{\text{Remap}}$ and $\bar{\theta}^{\text{Remap}} + \sigma^{\text{Remap}}$ give “ 90° ” and “ 270° ” lines respectively before rescaling.

After solving Eq. 3.8 and plugging the results into Eq. 3.7, we have the equation for ramp rescaling:

$$\theta_i^{\text{Rescale}} = \frac{90}{\sigma^{\text{Remap}}} \cdot (\theta_i^{\text{Remap}} - \bar{\theta}^{\text{Remap}}) + 180, \quad (3.9)$$

where $\theta_i^{\text{Rescale}}$ is the rescaled ramp (Eq. 3.7) and θ_i^{Remap} is the remapped ramp (Eq. 3.4). $\bar{\theta}^{\text{Remap}}$ and σ^{Remap} are the average (Eq. 3.5) and width (Eq. 3.6) of remapped ramp. The index i runs from 1 to N^{Remap} and the rescaling should be applied for every remapped ramp. After this step, the rescaled ramp can range evenly between 0° and 360° with an average of 180° .

3.3.3 Comparison between Raw and Fixed Ramp

Through the procedure in Sect. 3.3.2, the raw ramp is remapped and rescaled. The fixed ramp points sit on the ramp line and have a full range of 360° . To compare the raw and fixed ramp, an example from one of the function generator signals is shown in Fig. 3.3.

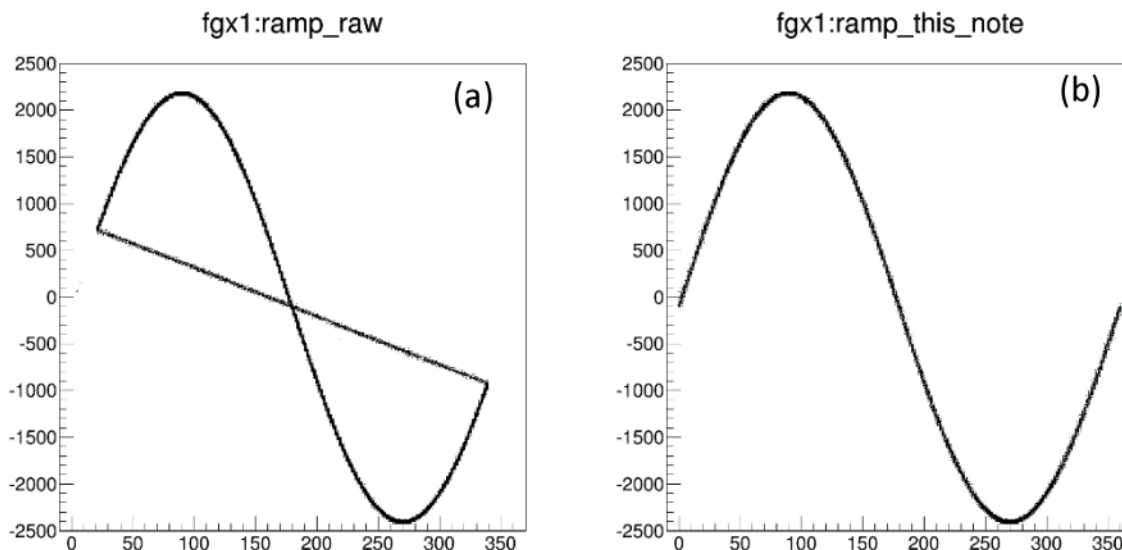


Figure 3.3: Comparison between raw and fixed ramp. (a): fgx1 vs raw ramp. (b): fgx1 vs fixed ramp.

In Fig. 3.3, the behavior of function generator fgx1 vs ramp is shown. This could be from other function generators as well, or the modulation response from main detector or beam monitor, which have similar phenomena as shown here. The plot on the left is fgx1 vs raw ramp before remapping and rescaling. It is a sine curve in general but there is a straight line that could affect proper sine fitting. The straight line is composed of “bad” raw ramp points (like points A, H in Fig. 3.1) from all ramp cycles during this modulation period. After ramp fixing, on the right hand side, the “bad” ramp points were fixed and moved towards both ends of the sine curve. We now have a clean sine curve. The rescaling of ramp also made sure that the period is 360° . Now we could fit the plot on the right with a normal sine function to extract dithering coefficients (amplitudes of modulation responses) for detectors and monitors.

3.4 Dithering Quality Checking

3.4.1 Dithering Coefficients

During beam modulation, the driving signals modulated the beam trajectory and energy. The detectors and monitors that were sensitive to the modulated beam parameters had dithering responses. With respect to fixed ramp from Sect. 3.3, the dithering response of detector or monitor has sinusoid form. The amplitude of sine wave represents how sensitive the device is to the modulated beam parameters. To find the amplitude quantitatively, a sine function is used to fit the dithering response against ramp. The amplitudes of sine or cosine curves are dithering coefficients of the detector or monitor.

The sin function used to fit the dithering response against the ramp is

$$Y = A \cdot \sin(\theta + \phi) + C, \quad (3.10)$$

where Y is output of the detector or monitor, θ the ramp and ϕ the phase when ramp is zero. The amplitude, A , is the strength of dithering response and C is the central value. To see the sine and cosine parts more clearly with a linear function, an equivalent and more convenient form of fitting is to break Eq. 3.10 into the sine and cosine responses:

$$Y = A \cdot \sin(\theta) + B \cdot \cos(\theta) + C. \quad (3.11)$$

Here dithering coefficients A and B are amplitudes of modulation responses from sine and cosine parts. Since the function generator signals are sine wave, it is convenient to refer to the sine and cosine responses in Eq. 3.11 as “in-phase” and ”out-of-phase” with respect to the driving signal. Therefore A and B are in-phase and out-of-phase dithering coefficients for the detector or monitor (see Tab. 3.4).

The dithering coefficients give the size of modulation responses in the detector or monitor. For each dithering pattern, several beam parameters were modulated. By

Table 3.4: In-phase and out-of-phase dithering coefficients.

Dithering Coefficients	Symbol	Response
Sine	A	in-phase with respect to modulation
Cosine	B	out-of-phase with respect to modulation

examining the dithering coefficients of the beam parameters, we know what beam properties were modulated for this pattern. And by looking at the size of dithering coefficients in a certain detector or monitor, we could have an idea which beam parameters could change output of the device we are interested in. If the dithering coefficient is high, it means the detector or monitor is sensitive to the beam parameters that were modulated. However, if the dithering coefficient is small, we know that the device is not sensitive to the beam change from this pattern.

In Eq. 3.11, fitting parameter C is the central value of the device output during modulation⁴. Normally we are more interested in the change of signals, dithering coefficients A and B . But for detectors, since the asymmetry is defined as amount of yield change divided by yield average under helicity reversal, the dithering coefficients for detectors should be modified to adapt the definition of asymmetry for later application. Therefore, the detector coefficients A and B from Eq. 3.11 are divided by the central value C . Now the units for the detector coefficients can be ppb or ppm, just like detector asymmetry.

When fitting dithering response vs ramp, not only can coefficients A and B can be obtained, but also the error of coefficients were calculated, which are represented by ΔA and ΔB here. The source of error is from beam natural motion. The beam width is often comparable to the amplitude of driven motion, but with many repeated ramp cycles in a modulation period the error of dithering coefficients from random beam natural fluctuation is averaged down with respect to the amplitude of its modulation response. The error of a dithering coefficient can help tell us if the coefficient is significantly non-zero; these error

⁴Symbol C with a subscript i , C_i , stands for dithering coefficient from a certain modulation pattern, which will be shown in Sect. 3.4.2.

quantities from different modulation patterns are useful for the quality of the dithering data, as seen in Sect. 3.4.4.

3.4.2 Sine and Cosine Dithering Patterns

The modulation signals applied for functions generators were pure sine wave, and the beam parameters were driven in sine form as well. We expect to only see a sine dithering response, if there is any, in a detector or monitor. The cosine dithering coefficient obtained in Eq. 3.11 should be vanishing within its error.

However, as noted in Tab. 3.2, for most of the modulation patterns, including X1, X2, Y1, Y2 (modulating beam position and angles at the target), the Fast Feedback system was on. The modulation system tried to drive the beam out of position while the FFB system tried to lock the beam in position. Therefore, the FFB system functioned effectively as the second driving force during beam modulation. There was a short delay for the FFB to react when the beam was modulated, so the driving signal from the FFB system was partially out of phase with respect to the sinusoid driving signal from the original modulation system. The combined driving force from the modulation system and FFB system has both sine and cosine signals.

$$\text{Combined driving system} \left\{ \begin{array}{l} \text{Original Modulation system} \longrightarrow \text{Sine driving signals} \\ \nearrow \\ \text{FFB system (X1-Y2 patterns)} \longrightarrow \text{Cosine driving signals} \end{array} \right.$$

In detectors and monitors, the sine signals of the combined driving system result in in-phase responses (non-zero dithering coefficients A in Eq. 3.11), and the cosine driving signals cause out-of-phase responses (non-zero dithering coefficients B in Eq. 3.11). As a consequence, for the modulation patterns when FFB was on, we could observe both in-phase and out-of-phase responses with respect to modulation signal. However, for the energy dithering pattern, the FFB was off, so only in-phase coefficients were apparent in

detectors and monitors during energy modulation.

If there are only sine driving signals, we have five modulation patterns designed that could be used to extract coefficients and calculate five dithering sensitivities. But since there are also cosine driving signals that resulted from the FFB system, we have, effectively, an extra set of modulation patterns. These extra modes add to the sine driving modes. Therefore, the total number of modulation modes is nearly doubled (no cosine response in energy pattern). These ten modulation modes are indexed and listed below.

Table 3.5: Dithering patterns for both in-phase and out-of-phase responses.

Pattern No.	Modulation Type	Fast Feedback	Response	Modulation Signal
0	X1	on	sine	in-phase
1	Y1	on	sine	in-phase
2	E	off	sine	in-phase
3	X2	on	sine	in-phase
4	Y2	on	sine	in-phase
5	X1	on	cosine	out-of-phase
6	Y1	on	cosine	out-of-phase
7	E	off	cosine	out-of-phase
8	X2	on	cosine	out-of-phase
9	Y2	on	cosine	out-of-phase

In Tab. 3.5, we have ten effective dithering patterns. They are named as pattern 0-9. No. 0-4 are in-phase modulation modes and No. 5-9 are out-of-phase modes. The dithering coefficients could be represented by C_0-C_9 for pattern 0-9. Or, in a more apparent way, the sine and cosine coefficients are labeled as $A_E, A_{X1}, A_{X2}, A_{Y1}, A_{Y2}$ and $B_E, B_{X1}, B_{X2}, B_{Y1}, B_{Y2}$ respectively.

Since the number of diving modes is doubled, we also have doubled the number of coefficients for detectors and monitors. Now we have ten dithering coefficients for a certain device during a complete modulation cycle. Originally, we needed five sets of coefficients to solve for the connections between a device response and five beam parameters. Now, since we have added information, we have extra solutions for these connections.

The original five driving patterns were designed to be sufficiently independent from each

other. This could help better decouple the dithering responses of beam parameters with relatively predictable results. The FFB system also worked as an additional driving force. If the original sine modulation modes were modified by possible superimposed sine responses from the FFB system, we don't know if the original five modes are still relatively independent from each other and whether or not they are still capable of decoupling beam parameters sufficiently. Additionally, the behavior of extra cosine modes from the FFB system are completely unknown. Whether or not the extra modes are well separated from the original modes or each other also becomes a question. Therefore, the relationship between the driving modes should be examined in detail.

3.4.3 Monitor Coefficient Vector

The dithering patterns were designed to make sure all five beam parameters could be properly modulated. Dithering patterns differ from each other by modulating selective parameters. For example, the energy modulation pattern is different from other patterns since it is the only mode that is dedicated to modulate beam energy. Also, the X patterns differ from Y patterns because they dither beam in horizontal and vertical directions separately. Therefore, we almost know by instinct that for sine dithering patterns (from the original modulation system), the three pattern groups, E, X1&X2, Y1&Y2, differ from each other's group in a significant way⁵. But a few questions remain:

- How well are sine patterns X1 and X2 separated? Or Y1 and Y2?
- What is the strength of cosine modulation patterns? How well are they separated?

Since we only know the modulation amplitudes of function generators, in principle we could only predict on some level the original sine responses from the modulation system.

But with FFB on for most of the patterns, new sine driving signals are imposed on original

⁵Here we assume the sine driving signal contribution from FFB system is small compared to sine driving signals from original modulation system.

ones and cosine patterns are also introduced. We don't have output from FFB driving coils. With only the information from function generators, it is not sufficient to answer the questions above.

The questions and their answers are related to dithering quality of the experiment. The modulation pattern combination might be too singular sometimes, which can bring greater error to the dithering correction. Here, a relatively convenient and effective method to check dithering quality and related problems is described. The method utilizes dithering coefficients from beam parameter monitors; it could provide us with lots of useful information about the relationship between dithering patterns.

Introducing Monitor Coefficient Vector

We have five beam parameters (see Tab. 3.1), and for each beam parameter, we have a beam monitor (mostly defined with original stripline BPMs, see Sect. 2.4) to measure it. Therefore, we have five beam monitors E, X, X', Y, Y' that can respond to driving signals from modulation and FFB systems. For different driving patterns (Tab. 3.5), the responses of beam monitors are different but each pattern has a signature in the combination of dithering coefficients from all five monitors. For example, patterns Y1 and Y2 have great responses in Y and Y' monitors while responses from other monitors, E, X, X', are minimal⁶. The signature belongs uniquely to a specific pattern and the five monitor dithering coefficients must be examined at the same time. A straightforward tool to look at a group of numbers simultaneously is naturally a vector. Therefore, we could define Monitor Coefficient Vector (MCV):

$$\mathbf{U}_i = (C_i^E, C_i^X, C_i^{X'}, C_i^Y, C_i^{Y'}) \equiv (C_i^m), \quad (3.12)$$

⁶These responses in horizontal monitors are small but not necessarily zero because in reality vertical patterns could result in small horizontal responses as well.

where \mathbf{U}_i is Monitor Coefficient Vector for dithering pattern i (i takes pattern 0-9, see Tab. 3.5 for all ten dithering patterns). $C_i^E, C_i^X, C_i^{X'}, C_i^Y, C_i^{Y'}$ are dithering coefficients of five beam monitors, and C_i^m represents all vector elements (m takes monitor 0-4, all five beam monitors, see Tab. 3.1).

In Eq. 3.12, Monitor Coefficient Vector \mathbf{U}_i contains all dithering coefficients from five beam monitors under modulation pattern i . It gives the signature of the current dithering mode. Specific driving signals determine a particular set of monitor coefficients. Therefore, the Monitor Coefficient Vector could represent the current pattern, and when compared to MCV from another pattern, the relationship between the two patterns can be revealed. After all, it is the monitor coefficients we use directly for detector dithering analysis.

There is also an alternative definition for MCV in Eq. 3.12. We could divide dithering coefficients C_i^m by their corresponding error ΔC_i^m and define Normalized Monitor Coefficient Vector (NMCV):

$$\tilde{\mathbf{U}}_i = \left(\frac{C_i^E}{\Delta C_i^E}, \frac{C_i^X}{\Delta C_i^X}, \frac{C_i^{X'}}{\Delta C_i^{X'}}, \frac{C_i^Y}{\Delta C_i^Y}, \frac{C_i^{Y'}}{\Delta C_i^{Y'}} \right) \equiv (\tilde{C}_i^m). \quad (3.13)$$

Here, \tilde{C}_i^m is the normalized dithering coefficient for the monitor and m takes 0-4. This definition can make units from different monitors uniform. For example, originally the unit for beam position is millimeter and the unit for beam angle is radian. Now they all have the same unit of 1. With a value divided by its own error, the new errors for the coefficients simply become 1.

Angle between two Monitor Coefficient Vectors

With Monitor Coefficient Vector introduced, each dithering pattern can now be represented by its corresponding MCV vector. We have ten vectors from all dithering patterns, but we only have five degrees of freedom from five monitors. Therefore, the ten vectors are not completely independent from each other. Whether this modulation cycle is good or not

depends on the question: can the modulation patterns form a good basis for dithering analysis?

It is possible that all ten dithering patterns together can't make a good basis for the current modulation cycle and the dithering analysis would fail. It could also happen that the patterns can cover the five degrees of freedom very well. To tell if the patterns are singular⁷ or not, we need to see how the patterns are related to each other, or in other words, how the Monitor Coefficient Vectors are related. For example, if we have two MCVs that are linearly dependent⁸, the two corresponding dithering patterns are redundant with respect to each other, and we need to rely on other patterns to look for a solid basis.

In principle, it is rare to have two MCVs completely dependent on each other since we have random beam natural motion all the time and dithering coefficients always fluctuate on a certain level. Unlike pure math, to tell if two MCVs are close, we can't just look at the element values because the numbers will never be completely the same. We also need to consider the error of vectors when comparing two MCVs.

To compare two MCVs, we first establish the two vectors from two dithering patterns by following Eq. 3.12

$$\begin{aligned}\mathbf{U}_i &= (C_i^E, C_i^X, C_i^{X'}, C_i^Y, C_i^{Y'}) \equiv (C_i^m), \\ \mathbf{U}_j &= (C_j^E, C_j^X, C_j^{X'}, C_j^Y, C_j^{Y'}) \equiv (C_j^m),\end{aligned}\tag{3.14}$$

where \mathbf{U}_i and \mathbf{U}_j are MCVs for patterns i and j respectively. Indexes i and j can both take from 0-9, the number of dithering patterns given in Tab. 3.5.

Now we can compare the two MCVs in Eq. 3.14. To tell if two vectors are linearly independent or not, a convenient quantity to examine is the angle between two vectors, assuming they are non-zero temporarily⁹. The angle can range from 0° to 180° . If the angle

⁷Here the concept of singularity is borrowed from the vector analysis. If the number of linearly independent vectors is less than the dimension of vector space, the vector basis is singular.

⁸If two vectors are linearly dependent, they can only be parallel or anti-parallel. Or maybe one of the MCVs is zero vector.

⁹The angle between a zero vector and another vector does not usually make sense but we shall see for

is sufficiently far away from 0° and 180° , the two vectors involved are linearly independent and the corresponding dithering patterns are not singular.

The angle between two Monitor Coefficient Vectors shown in Eq. 3.14 is

$$\alpha_{ij} = \frac{180^\circ}{\pi} \arccos\left(\frac{|\mathbf{U}_i \cdot \mathbf{U}_j|}{|\mathbf{U}_i| |\mathbf{U}_j|}\right), \quad (3.15)$$

where $|\mathbf{U}_i|$, and $|\mathbf{U}_j|$ are the module of vectors, $|\mathbf{U}_i \cdot \mathbf{U}_j|$ is the absolute value of the inner product of two vectors. The absolute value is taken because adding a negative sign to a dithering vector does not change the singularity checking, therefore, 0° has the same significance with 180° . The factor $180^\circ/\pi$ in the front changes the unit from radian to degrees.

The inner product between two MCVs, i and j , is

$$\mathbf{U}_i \cdot \mathbf{U}_j = \sum_{m=0}^4 C_i^m C_j^m, \quad (3.16)$$

in which C_i^m and C_j^m are dithering coefficients of monitor m from patterns i and j . Indexes i and j take value 0-9 for ten patterns and index m takes 0-4 for five monitors.

The modules of MCV i and j are

$$|\mathbf{U}_i| = \sqrt{\sum_{m=0}^4 (C_i^m)^2}, \quad |\mathbf{U}_j| = \sqrt{\sum_{m=0}^4 (C_j^m)^2}. \quad (3.17)$$

By plugging inner product and modules of MCVs into Eq. 3.15, the expression for MCV angle α_{ij} is

$$\alpha_{ij} = \frac{180^\circ}{\pi} \arccos\left(\frac{|\sum_{m=0}^4 C_i^m C_j^m|}{\sqrt{\sum_{m=0}^4 (C_i^m)^2} \sqrt{\sum_{m=0}^4 (C_j^m)^2}}\right). \quad (3.18)$$

This quantity only depends on the monitor coefficients from two dithering patterns.

With the angle between MCVs calculated, we can now look at the relationship between

the method described here with error analysis added later, the angle between a zero vector and another one have special characteristics.

two dithering patterns. The size of angle reflects how close two modulation patterns can be. With proper examination of an angle set, we could tell if the current modulation cycle is good or not for dithering analysis.

Error on the Angle between two MCVs

The angle in Eq. 3.15 ranges from 0° to 90° (by taking the absolute value for vector inner product), and it could typically show if two vectors are independent or not. The errors of these vectors can tell us how close two patterns are by comparing the separation between vectors with the size of their errors. This could be revealed conveniently with error of the angle between vectors.

By propagating error of dithering coefficients into MCV angle α_{ij} (Eq. 3.15), the error of the angle, $\Delta\alpha_{ij}$, is given by

$$\Delta\alpha_{ij} = \frac{180^\circ}{\pi} \sqrt{\frac{\sum_{m=0}^4 \left(C_j^m - C_i^m \frac{\sum_{n=0}^4 C_i^n C_j^n}{\sum_{n=0}^4 (C_i^n)^2} \right)^2 (\Delta C_i^m)^2 + \sum_{m=0}^4 \left(C_i^m - C_j^m \frac{\sum_{n=0}^4 C_i^n C_j^n}{\sum_{n=0}^4 (C_j^n)^2} \right)^2 (\Delta C_j^m)^2}{\sum_{m=0}^4 (C_i^m)^2 \sum_{m=0}^4 (C_j^m)^2 - \left(\sum_{m=0}^4 C_i^m C_j^m \right)^2}}, \quad (3.19)$$

in which C_i^m and C_j^m are dithering coefficients from pattern i and j . ΔC_i^m and ΔC_j^m are the error of dithering coefficients. Both indexes m and n take 0-4 for five monitors.

In Eq. 3.19, by checking the right hand side of the equation, the error of MCV angle depends only on monitor dithering coefficients and their errors, which can be obtained at the same time by fitting the monitor dithering responses against the ramp for each modulation pattern.

Now, both MCV angle (Eq. 3.15) and its error (Eq. 3.19) are defined and calculated. We should look at the angle and its error together for better understanding of the relationship between two dithering patterns. If the angle is zero within its error, the two patterns are singular¹⁰. If the angle is small but the error is even smaller, the two dithering patterns

¹⁰The patterns with zero angle don't necessarily have the same amplitudes but they have the same direction or differ in direction by 180° .

still decouple well enough. But even if the angle is close to 90° but has a very high error, like 100° , the two modulation patterns are still not well separated.

3.4.4 Checking Criteria and Results

Now with the Monitor Coefficient Vector, the MCV angle and error of the MCV angle introduced in Sect. 3.4.3, we have the quantities needed to perform dithering quality checking - an examination of different driving patterns. Checking the results will help answer the question brought up in Sect. 3.4.3: how well can dithering modes be independent from one another and work more effectively as a group?

To start with, we look at angle α_{ij} (Eq. 3.18) and angle error $\Delta\alpha_{ij}$ (Eq. 3.19) and find certain criteria about quality checking of dithering modes. To shed more light on these quantities and see how they work for quality checking, we look into the criteria by the order of introduction of the quantities described above.

Checking Criteria

First, with MCV angle introduced, the criteria sets its foundation following the basic properties of an angle between two vectors:

- Angle is 0° . Two vectors are in the same (or opposite¹¹) direction and linearly dependent. They can't form a vector basis for two independent beam monitors. Even though the angle is zero, the vectors are allowed to have different moduli. The module of one vector could differ significantly from the other and could still be linearly dependent. This is trivial in math but it will turn out to be very important when comparing two driving modes in the experiment.
- Angle is 90° . Two vectors are perpendicular with each other and they can form a good basis that is solid for further decoupling of the two beam monitors. To illustrate

¹¹We have taken absolute value for the inner product in Eq. 3.15 so when two vectors are in opposite direction, the angle is still 0° instead of 180° .

this more clearly, we take a simplified example. Suppose we only have two monitors, vertical position Y and angle Y' . The MCVs only contain two elements for these two monitors. Further, let's suppose the FFB was off and we only have two dithering patterns $Y1_{\sin}$ and $Y2_{\sin}$. When the angle between these two patterns is 90° , it is possible that we only have dithering response in monitor Y during modulation pattern $Y1_{\sin}$ and only Y' response in pattern $Y2_{\sin}$. This way we only dithered beam position in one mode and only beam angle in another. The beam position and angle are completely decoupled in this case and the angle between the two vectors is 90° .

- Angle is between 0° and 90° . In this case, the vectors can still form a vector basis. Perhaps not as good as the case when the angle is 90° , but separation of the two beam monitors is still possible. The higher the angle, the better two monitors can be decoupled in dithering analysis.

So far with only MCV angle introduced, we have a general idea of how the method works. Initial criteria involving only the concept of vector angle are summarized in Tab. 3.6. Three conditions with different angle values are listed in this table. Status of vector basis and monitor decoupling are also described for each condition.

Table 3.6: Dithering quality checking with MCV angle.

No.	MCV Angle ($^\circ$)	Vector Basis	Monitor Decoupling
1	0	singular	impossible
2	between 0 and 90	more solid with higher angle	better with higher angle
3	90	best	good decoupling

Now we add the concept of angle error to the quality checking criteria and then a few conditions are added to the criteria described above.

- If the error of angle is close to 0° , the small angle error tells us that both of the two vectors should have high moduli. This is a good sign and these two modulation modes have relatively large dithering responses in the monitors.

- If the angle error is over 90° , this means at least one of the MCVs is too “short.” One of the modes is vanishing and it has weak to none dithering responses in the monitors. To tell which one of the two modes is weak (or even if both of them are weak), we should look at the angle with other modulation modes besides the two. If one of the original two vectors has $>90^\circ$ angles with all other patterns, this specific modulation mode is too weak with hardly any dithering response in it at all. This mode can be discarded for the current modulation cycle because this empty mode is of no use for later analysis¹².
- If the angle error is between 0° and 90° , the two patterns can possibly still be distinguished from each other, and we should look at the value of the angle as well to tell if this is the case. If the angle error is greater than the angle itself, the two patterns are too close to be treated as two independent modes and we should look to other patterns for solution. If the angle error is way smaller than the angle value, the two patterns could function well for dithering analysis.

Generally speaking, the error of the angle alone could tell us if the modulation modes have strong dithering responses in the monitors. Stronger responses in the modulation modes give smaller angle error and help decouple the monitors. The additional criteria with angle error are shown in Tab. 3.7.

Table 3.7: Dithering quality checking with the error of MCV angle.

No.	Angle Error ($^\circ$)	Vector Module	Monitor Decoupling
1	close to 0	both modes have good strength	possibly good
2	between 0 and 90	stronger with smaller error	better with smaller error
3	over 90	at least one of the modes is weak	impossible

With the criteria related to angle and error shown in Tab. 3.6 and 3.7 respectively, we will examine the two quantities together.

¹²We could keep it as well for simplicity purpose. The weak mode is useless but it also doesn't hurt to keep it.

- ◆ The angle is (significantly) smaller than angle error. This means the angle is zero within the angle error, which corresponds to the first situation in Tab. 3.6 when angle is zero. The two modulation modes are singular and it is hard to decouple the two monitors. We need to look to other patterns for solution. This could be classified into two cases according to the size of angle error.
 - ◇ If the angle error is also small, close to zero (first rule in Tab. 3.7), we have a zero angle with a small error. This situation means the two dithering patterns all work well individually. They both have high modulation responses in the monitors. Two patterns work almost the same way as for dithering the beam, and one of the patterns is simply redundant. They could have different dithering amplitude in the monitors but one vector is proportional with the other.
 - ◇ If the angle error is high, close or over 90° , according to rule 3 in Tab. 3.7, one of the patterns is very weak, or the modulation didn't function properly during the experiment and there was no dithering at all for this pattern. We can look at the angle and error with other patterns to tell which one of them is a weak vector with small to zero module.

- ◆ The angle is (significantly) greater than angle error. The higher the angle the better. Or, the lower the angle error the better. Since the angle range is limited, the fact that the angle is greater than its error definitely means we have a small angle error. In this case, we look at rule 2, or even 1, in Tab. 3.7 and know that the two patterns both modulated the beam in a strong way. The angle is non-zero by its error, so we should look to rules 2 and 3 in Tab. 3.6 and understand that the two monitors can be decoupled for a good solution. In all, for the case here, the two patterns can be used together for dithering analysis.

- ◆ The angle is comparable to angle error. In this case, the decision about the two patterns depends. Clearly they could decouple monitors and give a solution in a

reasonable way if we have no other choices. As a result, we might have a relatively high error in the results of dithering analysis. But they are not as good as the situation when the angle is significantly greater than angle error. So if we have extra dithering patterns, we look at the MCV angles with other patterns and look for a more reliable solution.

Table 3.8: Dithering quality checking with MCV angle and error.

No.	Angle	Angle Error	Checking Result
1	0 within error	small, ~ 0	two good but redundant patterns
2		big, ~ 90	one or two weak patterns
3	close to error	close to angle	could work but with greater uncertainty
4	\gg error	small, ~ 0	very good pattern pair for analysis

The combined dithering quality checking criteria by examining both angle and its error are shown in Tab. 3.8. The different cases related to angle and its error are listed in different rows. There are four typical cases in total. During dithering quality checking, we should be able to tell which case the current pattern pair in the run falls into and pay attention to these runs during dithering analysis.

Examples

A few examples of the MCV angle between two dithering patterns are shown here. For each criterion shown in Tab. 3.8, a typical example is given here to show how the examination of dithering quality works for the two patterns we are looking at.

1. Example 1: angle $\sim 0^\circ$ and angle error $\sim 0^\circ$. In this case both the angle and its error are small or close to zero, which corresponds to criterion 1 from Tab. 3.8. The pattern angle history is shown in Fig. 3.4. The blue point and error bar in this figure are the MCV angle and its error for that modulation cycle. The green and black dashed lines are separations for run and slug level, respectively. The angle takes range of $0-90^\circ$. From Fig. 3.4, we can see that the cycles from the slugs in the middle

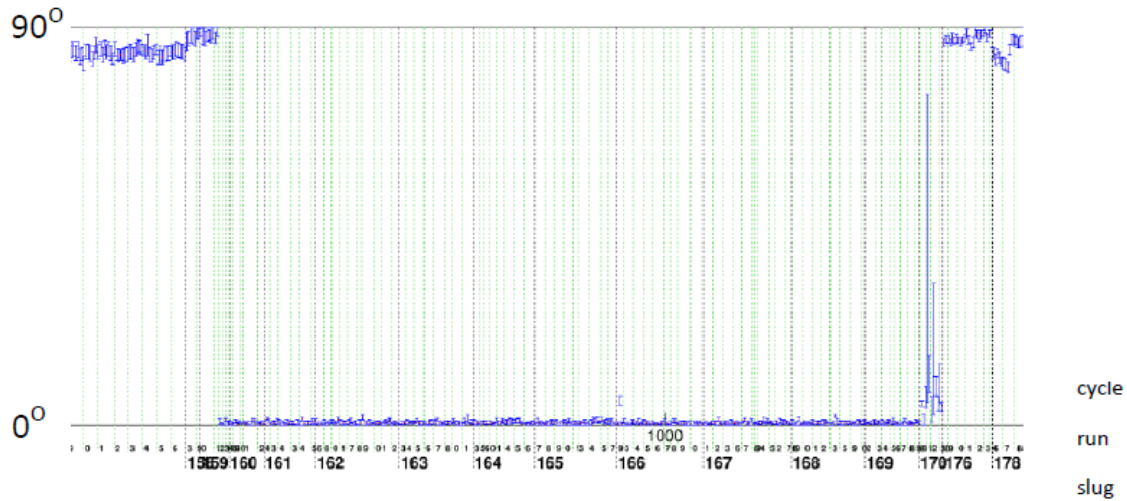


Figure 3.4: Angle history between pattern 0 (X1_sin) and pattern 3 (X2_sin) showing an example of redundant dithering patterns. Blue points with error bar: angle and its error for each modulation cycle. Green dashed line: separation of runs. Black dashed line: separation of slugs.

have zero angle and very small angle error. For the slugs before this period and after, the angle is close to 90° and the angle error is small, which are very “good” modulation patterns that can be used for dithering analysis. The comparison here is so distinct that we can tell immediately something is wrong with the cycles in-between. According to criterion 1 (Tab. 3.8) for the cycles with near zero angle and error, the two dithering patterns X1_sin and X2_sin are redundant and repeat each other even though they both have strong dithering responses in the monitors. So the two patterns function effectively only as one single dithering pattern, and we need to look to more patterns for dithering solution.

2. Example 2: angle error $\sim 90^\circ$. In this case the angle is zero within error and the angle is high, corresponding to criterion 2 from Tab. 3.8. Fig. 3.5 gives the angle history of such a pattern angle at modulation cycle level. In Fig. 3.5, the top plot, for some consecutive runs, shows the error bar of the angle between pattern 0 (X1_sin) and 2 (E_sin) is so high that the angle error almost exceeds the 90° range. This means that one of the two patterns is a very weak pattern or even zero pattern

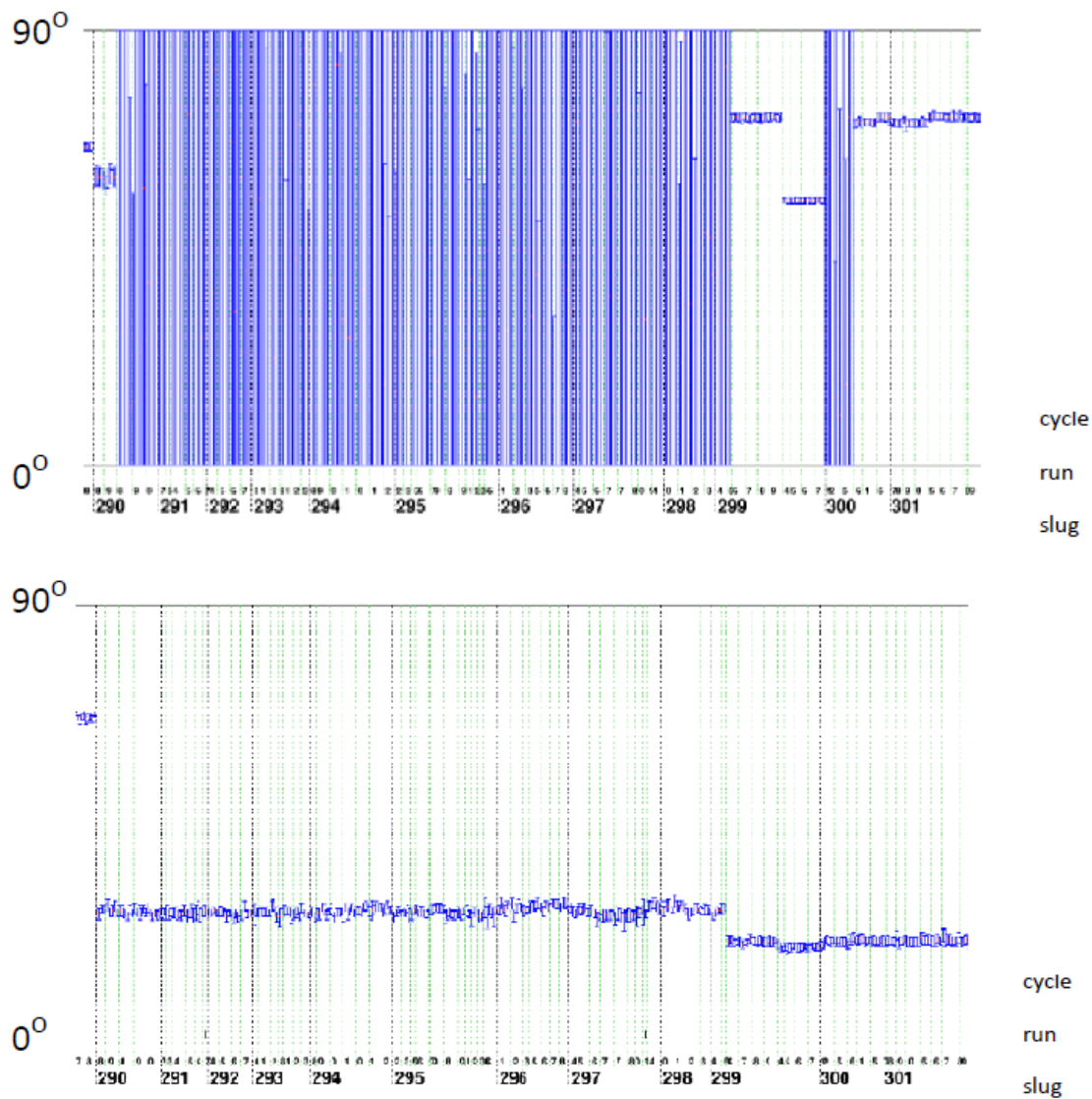


Figure 3.5: Angle history showing the example of weak or missing dithering pattern. Top: between pattern 0 (X1_sin) and 2 (E_sin). Bottom: between pattern 0 (X1_sin) and 3 (X2_sin).

(dithering didn't work for this pattern during these runs). To tell which one of the patterns 0 and 2 is weak, we can look at the angle with a third pattern, 3 (X2_sin) for example. The angle between patterns 0 and 3 is given in the bottom of Fig. 3.5. We can see that the angle between pattern 0 and 3 is normal, which means in the top of Fig. 3.5, the weak pattern is pattern 2, not pattern 0. Now we know that for the run periods shown here, pattern 2 is weak or missing. In this case, we don't need to look at more pattern angles to tell pattern 2 is weak because pattern 0 is shown to be OK; but, it could be possible that both pattern 0 and 2 are weak and we need to look at more pattern angles to make sure. If one pattern is weak, the angle between this pattern and other patterns all have high ($\sim 90^\circ$) angle errors.

3. Example 3: angle \simeq its error. Here the angle and error have approximately the same size, corresponding to criterion 3 in Tab. 3.8. Fig. 3.6 gives an angle between pattern 1 (Y1_sin) and 4 (Y2_sin), which can show a pattern angle that is close to its error for the run period. For the example here, we can see the angle error is only slightly

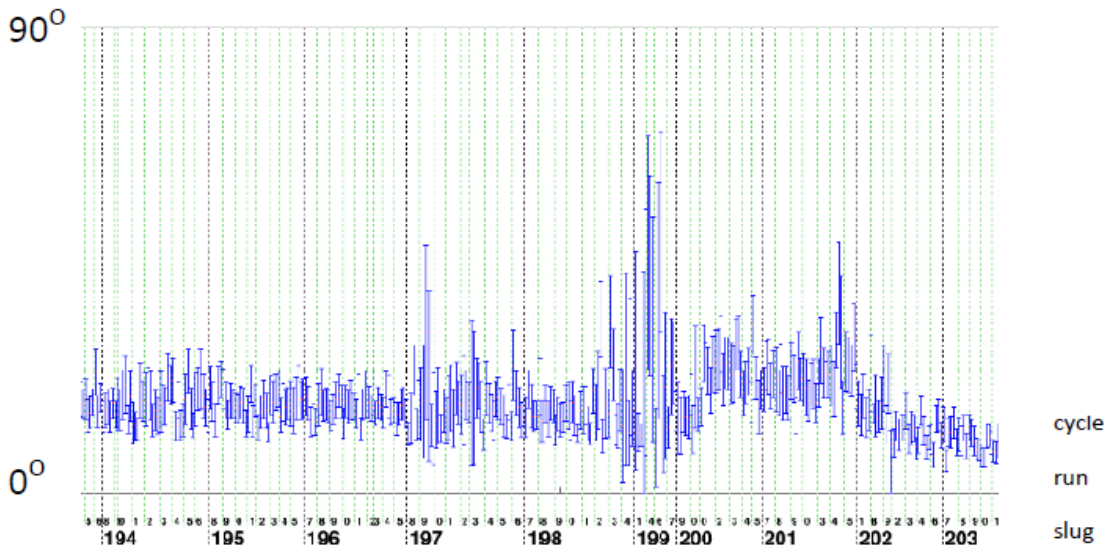


Figure 3.6: Angle history showing the example of a moderate dithering pattern pair between pattern 1 (Y1_sin) and 4 (Y2_sin).

smaller than the angle. The separation of the two patterns is not very clear. Since in this case the angle is not zero within its error, the two patterns can still result in usable (if not very stable) results for dithering analysis later. We could try to switch one of the two patterns with another Y modulation mode and see if the situation could improve. If not, we can still use this pair for monitor decoupling, even though it is not as good as a pattern pair that has a smaller angle error or a higher angle. We should try to evaluate all the pairs between Y modes and see if we could find a better combination of patterns.

4. Example 4: angle \gg its error. This case is when the two patterns work well to decouple monitors and give us good dithering results, according to the last criterion 4 from Tab. 3.8. Fig. 3.7 shows what good MCV angles should look like between two patterns. This is normally what we try to get when planning the modulation inputs,

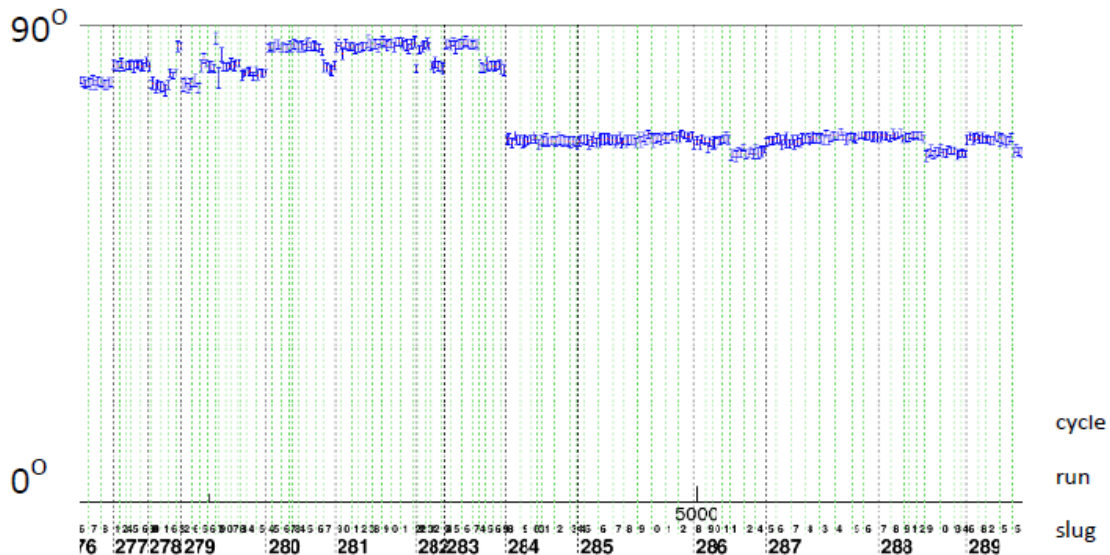


Figure 3.7: Angle history showing the example of a good dithering pattern pair between pattern 0 (X1.sin) and 3 (X2.sin).

even though, due to some beam optics limitations, we could not always get a high angle with small error between two modulation modes. In Fig. 3.7, we can see that

for patten 0 (X1_sin) and 3 (X2_sin), the two patterns originally designed to decouple horizontal position and angle, actually have a very high angle here for these runs. The angle ranges around 70-80° and some of the runs have an angle very close to 90°. For these runs, the pattern pair 0 and 3 can work well to give good dithering results.

Dithering Quality Checking Results

With the typical examples shown above, we now know how to tell if two modulation patterns are good or not for dithering analysis. As noted before, we should look at MCV angles, find the pattern pairs that are well separated and try to evaluate whether or not we have a good basis for this modulation cycle. If the dithering quality is good overall, we keep it for further analysis. Otherwise we discard this cycle. Since the modulation condition does not change very often, we usually have lots of consecutive runs that have close dithering quality.

Table 3.9: Runs with special dithering conditions by dithering quality checking [1].

No.	Condition	Range	Suitable for Analysis
1	E mode missing	212.15801.2 229.16210.1 236.16324 290.17248-299.17345 300.17401-300.17405	not for sensitivity extraction
2	X1 and X2 modes redundant	159.14422-170.14673	use X1(2)_sin and X1(2)_cos
3	Cosine modes missing	99.11405 307.18436-319.18829	FFB off

The results for dithering quality checking for the entire experiment are given in Tab. 3.9. The run periods that have special dithering conditions are summarized in this table. The run periods are marked by slug.run.cycle number. These runs are worth paying attention to when performing dithering analysis.

For the runs when E mode was missing, there is not enough information to extract the complete set of dithering sensitivities, especially the energy sensitivity since we are missing

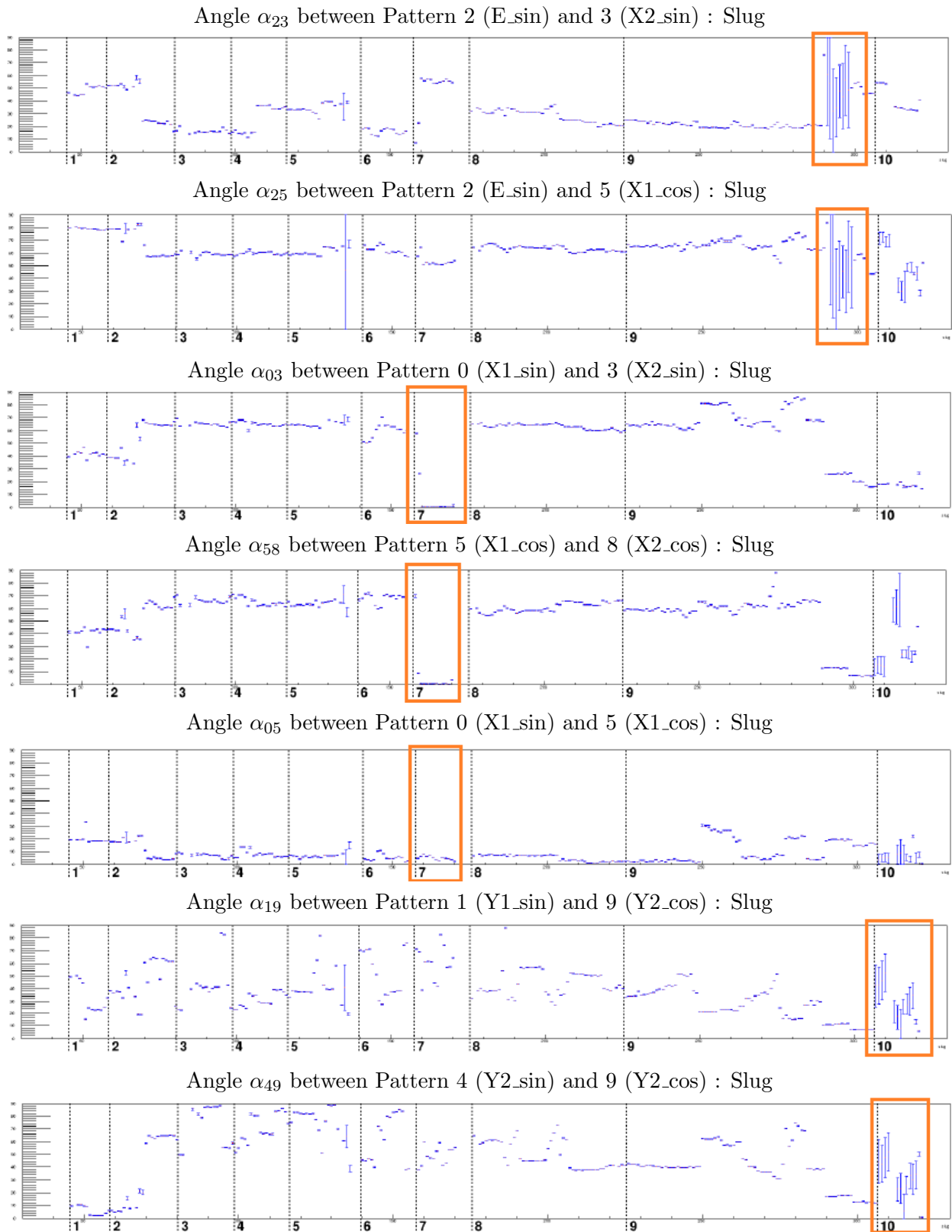


Figure 3.8: Angle history at slug level between pattern pairs.

the most important mode that modulated beam energy. Because the main detector is more sensitive to beam energy than position and angle, it is bad to miss the energy modulation for these runs. This is shown in Fig. 3.8 where the first two plots for angles α_{23} and α_{25} can be seen at slug level. These angles are between pattern 2 (E.sin), the energy modulation, and other patterns, 3 (X2.sin) and 5 (X1.cos) for example. By looking at the runs enclosed with the red frame, we can see the angle error is high for both of the angles, suggesting we are missing energy modulation mode. The angles between pattern 2 and the rest of patterns (0, 1, 4, 6, 7, 8, 9) show the same results, which can be found in Appx. A.

For the runs with redundant X1 and X2 patterns, the two modulation modes X1 and X2 have the MCV angle as zero, which means they are linearly dependent with each other. This is shown in Fig. 3.8, the angle α_{03} and α_{58} history at slug level. For the runs of interest in the red frame, the angle between 0 (X1.sin) and 3 (X2.sin) is zero. This means for the sine responses, X1 and X2 modes work the same way. Additionally, the angle is also zero for pattern 5 (X1.cos) and 8 (X2.cos), the cosine responses in X1 and X2 modulation modes. Since X2 is redundant with respect to X1, we should turn to other extra X pattern pairs for help. We can use a sine mode and corresponding cosine mode in either X1 or X2 modes to perform the dithering analysis for these runs. As shown in Fig. 3.8, angle α_{05} between pattern 0 (X1.sin) and 5 (X1.cos) is small but non-zero (even smaller angle error); for these runs and the patterns, 0 and 5 can be used for dithering analysis even though X1 and X2 modes are redundant for these runs.

For the runs with missing cosine modes, all the angles between cosine modes and other modes have high angle error, which means the cosine modes all have weak dithering responses. This is shown in Fig. 3.8, taking pattern 9 (Y2.cos) for example. The angles between this pattern and the other two patterns, 1 (Y1.sin) and 4 (Y2.sin), have high angle error for the runs enclosed in the red frame. The angles with other patterns (0, 2, 3, 5, 6, 7, 8) can be found in Appx. A. Because of the high angle error between pattern 9 and other patterns, we can conclude that this pattern 9 is weak. And since pattern 9 is the

cosine response for Y2 mode, we can tell that for Y2 mode, FFB was off and there was no cosine response. This happens to be true for other cosine responses (X1_cos, X2_cos, Y1_cos) as well, so FFB was off for X1, X2, Y1 and Y2 modes during these runs. For this run period, we can use the sine responses to perform dithering analysis.

So far, we have used the dithering quality checking method to look at the modulation cycles of this experiment and have provided the special run periods that we should pay attention to when performing dithering analysis. One of the main tasks of dithering analysis is to extract the dithering sensitivities for detectors. The dithering quality checking results we have so far are closely related to the sensitivity extraction described in the next section.

3.5 Beam Correction Sensitivities

The beam correction depends on two sets of quantities: monitor differences and dithering sensitivities. The sum of products between monitor difference and sensitivity for all monitors gives the beam correction. While monitor differences are provided in data files, the sensitivities must be carefully calculated in dithering analysis. And the successful extraction of sensitivities gives us good dithering results when performing beam correction on the detector asymmetry. The previous section focused on dithering quality checking on different patterns and discussed what kind of dithering patterns can give us better results. Each pattern dithered the beam in a certain way, with different responses in the monitors. These different dithering modes provide us with necessary information for the sensitivity calculation. A set of patterns can work together to decouple the monitor responses. Normally a set of five is needed in the standard method of sensitivity extraction. In this experiment, the Fast Feedback was on and we have more than five effective dithering patterns for each modulation cycle; a modified method of sensitivity calculation involving a set of patterns more than five is needed.

3.5.1 Standard Sensitivity Extraction Method

For the scenario with five dithering patterns, we have the standard way of calculating dithering sensitivities for the detector. With five beam monitors, energy E, horizontal position X and angle X', and vertical position Y and angle Y', there are five sensitivities to extract, $S_E, S_X, S_{X'}, S_Y, S_{Y'}$, corresponding to each of the monitors. Five different dithering patterns with different modulation responses in the monitors are required to calculate the sensitivities. In these five patterns, the energy pattern is the only mode that was designed to modulate beam energy, and it has a high response in the beam energy monitor. Two X modes are required for two horizontal parameters. The X1 and X2 patterns modulated beam horizontal position and angle with different relative amplitudes. The same applies to vertical Y patterns. Y1 and Y2 patterns were dedicated for decoupling vertical position and angle.

The response of each monitor can potentially result in change in the detector. During modulation, these responses are represented by corresponding dithering coefficients of the monitors and detector. The relationship between detector dithering response and monitor responses is

$$\sum_{m=0}^4 S_m C_i^m = C_i^D, \quad (3.20)$$

in which S_m is the sensitivity for monitor m . C_i^m is the dithering coefficient for monitor m in pattern i . Index m takes five monitors, E, X, X', Y, Y'. Or by expressing index m in an explicit way, we have

$$S_E C_i^E + S_X C_i^X + S_{X'} C_i^{X'} + S_Y C_i^Y + S_{Y'} C_i^{Y'} = C_i^D, \quad (3.21)$$

where C_i^D with a superscript D is the dithering coefficient for detector D in this pattern. D can be any detector from the main detector, background detector, etc. Index i can take values of 0-4 for the standard sensitivity extraction (it can take more than 4 if we have more patterns, which will be discussed in the next section).

Following Eq. 3.21, we have five equations for each dithering pattern from a total of five. These five equations can form an equation set used to calculation sensitivity S_m

$$\left\{ \begin{array}{l} S_E C_0^E + S_X C_0^X + S_{X'} C_0^{X'} + S_Y C_0^Y + S_{Y'} C_0^{Y'} = C_0^D \\ S_E C_1^E + S_X C_1^X + S_{X'} C_1^{X'} + S_Y C_1^Y + S_{Y'} C_1^{Y'} = C_1^D \\ S_E C_2^E + S_X C_2^X + S_{X'} C_2^{X'} + S_Y C_2^Y + S_{Y'} C_2^{Y'} = C_2^D \\ S_E C_3^E + S_X C_3^X + S_{X'} C_3^{X'} + S_Y C_3^Y + S_{Y'} C_3^{Y'} = C_3^D \\ S_E C_4^E + S_X C_4^X + S_{X'} C_4^{X'} + S_Y C_4^Y + S_{Y'} C_4^{Y'} = C_4^D \end{array} \right. , \quad (3.22)$$

in which C_i^m and C_i^D are known quantities from the fitting of dithering responses in monitor m and detector D in pattern i . The solution to the equation set gives the values of five dithering sensitivities for this detector.

To make Eq. 3.22 more clear and revealing, we define a few terms based on the quantities in the equation set. This way we could comprehend more quickly the method of sensitivity extraction, making it is easier to compare with the method provided in the following section when more patterns are introduced.

For the monitor coefficients, we define a matrix that could include all of them. This is a 5 by 5 matrix. For the standard method of sensitivity extraction, the matrix is composed of monitor coefficients from five monitors and five patterns. The standard matrix of monitor coefficients, \mathbf{M} , is defined by

$$\mathbf{M} = \begin{bmatrix} C_i^m \end{bmatrix} , \quad (3.23)$$

where the index m takes five monitors and the index i takes five patterns. By expressing

the monitor coefficients individually, we have a more explicit format

$$\mathbf{M} = \begin{bmatrix} C_0^E & C_0^X & C_0^{X'} & C_0^Y & C_0^{Y'} \\ C_1^E & C_1^X & C_1^{X'} & C_1^Y & C_1^{Y'} \\ C_2^E & C_2^X & C_2^{X'} & C_2^Y & C_2^{Y'} \\ C_3^E & C_3^X & C_3^{X'} & C_3^Y & C_3^{Y'} \\ C_4^E & C_4^X & C_4^{X'} & C_4^Y & C_4^{Y'} \end{bmatrix}, \quad (3.24)$$

in which each row contains coefficients of five monitors from a certain pattern. Each column has coefficients from five patterns for one monitor. The matrix \mathbf{M} contains all the information of monitor dithering for the current modulation cycle.

For the dithering responses in the detector, we introduce the vector that takes all the values of five coefficients of the detector from five patterns. For the sensitivities to be calculated, we define a vector that takes all five detector sensitivities for five monitors. For the standard method of sensitivity extraction, the stand vector of detector coefficients and the stand vector of detector sensitivities are introduced as

$$\mathbf{S} = \begin{pmatrix} S_m \end{pmatrix}, \quad \mathbf{D} = \begin{pmatrix} C_i^D \end{pmatrix}. \quad (3.25)$$

When Eq. 3.25 is expressed in an explicit form for indexes m and i , we have

$$\mathbf{S} = \begin{pmatrix} S_E \\ S_X \\ S_{X'} \\ S_Y \\ S_{Y'} \end{pmatrix}, \quad \mathbf{D} = \begin{pmatrix} C_0^D \\ C_1^D \\ C_2^D \\ C_3^D \\ C_4^D \end{pmatrix}. \quad (3.26)$$

Here the vector of detector coefficients, \mathbf{D} , includes all the dithering responses for this detector in each pattern and it is known based on measurements, just like the previous

matrix of monitor coefficients, \mathbf{M} . The vector of sensitivities, \mathbf{S} , is what we need to solve based on the measured quantities.

With the matrix of monitor coefficients \mathbf{M} , the vector of detector coefficients \mathbf{D} and the vector of detector sensitivities \mathbf{S} defined, the equation set in Eq. 3.22 can be simplified in a compact format:

$$\mathbf{D} = \mathbf{M} \cdot \mathbf{S} . \tag{3.27}$$

This is a matrix equation that needs to be solved for \mathbf{S} .

With five patterns provided, we have the standard method for dithering sensitivity extraction. When more patterns are added, we have a modified way of calculating sensitivities, which is different from the standard way described above. The modified way has different expressions for \mathbf{D} , \mathbf{M} and \mathbf{S} , which are changed to accommodate for more inputs. The modified method is discussed in the next section.

3.5.2 Sensitivity Calculation with More Patterns

In this experiment, the FFB was on during most of the modulation patterns. An extra five patterns with out-of-phase responses in the detector and monitors are added to the original structure. With five unknown sensitivities to solve, we have ten dithering patterns that can give us ten equations. In this case, a different sensitivity extraction method is given to find a solution for these dithering patterns. For the patterns from both in-phase and

out-of-phase responses, we have a set of equations

$$\left\{ \begin{array}{l} S_E C_0^E + S_X C_0^X + S_{X'} C_0^{X'} + S_Y C_0^Y + S_{Y'} C_0^{Y'} = C_0^D \\ S_E C_1^E + S_X C_1^X + S_{X'} C_1^{X'} + S_Y C_1^Y + S_{Y'} C_1^{Y'} = C_1^D \\ S_E C_2^E + S_X C_2^X + S_{X'} C_2^{X'} + S_Y C_2^Y + S_{Y'} C_2^{Y'} = C_2^D \\ S_E C_3^E + S_X C_3^X + S_{X'} C_3^{X'} + S_Y C_3^Y + S_{Y'} C_3^{Y'} = C_3^D \\ S_E C_4^E + S_X C_4^X + S_{X'} C_4^{X'} + S_Y C_4^Y + S_{Y'} C_4^{Y'} = C_4^D \\ S_E C_5^E + S_X C_5^X + S_{X'} C_5^{X'} + S_Y C_5^Y + S_{Y'} C_5^{Y'} = C_5^D \\ S_E C_6^E + S_X C_6^X + S_{X'} C_6^{X'} + S_Y C_6^Y + S_{Y'} C_6^{Y'} = C_6^D \\ S_E C_7^E + S_X C_7^X + S_{X'} C_7^{X'} + S_Y C_7^Y + S_{Y'} C_7^{Y'} = C_7^D \\ S_E C_8^E + S_X C_8^X + S_{X'} C_8^{X'} + S_Y C_8^Y + S_{Y'} C_8^{Y'} = C_8^D \\ S_E C_9^E + S_X C_9^X + S_{X'} C_9^{X'} + S_Y C_9^Y + S_{Y'} C_9^{Y'} = C_9^D \end{array} \right. . \quad (3.28)$$

We need to find a solution that can best fit the ten equations. The least square fitting method is utilized to find this solution for ten dithering patterns. To do this, we need to define the χ^2 for the equations above:

$$\begin{aligned} \chi^2 &= \sum_{i=0}^9 \left(C_i^D - \sum_{m=0}^4 S_m C_i^m \right)^2 \\ &= \sum_{i=0}^9 \left(C_i^D - S_E C_i^E - S_X C_i^X - S_{X'} C_i^{X'} - S_Y C_i^Y - S_{Y'} C_i^{Y'} \right)^2, \end{aligned} \quad (3.29)$$

in which m takes E, X, X', Y, Y'. The coefficients on right hand side runs through all ten patterns. The differences between both sides of the equation in each and every pattern are included in this χ^2 .

To find the optimal solution of sensitivities, we need to minimize χ^2 defined above. The solution of sensitivities that can minimize the χ^2 is given by the following equation set

composed of five equations

$$\left\{ \begin{array}{l} S_E \sum_{i=0}^9 C_i^E C_i^E + S_X \sum_{i=0}^9 C_i^X C_i^E + S_{X'} \sum_{i=0}^9 C_i^{X'} C_i^E + S_Y \sum_{i=0}^9 C_i^Y C_i^E + S_{Y'} \sum_{i=0}^9 C_i^{Y'} C_i^E = \sum_{i=0}^9 C_i^D C_i^E \\ S_E \sum_{i=0}^9 C_i^E C_i^X + S_X \sum_{i=0}^9 C_i^X C_i^X + S_{X'} \sum_{i=0}^9 C_i^{X'} C_i^X + S_Y \sum_{i=0}^9 C_i^Y C_i^X + S_{Y'} \sum_{i=0}^9 C_i^{Y'} C_i^X = \sum_{i=0}^9 C_i^D C_i^X \\ S_E \sum_{i=0}^9 C_i^E C_i^{X'} + S_X \sum_{i=0}^9 C_i^X C_i^{X'} + S_{X'} \sum_{i=0}^9 C_i^{X'} C_i^{X'} + S_Y \sum_{i=0}^9 C_i^Y C_i^{X'} + S_{Y'} \sum_{i=0}^9 C_i^{Y'} C_i^{X'} = \sum_{i=0}^9 C_i^D C_i^{X'} \\ S_E \sum_{i=0}^9 C_i^E C_i^Y + S_X \sum_{i=0}^9 C_i^X C_i^Y + S_{X'} \sum_{i=0}^9 C_i^{X'} C_i^Y + S_Y \sum_{i=0}^9 C_i^Y C_i^Y + S_{Y'} \sum_{i=0}^9 C_i^{Y'} C_i^Y = \sum_{i=0}^9 C_i^D C_i^Y \\ S_E \sum_{i=0}^9 C_i^E C_i^{Y'} + S_X \sum_{i=0}^9 C_i^X C_i^{Y'} + S_{X'} \sum_{i=0}^9 C_i^{X'} C_i^{Y'} + S_Y \sum_{i=0}^9 C_i^Y C_i^{Y'} + S_{Y'} \sum_{i=0}^9 C_i^{Y'} C_i^{Y'} = \sum_{i=0}^9 C_i^D C_i^{Y'} \end{array} \right. \quad (3.30)$$

And the modified matrix of monitor coefficients is now

$$\mathbf{M} = \left[\sum_{i=0}^9 C_i^m C_i^n \right], \quad (3.31)$$

where indexes m and n take five monitors and we have

$$\mathbf{M} = \left[\begin{array}{ccccc} \sum_{i=0}^9 C_i^E C_i^E & \sum_{i=0}^9 C_i^X C_i^E & \sum_{i=0}^9 C_i^{X'} C_i^E & \sum_{i=0}^9 C_i^Y C_i^E & \sum_{i=0}^9 C_i^{Y'} C_i^E \\ \sum_{i=0}^9 C_i^E C_i^X & \sum_{i=0}^9 C_i^X C_i^X & \sum_{i=0}^9 C_i^{X'} C_i^X & \sum_{i=0}^9 C_i^Y C_i^X & \sum_{i=0}^9 C_i^{Y'} C_i^X \\ \sum_{i=0}^9 C_i^E C_i^{X'} & \sum_{i=0}^9 C_i^X C_i^{X'} & \sum_{i=0}^9 C_i^{X'} C_i^{X'} & \sum_{i=0}^9 C_i^Y C_i^{X'} & \sum_{i=0}^9 C_i^{Y'} C_i^{X'} \\ \sum_{i=0}^9 C_i^E C_i^Y & \sum_{i=0}^9 C_i^X C_i^Y & \sum_{i=0}^9 C_i^{X'} C_i^Y & \sum_{i=0}^9 C_i^Y C_i^Y & \sum_{i=0}^9 C_i^{Y'} C_i^Y \\ \sum_{i=0}^9 C_i^E C_i^{Y'} & \sum_{i=0}^9 C_i^X C_i^{Y'} & \sum_{i=0}^9 C_i^{X'} C_i^{Y'} & \sum_{i=0}^9 C_i^Y C_i^{Y'} & \sum_{i=0}^9 C_i^{Y'} C_i^{Y'} \end{array} \right]. \quad (3.32)$$

The vector of sensitivities and the vector of detector coefficients are

$$\mathbf{S} = \begin{pmatrix} S_E \\ S_X \\ S_{X'} \\ S_Y \\ S_{Y'} \end{pmatrix}, \quad \mathbf{D} = \begin{pmatrix} \sum_{i=0}^9 C_i^D C_i^E \\ \sum_{i=0}^9 C_i^D C_i^X \\ \sum_{i=0}^9 C_i^D C_i^{X'} \\ \sum_{i=0}^9 C_i^D C_i^Y \\ \sum_{i=0}^9 C_i^D C_i^{Y'} \end{pmatrix}, \quad (3.33)$$

where the vector of sensitivities is unchanged and the vector of detector coefficients is modified for the current case of ten patterns.

3.5.3 Sensitivity History

With the sensitivity calculation procedure in the last section, we have the method to extract the main detector sensitivities for the case with more than five patterns. The method includes ten patterns of both in-phase and out-of-phase responses. Some of the patterns have weak responses for certain periods of runs, like the cosine patterns during the run period when FFB was off, or the cosine energy pattern when energy modulation signal was pure sine form. In these weak pattern cases, the corresponding dithering coefficients of detector and monitors, C_i^D and C_i^m , are near zero. Therefore the term

$(C_i^D - \sum_{m=0}^4 S_m C_i^m)$ from that weak pattern is vanishing in the χ^2 defined by Eq. 3.29 for these runs. The χ^2 sums over ten patterns ($i=0-9$) and the contribution from a weak pattern does little to the sum. This way we don't need to specifically remove this pattern from the index i when taking the sum from all patterns during our calculation. We could keep them and bind them with other relatively strong patterns. Or, we could throw them away in the process of calculation simply by skipping index i for them when going from 0-9 for the specific runs. But since they are weak, it is normally irrelevant whether we keep them for calculation or simply throw them away.

The case above seems trivial for the case of weak patterns. But for the strong patterns,

which have relatively high responses in the detector and monitors, the choice of patterns becomes more important. In the following sections, the selection of patterns is going to determine how we justify the results from different combinations of the patterns¹³. Right now, we look at the sensitivity results from the full ten pattern (coil) analysis, which are calculated with the method from Sect. 3.5.2. The full ten pattern analysis gives balance between the patterns, utilizing the information from both in-phase and out-of-phase responses. Our first thought might be that we trust the in-phase modes a bit more because they were supposed to modulate the beam as designed. The out-of-phase responses are from FFB modes and we are not sure how the FFB works to modulate the beam. But there is no established reason to prefer in-phase modes more than the out-of-phase modes. Therefore, here both sine and cosine patterns are both utilized during the ten pattern analysis.

Energy Monitor Sensitivity History

In Fig. 3.9, we have the main detector sensitivity (slope) history plot at slug level for the energy monitor. In this plot (and the following plots for position and angle), the slugs after 290 are not shown because according to Tab. 3.9, these slugs either suffered from loss of the energy modulation mode (the main mode for beam correction analysis) or had FFB off for special run periods. We can see from Fig. 3.9 that the energy sensitivity is relatively stable through the runs. The energy slope slowly increased from Run 1 to Run 2 in the experiment, by less than $\sim 15\%$. The energy slope is stable for the majority of Run 2. The variation from slug to slug is well within 10%. This means the energy sensitivity is well measured and under control during the experiment.

¹³We will deliberately omit one or two of the patterns and find the results based on 9 patterns or 8 patterns in the equation set.

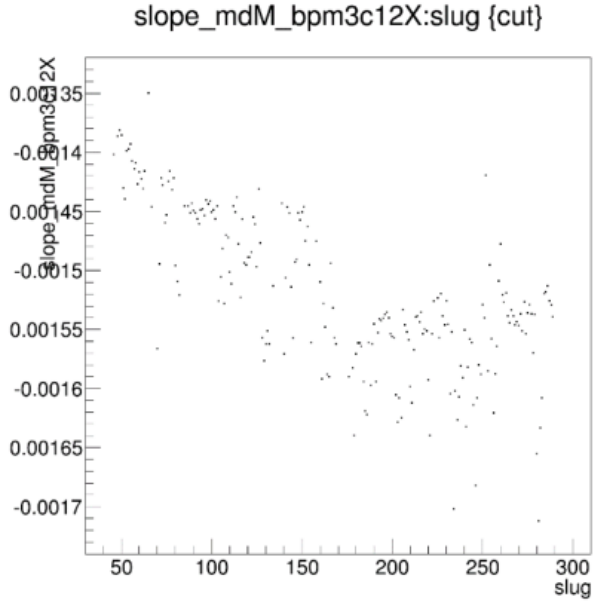


Figure 3.9: Main detector energy sensitivity slug history for 10 coil (pattern) analysis.

Horizontal Position and Angle Sensitivity History

In Fig. 3.10, we have the sensitivities for horizontal position and angle. On the left, the slope history versus slug is shown for horizontal position monitor X (or targetX for full name). On the right, we have horizontal angle X' (or targetXSlope). We can see that these slopes are not as stable as the energy slope from Fig. 3.9.

During the run period around slug 159-170, which is from Wien 7 of the experiment, the horizontal position and angle slopes changed dramatically compared to the slugs prior to slug 159 and the ones after slug 170. This is the period when the two modulation patterns X1 and X2 are redundant, as shown in Tab. 3.9. Because of the redundancy in X1 and X2, when performing the full ten pattern sensitivity calculation, we actually relied on the information from patterns X1_sin and X1_cos (or the pair of X2_sin and X2_cos) to calculate the slopes for these runs. For other runs besides these ones, we relied on patterns X1_sin, X1_cos, X2_sin and X2_cos together and found the solution that could represent the best out of the four patterns. We can see in Fig. 3.10 that for these slugs, the horizontal position and angle slopes become very close to zero and differ greatly from the rest of the

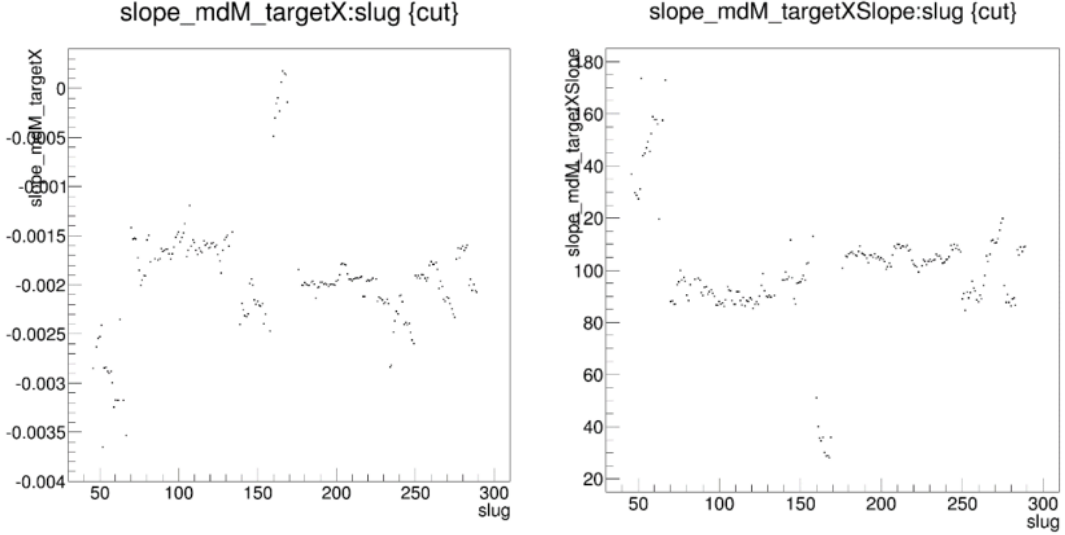


Figure 3.10: Main detector horizontal position and angle sensitivities slug history for 10 coil (pattern) analysis. (Left) horizontal position. (Right) horizontal angle.

runs. However, we can also see in Fig. 3.9 that the energy slope is pretty constant with other runs. This means the X modulation patterns could affect horizontal and angle slopes in a significant way but not the energy slope. The energy slope is pretty much dominated by the energy modulation pattern E_{\sin} (the other energy pattern, E_{\cos} , the out-of-phase pattern of the energy mode, is generally zero because the FFB was off during E modulation), which is the only pattern that was designed to modulate beam energy. Even though there are differences from run to run for the X modulation patterns, the energy slope could still be relatively stable.

Another observation in Fig. 3.10 is that the horizontal position and angle slopes seem anti-correlated. For example, during the first few slugs, ten or so, the slope is higher than average for X slope but lower than average for X' slope. Also, for the slugs mentioned previously during Wien 7, the slopes are higher than average for X and lower than average for X'. This means there is a high (anti-)correlation between horizontal position and angle.

Vertical Position and Angle Sensitivity History

In Fig. 3.11, we have the sensitivities from vertical position (left) and angle (right). We can see that compared to horizontal parameters, the vertical slopes are relatively more stable.

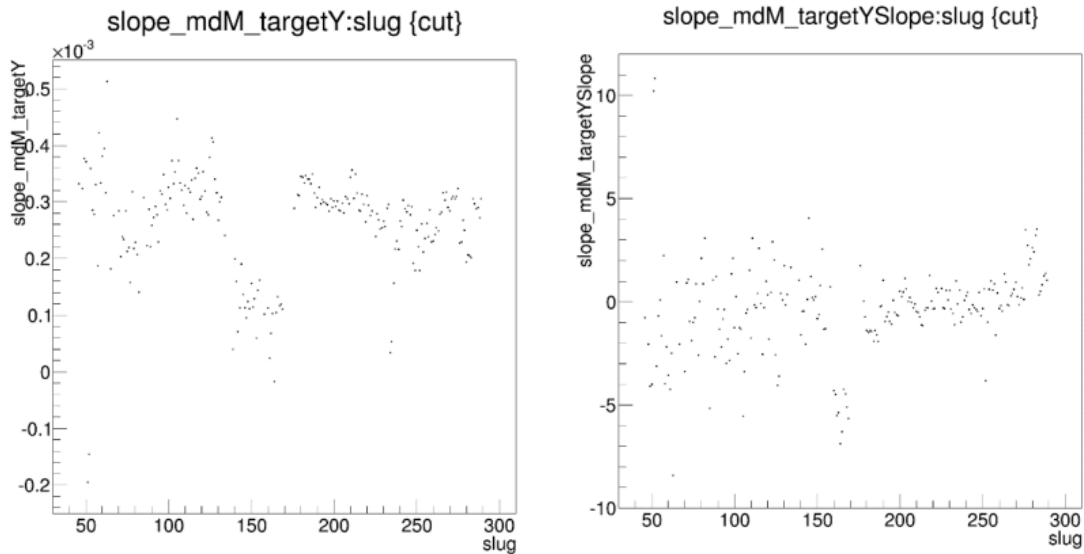


Figure 3.11: Main detector vertical position and angle sensitivities slug history for 10 coil (pattern) analysis. (Left) vertical position. (Right) vertical angle.

For the vertical angle slope on the right, the slope is consistent with zero for the majority of the runs. For the vertical position slope on the left, the sensitivity is also very small, and for some of the runs, the vertical position slope is close to zero as well. This means in the vertical directions, the main detector sensitivities are pretty much consistent with zero. This is what we expect from the layout of the individual detectors. Since the eight main detector bars are azimuthally positioned, we expect cancellations of detector sensitivities from the opposite detector bars. The main detector array was designed to suppress some of the beam parameter sensitivities given a symmetric layout, including the vertical position and angle slopes we are looking at here. The bar at the top and the one at the bottom of the array respond in an opposite way with respect to the vertical position and angle of the beam. Shifting the beam upward or downward can cause yield in one bar to increase and yield in the other bar to decrease. The total effect of change tends to be zero when the bar

responses are combined and averaged.

3.6 Beam Correction with Residual

The sensitivities calculated in the last section were based on the full ten pattern extraction method. The χ^2 in Eq. 3.29 was minimized to give the solution for the ten equations from a full pattern set. Normally the χ^2 could not be minimized to a zero value since each pattern differs from the solution of sensitivities more or less by a certain amount. Then we need to look at the deviation of each pattern from this solution. We only dithered five beam parameters (E, X, X', Y, Y') during the modulation stage, and the detector yield should only respond to the five beam parameters. If this is case, the χ^2 should be vanishing. But if there are other parameters of the beam, like some parameter we were not aware of, that also introduced some response in the main detector accidentally, the χ^2 couldn't be minimized normally. To tell if this is the case, we need to look at the dithering residuals.

3.6.1 Dithering Residual

Dithering residual refers to the residual response in the main detector after the correction from solution given by the χ^2 minimization method. After having a solution of five sensitivities, we plug in the monitor coefficients and the obtained sensitivities on the left hand side of the equations in Eq. 3.28. Then we have the “projected” response in the main detector. On the right hand side of the equations, we have the actual measured responses of the main detector for each pattern. The discrepancy between the projected response and the measured response is dithering residual for this pattern.

The projected dithering response in the main detector is

$$P_i^D \equiv S_E C_i^E + S_X C_i^X + S_{X'} C_i^{X'} + S_Y C_i^Y + S_{Y'} C_i^{Y'} , \quad (3.34)$$

where index i takes pattern 0-9. The projected detector response is established for each

dithering pattern. Since the monitor coefficients are different from pattern to pattern, the projected response P_i^D differs by pattern as well.

Different patterns have different sizes of projected responses and they could be estimated on a certain level. For example, the projected response is expected to be relatively suppressed in the position and angle modulation modes since the main detector is less sensitive to position and angle than beam energy. But for the energy modulation mode, we expect the projected response to be high since main detector yield is sensitive to beam energy change.

Compared to the projected detector response P_i^D in Eq. 3.34, the actual measured dithering response in the main detector is its dithering coefficient C_i^D . The discrepancy between the projected response and the measured response is the dithering residual response for that pattern. The dithering residual for pattern i is

$$R_i^D \equiv D_i^D - P_i^D, \quad (3.35)$$

or, in a more explicit way with monitor coefficients and sensitivities plugged in

$$\begin{aligned} R_i^D &= D_i^D - \sum_{m=0}^4 S_m C_i^m \\ &= D_i^D - S_E C_i^E - S_X C_i^X - S_{X'} C_i^{X'} - S_Y C_i^Y - S_{Y'} C_i^{Y'}, \end{aligned} \quad (3.36)$$

in which index i takes ten patterns 0-9. Index m takes five beam parameters. S_m is the detector sensitivity for monitor m . C_i^m is the monitor coefficient of monitor m in pattern i . The dithering residual R_i^D is the measured detector response minus the individual projected detector responses from each monitor.

With the dithering residual in Eq. 3.36, we take another look at the χ^2 given earlier in Eq. 3.29. The χ^2 can be expressed with dithering residual as

$$\chi^2 = \sum_{i=0}^9 (R_i^D)^2, \quad (3.37)$$

where the sum takes all ten patterns and the residuals are squared to maintain a non-negative contribution to the χ^2 . The χ^2 minimization method in Sect. 3.5.2 was trying to minimize the dithering residuals from the patterns. The solution of sensitivities was calculated so that the resulted residual responses in the detector can be minimal. But non-vanishing nonetheless, as we shall see later.

3.6.2 Residual History

There are fitting errors in the monitor and detector coefficients, and these errors are statistical from beam natural motion. This results in statistical error in the dithering residual as well. So for a slug or run, the residuals from the patterns could not have a zero value but should be within the statistical reach of zero. If not, we observe a systematic non-zero residual effect in the dithering analysis. To tell if this is the case for the experiment, we look at the dithering residuals for the main detector in each of the ten patterns.

First we look at the residuals in the vertical direction modulation patterns, Y1 and Y2 modes. There are sine and cosine responses for each of the two modes. The residual vs. slug history plots are shown in Fig. 3.12.

In Fig. 3.12, we have four slug history plots from four patterns, Y1_sin (top left), Y1_cos (top right), Y2_sin (bottom left), Y2_cos (bottom right). They have corresponding pattern numbers 1, 6, 4, 9, respectively. The unit of the detector residual in these plots is parts per million. By looking at the Y1_sin slug history plot (top left), we can see that there are statistical fluctuations in the residual from slug to slug, and for most of the slugs, the residual is close to zero. The same happens to the other three Y residual history plots. We could observe all zero or near zero residuals in the Y patterns.

The small or vanishing residuals in the Y modulation modes mean that four different Y patterns can give solutions that generally agree with each other. The sensitivities for vertical position and angle are well determined, just like what has been shown before in the

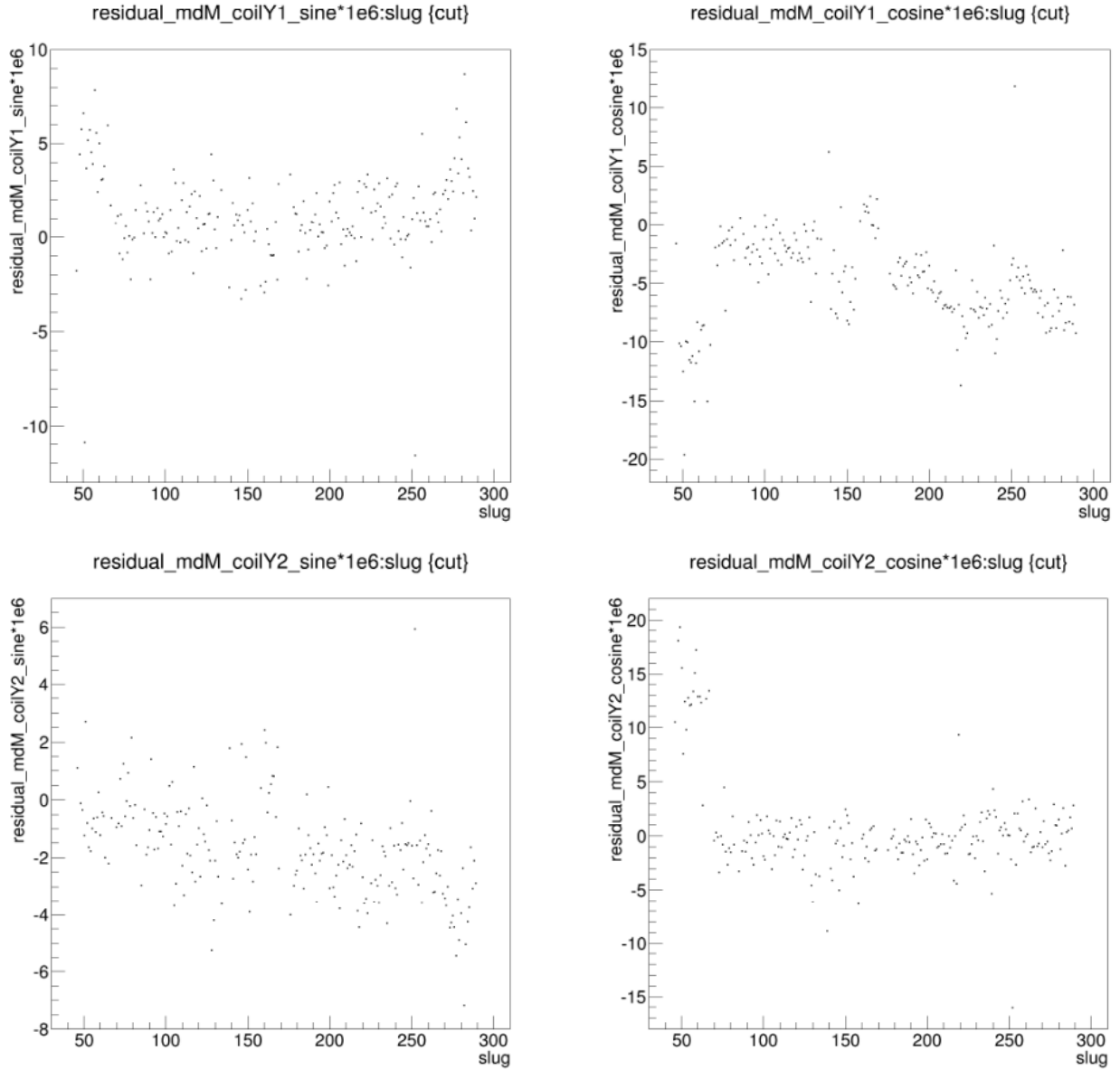


Figure 3.12: Main detector dithering residual slug history in pattern Y1 and Y2. (Top left) Y1 pattern sine residual. (Top right) Y1 pattern cosine residual. (Bottom left) Y2 pattern sine residual. (Bottom right) Y2 pattern cosine residual.

sensitivity history plots (Fig. 3.11). The sensitivities for Y direction parameters are close to zero and relatively stable. This also means that the responses in the main detector during Y1 and Y2 modes can be well covered by beam parameters, especially the vertical position and angle. There is not much mystery in the Y dithering modes, but we shall see a different story in the X modes.

In Fig. 3.13, we have the dithering residual slug history plots for all X modulation patterns, including X1_sin (top left), X1_cos (top right), X2_sin (bottom left), and X2_cos (bottom right), corresponding to pattern 0, 3, 5, 8, respectively. By looking at the four plots in general, we immediately notice that unlike the situation in the Y direction modes, the residuals in the X patterns are much higher. For example, in X1_sin and X1_cos modes, the residuals can be as high as 50-80 ppm, but this is not within the statistical fluctuation allowance of the residuals from slug to slug.

For the X1_sin pattern (top left in Fig. 3.13), the residual can range from 0 to 50 ppm. For the X1_cos pattern (top right), the residual can be as high as 80 ppm, which is the highest among the four X modulation patterns (the next highest is pattern X1_sin). It is also worth noticing that for the X1_sin and X1_cos patterns, the residuals are compensating for each other. They have opposite signs but about the same magnitude (actually the magnitude of residual in the X1_cos pattern is about 1.5 times the magnitude in the X1_sin pattern). For the X2_sin pattern (bottom left), the residual is between 0 and 40 ppm, about half of the size as in the X1_cos pattern. The residual in the X2_cos pattern is the smallest, which is between -10 to 30 ppm. The residual in X2_cos is close to zero for most of the slugs.

One special case should be made about the slugs 159-170. We can see from Fig. 3.13 that for these slugs, the dithering residuals for the X patterns are zero within statistical error. To explain this, we have to use the dithering quality checking results in Sect. 3.4.4, which have shown that for these slugs, the X1 and X2 modulation modes are redundant (see Tab. 3.9). We can effectively use two X1 patterns (in-phase and out-of-phase) or two X2 patterns.

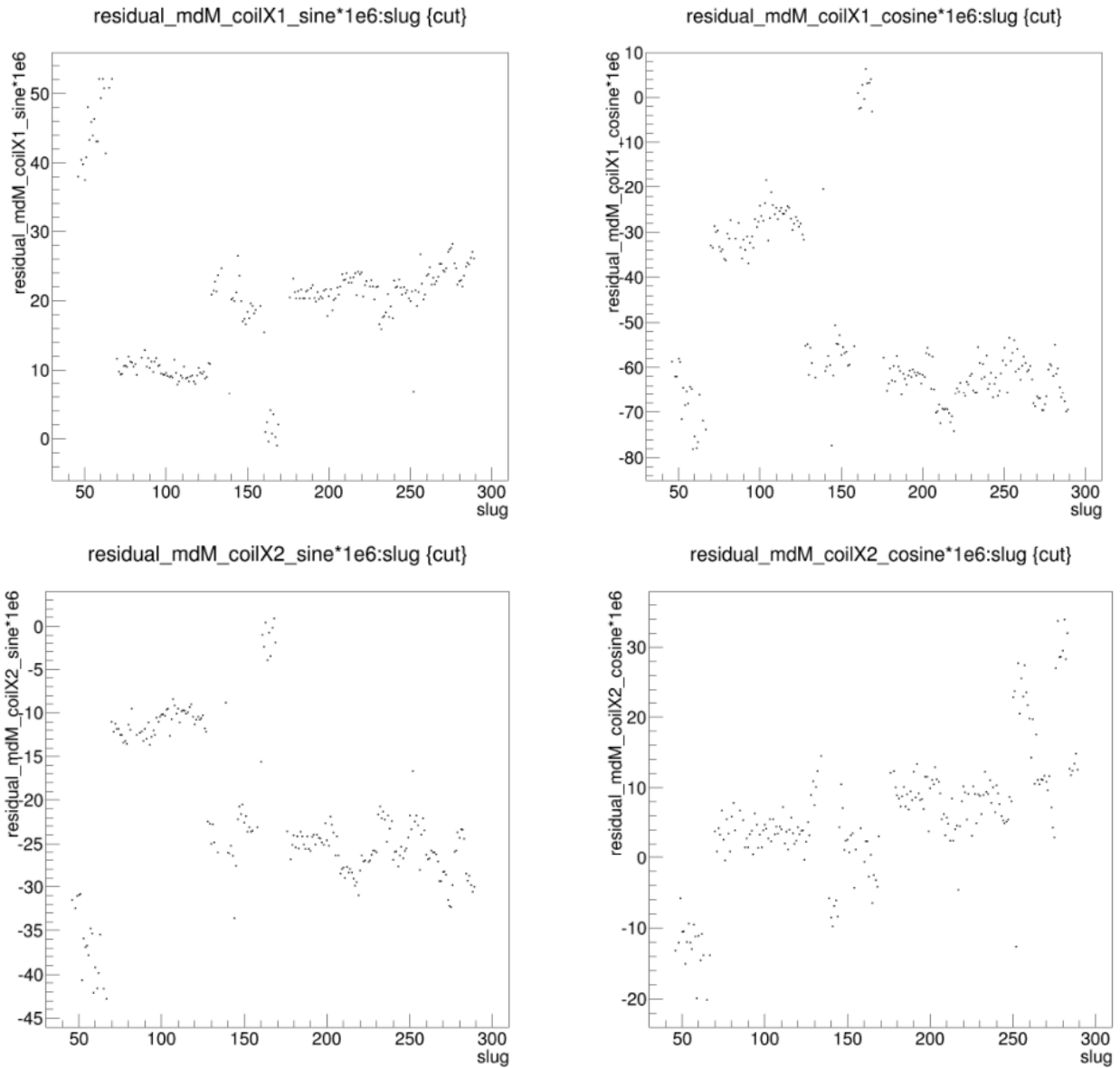


Figure 3.13: Main detector dithering residual slug history in pattern X1 and X2. (Top left) X1 pattern sine residual. (Top right) X1 pattern cosine residual. (Bottom left) X2 pattern sine residual. (Bottom right) X2 pattern cosine residual.

This means two equations in the set of four X equations are redundant with respect to the remaining two. When two equations are satisfied, the rest two are at the same time fulfilled. For the two parameters involved, horizontal position X and angle X', we only have two effective equations. Therefore the two effective equations can solve horizontal position and angle sensitivities sufficiently. In this case, the dithering residuals for the two patterns are zero within statistical error when all ten pattern equations are included.

We now look at the dithering residual in the energy modulation patterns in Fig. 3.14. On the left, we have the dithering residual from pattern E_sin, the dominate energy modulation pattern. We can see that the residual is approximately within ~ 5 ppm. This is good compared to the X mode residuals (typically ~ 50 ppm). This means for the energy dominated modulation pattern, the residual is small compared to the energy induced response in the main detector.

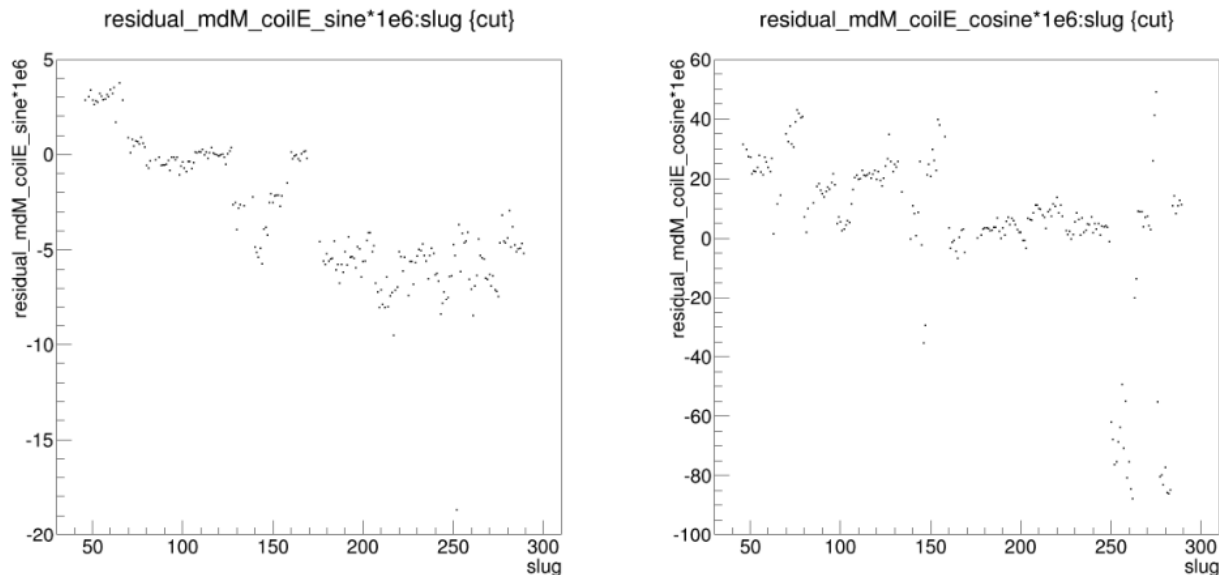


Figure 3.14: Main detector dithering residual slug history in pattern E. (Left) E pattern sine residual. (Right) E pattern cosine residual.

Since the modulation modes in the X direction are well separated from the Y modulation modes (we have seen before in Sect. 3.4.4 that many angles between X and Y pattern pairs are close to 90°), we could consider the three parameters, E, X, X', as a group. From the

residuals in X modulation patterns (Fig. 3.13) and energy pattern (Fig. 3.14), we can see that the main detector responses can't be fully described by the three parameters. We know that energy can result in a considerable amount of change in the main detector. But when the three parameters are analyzed together, we still have an unexplained residual response in the detector.

In general, in this section we have seen that the dithering residuals are not zero in some of the patterns. The statistical deviation from zero is normal, which can be explained by the statistical error of the dithering coefficients. But we have seen that there could be a systematic effect for non zero dithering residuals in some patterns. One possible reason is that we have another source of beam parameter that can result in the main detector response during beam modulation. Even though we didn't modulate this "hidden" variable intentionally, it happened to be non zero during the modulation stage and the extra response in the main detector cannot be explained completely by the five beam parameters (energy, position, angle). This might turn out to be difficult to identify the source of the residuals because we don't have direction measurements from this possible variable.

3.7 Beam Correction Systematic Error

In the last section, we calculated the detector residuals for each dithering pattern. We have seen that for different dithering patterns, the residual can be quite different. The residuals are generally higher in X-like patterns (Fig. 3.13) and lower in Y like patterns (Fig. 3.12). Since we have different residuals in different patterns, the solution of sensitivities can depend on what dithering patterns we choose. For example, if we choose to omit one of the X patterns and use the rest to calculate sensitivity, since the residuals in X patterns are high, the sensitivities for X parameters, like horizontal position and angle, are likely to be altered from the full ten pattern results. With this different set of detector sensitivities, the beam correction can be different as well since it is based on sensitivities and monitor

differences (Eq. 3.2). Therefore, we need to study the effects of omitting patterns during the calculation of sensitivities and see how they can affect the main detector asymmetry results.

3.7.1 Dithering Schemes

The dithering sensitivities calculated previously in Sect. 3.5.2 utilized all ten effective patterns. All ten equations are included in the χ^2 minimization (Eq. 3.29). When all ten patterns are included, this dithering scheme is referred to as “10 coil” scheme. It is a conservative scheme since we have no preference for any of the patterns we have.

Therefore, this scheme can serve as a candidate for the central value of beam correction. We shall see later how this works.

We have more patterns than we need (five is enough to solve the equation set and we have ten), and this redundancy can result in the discrepancies of the sensitivities calculated. To study the influence of this redundancy on our results, patterns are selectively removed to test the resulted sensitivities. We remove one or two patterns out of ten at a time to form a new dithering scheme. Different schemes have different results, and each scheme has its own dithering sensitivities calculated. A systematic error term is introduced to cover the discrepancies in the results.

During the experiment, five dithering patterns, X1, Y1, E, X2, Y2, were performed. The sine and cosine responses together provide ten dithering coils, which are named pattern (or coil) 0-9 following the order of X1_sin, Y1_sin, E_sin, X2_sin, Y2_sin and X1_cos, Y1_cos, E_cos, X2_cos, Y2_cos (see details in Tab. 3.5). We remove one coil at a time, which we call the “single-coil-removal” procedure. We can also remove two coils at a time, or a “double-coil-removal” procedure. Since FFB was off during energy modulation, the energy patterns are not redundant. We should keep the energy patterns (2 and 7), and we can remove the rest of the coils safely as long as we don’t exceed two coils at a time (at least two patterns are required to decouple position and angle, horizontally or vertically).

Therefore, the dithering schemes we can use are summarized in Tab. 3.10.

Table 3.10: Dithering schemes with select pattern removal .

Scheme Category	No. of Coils Removed	No. of Coils Kept	Dither Schemes
Full	0	10	10coil
Sing-Coil Removal	1	9	OmitCoil0, OmitCoil1, OmitCoil3, OmitCoil4, OmitCoil5, OmitCoil6, OmitCoil8, OmitCoil9
Double-Coil Removal	2	8	OmitCoil05, OmitCoil01, OmitCoil06, OmitCoil03, OmitCoil08, OmitCoil04, OmitCoil09, OmitCoil15, OmitCoil56, OmitCoil35, OmitCoil58, OmitCoil45, OmitCoil59, OmitCoil16, OmitCoil13, OmitCoil18, OmitCoil14, OmitCoil19, OmitCoil36, OmitCoil68, OmitCoil46, OmitCoil69, OmitCoil38, OmitCoil34, OmitCoil39, OmitCoil48, OmitCoil89, OmitCoil49

The schemes with certain patterns removed are referred to as “OmitCoil” schemes, followed by the pattern number(s) removed in this scheme. For the schemes with a single pattern removed, the ten patterns are removed one at a time (skipping 2 and 7), so we have 8 single-coil-removal schemes. When we remove two patterns for sensitivity calculation, each pair of patterns are selectively removed from the combinations (no pattern 2 or 7 involved), and in the end, we have 28 double-coil-removal schemes. Compared to the “10 coil” scheme which utilized all 10 patterns, the single-coil-removal and double-coil-removal schemes utilized 9 and 8 patterns out of 10, respectively. Including the full 10 coil scheme, the “single-coil-removal” and “double-coil-removal” schemes, we have 37 schemes in total.

3.7.2 Sensitivities with Different Schemes

By selecting different patterns to remove, we can calculate the corresponding sensitivities based on patterns available in each dithering scheme. The schemes with two patterns removed are not completely independent from the schemes with single pattern removal. To illustrate this more clearly, here the sensitivities with one pattern removal are shown for analysis. The one pattern removal schemes should show more clearly what effect we have on the sensitivities when that pattern is excluded. This way we can tell what role each coil plays in the sensitivity calculation. The scheme with two patterns removed can typically show the combined effects of the two corresponding single-coil-removal schemes.

Energy Sensitivities with Different Schemes

In Fig. 3.15, we have the dithering sensitivity for the energy monitor from different schemes, including 10 coil and single-coil-removal schemes. The full 10 coil scheme is marked with black and the other schemes with a single coil removed are marked with various colors. The schemes with X-like pattern removed have red or orange colors, and the schemes with Y like pattern removed are in blue or green colors. The zero dashed line is drawn here to typically show the variation of energy sensitivity over time; we can see that the energy slope is relatively stable across Run 1 and Run 2.

Also from Fig. 3.15, we can see that the energy sensitivities from different schemes are generally close to one another. For the slugs around Wien 9a and 9b, omitting pattern 0 or 3 can cause the energy sensitivity to shift. This means pattern 0 or 3 plays an important role in the energy sensitivity determination. We have kept the energy modulation patterns for the single-coil-removal schemes, which are dominate modulation modes that help determine energy sensitivity. For most of the slugs, the energy sensitivity is not affected by much by removing the modulation patterns that were mainly focused on dithering (horizontal or vertical) position and angle. Since the main detector is more sensitive to energy, we can't lose the energy modulation pattern, which is why pattern 2 or 7 was kept

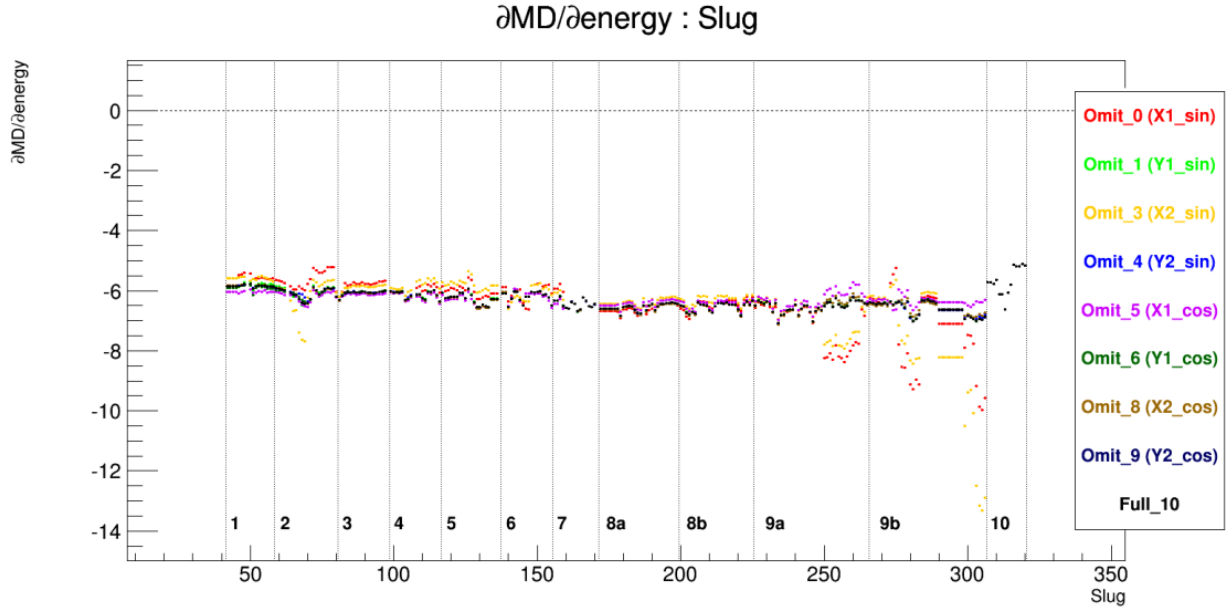


Figure 3.15: Main detector energy sensitivity slug history from different dithering schemes.

during pattern removal in the schemes listed in Tab. 3.10.

Vertical Position and Angle Sensitivities with Different Schemes

In Fig. 3.16 and 3.17, we have the dithering sensitivities for vertical beam parameters calculated by different dithering schemes. Vertical position and angle are in Fig. 3.17 and 3.16, respectively. Just like Y and Y' sensitivity results for the ten pattern scheme (Fig. 3.11), the sensitivities in vertical directions from different schemes are all generally close to zero for the majority of the data, and the agreement between different schemes is good. This is consistent with the observation in Sect. 3.6.2 when we looked at the residual history for Y like patterns (Fig. 3.12). The residuals for Y patterns, including pattern 1, 4, 6, 9, are small. The results from different Y pattern combinations should agree with each other. When removing one of the Y patterns, the sensitivities in the Y directions don't change much.

Since the Y patterns are dominant modulation modes that help determine sensitivities in the vertical directions, removing one of the X patterns doesn't affect the Y sensitivities

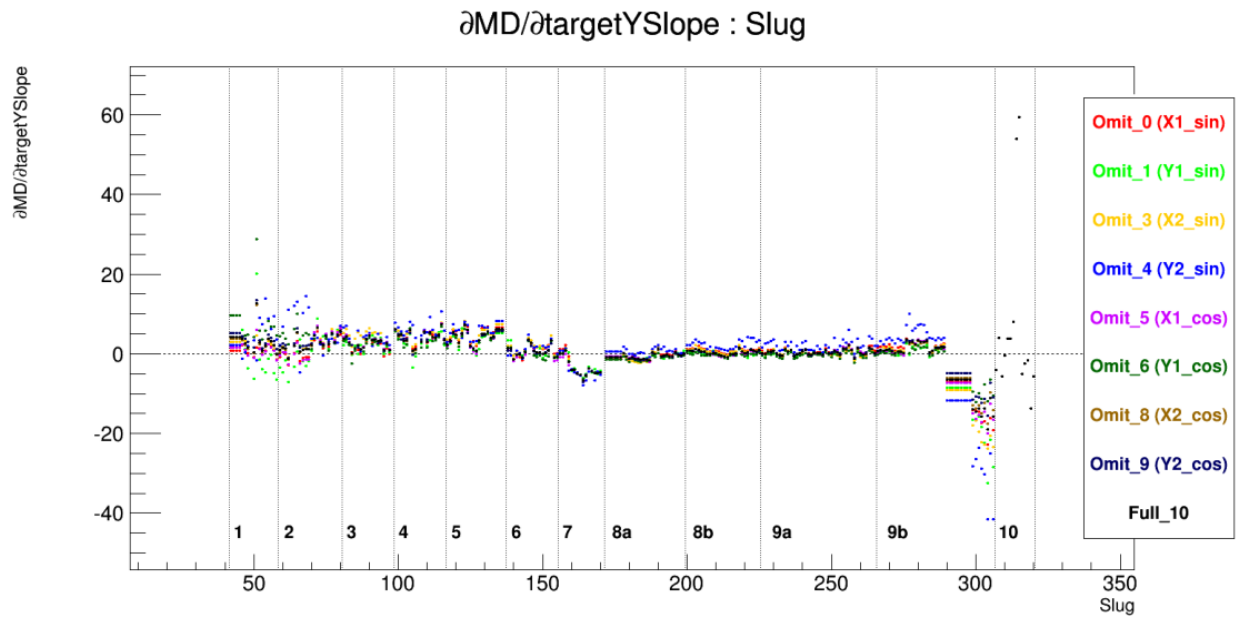


Figure 3.16: Main detector vertical angle sensitivity slug history from different dithering schemes.

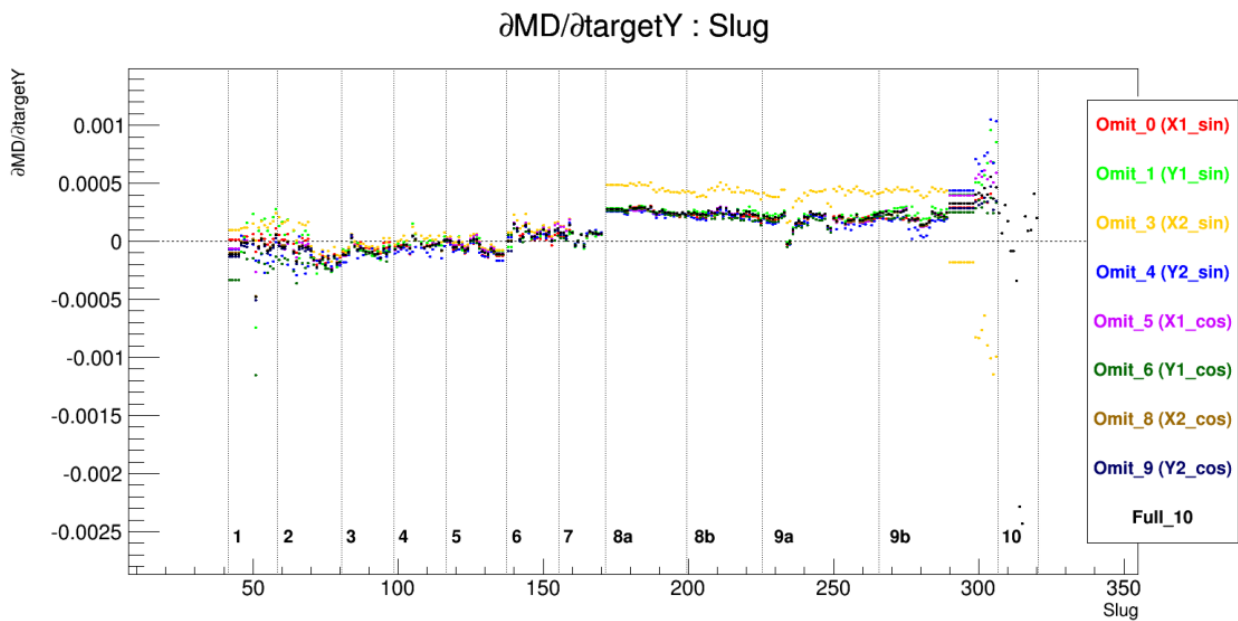


Figure 3.17: Main detector vertical position sensitivity slug history from different dithering schemes.

either. However, for the vertical position sensitivity in Fig. 3.17, we can see that omitting coil 3 (X2_sin) can change the vertical position sensitivity by almost a factor of 2 in Wien 8 and 9. This means pattern 3 also plays a role in the vertical position sensitivity determination. Even though pattern 3 is sine response from horizontal X2 modulation mode, the dithering motion of the beam in X2 pattern was involved with some vertical motion as well.

Horizontal Position and Angle Sensitivities with Different Schemes

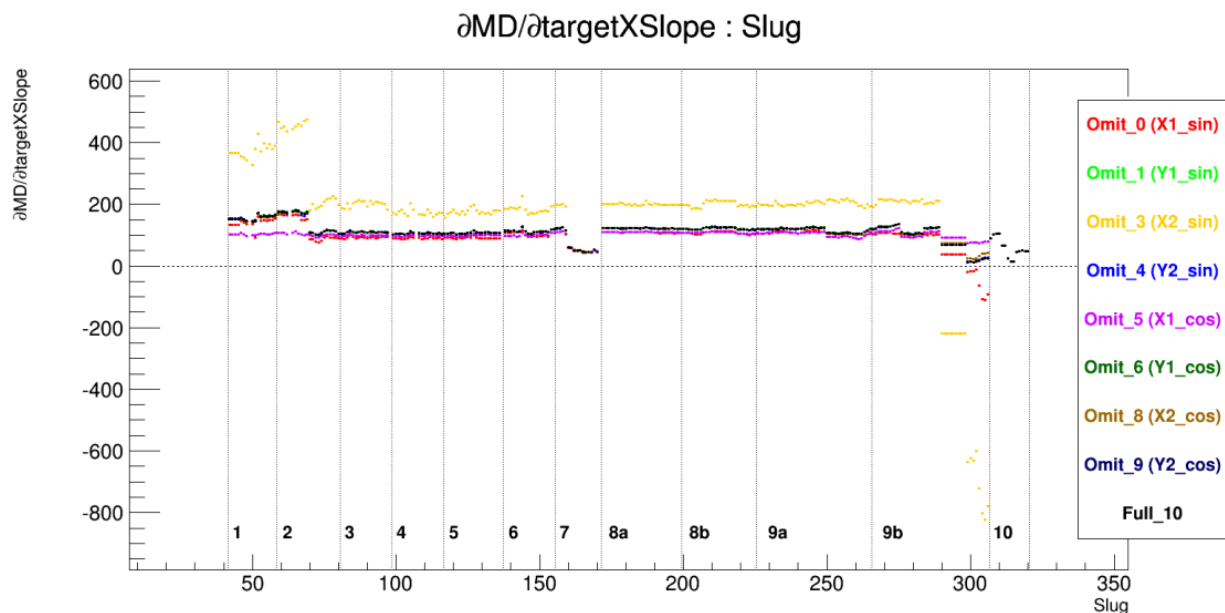


Figure 3.18: Main detector horizontal angle sensitivity slug history from different dithering schemes.

The sensitivity history plots for horizontal directions are shown in Fig. 3.18 and Fig. 3.19. The horizontal position sensitivity history plot is in Fig. 3.19 and the horizontal angle plot is in Fig. 3.18. We can see that in general, the sensitivities from different schemes differ quite a bit in the horizontal direction. When removing X like patterns (pattern 0, 3, 5, 8), the sensitivities can be altered by a lot. And the removal of Y like patterns (pattern 1, 4, 6, 9) don't affect the X sensitivities by much, as expected, since we don't have much horizontal motion in the beam during Y modulation modes. The different sensitivities from

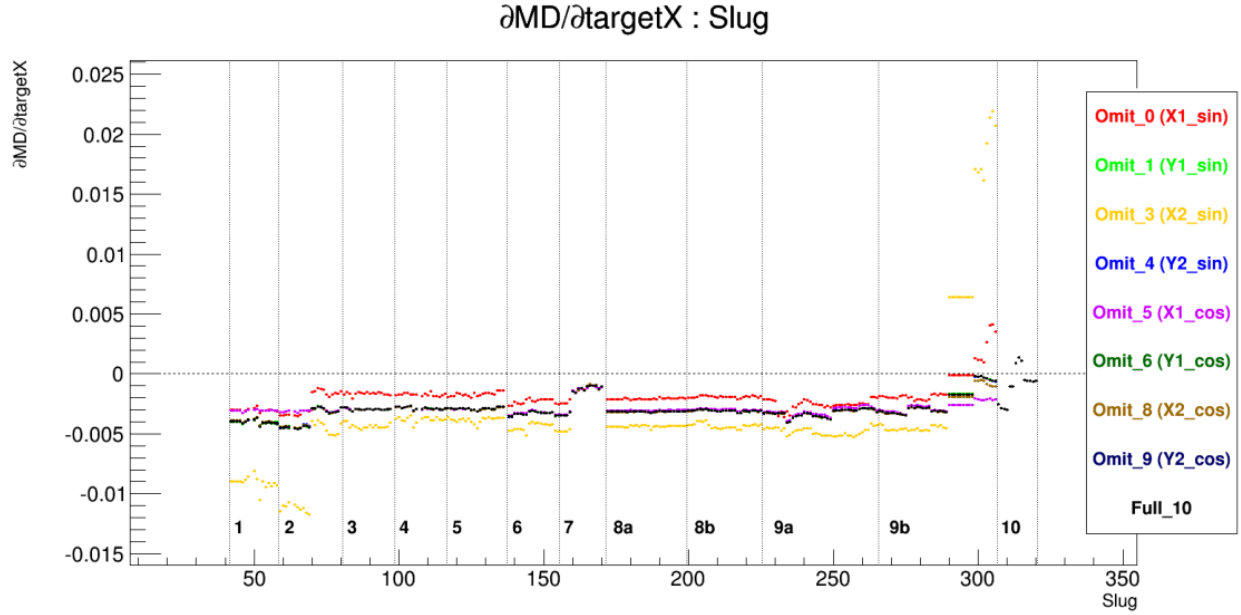


Figure 3.19: Main detector horizontal position sensitivity slug history from different dithering schemes.

different schemes by removing X patterns agree with the observation we had in the residual history plots (Sect. 3.6.2). From the residuals' perspective, we have high residuals in the X patterns, and removing one of them can greatly alter the X sensitivities.

In Fig. 3.18, we have the dithering sensitivities for horizontal angle motion. Different dithering schemes, especially the schemes with X like patterns removed, can mostly agree within about 10%. But removing pattern 3 can change the slope by a factor of 2, just like it did for vertical position (Fig. 3.17) in Wien 8 and 9. Also removing coil 0 or 5 can slightly shift the sensitivity toward zero.

In Fig. 3.19, for the horizontal position monitor, the schemes can also differ by much, especially when we remove pattern 0 or 3. When omitting coil 3, the horizontal position sensitivity is almost doubled. And when removing coil 0, the slope is shifted toward zero by up to 50%.

In general, the discrepancies of dithering schemes mainly come from the cases when we remove the X like patterns. This agrees with the high dithering residual observed for these patterns. Sometimes, not only the removal of these patterns can affect horizontal

sensitivities, they can affect other sensitivities to some level as well. The altered sensitivities for different coil removal options can affect the results of dithering correction and the dither corrected main detector asymmetries.

3.7.3 Main Detector Asymmetries with Different Schemes

The HCBA's in main detector raw asymmetries can be corrected with different sets of sensitivities from different dithering schemes. The discrepancy in the dithering sensitivities from these dithering schemes can result in different beam correction values and main detector asymmetry results. In this section, the main detector asymmetries at Wien level are shown here for comparison between the schemes. Like the previous section, for the purpose of clarity, we show single-coil-removal schemes together with the full 10 coil scheme.

In Fig. 3.20, we have main detector asymmetries at Wien level for Run 1 from different schemes. Five Wiens (1-5) from Run 1 are included. The schemes from various coil removal options are represented by different colors. The schemes of most interest are from X coil removal options, like coil 0 (X1_sin), 3 (X2_sin), 5 (X1_cos), and 8 (X2_cos). For Wien 5, the asymmetries from different schemes agree pretty well. But for other Wiens, the schemes can have different asymmetries, especially Wien 2. Omitting coil 0 (red), 3 (orange) and 5 (magenta) can clearly alter the main detector asymmetry. These are the coils in the horizontal modulation patterns, like X1 and X2 sine and cosines responses.

Still in Fig. 3.20, the average of the five Wiens give the physics asymmetries for Run 1. We can tell from the dashed lines that all colored lines almost coincide with each other, while the pattern 5 removal scheme sits below other schemes, and the pattern 3 removal scheme asymmetry is smaller than others. The full 10 coil scheme is mixed with all other schemes.

In Fig. 3.21, we have the physics asymmetries Wien plot for Run 2. Run 2 in general is in a better situation than Run 1 because we can see that only one Wien (Wien 8a)

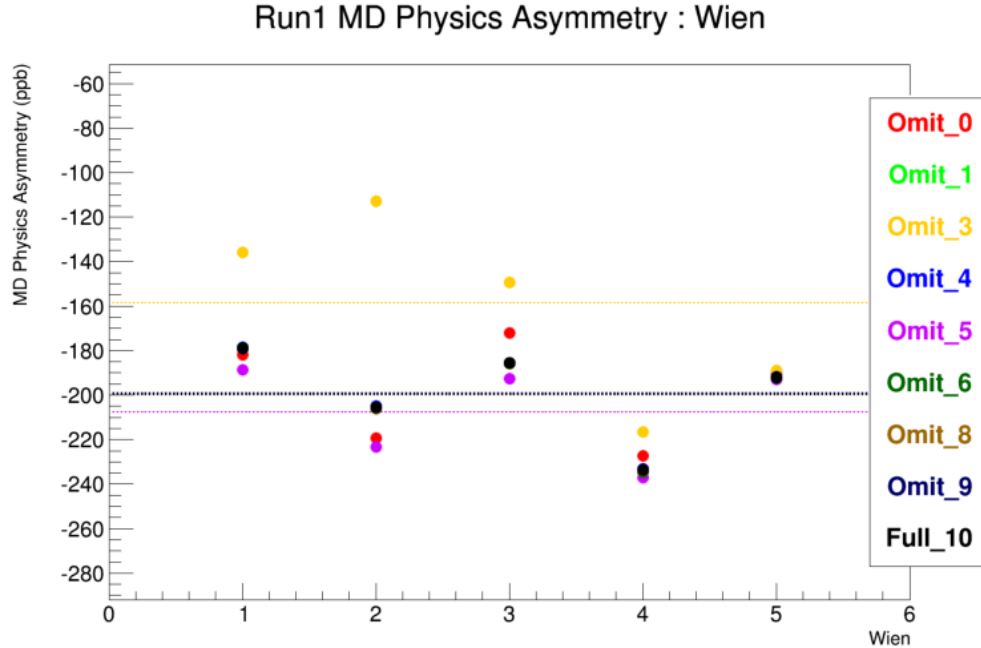


Figure 3.20: Main detector physics asymmetry in Run 1 with different dithering schemes.

disagrees for different dither schemes.

By looking at different Wiens in Run 2, Wien 6, 7, 8b, 9a, and 9b agree well for different schemes (Wien 10 is special because in most of Wien 10 the FFB was turned off for all dithering patterns, so removal of a cosine coil won't change things, but removal of a sine coil is not appropriate. In this case, the Wien 10 coil-removal scheme is replaced with 10 coil scheme.) But in Wien 8a, we can see that the different schemes can differ by 20 ppb or even higher.

By comparing Run 1 and Run 2, we can see that different dithering schemes can give very different asymmetries. We need to set rules that can serve as criteria for picking out the good schemes from the rest.

3.7.4 Scheme Selection Criteria

Different dithering schemes give quite different main detector asymmetries, so we need to carefully choose from the schemes and remove those that don't work and cause wrong main

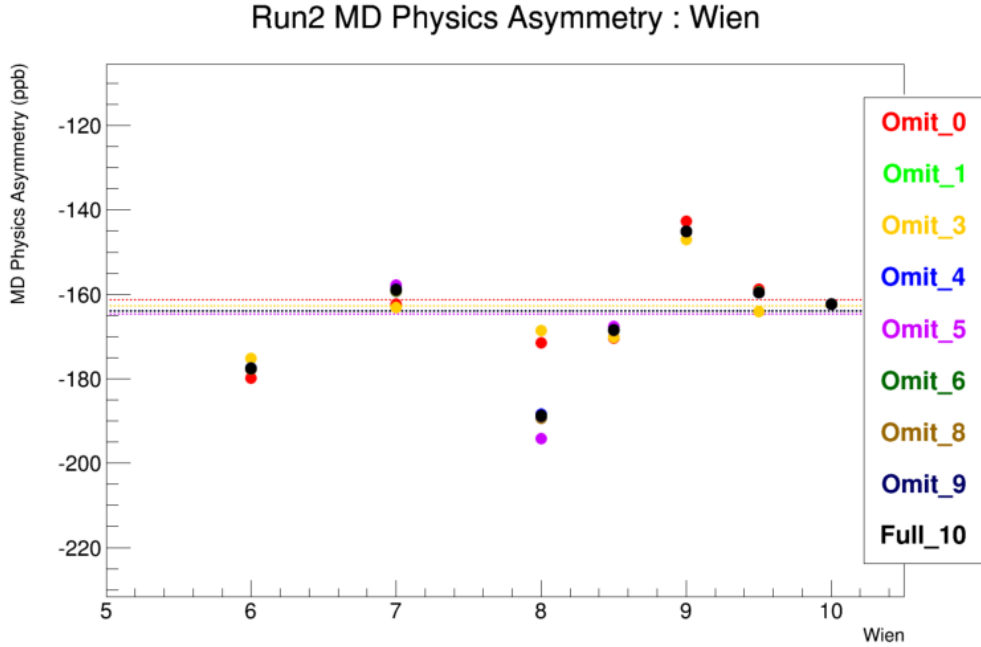


Figure 3.21: Main detector physics asymmetry in Run 2 with different dithering schemes.

detector asymmetries. To choose the good schemes from all the schemes listed in Tab.

3.10, we need a few criteria listed below:

- **MD Asymmetry Stability.** Or the χ^2 and probability at slug level. This gives a direct look into the quality of the data after beam correction from each dither scheme.
- **Residual Correlations.** The correlation to beam parameters after beam correction, including beam energy, position and angle. The residual corrections should be well controlled.
- **MD Asymmetry Error.** Statistical error of main detector asymmetry. Or, equivalently the main detector asymmetry width after beam false asymmetry removal. The main detector asymmetry width should be reduced after the beam correction.

With the three criteria listed above, we look at those quantities for all the available dithering schemes. The results are shown in Fig 3.22 (Run 1) and Fig 3.23 (Run 2).

In these two tables, for each dithering scheme, we have slug level χ^2 and probability, residual correlation to beam energy, horizontal position (targetX) & angle (targetXSlope),

Dither Schemes	Chi2	Prob	Corr Energy (ppb/1e-6)	Corr targetX (ppb/um)	Corr targetXSlope (ppb/nrad)	Corr targetY (ppb/um)	Corr targetYSlope (ppb/nrad)	MD Asym Error (ppb)	MD Asym (ppb)
OmitCoil01	1.19	0.103	-291.0+-681.2 (0.4)	-106.7+-197.9 (0.5)	-2.1+-5.6 (0.4)	-113.2+-309.7 (0.4)	-4.1+-6.9 (0.6)	13.155	-199.18
OmitCoil06	1.19	0.103	-310.3+-681.2 (0.5)	-96.1+-197.9 (0.5)	-1.9+-5.6 (0.3)	-92.1+-309.7 (0.3)	-3.6+-6.9 (0.5)	13.155	-199.42
OmitCoil0	1.19	0.100	-315.5+-681.2 (0.5)	-102.7+-197.9 (0.5)	-2.1+-5.6 (0.4)	-117.9+-309.7 (0.4)	-4.3+-6.9 (0.6)	13.155	-199.18
OmitCoil09	1.20	0.100	-321.7+-681.2 (0.5)	-102.5+-197.9 (0.5)	-2.1+-5.6 (0.4)	-117.0+-309.7 (0.4)	-4.2+-6.9 (0.6)	13.155	-199.21
OmitCoil04	1.20	0.093	-349.6+-681.2 (0.5)	-112.0+-197.9 (0.6)	-2.5+-5.6 (0.5)	-133.9+-309.7 (0.4)	-4.7+-6.9 (0.7)	13.155	-198.55
OmitCoil05	1.25	0.058	552.5+-681.1 (0.8)	318.6+-197.9 (1.6)	10.7+-5.6 (1.9)	178.9+-309.6 (0.6)	4.8+-6.9 (0.7)	13.152	-202.66
OmitCoil69	1.27	0.041	-57.2+-681.1 (0.1)	632.4+-197.9 (3.2)	16.7+-5.6 (3.0)	527.2+-309.6 (1.7)	12.5+-6.9 (1.8)	13.151	-202.35
OmitCoil1	1.28	0.039	-151.2+-681.1 (0.2)	568.5+-197.9 (2.9)	14.1+-5.6 (2.5)	192.0+-309.6 (0.6)	5.0+-6.9 (0.7)	13.150	-199.63
OmitCoil19	1.28	0.039	-159.3+-681.1 (0.2)	569.0+-197.9 (2.9)	14.1+-5.6 (2.5)	189.9+-309.6 (0.6)	4.9+-6.9 (0.7)	13.150	-199.68
10coil	1.28	0.037	-174.6+-681.1 (0.3)	568.8+-197.9 (2.9)	14.0+-5.6 (2.5)	185.2+-309.6 (0.6)	4.8+-6.9 (0.7)	13.150	-199.49
OmitCoil18	1.28	0.037	-82.9+-681.0 (0.1)	590.4+-197.9 (3.0)	14.8+-5.6 (2.6)	218.1+-309.6 (0.7)	5.7+-6.9 (0.8)	13.149	-200.02
OmitCoil6	1.28	0.037	-169.1+-681.1 (0.2)	576.1+-197.9 (2.9)	14.2+-5.6 (2.5)	208.4+-309.6 (0.7)	5.4+-6.9 (0.8)	13.150	-199.79
OmitCoil9	1.28	0.037	-181.4+-681.1 (0.3)	568.9+-197.9 (2.9)	14.0+-5.6 (2.5)	184.4+-309.6 (0.6)	4.8+-6.9 (0.7)	13.150	-199.53
OmitCoil08	1.29	0.035	-952.8+-681.9 (1.4)	-506.9+-198.1 (2.6)	-13.6+-5.6 (2.4)	-404.0+-310.1 (1.3)	-12.4+-6.9 (1.8)	13.173	-195.73
OmitCoil68	1.29	0.035	-96.4+-681.1 (0.1)	601.1+-197.9 (3.0)	15.1+-5.6 (2.7)	239.5+-309.6 (0.8)	6.2+-6.9 (0.9)	13.149	-200.20
OmitCoil8	1.29	0.035	-106.5+-681.0 (0.2)	591.8+-197.9 (3.0)	14.8+-5.6 (2.6)	211.9+-309.6 (0.7)	5.5+-6.9 (0.8)	13.149	-199.89
OmitCoil89	1.29	0.035	-111.3+-681.0 (0.2)	592.7+-197.9 (3.0)	14.8+-5.6 (2.6)	213.5+-309.6 (0.7)	5.6+-6.9 (0.8)	13.149	-199.95
OmitCoil4	1.29	0.035	-207.9+-681.1 (0.3)	560.4+-197.9 (2.8)	13.6+-5.6 (2.4)	165.8+-309.6 (0.5)	4.3+-6.9 (0.6)	13.150	-199.09
OmitCoil49	1.29	0.035	-237.4+-681.1 (0.3)	562.9+-197.9 (2.8)	13.6+-5.6 (2.4)	136.8+-309.6 (0.4)	3.8+-6.9 (0.5)	13.150	-199.97
OmitCoil48	1.29	0.033	-142.1+-681.0 (0.2)	583.7+-197.9 (3.0)	14.4+-5.6 (2.6)	191.0+-309.6 (0.6)	5.0+-6.9 (0.7)	13.149	-199.52
OmitCoil46	1.31	0.026	-132.7+-681.3 (0.2)	560.3+-197.9 (2.8)	13.8+-5.6 (2.5)	299.4+-309.6 (1.0)	6.8+-6.9 (1.0)	13.153	-195.38
OmitCoil5	1.40	0.007	829.8+-680.7 (1.2)	810.9+-197.8 (4.1)	23.1+-5.6 (4.1)	460.4+-309.5 (1.5)	12.1+-6.9 (1.8)	13.144	-207.73
OmitCoil15	1.40	0.007	866.4+-680.7 (1.3)	810.9+-197.8 (4.1)	23.3+-5.6 (4.2)	471.7+-309.5 (1.5)	12.5+-6.9 (1.8)	13.144	-207.80
OmitCoil56	1.40	0.007	828.9+-680.7 (1.2)	815.2+-197.8 (4.1)	23.2+-5.6 (4.1)	468.4+-309.5 (1.5)	12.3+-6.9 (1.8)	13.144	-207.85
OmitCoil45	1.41	0.007	807.4+-680.7 (1.2)	802.9+-197.8 (4.1)	22.8+-5.6 (4.1)	445.0+-309.5 (1.4)	11.7+-6.9 (1.7)	13.144	-207.39
OmitCoil59	1.40	0.007	821.2+-680.7 (1.2)	810.1+-197.8 (4.1)	23.1+-5.6 (4.1)	450.6+-309.5 (1.5)	11.9+-6.9 (1.7)	13.144	-207.72
OmitCoil58	1.43	0.005	984.7+-680.6 (1.4)	858.5+-197.8 (4.3)	24.8+-5.6 (4.4)	519.0+-309.5 (1.7)	13.7+-6.9 (2.0)	13.143	-208.76
OmitCoil16	1.44	0.004	-481.4+-683.3 (0.7)	746.9+-198.3 (3.8)	17.3+-5.6 (3.1)	271.2+-309.9 (0.9)	6.1+-6.9 (0.9)	13.184	-204.27
OmitCoil03	2.07	0.000	-4677.1+-683.8 (6.8)	-995.8+-198.7 (5.0)	-42.4+-5.6 (7.5)	-1726.7+-310.9 (5.6)	-46.7+-6.9 (6.8)	13.213	-172.46
OmitCoil35	1.58	0.000	-3228.7+-683.3 (4.7)	-50.2+-198.5 (0.3)	-11.8+-5.6 (2.1)	-775.8+-310.3 (2.5)	-20.5+-6.9 (3.0)	13.187	-178.05
OmitCoil13	2.33	0.000	-5930.3+-687.4 (8.6)	-408.4+-199.3 (2.0)	-29.5+-5.6 (5.2)	-1338.5+-311.1 (4.3)	-35.7+-6.9 (5.2)	13.245	-158.33
OmitCoil14	3.37	0.000	-3831.5+-687.6 (5.6)	-156.6+-200.1 (0.8)	-24.0+-5.7 (4.2)	-1789.9+-314.4 (5.7)	-62.9+-6.9 (9.1)	13.296	-176.95
OmitCoil36	2.32	0.000	-5922.5+-687.3 (8.6)	-398.0+-199.3 (2.0)	-29.3+-5.6 (5.2)	-1325.5+-311.1 (4.3)	-35.4+-6.9 (5.1)	13.243	-158.78
OmitCoil3	2.32	0.000	-5931.1+-687.3 (8.6)	-405.2+-199.3 (2.0)	-29.5+-5.6 (5.2)	-1342.2+-311.1 (4.3)	-35.8+-6.9 (5.2)	13.243	-158.59
OmitCoil38	2.50	0.000	-6427.2+-688.2 (9.3)	-479.8+-199.5 (2.4)	-33.0+-5.6 (5.9)	-1458.3+-311.3 (4.7)	-39.1+-6.9 (5.7)	13.262	-155.00
OmitCoil34	2.35	0.000	-5972.3+-687.3 (8.7)	-412.7+-199.3 (2.1)	-29.9+-5.6 (5.3)	-1363.1+-311.1 (4.4)	-36.3+-6.9 (5.3)	13.243	-158.21
OmitCoil39	2.33	0.000	-5944.8+-687.3 (8.6)	-407.9+-199.3 (2.0)	-29.6+-5.6 (5.3)	-1351.2+-311.1 (4.3)	-36.0+-6.9 (5.2)	13.243	-158.58

Figure 3.22: Summary of results for dither schemes in Run 1.

Dither Schemes	Chi2	Prob	Corr Energy (ppb/1e-6)	Corr targetX (ppb/um)	Corr targetXSlope (ppb/nrad)	Corr targetY (ppb/um)	Corr targetYSlope (ppb/nrad)	MD Asym Error (ppb)	MD Asym (ppb)
OmitCoil05	1.12	0.123	998.5+1052.9 (0.9)	-89.9+130.4 (0.7)	-1.9+4.9 (0.4)	-356.4+202.0 (1.8)	-12.9+6.8 (1.9)	7.339	-162.94
OmitCoil16	1.13	0.108	824.7+1053.1 (0.8)	-44.6+130.5 (0.3)	-0.3+4.9 (0.1)	-323.3+202.0 (1.6)	-11.7+6.8 (1.7)	7.343	-164.04
OmitCoil1	1.13	0.106	809.9+1053.1 (0.8)	-54.8+130.5 (0.4)	-0.7+4.9 (0.1)	-332.8+202.0 (1.6)	-12.1+6.8 (1.8)	7.342	-164.00
OmitCoil19	1.13	0.106	792.5+1053.1 (0.8)	-53.1+130.5 (0.4)	-0.7+4.9 (0.1)	-330.4+202.0 (1.6)	-12.0+6.8 (1.8)	7.342	-163.95
OmitCoil46	1.13	0.106	832.3+1053.1 (0.8)	-48.3+130.5 (0.4)	-0.5+4.9 (0.1)	-327.2+202.0 (1.6)	-11.8+6.8 (1.7)	7.343	-164.08
OmitCoil6	1.13	0.105	826.9+1053.1 (0.8)	-48.2+130.5 (0.4)	-0.5+4.9 (0.1)	-327.6+202.0 (1.6)	-11.8+6.8 (1.7)	7.343	-164.10
10coil	1.13	0.104	814.1+1053.1 (0.8)	-54.9+130.5 (0.4)	-0.7+4.9 (0.1)	-333.6+202.0 (1.7)	-12.1+6.8 (1.8)	7.342	-164.01
OmitCoil9	1.13	0.104	798.9+1053.1 (0.8)	-53.5+130.5 (0.4)	-0.7+4.9 (0.1)	-331.8+202.0 (1.6)	-12.0+6.8 (1.8)	7.342	-163.97
OmitCoil69	1.14	0.103	777.2+1053.2 (0.7)	-18.5+130.5 (0.1)	0.6+4.9 (0.1)	-294.0+202.1 (1.5)	-10.4+6.8 (1.5)	7.344	-164.10
OmitCoil4	1.14	0.103	824.7+1053.1 (0.8)	-56.3+130.5 (0.4)	-0.8+4.9 (0.2)	-335.4+202.0 (1.7)	-12.2+6.8 (1.8)	7.342	-163.94
OmitCoil49	1.14	0.102	808.2+1053.1 (0.8)	-55.4+130.5 (0.4)	-0.7+4.9 (0.2)	-333.8+202.0 (1.7)	-12.2+6.8 (1.8)	7.342	-163.87
OmitCoil18	1.14	0.099	788.4+1053.1 (0.7)	-37.2+130.5 (0.3)	-0.1+4.9 (0.0)	-321.0+202.0 (1.6)	-11.6+6.8 (1.7)	7.343	-164.13
OmitCoil68	1.14	0.098	804.3+1053.1 (0.8)	-28.3+130.5 (0.2)	0.3+4.9 (0.1)	-313.8+202.0 (1.6)	-11.3+6.8 (1.7)	7.343	-164.25
OmitCoil89	1.14	0.098	776.8+1053.1 (0.7)	-35.5+130.5 (0.3)	-0.0+4.9 (0.0)	-319.6+202.0 (1.6)	-11.6+6.8 (1.7)	7.343	-164.11
OmitCoil8	1.14	0.097	792.5+1053.1 (0.8)	-37.4+130.5 (0.3)	-0.1+4.9 (0.0)	-322.0+202.0 (1.6)	-11.7+6.8 (1.7)	7.343	-164.14
OmitCoil48	1.14	0.096	802.6+1053.1 (0.8)	-38.8+130.5 (0.3)	-0.1+4.9 (0.0)	-323.7+202.0 (1.6)	-11.8+6.8 (1.7)	7.343	-164.08
OmitCoil35	1.15	0.083	933.6+1054.0 (0.9)	-337.4+130.7 (2.6)	-11.8+4.9 (2.4)	-555.5+202.2 (2.7)	-19.2+6.8 (2.8)	7.373	-162.75
OmitCoil15	1.16	0.071	717.0+1053.1 (0.7)	133.5+130.5 (1.0)	6.6+4.9 (1.3)	-180.6+202.0 (0.9)	-7.0+6.8 (1.0)	7.343	-164.67
OmitCoil5	1.16	0.069	722.6+1053.1 (0.7)	134.0+130.5 (1.0)	6.6+4.9 (1.4)	-181.1+202.0 (0.9)	-7.0+6.8 (1.0)	7.343	-164.64
OmitCoil56	1.16	0.069	741.8+1053.1 (0.7)	134.3+130.5 (1.0)	6.7+4.9 (1.4)	-181.6+202.0 (0.9)	-7.0+6.8 (1.0)	7.343	-164.71
OmitCoil59	1.16	0.069	710.6+1053.1 (0.7)	133.2+130.5 (1.0)	6.6+4.9 (1.3)	-181.8+202.0 (0.9)	-7.0+6.8 (1.0)	7.343	-164.59
OmitCoil45	1.16	0.068	733.8+1053.1 (0.7)	132.5+130.5 (1.0)	6.6+4.9 (1.3)	-182.7+202.0 (0.9)	-7.1+6.8 (1.0)	7.343	-164.60
OmitCoil58	1.18	0.053	679.6+1053.1 (0.6)	169.3+130.5 (1.3)	8.0+4.9 (1.6)	-155.9+202.0 (0.8)	-6.1+6.8 (0.9)	7.345	-164.83
OmitCoil06	1.24	0.015	1280.0+1053.4 (1.2)	-582.9+130.5 (4.5)	-20.9+4.9 (4.3)	-763.0+202.1 (3.8)	-26.8+6.8 (3.9)	7.347	-161.46
OmitCoil0	1.24	0.014	1266.7+1053.4 (1.2)	-589.0+130.5 (4.5)	-21.2+4.9 (4.3)	-768.8+202.1 (3.8)	-27.1+6.8 (4.0)	7.347	-161.37
OmitCoil01	1.24	0.014	1261.7+1053.4 (1.2)	-589.0+130.5 (4.5)	-21.2+4.9 (4.3)	-768.1+202.1 (3.8)	-27.1+6.8 (4.0)	7.347	-161.36
OmitCoil04	1.25	0.014	1279.2+1053.4 (1.2)	-590.6+130.5 (4.5)	-21.2+4.9 (4.3)	-770.6+202.1 (3.8)	-27.2+6.8 (4.0)	7.347	-161.31
OmitCoil09	1.24	0.014	1250.6+1053.4 (1.2)	-587.4+130.5 (4.5)	-21.1+4.9 (4.3)	-766.7+202.1 (3.8)	-27.0+6.8 (4.0)	7.347	-161.33
OmitCoil14	1.26	0.011	1240.1+1059.6 (1.2)	-102.0+131.1 (0.8)	-1.5+4.9 (0.3)	-426.4+202.6 (2.1)	-19.6+6.8 (2.9)	7.397	-157.83
OmitCoil03	1.36	0.001	241.5+1056.7 (0.2)	-732.9+131.6 (5.6)	-28.7+5.0 (5.8)	-888.8+202.8 (4.4)	-30.1+6.8 (4.4)	7.424	-160.51
OmitCoil13	1.36	0.001	1053.8+1056.2 (1.0)	-791.6+131.2 (6.0)	-29.6+4.9 (6.0)	-921.7+202.6 (4.6)	-31.3+6.8 (4.6)	7.446	-162.77
OmitCoil36	1.35	0.001	1074.9+1056.2 (1.0)	-784.9+131.2 (6.0)	-29.4+4.9 (5.9)	-917.4+202.6 (4.5)	-31.2+6.8 (4.6)	7.445	-162.87
OmitCoil3	1.36	0.001	1057.7+1056.2 (1.0)	-790.2+131.2 (6.0)	-29.6+4.9 (6.0)	-921.4+202.6 (4.5)	-31.3+6.8 (4.6)	7.444	-162.76
OmitCoil34	1.36	0.001	1072.6+1056.2 (1.0)	-792.1+131.2 (6.0)	-29.6+4.9 (6.0)	-923.2+202.6 (4.5)	-31.4+6.8 (4.6)	7.446	-162.72
OmitCoil39	1.36	0.001	1045.3+1056.2 (1.0)	-790.4+131.2 (6.0)	-29.6+4.9 (6.0)	-921.2+202.6 (4.5)	-31.3+6.8 (4.6)	7.445	-162.72
OmitCoil08	1.59	0.000	1682.1+1054.7 (1.6)	-1094.1+130.9 (8.4)	-40.6+4.9 (8.2)	-1175.6+202.3 (5.8)	-41.2+6.8 (6.0)	7.373	-159.33
OmitCoil38	1.48	0.000	1238.5+1058.0 (1.2)	-903.7+131.5 (6.9)	-33.8+4.9 (6.8)	-1007.1+202.7 (5.0)	-34.1+6.8 (5.0)	7.571	-163.77

Figure 3.23: Summary of results for dither schemes in Run 2.

vertical position (targetY) & angle (targetYSlope), the main detector asymmetry error and asymmetry value. For the residual correlation factors, we have value and error of the factor with sigma level of the correlation factor in the parentheses. The schemes are sorted in such an order that the slug-level probability decreases from top to bottom.

Now we apply the three criteria we have previous listed. We look at residual correlation factors first, since the direct effect of beam correction is that it should remove the correlation between main detector asymmetry and beam parameter differences.

In Run 1 (Fig. 3.22), we look at the sigma level of correlation with beam parameters and cut the schemes that have three sigma or higher correlations. After this cut, we have the schemes marked with red. Each of the schemes has at least one correlation that is higher than three sigma. For example, the schemes with coil 3 removed (OmitCoil3, OmitCoil38, etc.) are focused to the very bottom part. The residual correlation for these schemes are generally 5+ sigma. The energy correlation can even reach 9 sigma. With removal of coil 3, the probability is very bad, not even 0.001, and the asymmetry error is also the highest among the schemes.

After we cut on residual correlations, we have the schemes in the top part, which passed our correlation test. In the bottom part, we have schemes with large residual correlations. It “happens” that the schemes with high correlations also turn out to have low probability. The first and the second criterion of our scheme selection are connected. Better residual correlations often suggest better χ^2 .

We have removed the schemes with probability lower than 0.01 after the cut on residual correlations. Scheme OmitCoil69 (with 0.04 probability) is also removed. We now turn to the third criteria, the main detector asymmetry error. The schemes that passed 3-sigma correlation cut have, in general, an asymmetry error in the range of 13.14-13.15 ppb. But OmitCoil08 scheme has an asymmetry error of 13.17 ppb. So this scheme is also removed.

In Fig. 3.23, we have the summary of results for different schemes in Run 2. Like Run 1, we also first cut on schemes with any residual correlations that are higher than 3 sigma.

This also leaves the bottom part of the table to be red and excluded. In Run 2, the schemes with probability that is lower than 0.02 are removed. The rest of the schemes all have probability higher than 0.06. Then we perform the main detector asymmetry error check, the third criteria. The rest of the schemes after the correlation cut generally have asymmetry error ranging in 7.33-7.34 ppb. However, OmitCoil35 scheme has an asymmetry error of 7.37, which is obviously higher than the rest of the low correlation schemes. So OmitCoil35 scheme is also excluded in Run 2.

3.7.5 Schemes Systematic Error Assignment

After the correlation cut (close to χ^2 cut) and the MD error cut, we are left with a set of working schemes in Run 1 and Run 2. The schemes and the corresponding main detector asymmetries are summarized in Fig. 3.24 and Fig. 3.25. They are sorted in asymmetry increasing order to show the span of the asymmetry distribution, including the boundaries of the asymmetries.

In Fig. 3.24, we can see that different schemes give nearly identical MD asymmetries. The maximum and the minimum differ by about 7 ppb. We would like to choose a central value and an error that can represent the average of the schemes and also cover the span of the asymmetry distribution.

The 10 coil scheme gives an asymmetry of ~ 199 ppb. The OmitCoil46 scheme has the smallest asymmetry, ~ 195 ppb, while OmitCoil05 scheme gives the highest asymmetry of ~ 203 ppb. Therefore, the 10 coil sits approximately in the median of the asymmetry range. This can be used for the central value in Run 1.

To properly cover the range of asymmetries in Run 1, we need to assign an error that can span the coverage. We can find the distance between the chosen central value (10 coil) to the minimum asymmetry (OmitCoil46) and the distance between 10 coil and OmitCoil05, compare them, find the higher of the two distances and use it as the systematic error. By doing this, we make sure the asymmetries from the working schemes can all be properly

covered.

In Run 1, the distance between the central value and minimum (absolute value) asymmetry is

$$\text{Run 1 : } |A_{10\text{coil}} - A_{\text{OmitCoil46}}| = |-199.49 - (-195.38)| = 4.11 \text{ ppb.} \quad (3.38)$$

And the distance from central to maximum is

$$\text{Run 1 : } |A_{10\text{coil}} - A_{\text{OmitCoil05}}| = |-199.49 - (-202.66)| = 3.17 \text{ ppb.} \quad (3.39)$$

The higher of the two above is taken as systematic error in Run 1

$$\text{Run 1 : } \Delta A_{\text{scheme}} = 4.11 \text{ ppb.} \quad (3.40)$$

For Run 2, we look at Fig. 3.25. The range of the asymmetries is clearly smaller than Run 1. From the lower bound to the higher bound, we have a 2 ppb discrepancy. The lower bound comes from the OmitCoil05 scheme, ~ 163 ppb. The higher bound is OmitCoil58, ~ 165 ppb. The 10 coil scheme asymmetry, ~ 164 ppb, sits around the median of the range. So just like Run 1, the 10 coil scheme can be used as the central value.

In Run 2, we have the shift between central value and minimum (absolute value) asymmetry as

$$\text{Run 2 : } |A_{10\text{coil}} - A_{\text{OmitCoil05}}| = |-164.01 - (-162.94)| = 1.07 \text{ ppb.} \quad (3.41)$$

And the distance between central and maximum asymmetry is

$$\text{Run 2 : } |A_{10\text{coil}} - A_{\text{OmitCoil58}}| = |-164.01 - (-164.83)| = 0.82 \text{ ppb.} \quad (3.42)$$

The greater value of the two quantities above is utilized as systematic error to cover the

range in Run 2

$$\text{Run 2 : } \Delta A_{\text{scheme}} = 1.07 \text{ ppb} . \quad (3.43)$$

Dither Schemes	MD Asymmetry (ppb)
OmitCoil46	-195.38
OmitCoil04	-198.55
OmitCoil4	-199.09
OmitCoil01	-199.18
OmitCoil0	-199.18
OmitCoil09	-199.21
OmitCoil06	-199.42
10Coil	-199.49
OmitCoil48	-199.52
OmitCoil9	-199.53
OmitCoil1	-199.63
OmitCoil19	-199.68
OmitCoil6	-199.79
OmitCoil8	-199.89
OmitCoil89	-199.95
OmitCoil49	-199.97
OmitCoil18	-200.02
OmitCoil68	-200.20
OmitCoil05	-202.66

Figure 3.24: Main detector asymmetries from working dither schemes in Run 1.

3.8 Beam Correction Results

3.8.1 Beam Correction to Raw Asymmetry

We have raw main detector asymmetries for Run 1 and Run 2, -217.99 ppb and -164.01 ppb for Pass5c+ data set [11]. And based on Fig. 3.24 and 3.25, we have the central value of corrected asymmetries. Now we have the beam corrections for Run 1 and Run 2 as (including the systematic error previously defined)

$$A_{\text{beam}}^{\text{Run1}} = 18.50 \pm 4.11 \text{ ppb} , \quad (3.44)$$

$$A_{\text{beam}}^{\text{Run2}} = 0.00 \pm 1.07 \text{ ppb} . \quad (3.45)$$

<i>Dither Schemes</i>	<i>MD Asymmetry (ppb)</i>
OmitCoil05	-162.94
OmitCoil49	-163.87
OmitCoil4	-163.94
OmitCoil19	-163.95
OmitCoil9	-163.97
OmitCoil1	-164.00
10coil	-164.01
OmitCoil16	-164.04
OmitCoil46	-164.08
OmitCoil48	-164.08
OmitCoil6	-164.10
OmitCoil69	-164.10
OmitCoil89	-164.11
OmitCoil18	-164.13
OmitCoil8	-164.14
OmitCoil68	-164.25
OmitCoil59	-164.59
OmitCoil45	-164.60
OmitCoil5	-164.64
OmitCoil15	-164.67
OmitCoil56	-164.71
OmitCoil58	-164.83

Figure 3.25: Main detector asymmetries from working dither schemes in Run 2.

Please note that in Run 2, the 0.00 ppb is actually 0.0031 ppb when we show more digits.

3.8.2 Wien and HWP Cancellations

The beam correction is 18.50 ppb for Run 1, which seems too large. The beam correction of 0.0031 ppb for Run 2 seems too small. Why these values are what they are now depends on cancellation between different spin states.

Table 3.11: Beam correction at Wien level in Run 1.

Wien No.	Wien Reversal	Precession Reversal	IN (ppb)	OUT (ppb)	PHYS (ppb)
1	1	0	42.37	9.95	29.54
2	0	0	10.73	-16.18	-2.36
3	1	0	6.52	70.83	40.07
4	0	0	118.27	-88.75	20.30
5	1	0	-0.42	22.02	12.19

In Tab. 3.11, the beam correction in each Wien is given for Run 1. The HWP IN and

OUT states beam are listed separately. The combined beam correction to physics asymmetry (IN+OUT) is also listed in the last column.

In Wien 1, the HWP cancellation is not very good. The beam correction to HWP IN state is 42.37 ppb, while for the HWP OUT state it is 9.95 ppb - and they even have the same sign. The same thing happens to Wien 3, which also have large and same-sign corrections for IN and OUT states. For Wien 5, one HWP state dominates the correction but the correction is small. However, for Wien 2 and 4 , the HWP cancellations are good. The IN and OUT beam correction values are close.

Table 3.12: Beam correction at Wien level in Run 2.

Wien No.	Wien Reversal	Precession Reversal	IN (ppb)	OUT (ppb)	PHYS (ppb)
6	0	1	-2.43	34.84	18.11
7	1	1	-126.25	48.42	-40.12
8a	1	0	27.26	-8.27	9.17
8b	1	0	23.77	-14.22	4.93
9a	0	0	-5.52	0.42	-2.89
9b	0	0	8.41	-10.45	-1.22
10	1	0	-12.89	25.73	8.86

We turn to Run 2 in Tab. 3.12. Generally speaking, Run 2 is in better shape than Run 1. We can tell this from the fact that beam corrections for IN and OUT states all have the opposite sign for Run 2. This means the HWP cancellations work much better in Run 2 than Run 1. Wien 8b and 9b show good examples of effective HWP states cancellations.

Tab 3.11 and 3.12 are “unweighted” beam correction values. For the total correction in Run 1 and Run 2, the Wien level beam corrections have to be weighted and added. The weighting here is the main detector asymmetry error. After the multiplication with this weighting, we have effective beam correction values for Run 1 in Tab 3.13. In this table, the corrections values can be added directly for the total beam correction in Run 1.

In Tab. 3.13, the total beam correction of the last column agrees with Eq. (3.44). In Run 1, the large beam corrections come from Wien 1 and 3. These two Wiens don’t have good HWP cancellations (the IN and OUT correction have the same sign) so the beam

Table 3.13: Beam correction at Wien level in Run 1, weighted.

Wien No.	Wien Reversal	Precession Reversal	IN (ppb)	OUT (ppb)	PHYS (ppb)
1	1	0	4.23	0.65	4.88
2	0	0	1.36	-1.94	-0.58
3	1	0	0.62	7.34	7.96
4	0	0	11.42	-7.70	3.72
5	1	0	-0.04	2.55	2.52
Beam Correction Sum			17.59	0.90	18.50

corrections for these two Wiens are large. They both happen to have positive physics beam correction values. These two Wiens caused the large net beam correction value in Run 1.

We can also look at the Wien cancellations in Run 1, from the last column in Tab. 3.13. Wien 2 and 4 have wien-reversal 0 state while Wien 1, 3, 5 have wien-reversal 1 state. There is no obvious change of beam correction signs when the Wien state is flipped, even though Wien 2 has a negative beam correction while other Wiens are positive.

Table 3.14: Beam correction at Wien level in Run 2, weighted

Wien No.	Wien Reversal	Precession Reversal	IN (ppb)	OUT (ppb)	PHYS (ppb)
6	0	1	-0.11	1.98	1.87
7	1	1	-5.41	2.02	-3.39
8a	1	0	2.09	-0.66	1.43
8b	1	0	1.75	-1.03	0.72
9a	0	0	-0.70	0.04	-0.66
9b	0	0	1.00	-1.30	-0.30
10	1	0	-0.21	0.54	0.33
Beam Correction Sum			-1.59	1.59	0.0031

In Tab. 3.14, we have the weighted beam corrections for Run 2. The correction values are generally smaller than Run 1 (Tab. 3.13) and the HWP cancellations are good. For the last row, the HWP IN and OUT states have almost exactly the same total correction, -1.59 ppb and 1.59 ppb, which is why we have such small beam correction for Run 2.

In Run 2 there is suggestion of good Wien cancellations as well. The Wien pair of 6&7 can cancel some of their beam corrections. Wien 6 has positive correction and Wien 7 has negative correction. Wien 8 has positive correction while Wien 9 is negative, which have

different wien-reversal states. The Wien 8&9 pair can also cancel some of the correction, lowering the beam correction systematics in Run 2.

In Run 2, the precession reversal is important as well. From Wien 7 to Wien 8, the precession sign is changed and the sign of correction changed accordingly. This helped to reduce the net correction in Run 2 as well.

Chapter 4

Regression and Dithering

This chapter focuses on the comparison between two different beam correction methods—regression and dithering correction. The two methods utilize different beam responses, beam natural and driven motion, to calculate main detector sensitivities. The regression sensitivity is more affected by instrumental noise of the monitors which dithering is almost immune to. Examples including the main detector dipole asymmetries are given to compare the results of regression and dithering.

4.1 Natural and Driven Motion

Regression and dithering are two different methods for beam correction and both of them are intended to remove the HCBA's in main detector asymmetry. The difference between them is how the detector sensitivities are extracted. Regression and dithering use different kinds of beam motion, natural and driven respectively, to calculate the sensitivities. These two beam motion types differ from each other in a few ways.

For natural motion of the beam, beam trajectory and energy fluctuate around the equilibrium during normal beam running. The beam parameters (energy, position and angle) vary quickly in time and result in different values for sequential events. This beam natural motion results in monitor differences at quartet level. In principle, every beam

parameter has certain amount of fluctuation around its average position. Since the beam natural motion is not well controlled, the relative amplitude of fluctuation could differ from one parameter to another. Some parameters have weak natural motion and could not be successfully resolved from the instrumental noise of the apparatus. Besides, beam parameter differences can be highly correlated and therefore even if they have relatively large amplitude of motion, it is hard to decouple the correlated directions and the residual degree of freedom is suppressed.

Driven motion of the beam is different from natural beam movement described above. A beam modulation system is designed to deliberately drive the beam periodically out of balance. This way the amplitude of motion can be made greater and also we could have different driving patterns and give corresponding motion modes to the beam. Modulation modes differ from each other in the driving amplitudes of beam parameters. The relative strength profile of these beam properties is different from one driven motion pattern to another. Therefore the beam parameters can be better separated and analyzed with proper settings of modulation modes. The comparison between beam natural and driven motion is shown in Tab. 4.1.

Table 4.1: Comparison between beam natural and driven motion.

Type	Amplitude	Decoupling	Note
Natural motion	small	correlated	convenient to perform with parity data
Driven motion	greater	good	dedicated experiment running and analysis

With different kinds of beam motion, regression and dithering calculate the sensitivities differently. The former regresses main detector asymmetry against beam parameter differences to remove the correlation between them. The resulted regression fitting parameters are the beam regression sensitivities. As for the dithering, a dedicated beam modulation method was utilized to extract the beam dithering sensitives. The modulation of beam energy and trajectory has greater amplitude and better decoupling than beam natural motion to provide more accurate extraction of beam sensitivities.

4.2 Main Detector Dipole

4.2.1 Main Detector Combinations

The eight detector bars were located azimuthally around the beam axis in the plane of the main detector array. Each of the detectors can have its own asymmetry formed¹. The eight detector bars can be combined in different ways to reveal different quantities of interest, including parity asymmetry and transverse asymmetry. Among the possible combinations, the parity asymmetry is from main detector monopole—an average of the eight detectors. Further more, we could form detector dipoles, with opposite bars subtracted instead of added together. The most typical combinations of the detectors are illustrated in Fig. 4.1.

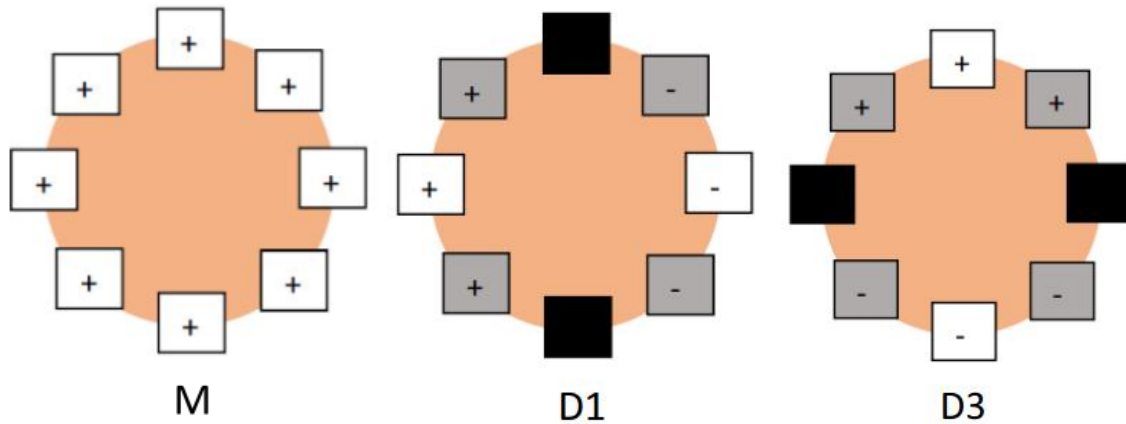


Figure 4.1: Different combinations of the main detector array. (Left) main detector monopole. (Middle) detector dipole 1. (Right) detector dipole 3.

In the left of Fig. 4.1, we have main detector monopole, M (or in short mdM). This is the combination we use for parity asymmetry A . The second and third combinations are main detector dipoles—horizontal and vertical respectively. The main detector dipoles D1 and D3² (mdD1 and mdD3) give us transverse asymmetries for the detector array. The relative weighting factors for each detector combination are shown in Tab. 4.2.

In Fig. 4.1, white color stands for a relative weighting factor of 1. Grey stands for $\sqrt{2}/2$

¹Each bar has two PMTs on its two ends, neg and pos, so during analysis, for each detector bar we have two asymmetries formed, which are then averaged to obtain the asymmetry for that detector bar.

²The “positive” direction of dipoles D1 and D3 points to octant 1 and octant 3 respectively.

Table 4.2: The detector combinations and relative weights.

Detector Combination	Monopole	Horizontal Dipole	Vertical Dipole
Code Name	M	D1	D3
Octant 1 Weight	1	1	0
Octant 2 Weight	1	$\sqrt{2}/2$	$\sqrt{2}/2$
Octant 3 Weight	1	0	1
Octant 4 Weight	1	$-\sqrt{2}/2$	$\sqrt{2}/2$
Octant 5 Weight	1	-1	0
Octant 6 Weight	1	$-\sqrt{2}/2$	$-\sqrt{2}/2$
Octant 7 Weight	1	0	-1
Octant 8 Weight	1	$\sqrt{2}/2$	$-\sqrt{2}/2$

or 0.707. Black has zero weight. The “diagonal” weighting factors for the detector dipoles can also be 1/2 alternatively. Here factor $\sqrt{2}/2$ is taken so when fitting the asymmetries from octant 1 to 8 with a sine function, the resulted transverse asymmetries can be connected to the detector dipole asymmetries introduced here.

4.2.2 Main Detector Dipole Asymmetries

The main detector dipole asymmetries with beam correction can be used to compare the regression and dithering corrections. The HCBAs in the dipole (transverse) asymmetry is mainly from beam position and angle. The other HCBAs are largely suppressed since the opposite bars in the main detector dipole cancel each other with opposite signs. Therefore, the dipole asymmetries can check against the effectiveness of the two beam correction methods at false asymmetry removal.

In Fig. 4.2, we have the asymmetries from main detector dipole D1 with regression and dithering correction independently applied. The points and markers with black color is raw asymmetry without beam correction. Red is regressed asymmetry and blue is dither-corrected. From the null asymmetry on the left, we can see that for the raw asymmetry, the χ^2 is bad because of false asymmetries from the beam. After regression, the χ^2 is improved to about 4 per degrees of freedom, but still the false asymmetries are

not completely removed. In the case of dithering correction, the χ^2 is very good, about 1, which means the false asymmetries are removed after dithering correction is applied.

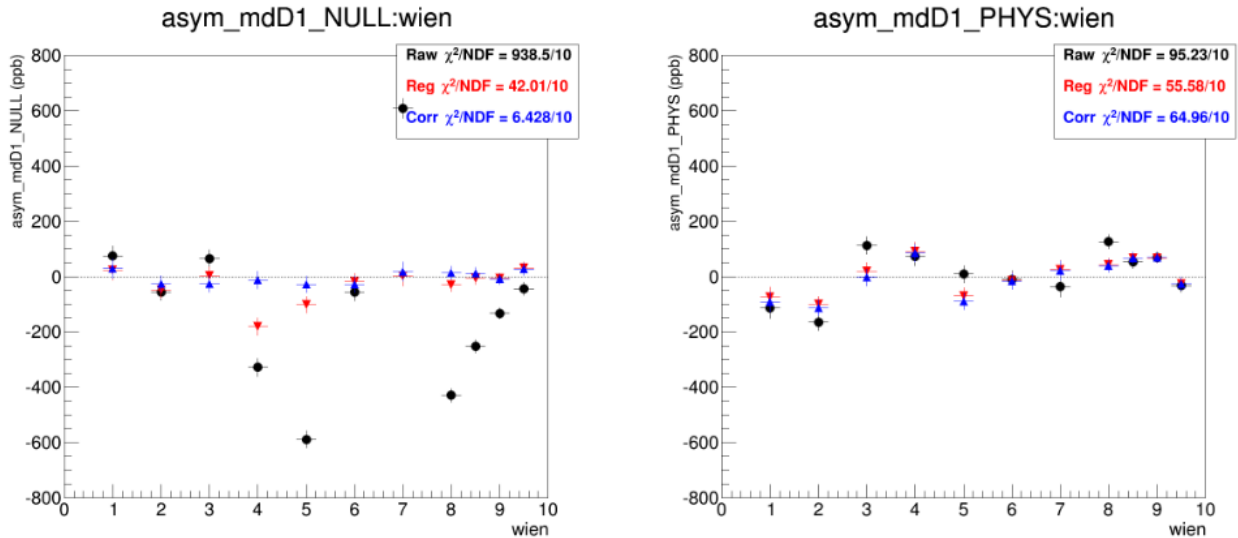


Figure 4.2: Comparison between regressed and dither-corrected main detector dipole D1 asymmetries.

More over, we have the asymmetries from main detector dipole D3 in Fig. 4.3. For the raw null asymmetry, the χ^2 is about 20 per degrees of freedom, which suggests large amount of false asymmetries. After regression and dithering correction, the χ^2 is improved. The dither-corrected null asymmetry for main detector dipole D3 has a χ^2 of nearly 1, just like the case of horizontal dipole asymmetry.

In general, for both of the main detector dipole asymmetries, D1 and D3, we can see that dithering can do a better job at HCBA removal than regression. Dithering correction can bring the dipole null asymmetries to a minimum level.

4.3 Correlation between Monitors

Regression and dithering correction have different detector sensitivities, which result in different corrected asymmetries from the two methods. To further study the relationship between sensitivities and corrected asymmetries, and at the same time to perform

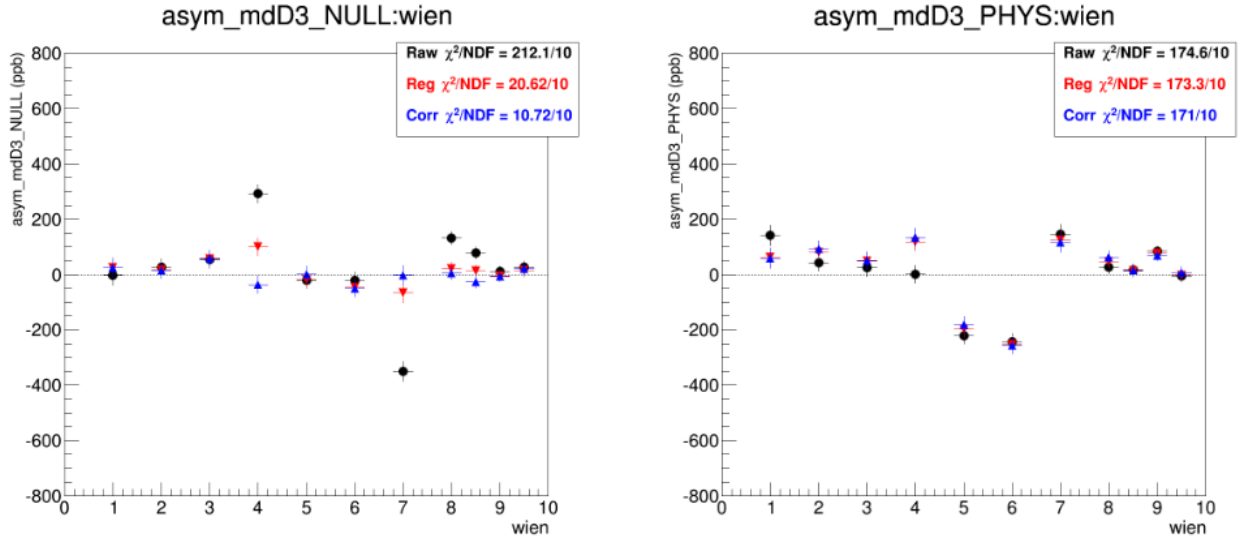


Figure 4.3: Comparison between regressed and dither-corrected main detector dipole D3 asymmetries.

comparison between regression and dithering, we need to look closely into the sensitivities from different monitors (five beam parameters E, X, X', Y, Y'). During beam motion, especially beam natural motion³, the monitors are correlated. Between certain monitors, the correlation between monitors differences can be very high. For example, the horizontal position and angle differences are highly correlated, so are the position and angle in the vertical direction. To understand better the beam-corrected results, we can try to define a set of monitors with less correlation based on original ones. To start with, we can define a new set of monitors that are designed to remove the highest correlations.

³During beam driven motion, there are some level of correlation between dithering coefficients as well, but we tried to separate the beam motion when we designed the modulation patterns.

4.3.1 Partially Uncorrelated Monitors

The uncorrelated monitor set M1X, M2X, M1Y and M2Y are defined as (based on original monitors X, X', Y, Y'⁴)

$$\left\{ \begin{array}{l} \text{M1X} = \text{X}(\text{um}) + 38.45 * \text{X}'(\text{urad}) \\ \text{M2X} = \text{X}(\text{um}) - 38.45 * \text{X}'(\text{urad}) \\ \text{M1Y} = \text{Y}(\text{um}) + 33.34 * \text{Y}'(\text{urad}) \\ \text{M2Y} = \text{Y}(\text{um}) - 33.34 * \text{Y}'(\text{urad}) \end{array} \right. , \quad (4.1)$$

where the factors 38.45 and 33.34 are calculated based on the correlation slope between corresponding monitor differences at quartet level. These correlation factors between original monitors X and X', or Y and Y', are pretty stable during the experiment. The units for original monitors here are um for position X(Y) and urad for angle X'(Y'). The units for the defined uncorrelated monitors can be arbitrary, here for simplicity the factors in front of X and Y are taken to be 1.

In Fig. 4.4, we have the correlation factors between the monitors differences before and after the correlation removal. In the top row we have the original correlation factors between X & X', Y & Y'. We can see that the correlation factors were very high for original position and angle correlation. For correlation between horizontal position and angle, the correlation was as high as 1 most of the time. In the vertical direction, correlation between Y and Y' was at a level of 0.8. In the bottom row, we have the correlation factors between the defined monitors. For correlation between M1X and M2X in the bottom left, the correlation factor is ± 0.2 . Compared to original correlation factor of nearly 1, this is greatly reduced. For M1Y and M2Y in the bottom right plot, the correlation factor is less than 0.6 most of the time, which also has reduced correlation compared to original monitors⁵.

⁴During analysis, the full names of these monitors are targetX, targetXSlope, targetY and targetYSlope respectively.

⁵The factors calculated in Eq. 4.1 were based on the fitting slopes in the correlation plots of original monitor differences for all the slugs in Run 2.

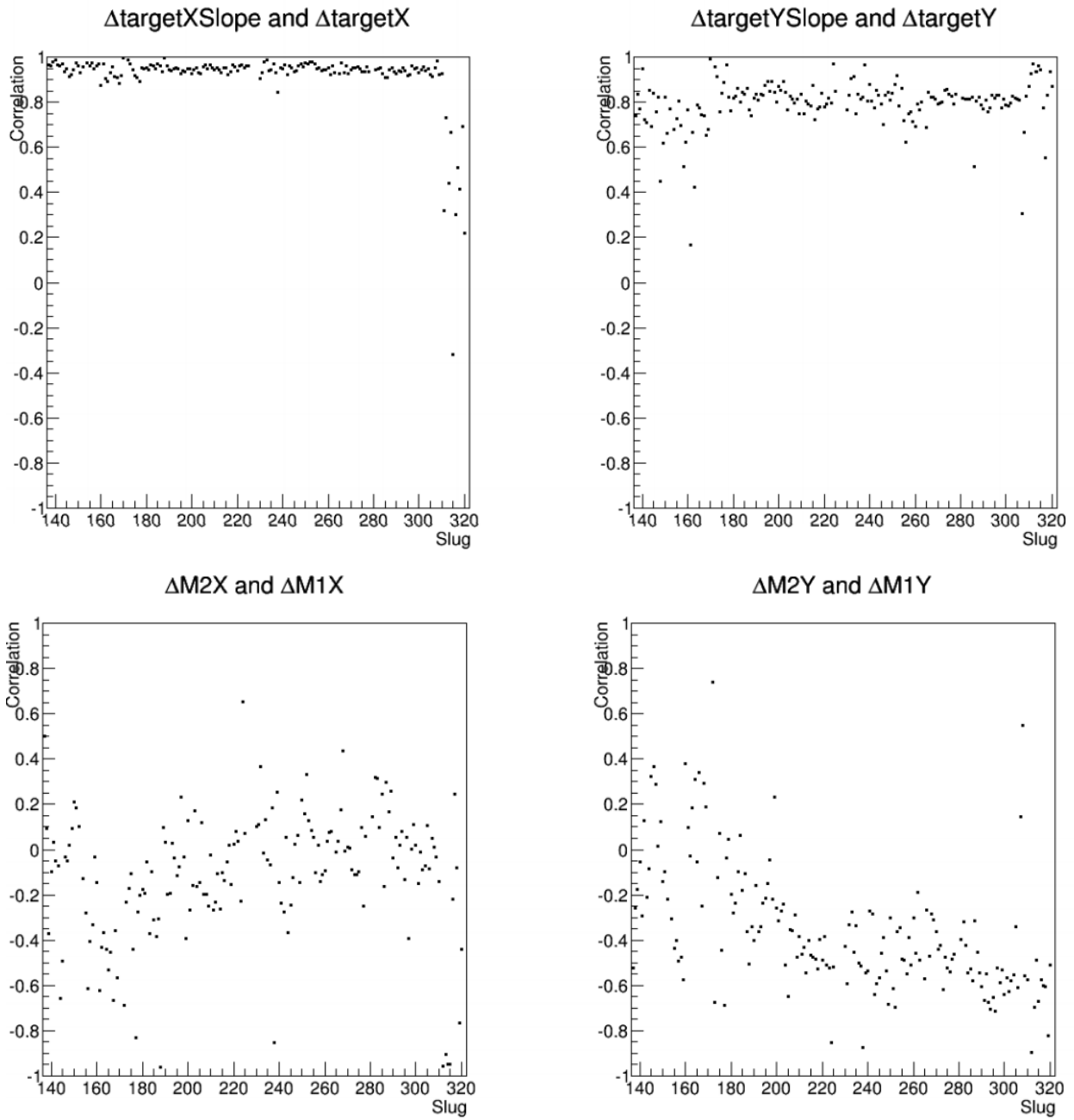


Figure 4.4: Correlation factors between monitor differences at slug level before and after correlation removal. (Top left) before correlation removal, X and X'. (Top right) before correlation removal, Y and Y'. (Bottom left) after correlation removal, M1X and M2X. (Bottom right) after correlation removal, M1Y and M2Y.

With the uncorrelated monitors defined in Eq. 4.1, the two highest correlations between the monitors are removed. There are possibly weak correlations between other monitor differences but not as high as the correlation between position and angle. With the correlation gone, not only the monitor differences (between position and angle) can be un-correlated, the corresponding sensitivities can be de-correlated as well. The correlation between main detector sensitivities before and after monitor correlation removal are shown in Fig. 4.5 and Fig. 4.6.

For the original monitors before correlation removal on the left (Fig. 4.5), we have the correlation factors between horizontal position and angle sensitivities. The correlation factor was about higher than 0.8. After the correlation removal, on the right, the correlation factor between M1X and M2X sensitivities is reduced to about less than 0.4.

4.3.2 Fully Uncorrelated Monitors

With the highest correlation between position and angle removed by uncorrelated monitors, M1X(Y), M2X(Y), we are left with a monitor set that is partially correlation free. There are still correlations in the rest of the monitors, which can be removed as well. To achieve a fully correlation free monitor set, we introduce another set of monitors that are good at the comparison between regression and dithering corrections.

Based on original monitors, the fully correlation free monitors are introduced with a few steps, including BPM noise normalization, eigen matrix de-correlation and eigen monitor identification. These steps will be explained in the following sections.

BPM Noise Normalization

Difference BPMs have different instrumental noise (or resolution), which depends on what kind of monitor we are looking at. The stripline beam position monitors have a typical resolution of $\sim 1\mu\text{m}$. The defined monitors have unique noises depending on the specific definition. For example, the position monitor X (or targetX) is defined with a few stripline

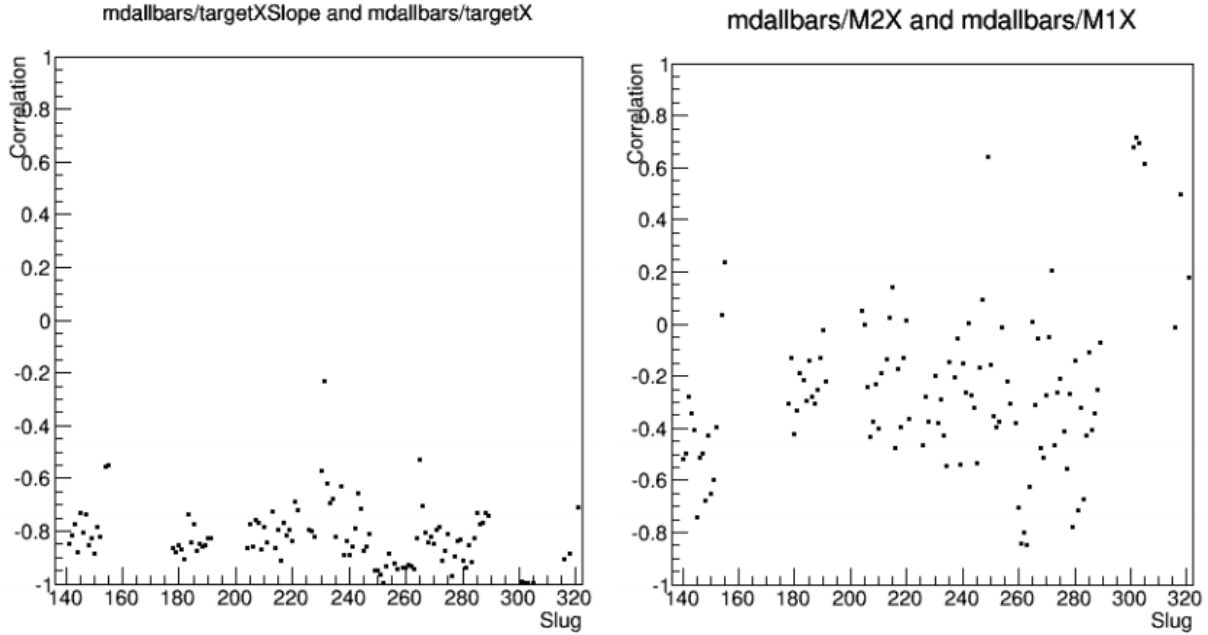


Figure 4.5: Correlation factors between horizontal detector sensitivities at slug level before and after correlation removal. (Left) before correlation removal, X and X'. (Right) after correlation removal, M1X and M2X.

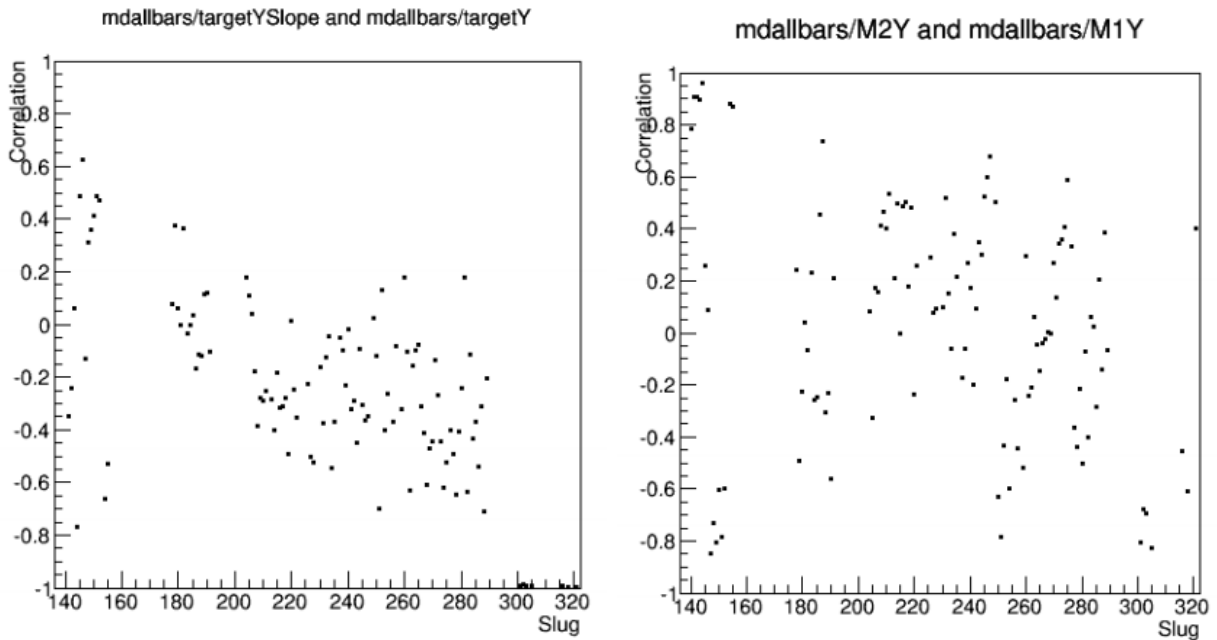


Figure 4.6: Correlation factors between vertical detector sensitivities at slug level before and after correlation removal. (Left) before correlation removal, X and X'. (Right) after correlation removal, M1X and M2X.

monitors upstream of the target and has its own unique resolution. This applies to other monitors as well, including X', Y, Y'. The energy monitor E is defined with bpm3c12X, X and X', which is effectively based on a couple of stripline monitors along the beamline. Therefore, these defined monitors have resolution that are determined by corresponding definition.

BPM noise normalization is to divide the the monitor differences from E, X, X', Y, Y' by their specific resolution. In other words, the monitor differences are normalized to the monitor resolution. Originally, the monitors have their own units, like microns or radians. After BPM noise normalization, the new monitor differences are unitless, or effectively speaking, they are put under the same natural unit system. Now the monitor differences are all simply numbers with no specific units and they can be compared relatively easily for later use.

Suppose the resolution of monitors E, X, X', Y, Y' are $\sigma_E, \sigma_X, \sigma_{X'}, \sigma_Y, \sigma_{Y'}$ respectively. Then the BPM noise normalization step is to divide the monitor differences by the corresponding resolution

$$\delta x = \frac{dx}{\sigma_x}, \quad (4.2)$$

where dx is original monitor difference and δx is the noise-normalized monitor difference. Here x can take monitors from E, X, X', Y, Y' and we have

$$\delta E = \frac{dE}{\sigma_E}, \quad \delta X = \frac{dX}{\sigma_X}, \quad \delta X' = \frac{dX'}{\sigma_{X'}}, \quad \delta Y = \frac{dY}{\sigma_Y}, \quad \delta Y' = \frac{dY'}{\sigma_{Y'}}. \quad (4.3)$$

Please note that for beam correction results, the monitors we used for E, X, X', Y, Y' were energy, targetX, targetXSlope, targetY and targetYSlope. But for the regression and dithering analysis here, we could try other monitor sets. Monitor set 11 (bpm3c12X, targetX, targetXSlope, targetY and targetYSlope) and 7 (bpm3c12X, bpm3h09X, bpm3h04X, bpm3h09Y, bpm3h04Y) will be used as well for some of following sections of the related analysis to compare regression and dithering. The procedure described here use

a generic monitor set E, X, X', Y, Y' , in which the individual monitors could be replaced by others.

Eigen Matrix De-correlation

The normalization procedure in the last part gives the same units to all five original monitors from different categories of beam properties. After BPM noise normalization, they can be unified and transformed more freely. We can see later in this section how the correlation matrix between monitor differences benefit from this uniform unit system.

First, we have covariance between monitor differences from monitors x and y as $\text{cov}(\delta x \delta y)$. When monitors x and y represent the same monitor, we have $\text{cov}(\delta x \delta x)$, $\text{cov}(\delta y \delta y)$, or simply $\text{var}(\delta x)$, $\text{var}(\delta y)$, which stand for variances from these monitors. The correlation matrix between monitor differences is

$$\mathbf{C} = \left[\text{cov}(\delta x \delta y) \right], \quad (4.4)$$

in which δx and δy are BPM-noise-normalized monitor differences. The diagonal elements in matrix \mathbf{C} are the variances from five monitors, $\text{var}(\delta x)$. x and y can take monitors from E, X, X', Y, Y' . The explicit form of Eq. 4.4 is

$$\mathbf{C} = \begin{bmatrix} \text{var}(\delta E) & \text{cov}(\delta X \delta E) & \text{cov}(\delta X' \delta E) & \text{cov}(\delta Y \delta E) & \text{cov}(\delta Y' \delta E) \\ \text{cov}(\delta E \delta X) & \text{var}(\delta X) & \text{cov}(\delta X' \delta X) & \text{cov}(\delta Y \delta X) & \text{cov}(\delta Y' \delta X) \\ \text{cov}(\delta E \delta X') & \text{cov}(\delta X \delta X') & \text{var}(\delta X') & \text{cov}(\delta Y \delta X') & \text{cov}(\delta Y' \delta X') \\ \text{cov}(\delta E \delta Y) & \text{cov}(\delta X \delta Y) & \text{cov}(\delta X' \delta Y) & \text{var}(\delta Y) & \text{cov}(\delta Y' \delta Y) \\ \text{cov}(\delta E \delta Y') & \text{cov}(\delta X \delta Y') & \text{cov}(\delta X' \delta Y') & \text{cov}(\delta Y \delta Y') & \text{var}(\delta Y') \end{bmatrix}. \quad (4.5)$$

The matrix \mathbf{C} represent the correlation between monitors. Generally the non-diagonal elements are non-zero and typical correlations are within X-like monitors or Y-like monitors (there could be some level of correlation between X and Y monitors as well

depending on the beam motion). In the uncorrelated monitors (M1X, M2X, M1Y, M2Y) introduced before, $\text{cov}(\delta X \delta X')$ and $\text{cov}(\delta Y \delta Y')$ were greatly reduced. Here we need to find a way to bring down all the non-diagonal elements. Just like de-correlation for position and angle, we defined a new set of monitor for these beam parameters. We here further define another set of monitors that involve all beam parameters and apply monitor transformation to the correlation matrix \mathbf{C} to transform it into diagonal matrix.

To diagonalize matrix \mathbf{C} , we can solve the eigen problem below

$$\mathbf{C}V = \lambda V, \quad (4.6)$$

where λ and V are eigenvalues and corresponding eigenvectors. We have five eigenvalues $\lambda_1, \lambda_2, \lambda_3, \lambda_4, \lambda_5$ and five eigenvectors V_1, V_2, V_3, V_4, V_5 .

The transformation matrix that can bring correlation matrix \mathbf{C} into a diagonal form is

$$\mathbf{T} = [V_1, V_2, V_3, V_4, V_5], \quad (4.7)$$

which is composed of the elements from five eigenvectors. The new form of correlation matrix after diagonalization is

$$\mathbf{C}' = \text{diag}(\lambda_1, \lambda_2, \lambda_3, \lambda_4, \lambda_5). \quad (4.8)$$

Now we introduce a new set of monitors M_1, M_2, M_3, M_4, M_5 . Please note that for monitors here, also like eigenvalues and eigenvectors, we have used the indexes 1-5. The numbers will be replaced by monitor names later in the next step of the entire procedure. For now, they are indexed with the order of eigenvalues, for example, λ_1 is the highest eigenvalue and λ_5 is the smallest. The transformation from BPM-noise-normalized monitor

differences to the eigen monitor differences is

$$\left\{ \begin{array}{l} \delta M_1 = \frac{\partial M_1}{\partial E} \delta E + \frac{\partial M_1}{\partial X} \delta X + \frac{\partial M_1}{\partial X'} \delta X' + \frac{\partial M_1}{\partial Y} \delta Y + \frac{\partial M_1}{\partial Y'} \delta Y' \\ \delta M_2 = \frac{\partial M_2}{\partial E} \delta E + \frac{\partial M_2}{\partial X} \delta X + \frac{\partial M_2}{\partial X'} \delta X' + \frac{\partial M_2}{\partial Y} \delta Y + \frac{\partial M_2}{\partial Y'} \delta Y' \\ \delta M_3 = \frac{\partial M_3}{\partial E} \delta E + \frac{\partial M_3}{\partial X} \delta X + \frac{\partial M_3}{\partial X'} \delta X' + \frac{\partial M_3}{\partial Y} \delta Y + \frac{\partial M_3}{\partial Y'} \delta Y' \\ \delta M_4 = \frac{\partial M_4}{\partial E} \delta E + \frac{\partial M_4}{\partial X} \delta X + \frac{\partial M_4}{\partial X'} \delta X' + \frac{\partial M_4}{\partial Y} \delta Y + \frac{\partial M_4}{\partial Y'} \delta Y' \\ \delta M_5 = \frac{\partial M_5}{\partial E} \delta E + \frac{\partial M_5}{\partial X} \delta X + \frac{\partial M_5}{\partial X'} \delta X' + \frac{\partial M_5}{\partial Y} \delta Y + \frac{\partial M_5}{\partial Y'} \delta Y' \end{array} \right. , \quad (4.9)$$

in which the transformation factors $\partial M_i / \partial x$ are from the eigenvectors found when diagonalizing the correlation matrix. With the elements for eigenvectors filled in, the transformation matrix \mathbf{T} becomes

$$\mathbf{T} = \begin{bmatrix} \frac{\partial M_1}{\partial E} & \frac{\partial M_2}{\partial E} & \frac{\partial M_3}{\partial E} & \frac{\partial M_4}{\partial E} & \frac{\partial M_5}{\partial E} \\ \frac{\partial M_1}{\partial X} & \frac{\partial M_2}{\partial X} & \frac{\partial M_3}{\partial X} & \frac{\partial M_4}{\partial X} & \frac{\partial M_5}{\partial X} \\ \frac{\partial M_1}{\partial X'} & \frac{\partial M_2}{\partial X'} & \frac{\partial M_3}{\partial X'} & \frac{\partial M_4}{\partial X'} & \frac{\partial M_5}{\partial X'} \\ \frac{\partial M_1}{\partial Y} & \frac{\partial M_2}{\partial Y} & \frac{\partial M_3}{\partial Y} & \frac{\partial M_4}{\partial Y} & \frac{\partial M_5}{\partial Y} \\ \frac{\partial M_1}{\partial Y'} & \frac{\partial M_2}{\partial Y'} & \frac{\partial M_3}{\partial Y'} & \frac{\partial M_4}{\partial Y'} & \frac{\partial M_5}{\partial Y'} \end{bmatrix} . \quad (4.10)$$

And the diagonalized correlation matrix is

$$\mathbf{C}' = \text{diag} \left(\text{var}(M_1), \text{var}(M_2), \text{var}(M_3), \text{var}(M_4), \text{var}(M_5) \right) . \quad (4.11)$$

Eigen Monitor Identification

The eigen monitors M_{1-5} transformed with matrix \mathbf{T} from last section were named according to the size of the eigen values. Monitor M_1 was from the highest eigenvalue and monitor M_5 was from the smallest. The choice was for the purpose of convenience and it could be the other way around or any eigen monitor can be assigned to any eigenvalue. From one run to another, the eigenvalues of the monitors can change and therefore the order of the eigenvalues can change as well. When two eigenvalues are too close, the order of the monitors can be flipped from time to time. Besides, the monitors numbers 1-5 are not directly related to any beam parameters. The physics significance of the eigen monitors is not clear. To make the order of the eigen monitors more stable, we need to “identify” the monitors. The procedure is shown as below.

1. Check the absolute value of component $|\partial M_i/\partial E|$ of all eigenvectors V_i . Pick the biggest one and assign this eigenvector to monitor E.
2. Check the component $|\partial M_i/\partial X|$ of the rest four eigenvectors. Pick the biggest and assign the eigenvector to monitor X.
3. Check $|\partial M_i/\partial Y|$ for the rest three eigenvectors. Pick the biggest one and assign Y.
4. Check $|\partial M_i/\partial X'|$ for the rest two eigenvectors. Assign X' .
5. Assign the last eigenvector to monitor Y' .

After the above “sorting” procedure, random eigen monitors M_1, M_2, M_3, M_4, M_5 are now physically significant and have new names $M_E, M_X, M_{X'}, M_Y, M_{Y'}$, which means that M_E is dominated by monitor E, M_X dominated by monitor X, etc. To show this more clearly, the transformation matrix at slug level is in Fig. 4.7. We can see that for monitor set $M_E, M_X, M_{X'}, M_Y, M_{Y'}$, the dominant (diagonal) components are close to 1 and the rest of the components are relatively smaller or close to zero. For example, the last row is $M_{Y'}$ monitor. It is dominated by original Y' monitor (component in fifth column is close to 1) and has some contribution from other monitors as well. This agrees with the procedure of eigen monitor identification above.

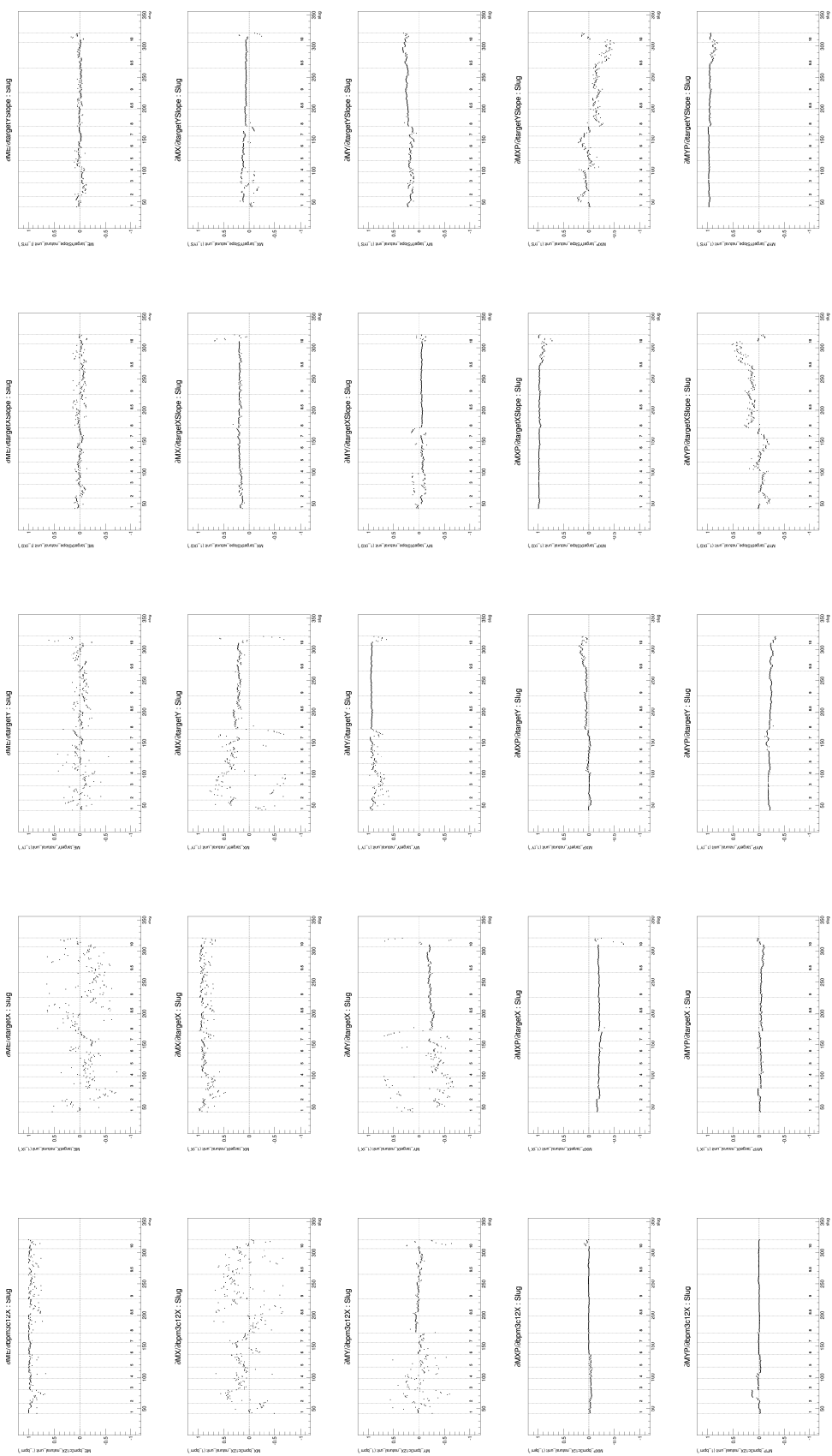


Figure 4.7: Transformation matrix slug level history.

4.4 Comparison between Regression and Dithering

With the monitors M_E , M_X , $M_{X'}$, M_Y , $M_{Y'}$ introduced following the steps, we now have a monitor set that is fully correlation free based on original monitors E , X , X' , Y , Y' . The original covariance matrix has twenty-five elements and the monitors are all coupled to one another. The covariance matrix for the new monitor set is a diagonal matrix with all covariance terms reduced to zero. The benefits of correlation free monitor difference matrix will be revealed in later sections, especially for the comparison between regression and dithering.

4.4.1 Monitor Difference Width

The monitor difference width gives us the “amplitude” of beam natural motion, combined with the monitor instrumental noise. If the width is high, we have stronger beam jitter in the corresponding beam parameter and if the width is low, the beam jitter in this direction is small and we are almost left with monitor instrumental noise. Since regression utilizes beam natural motion to determine detector sensitivities, the width of the monitor differences are crucial for regression correction. Higher widths in the monitor differences are important for successful extraction of regression sensitivities, otherwise we have less accurate regression correction in the low-width beam parameters.

The slug history plots of monitor difference widths are shown in Fig. 4.8, with comparison between original monitors and correlation-free monitors. In the top, we have the monitor difference widths after correlation removal. We can see that monitors ME , MX and MY have high widths while MXP and MYP have low monitor widths. In the bottom, we have the monitor difference widths for monitors before correlation removal. We can see that the monitor difference widths from $bpm3c12X$, $targetX$ and $targetY$ monitors are high as well. And for the low width monitors $targetXSlope$ and $targetYSlope$, the widths are slightly higher than MXP and MYP monitors in the top plot.

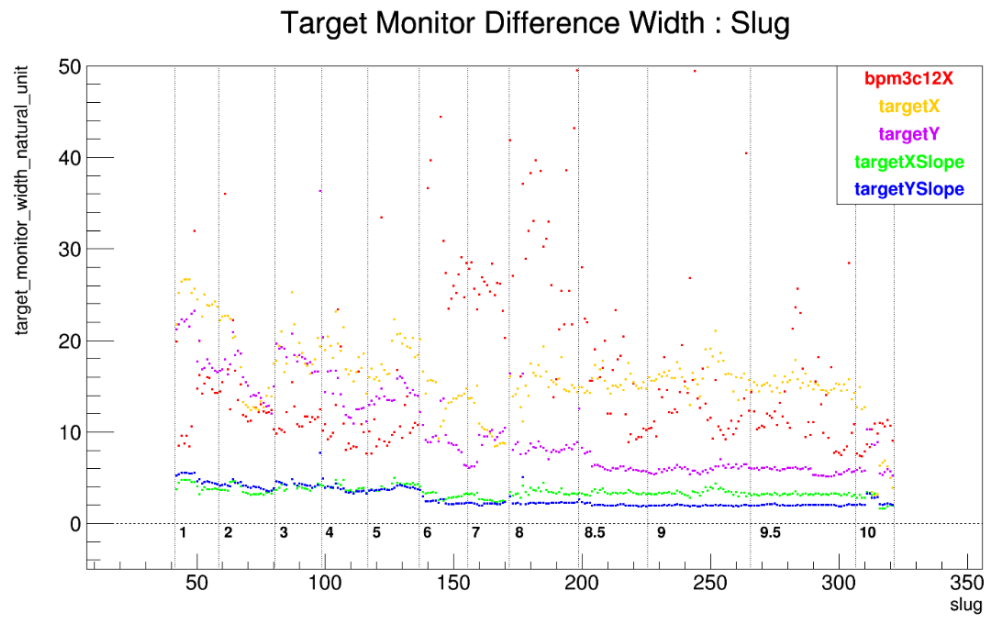
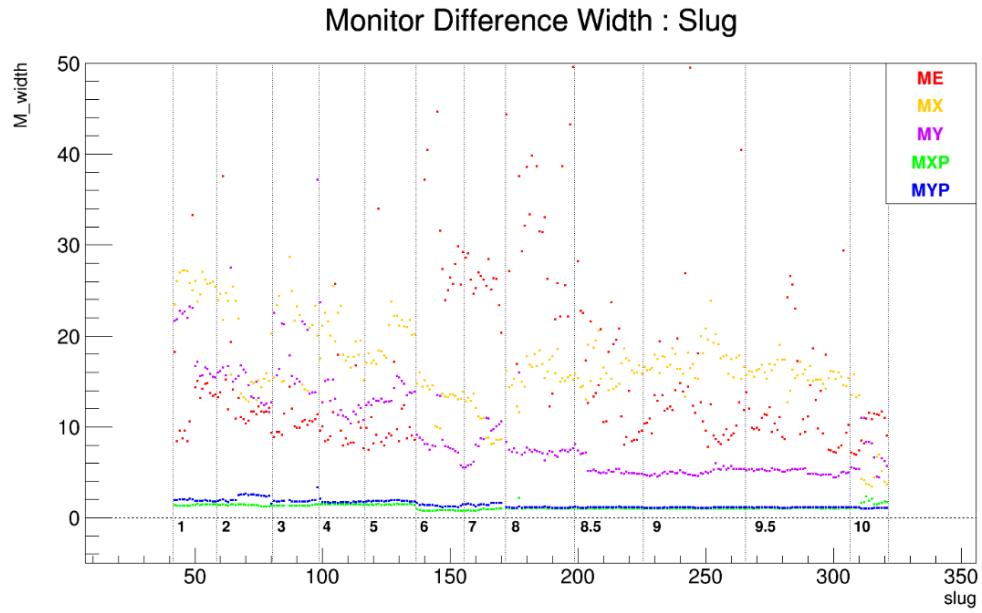


Figure 4.8: Monitor differences width slug history.

From the examination of monitor difference widths, we can see that for three beam parameters, ME, MX, MY, we have higher width, in which we have plenty of beam motion. For two directions MXP, MYP, the width is very low, which means we don't have much beam natural motion in these two monitors and the beam information is insufficient for regression to extract accurate sensitivities.

4.4.2 The Comparison of Regression and Dithering Sensitivities

The detector sensitivities can be different between regression and dithering since they utilize different types of beam motion. To study how the correction results differ between the two methods, we compare the sensitivities for the five beam parameters. With the monitors defined in the last section, we can look at sensitivities in the basis of the correlation-free monitors, in which the comparison between regression and correction is more clear. With the monitor difference width information, we could try to understand how regression generally differ from dithering correction for detector combinations.

In Fig. 4.9, we have the comparison between regression and dithering sensitivities for detector monopole. Five monitors (ME, MX, MY, MXP, MYP) are shown here in different plots. Red points are regression sensitivities and blue points are dithering ones. We can see that for monitors ME, MX and MY with large monitor widths, the regression and dithering sensitivities are close. Especially for monitor ME, the sensitivities from two methods are very close to each other. For monitors MXP and MYP with small monitor difference widths, regression and dithering tend to disagree. Dithering sensitivity has a finite size for most of the slugs, especially for MXP monitor, and regression sensitivity is close to zero.

The comparison between regression and dithering sensitivities for detectors dipoles are shown in Fig. 4.10 and 4.11. In these plots, we can see that the regression and dithering sensitivities are close for high width monitors ME, MX, MY and the regression sensitivity is generally lower than dithering, especially for MY monitor. For example, in the plot of $\partial D3/\partial MY$ sensitivity, we can see that the regression sensitivity is significantly lower than

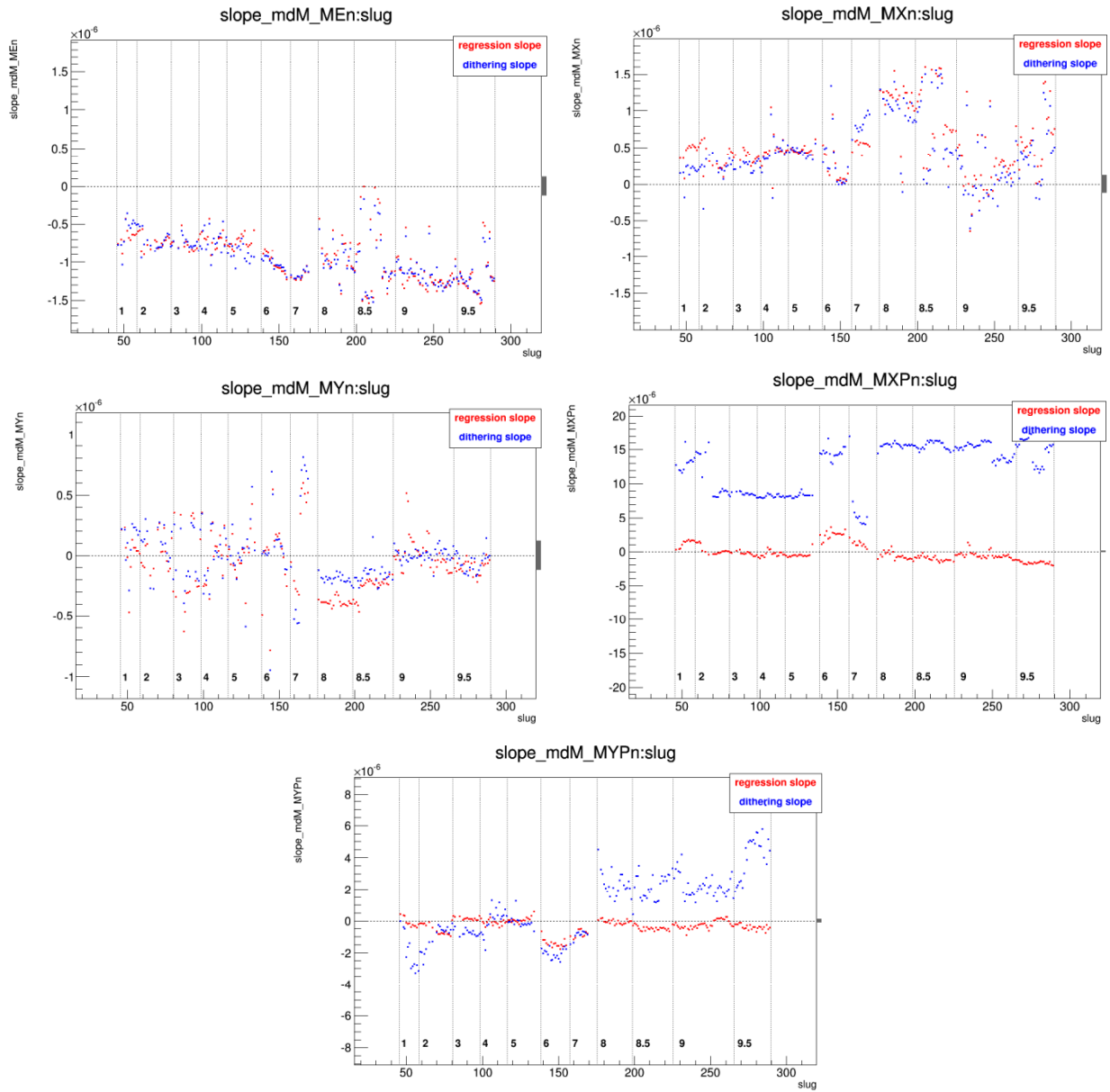


Figure 4.9: Detector monopole sensitivity slug history.

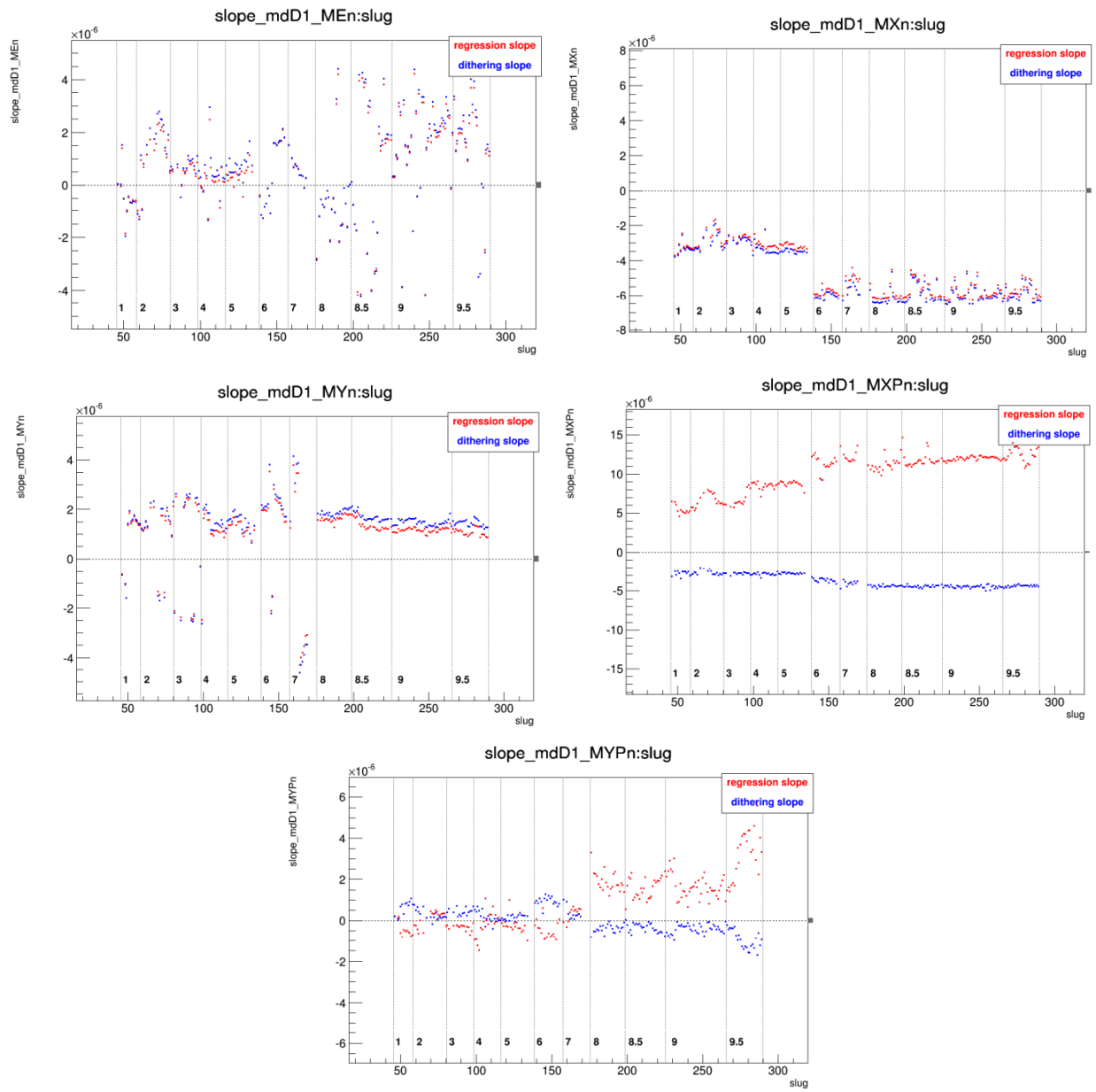


Figure 4.10: Detector dipole 1 sensitivity slug history.

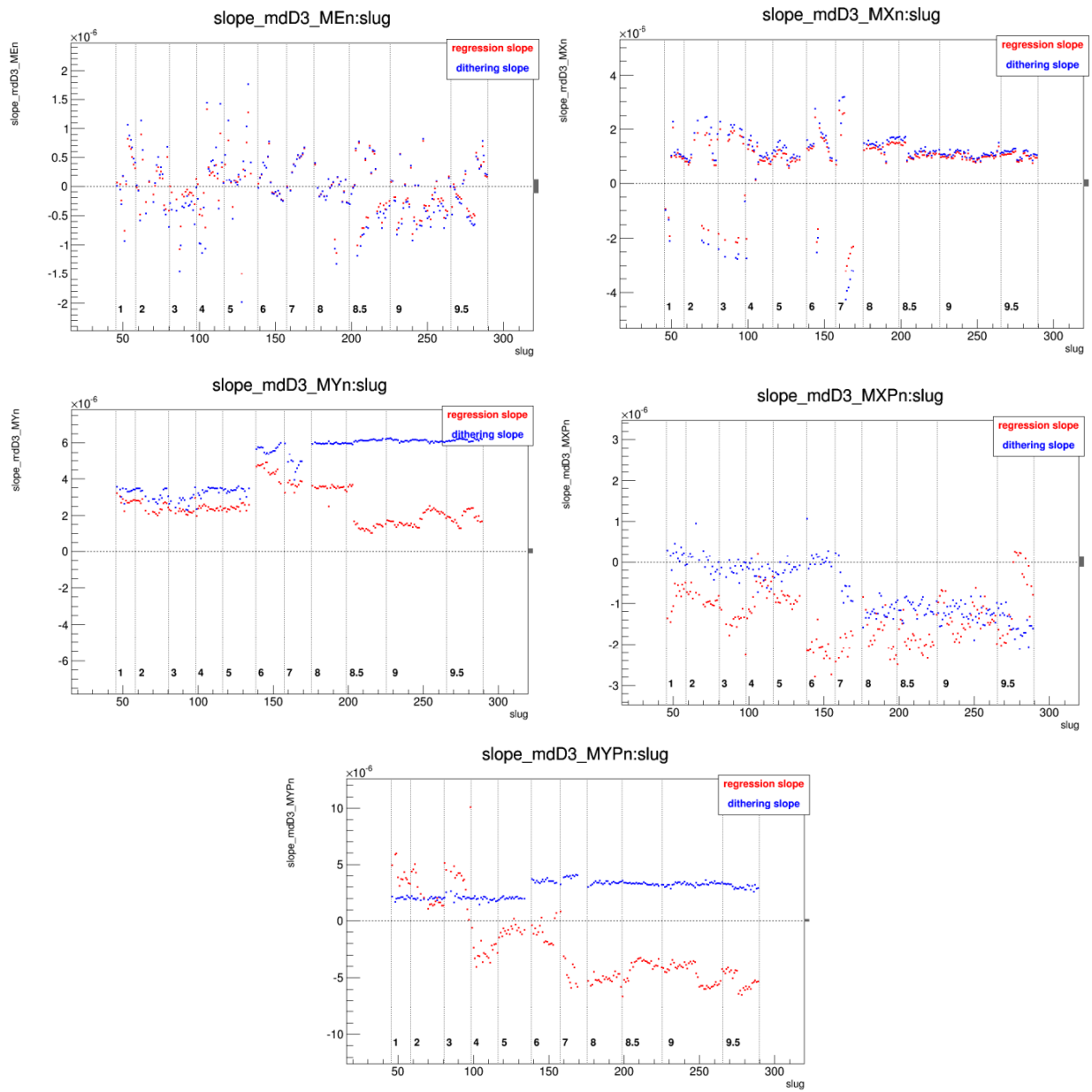


Figure 4.11: Detector dipole 3 sensitivity slug history.

dithering for most of the slugs.

By comparing the sensitivities between regression and dithering for different detector combinations, we can see that in general, for higher width monitors, regression and dithering agree better and regression sensitivities are normally smaller than dithering. For lower width monitors, the discrepancy between regression and dithering are greater.

4.4.3 The Comparison of Regression and Dithering Correction

With the un-correlated monitor set, we look at the separate corrections due to each monitor to find the difference between regression and dithering correction. As we have seen previously in the last section, the sensitivities differ from regression to dithering for different monitors. Therefore, the separate corrections from individual monitors should be related to monitor widths as well. Since for lower monitor width, the discrepancy between regression and dithering sensitivities is higher, we expect the correction from high width monitor to agree better between regression and dithering.

To compare the beam corrections from regression and dithering, we look at monitor differences first. In Fig. 4.12, we have the monitor differences at Wien level for monitors ME, MX, MY, MXP and MYP. We can see that the monitor differences from the high width monitors, ME, MX, MY, are generally higher than the low width monitors. For MXP and MYP, the monitor differences are closer to zero than other monitors. We could also notice that the monitor differences for these two low width monitors are higher in Run 1 than Run 2. The monitor differences, combined with the sensitivities, form the beam corrections for individual monitors.

In Fig. 4.13, we have the beam corrections from individual monitors for main detector monopole, which are the sensitivities multiplied by the monitor differences. The comparison is made between regression (red) and dithering (blue). From previous comparison of sensitivities, we know that for the high width monitors ME, MX and MY, the regression and dithering sensitivities are close to each other. Therefore the beam

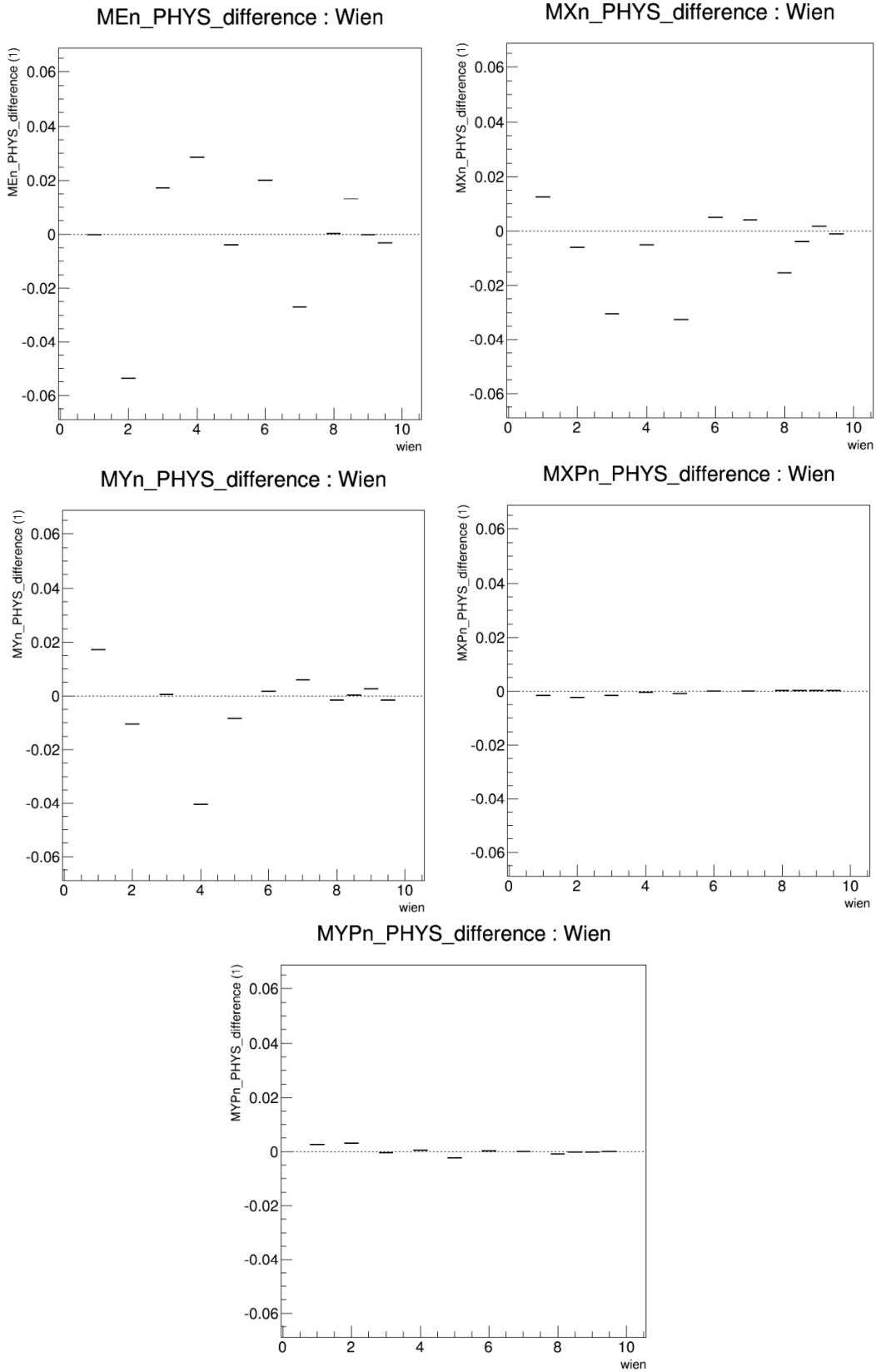


Figure 4.12: Monitor differences at Wien level.

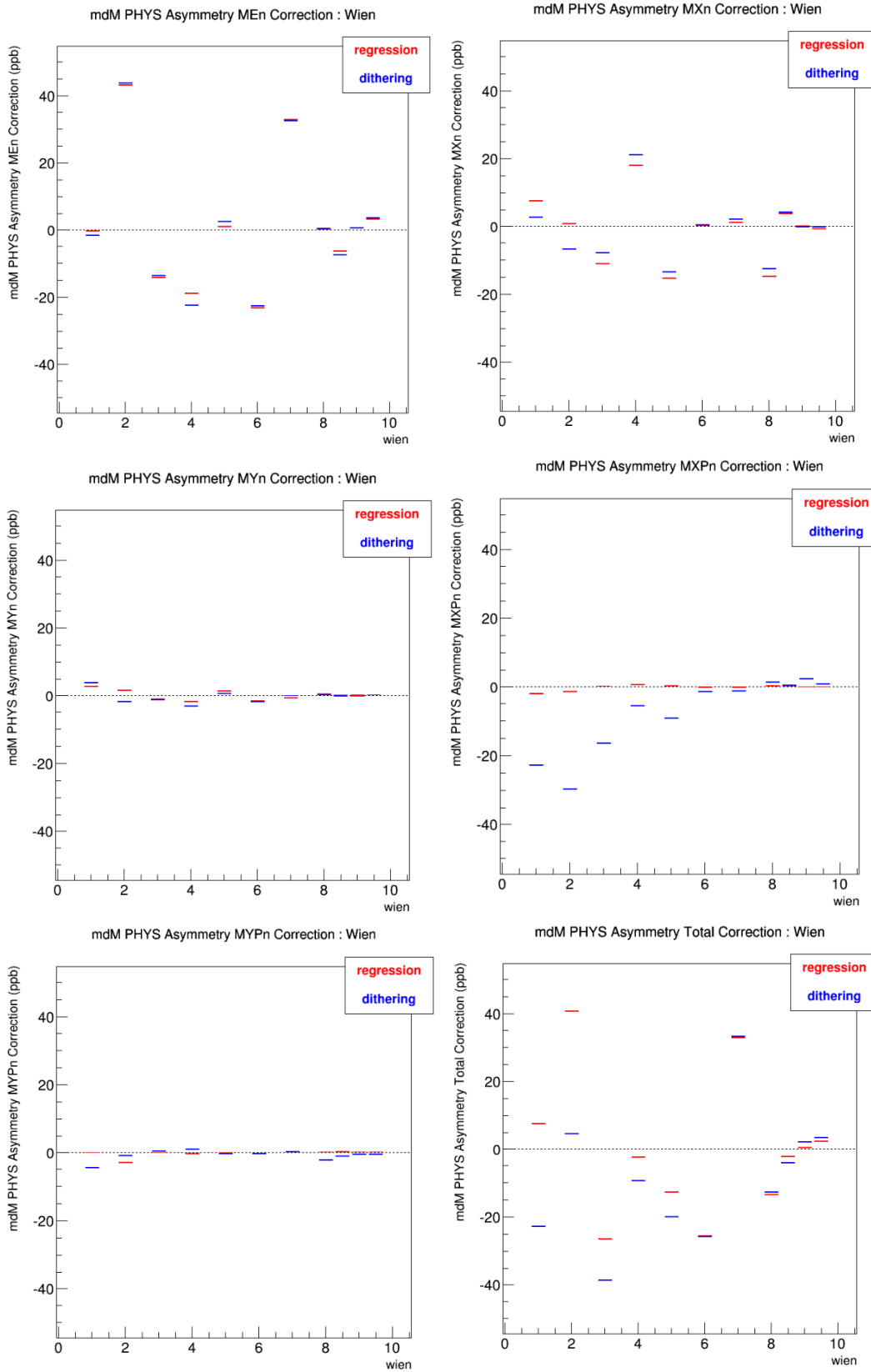


Figure 4.13: Detector monopole beam corrections at Wien level.

correction contributions from these three monitors are close for regression and dithering as well. However, for MXP and MYP, the low width monitors, we have great discrepancies between regression and dithering sensitivities, so we should expect different beam correction contributions from these monitors for regression and dithering. Even though the monitor differences are small for MXP and MYP, they are still not zero. Besides, we have large sensitivity in MXP monitor, as shown in Fig. 4.9. The beam correction from MXP monitor still has a comparable size with other monitors and the discrepancy between regression and dithering for MXP monitor is significant. By looking at all five monitors, we can see from Fig. 4.13 that the discrepancy from MXP monitor is the highest. With the combined beam corrections shown in the last plot of Fig. 4.13, the total correction differ from regression to dithering. However, this mostly happens in the Wiens from Run 1. As we have noticed before, the monitor differences for low width monitors is lower in Run 2, and we have better agreement between regression and dithering in Run 2 than Run 1.

We now look at the comparison between regression and dithering corrections for main detector dipoles. In Fig. 4.14, we have beam corrections from monitors for main detector dipole 1. From previous study of sensitivities in Fig. 4.10, we know that for high width monitors, the regression sensitivity for dipole 1 is smaller than dithering sensitivity. Therefore, in Fig. 4.14, we can see that for ME, MX and MY, the beam correction from dithering has a higher absolute value than regression. For the low width monitor MXP, the monitor difference has a non-zero value, especially in Run 1 and the beam correction contribution from MXP has discrepancy between regression and dithering for the Wiens in Run 1. Since the MYP monitor sensitivity is smaller than MXP for detector dipole 1, we can see that even MXP and MYP have comparable sizes in monitor difference values, the beam correction contribution from MYP monitor is still small. When the corrections from the monitors are combined for the total beam correction, regression differ from dithering from Wien to Wien.

In Fig. 4.15, we have beam corrections for main detector dipole 3. For the high width

monitors, since the regression sensitivity for detector dipole 3 is generally smaller than dithering sensitivity, we have regression corrections that are closer to zero than dithering corrections. For the low width monitors, since the monitor differences are relatively small, the beam correction contribution to the total correction is small as well. For detector dipole 3, the correction discrepancy mainly comes from the high width monitors. We have discrepancy between regression and dithering for dipole 3 in the total correction.

After applying beam corrections to main detector asymmetries, we have the comparison between regressed and dither-corrected asymmetries. The detector monopole is shown in Fig. 4.16. The red is regressed asymmetry and blue is dither-corrected asymmetry. We can see that for the Wiens in Run 1, the regressed and dither-corrected results don't quite agree and they agree well for the Wiens in Run 2.

In Fig. 4.17, we have the asymmetries for detector dipoles. For dipole 1 on the left, we have discrepancies between regression and dithering in Run 1 and the agreement in Run 2 is better than Run 1. For dipole 3, we have different regressed and dither-corrected results in the Wiens for both Run 1 and Run 2.

With the beam corrections from individual monitors studied for detector combinations, we can understand better the main detector asymmetries from regression and dithering. The discrepancy between regression and dithering corrections results from the discrepancy in the sensitivities. In general, the sensitivities agree better for high width monitors. With non-zero monitor differences, we can have different net beam corrections between the two methods, which leads to different main detector asymmetries.

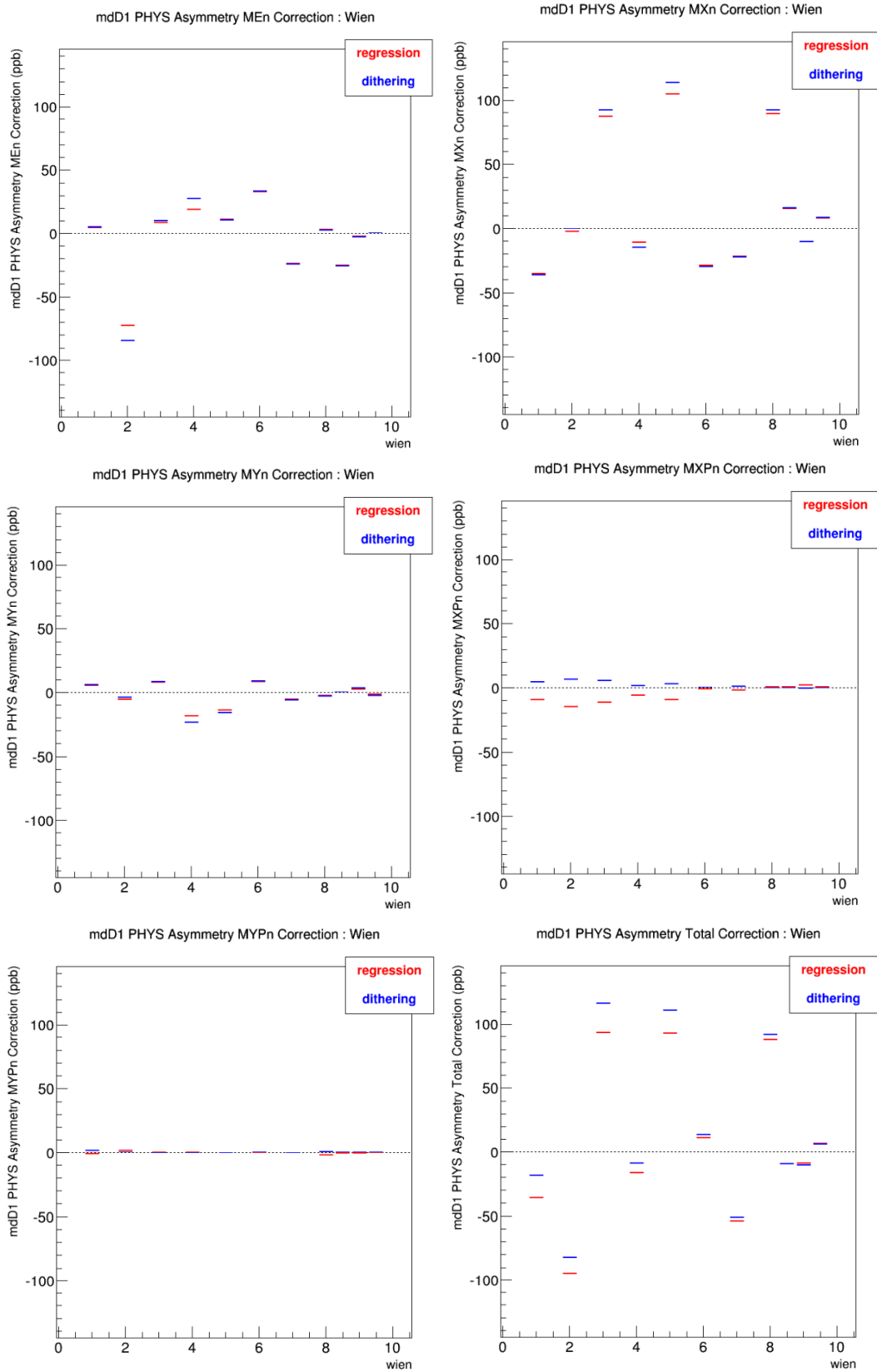


Figure 4.14: Detector dipole 1 beam corrections at Wien level.

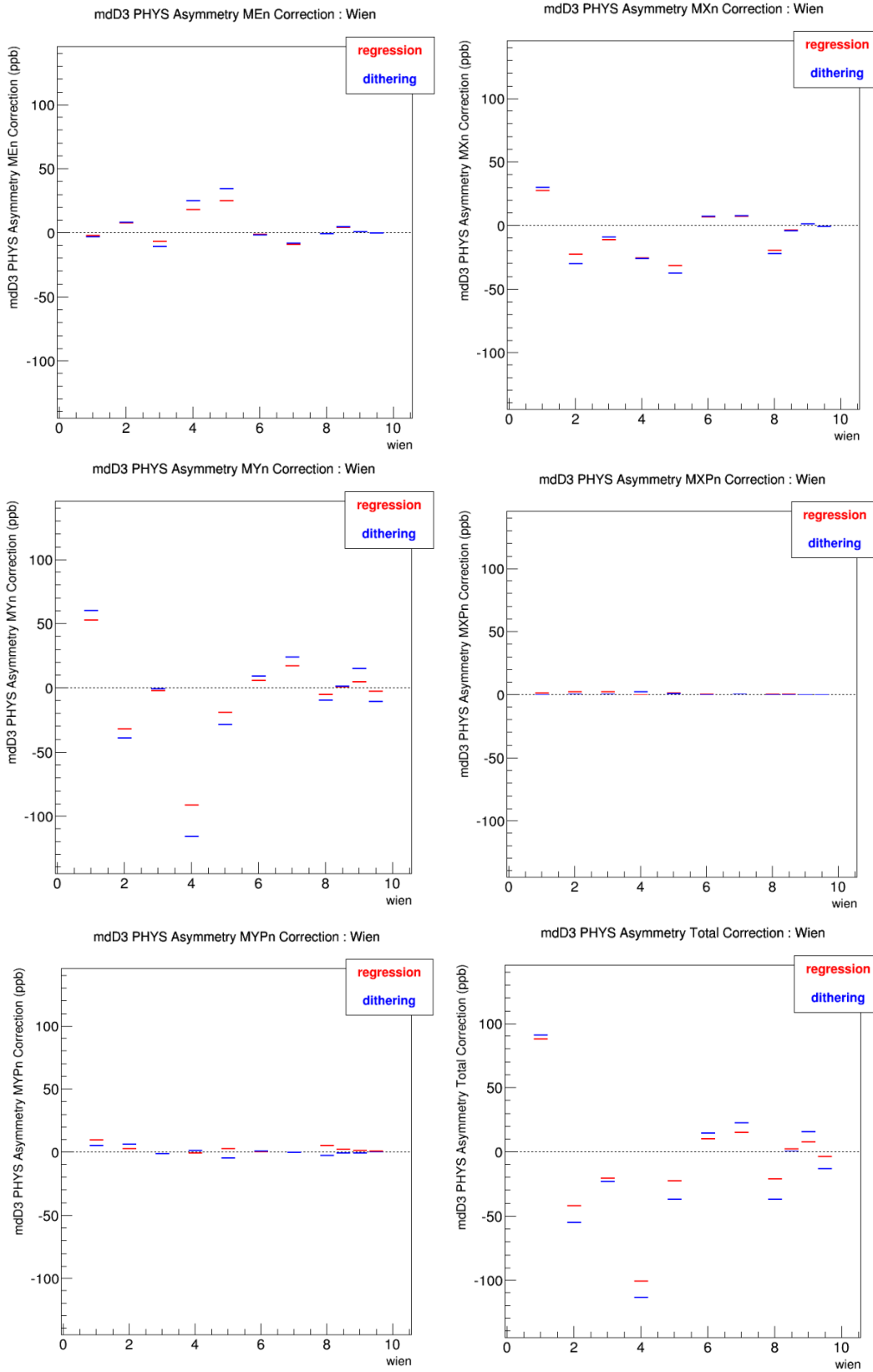


Figure 4.15: Detector dipole 3 beam corrections at Wien level.

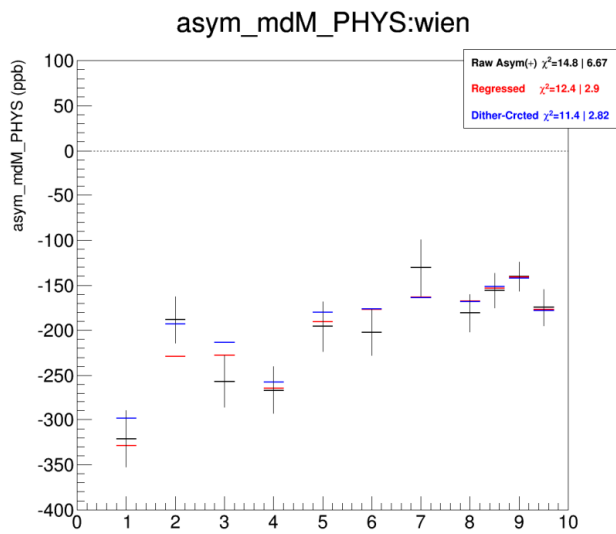


Figure 4.16: Detector monopole asymmetries at Wien level.

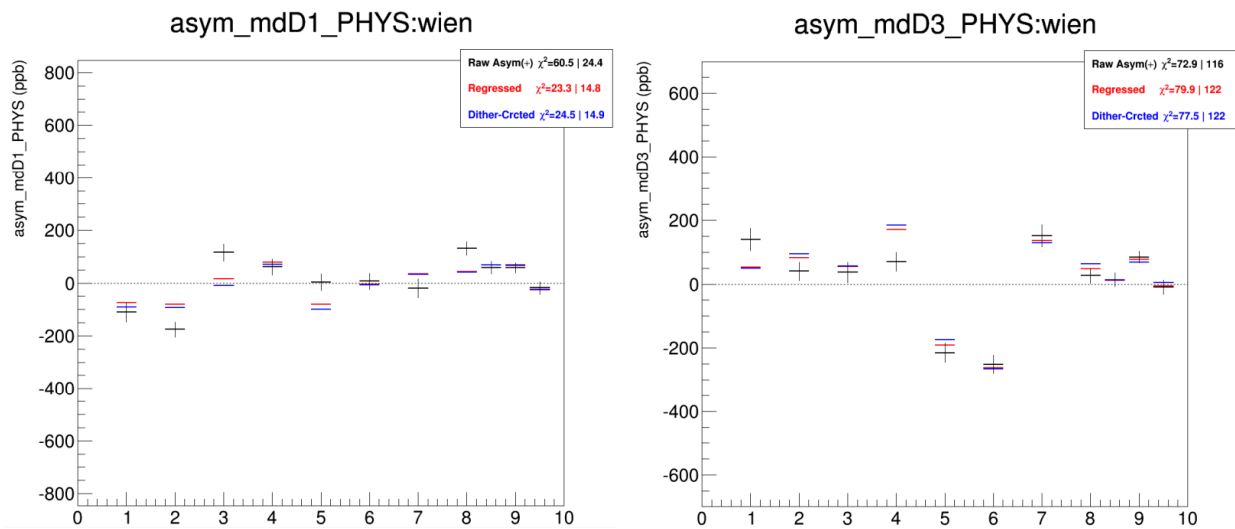


Figure 4.17: Detector dipole asymmetries at Wien level.

Chapter 5

Beam Current Correction

This chapter focuses on the beam current monitor (BCM) analysis, including the BCM choices made for each Run of the experiment and the errors assigned for BCM normalization. The beam current false asymmetry during helicity reversal is dealt with by normalizing main detector yield to beam current. Since we have multiple BCMs, which BCMs to use and how to combine them become the central question.

5.1 BCM Choices

Several BCMs were utilized in each Run of the experiment. In Run 1, we have BCMs 1, 2, 5 and 6. In Run 2, we have BCMs 1–2, 5–6, 7–8. During the data acquisition, virtual BCM “charge” was utilized to normalize main detector signal, which was defined as the average of BCM 1&2 in Run 1 and BCM 8 in Run 2.

After the main detector signal is normalized to the beam current, the residual correlation between the main detector and BCM asymmetries should be small. However, in Run 1, the residual correlations with BCM 1 and 2 were relatively high, about 30% (see Fig. 5.1), while the residual correlations with BCM 5 and 6 are small [12]. Besides, when normalized to BCM 5 and 6, the main detector Null asymmetries have also improved [13]. In Run 1, the average of BCM 5 and 6 was used to normalize the main detector.

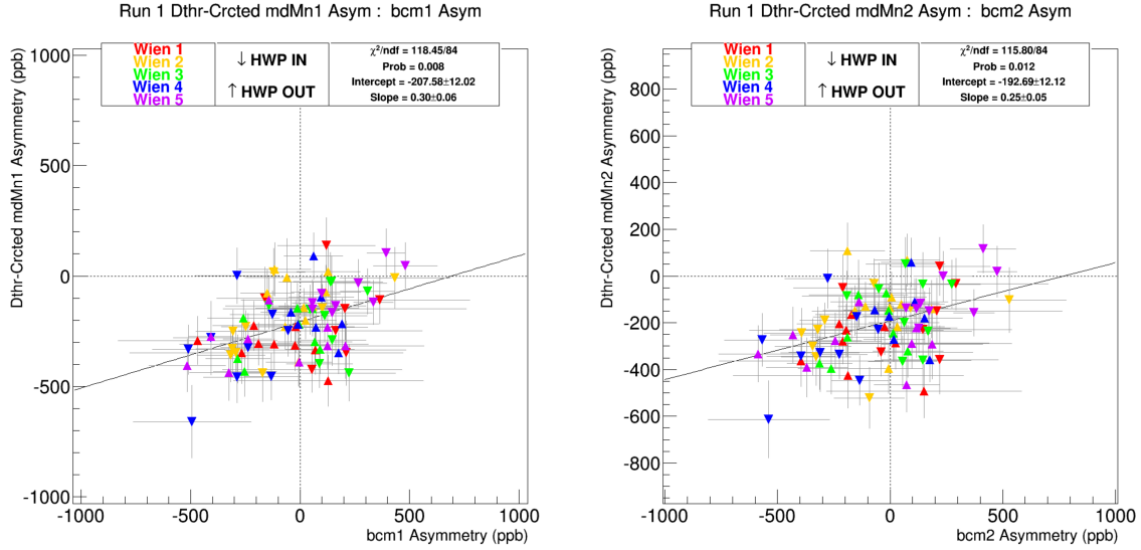


Figure 5.1: Residual correlation between main detector and BCM asymmetries in Run 1.

In Run 2, the residual correlation is small for all BCMS [12]. After Wien 9, the BCM double difference between BCM 1 and 2 had very high width which indicated something wrong with them in that period [14], while BCM 5 and 6 had normal behavior in Run 2 (correlation with other BCMS look normal as well [15]). BCM 5, 6 and 8 were combined to normalize main detector in Run 2.

5.2 Combining Different BCMS

To combine different BCMS, the BCM asymmetries at quartet level were averaged. In Run 1, the average BCM asymmetry from two BCM 5 and 6 is

$$A_{\text{BCM}} = \frac{A_{\text{BCM5}} + A_{\text{BCM6}}}{2}. \quad (5.1)$$

Since the main detector asymmetry was pre-normalized to charge (average of BCM 1 and 2 in Run 1), the main detector was renormalized to the average of BCM 5 and 6 at quartet level by

$$A_{\text{MD}}^{\text{Renorm}} = A_{\text{MD}} + A_{\text{charge}} - A_{\text{BCM}}. \quad (5.2)$$

So effectively the main detector asymmetry is the average of asymmetries renormalized to BCM 5 and 6 separately:

$$A_{\text{MD}}^{\text{Renorm}} = \frac{A_{\text{MD}}^{\text{BCM5}} + A_{\text{MD}}^{\text{BCM6}}}{2}. \quad (5.3)$$

Plugging in the asymmetry values, we have

$$A_{\text{MD}}^{\text{Renorm}} = \frac{-204.41 - 194.58}{2} \text{ ppb} = -199.49 \text{ ppb}. \quad (5.4)$$

For Run 2, using the same procedure for BCM 5, 6 and 8:

$$A_{\text{BCM}} = \frac{A_{\text{BCM5}} + A_{\text{BCM6}} + A_{\text{BCM8}}}{3}, \quad (5.5)$$

$$A_{\text{MD}}^{\text{Renorm}} = A_{\text{MD}} + A_{\text{charge}} - A_{\text{BCM}}, \quad (5.6)$$

$$A_{\text{MD}}^{\text{Renorm}} = \frac{A_{\text{MD}}^{\text{BCM5}} + A_{\text{MD}}^{\text{BCM6}} + A_{\text{MD}}^{\text{BCM8}}}{3}. \quad (5.7)$$

The renormalized main detector asymmetry in Run 2 is

$$A_{\text{MD}}^{\text{Renorm}} = \frac{-167.86 - 159.91 - 164.26}{3} \text{ ppb} = -164.01 \text{ ppb}. \quad (5.8)$$

5.3 Statistical Error of Renormalized Asymmetry

To find statistical error of the renormalized main detector asymmetry, the asymmetry at quartet level should be averaged through runlet, slug, Wien and Run level. Alternatively, with BCM double differences (BCMDD, difference between asymmetries from a pair of BCMs), the statistical error could be calculated using the covariance terms from BCM asymmetry correlations.

Run 1

In Run 1, first we take Eq. 5.3

$$A_{\text{MD}}^{\text{Renorm}} = \frac{A_{\text{MD}}^{\text{BCM5}} + A_{\text{MD}}^{\text{BCM6}}}{2}.$$

The statistical error of the renormalized asymmetry is (including the covariance terms):

$$\sigma_{\text{stat}}(A_{\text{MD}}^{\text{Renorm}}) = \frac{1}{2} \sqrt{\sigma_{\text{stat}}^2(A_{\text{MD}}^{\text{BCM5}}) + \sigma_{\text{stat}}^2(A_{\text{MD}}^{\text{BCM6}}) + 2\text{cov}(A_{\text{MD}}^{\text{BCM5}} A_{\text{MD}}^{\text{BCM6}})}. \quad (5.9)$$

Since the BCM double difference is defined as

$$\begin{aligned} \text{BCMDD56} &= A_{\text{BCM5}} - A_{\text{BCM6}} \\ &= -(-A_{\text{BCM5}}) + (-A_{\text{BCM6}}) \\ &= -(A_{\text{MD}} + A_{\text{charge}} - A_{\text{BCM5}}) + (A_{\text{MD}} + A_{\text{charge}} - A_{\text{BCM6}}) \\ &= -A_{\text{MD}}^{\text{BCM5}} + A_{\text{MD}}^{\text{BCM6}} \\ &= A_{\text{MD}}^{\text{BCM6}} - A_{\text{MD}}^{\text{BCM5}}, \end{aligned} \quad (5.10)$$

we have the statistical error of the BCM double difference

$$\sigma_{\text{stat}}(\text{BCMDD56}) = \sqrt{\sigma_{\text{stat}}^2(A_{\text{MD}}^{\text{BCM5}}) + \sigma_{\text{stat}}^2(A_{\text{MD}}^{\text{BCM6}}) - 2\text{cov}(A_{\text{MD}}^{\text{BCM5}} A_{\text{MD}}^{\text{BCM6}})}. \quad (5.11)$$

Then we could have the statistical error of the renormalized main detector asymmetry directly from the BCM double difference error and the main detector error normalized to each BCM:

$$\sigma_{\text{stat}}(A_{\text{MD}}^{\text{Renorm}}) = \frac{1}{2} \sqrt{2\sigma_{\text{stat}}^2(A_{\text{MD}}^{\text{BCM5}}) + 2\sigma_{\text{stat}}^2(A_{\text{MD}}^{\text{BCM6}}) - \sigma_{\text{stat}}^2(\text{BCMDD56})}. \quad (5.12)$$

By applying the numbers we have

$$\sigma_{\text{stat}}(A_{\text{MD}}^{\text{Renorm}}) = \frac{1}{2} \sqrt{2 * 13.78^2 + 2 * 12.84^2 - 4.22^2} \text{ ppb} = 13.15 \text{ ppb}. \quad (5.13)$$

The indirect calculation using the BCM double difference resulted in a statistical error that agreed with the direct calculation from quartet level. This means the indirect calculation works fine and we could as well apply it in Run 2 as below.

Run 2

We start with Eq. 5.7

$$A_{\text{MD}}^{\text{Renorm}} = \frac{A_{\text{MD}}^{\text{BCM5}} + A_{\text{MD}}^{\text{BCM6}} + A_{\text{MD}}^{\text{BCM8}}}{3}.$$

The statistical error of the renormalized asymmetry in Run 2 is (we have more covariance terms compared with Run 1):

$$\begin{aligned} \sigma_{\text{stat}}(A_{\text{MD}}^{\text{Renorm}}) &= \frac{1}{3} \left[\sigma_{\text{stat}}^2(A_{\text{MD}}^{\text{BCM5}}) + \sigma_{\text{stat}}^2(A_{\text{MD}}^{\text{BCM6}}) + \sigma_{\text{stat}}^2(A_{\text{MD}}^{\text{BCM8}}) \right. \\ &\quad \left. + 2\text{cov}(A_{\text{MD}}^{\text{BCM5}} A_{\text{MD}}^{\text{BCM6}}) + 2\text{cov}(A_{\text{MD}}^{\text{BCM5}} A_{\text{MD}}^{\text{BCM8}}) + 2\text{cov}(A_{\text{MD}}^{\text{BCM6}} A_{\text{MD}}^{\text{BCM8}}) \right]^{1/2}. \end{aligned} \quad (5.14)$$

Since the BCM double differences are (we have three BCMs and we have three pairs of BCM double differences in Run 2)

$$\begin{aligned} \text{BCMDD56} &= A_{\text{MD}}^{\text{BCM6}} - A_{\text{MD}}^{\text{BCM5}}, \\ \text{BCMDD58} &= A_{\text{MD}}^{\text{BCM8}} - A_{\text{MD}}^{\text{BCM5}}, \\ \text{BCMDD68} &= A_{\text{MD}}^{\text{BCM8}} - A_{\text{MD}}^{\text{BCM6}}. \end{aligned} \quad (5.15)$$

The statistical errors of the BCM double differences are

$$\begin{aligned} \sigma_{\text{stat}}(\text{BCMDD56}) &= \sqrt{\sigma_{\text{stat}}^2(A_{\text{MD}}^{\text{BCM5}}) + \sigma_{\text{stat}}^2(A_{\text{MD}}^{\text{BCM6}}) - 2\text{cov}(A_{\text{MD}}^{\text{BCM5}} A_{\text{MD}}^{\text{BCM6}})}, \\ \sigma_{\text{stat}}(\text{BCMDD58}) &= \sqrt{\sigma_{\text{stat}}^2(A_{\text{MD}}^{\text{BCM5}}) + \sigma_{\text{stat}}^2(A_{\text{MD}}^{\text{BCM8}}) - 2\text{cov}(A_{\text{MD}}^{\text{BCM5}} A_{\text{MD}}^{\text{BCM8}})}, \\ \sigma_{\text{stat}}(\text{BCMDD68}) &= \sqrt{\sigma_{\text{stat}}^2(A_{\text{MD}}^{\text{BCM6}}) + \sigma_{\text{stat}}^2(A_{\text{MD}}^{\text{BCM8}}) - 2\text{cov}(A_{\text{MD}}^{\text{BCM6}} A_{\text{MD}}^{\text{BCM8}})}. \end{aligned} \quad (5.16)$$

Then the statical error of the renormalized asymmetry can be calculated as

$$\sigma_{\text{stat}}(A_{\text{MD}}^{\text{Renorm}}) = \frac{1}{3} \left[3\sigma_{\text{stat}}^2(A_{\text{MD}}^{\text{BCM5}}) + 3\sigma_{\text{stat}}^2(A_{\text{MD}}^{\text{BCM6}}) + 3\sigma_{\text{stat}}^2(A_{\text{MD}}^{\text{BCM8}}) - \sigma_{\text{stat}}^2(\text{BCMDD56}) - \sigma_{\text{stat}}^2(\text{BCMDD58}) - \sigma_{\text{stat}}^2(\text{BCMDD68}) \right]^{1/2}. \quad (5.17)$$

After applying the numbers we have

$$\sigma_{\text{stat}}(A_{\text{MD}}^{\text{Renorm}}) = \frac{1}{3} \sqrt{3 * 7.39^2 + 3 * 7.69^2 + 3 * 7.36^2 - 2.81^2 - 1.8^2 - 2.73^2} \text{ ppb} = 7.34 \text{ ppb}. \quad (5.18)$$

The statistical error after renormalization to the average of BCM 5, 6 and 8 is 7.34 ppb.

When originally normalized to BCM 8, the statistical error was 7.36 ppb.

5.4 Systematic Error

A BCM systematic error is assigned to cover the BCM double differences. In Run 1, BCMDD56 is 9.9 ± 4.2 ppb, higher than 2 sigma. In Run 2, BCMDD56 is 8.0 ± 2.8 ppb, BCMDD58 is 3.6 ± 1.8 ppb, BCMDD68 is -4.4 ± 2.7 ppb, which are all about 2 sigma level. These BCM double difference errors indicate that there are systematic differences between different BCMs, and we need a systematic error term associated with this difference.

Run 1

In Run 1, half of the distance between the main detector asymmetries normalized to BCM 5 and 6 respectively was used as the systematic error:

$$\sigma'_{\text{syst}}(A_{\text{MD}}^{\text{Renorm}}) = \left| \frac{A_{\text{MD}}^{\text{BCM5}} - A_{\text{MD}}^{\text{BCM6}}}{2} \right|. \quad (5.19)$$

The following shows how the above can be calculated.

In Run 1, we have the average of main detector asymmetries as

$$A_{\text{MD}}^{\text{Renorm}} = \frac{A_{\text{MD}}^{\text{BCM5}} + A_{\text{MD}}^{\text{BCM6}}}{2}. \quad (5.20)$$

We assume the BCMs have close uncorrelated resolution σ_{BCM} , which is effectively equal weighting for the BCMs.

Then the χ^2 of averaging all main detector asymmetries is

$$\begin{aligned}
\chi^2 &= \frac{(A_{\text{MD}}^{\text{BCM5}} - A_{\text{MD}}^{\text{Renorm}})^2}{\sigma_{\text{BCM}}^2} + \frac{(A_{\text{MD}}^{\text{BCM6}} - A_{\text{MD}}^{\text{Renorm}})^2}{\sigma_{\text{BCM}}^2} \\
&= \frac{\left(\frac{A_{\text{MD}}^{\text{BCM5}} - A_{\text{MD}}^{\text{BCM6}}}{2}\right)^2}{\sigma_{\text{BCM}}^2} + \frac{\left(\frac{A_{\text{MD}}^{\text{BCM6}} - A_{\text{MD}}^{\text{BCM5}}}{2}\right)^2}{\sigma_{\text{BCM}}^2} \\
&= \frac{(A_{\text{MD}}^{\text{BCM5}} - A_{\text{MD}}^{\text{BCM6}})^2}{2\sigma_{\text{BCM}}^2}.
\end{aligned} \tag{5.21}$$

The χ^2 is divided by d , the number of degrees of freedom.

$$\tilde{\chi}^2 = \frac{\chi^2}{d} = \frac{\chi^2}{2-1} = \frac{(A_{\text{MD}}^{\text{BCM5}} - A_{\text{MD}}^{\text{BCM6}})^2}{2\sigma_{\text{BCM}}^2}. \tag{5.22}$$

We scale the BCM error based on the reduced χ^2

$$\sigma_{\text{BCM}} \sqrt{\tilde{\chi}^2} = \sqrt{\frac{(A_{\text{MD}}^{\text{BCM5}} - A_{\text{MD}}^{\text{BCM6}})^2}{2}}. \tag{5.23}$$

Then the systematic error is defined as the quantity above divided by square root of n , the number of BCMs in Run 1. We have

$$\sigma'_{\text{syst}}(A_{\text{MD}}^{\text{Renorm}}) = \frac{\sigma_{\text{BCM}} \sqrt{\tilde{\chi}^2}}{\sqrt{n}} = \frac{\sqrt{\frac{(A_{\text{MD}}^{\text{BCM5}} - A_{\text{MD}}^{\text{BCM6}})^2}{2}}}{\sqrt{2}} = \left| \frac{A_{\text{MD}}^{\text{BCM5}} - A_{\text{MD}}^{\text{BCM6}}}{2} \right|. \tag{5.24}$$

The result above is the same as the half of the distance between BCM 5 and BCM 6 normalized asymmetries, Eq. 5.19.

Combine Eq. 5.21-5.24 and we have:

$$\sigma'_{\text{syst}}(A_{\text{MD}}^{\text{Renorm}}) = \frac{\sigma_{\text{BCM}}}{\sqrt{n}} \sqrt{\frac{\chi^2}{d}}. \tag{5.25}$$

There is one more modification we should make to Eq. 5.25. The χ^2 (Eq. 5.21) not only

has the BCM systematic effect in it, also it has contribution from BCM resolution. When we normalize the main detector asymmetry, the BCM instrumental noise is already propagated into the statistical error for the main detector asymmetry. To avoid double counting of the BCM instrumental noise, we should remove the contribution of BCM resolution from the BCM systematic error. The BCM error should be subtracted from the left hand side of Eq. 5.23

$$\sqrt{\left(\sigma_{\text{BCM}}\sqrt{\tilde{\chi}^2}\right)^2 - \left(\sigma_{\text{BCM}}\right)^2} = \sigma_{\text{BCM}}\sqrt{\tilde{\chi}^2 - 1}. \quad (5.26)$$

And Eq. 5.24 becomes

$$\sigma_{\text{syst}}(A_{\text{MD}}^{\text{Renorm}}) = \frac{\sigma_{\text{BCM}}\sqrt{\tilde{\chi}^2 - 1}}{\sqrt{n}}. \quad (5.27)$$

In the end we have the systematic error as

$$\boxed{\sigma_{\text{syst}}(A_{\text{MD}}^{\text{Renorm}}) = \frac{\sigma_{\text{BCM}}}{\sqrt{n}} \sqrt{\frac{\chi^2}{d} - 1}}, \quad (5.28)$$

in which σ_{BCM} is the BCM resolution, n is the number of BCMs and d is the number of degrees of freedom.

A user-friendly version of Eq. 5.28 can be expressed with the main detector asymmetries as

$$\sigma_{\text{syst}}(A_{\text{MD}}^{\text{Renorm}}) = \frac{1}{\sqrt{n}} \sqrt{\frac{\sum_i^n (A_{\text{MD}}^{\text{BCM}i} - A_{\text{MD}}^{\text{Renorm}})^2}{d} - \sigma_{\text{BCM}}^2}, \quad (5.29)$$

in which the index i takes all the BCMs available.

Additionally, a convenient relationship between Eq. 5.25 and Eq. 5.28 is

$$\sigma_{\text{syst}}(A_{\text{MD}}^{\text{Renorm}}) = \sqrt{\sigma_{\text{syst}}'^2(A_{\text{MD}}^{\text{Renorm}}) - \frac{\sigma_{\text{BCM}}^2}{n}}, \quad (5.30)$$

which suggests that in order to calculate the effective systematic error, we need to subtract the BCM resolution divided by square root of n from the ‘‘total’’ systematic error.

In Run 1, applying numbers into Eq. 5.19 or Eq. 5.24, we have

$$\sigma'_{\text{syst}}(A_{\text{MD}}^{\text{Renorm}}) = \left| \frac{-204.41 - (-194.58)}{2} \right| = 4.92 \text{ ppb}. \quad (5.31)$$

To remove the BCM noise contribution from the above, we could use the error of BCM double difference to calculate the BCM noise. In Run 1, the BCMDD56 error is 4.2 ppb. We can take an estimate of BCM noise using this BCMDD56 error, and we have

$$\sigma_{\text{BCM}} = \frac{\sigma_{\text{stat}}(\text{BCMDD56})}{\sqrt{2}} = \frac{4.22}{\sqrt{2}} = 2.99 \text{ ppb}. \quad (5.32)$$

Applying Eq. 5.30 we have the effective systematic error in Run 1:

$$\begin{aligned} \sigma_{\text{syst}}(A_{\text{MD}}^{\text{Renorm}}) &= \sqrt{\sigma'^2_{\text{syst}}(A_{\text{MD}}^{\text{Renorm}}) - \frac{\sigma_{\text{BCM}}^2}{n}} \\ &= \sqrt{4.92^2 - \frac{2.99^2}{2}} \\ &= 4.44 \text{ ppb}. \end{aligned} \quad (5.33)$$

Run 2

For Run 2, we apply the same procedure as we have developed for Run 1.

Again we start with Eq. 5.7, the renormalized asymmetry from three BCMs,

$$A_{\text{MD}}^{\text{Renorm}} = \frac{A_{\text{MD}}^{\text{BCM5}} + A_{\text{MD}}^{\text{BCM6}} + A_{\text{MD}}^{\text{BCM8}}}{3}.$$

The χ^2 is

$$\chi^2 = \frac{(A_{\text{MD}}^{\text{BCM5}} - A_{\text{MD}}^{\text{Renorm}})^2}{\sigma_{\text{BCM}}^2} + \frac{(A_{\text{MD}}^{\text{BCM6}} - A_{\text{MD}}^{\text{Renorm}})^2}{\sigma_{\text{BCM}}^2} + \frac{(A_{\text{MD}}^{\text{BCM8}} - A_{\text{MD}}^{\text{Renorm}})^2}{\sigma_{\text{BCM}}^2}. \quad (5.34)$$

When divided by d , the degrees of freedom, which is $3 - 1$ in Run 2,

$$\tilde{\chi}^2 = \frac{\chi^2}{d} = \frac{\chi^2}{3-1} = \frac{(A_{\text{MD}}^{\text{BCM5}} - A_{\text{MD}}^{\text{Renorm}})^2 + (A_{\text{MD}}^{\text{BCM6}} - A_{\text{MD}}^{\text{Renorm}})^2 + (A_{\text{MD}}^{\text{BCM8}} - A_{\text{MD}}^{\text{Renorm}})^2}{2\sigma_{\text{BCM}}^2}. \quad (5.35)$$

The scaled BCM error is

$$\sigma_{\text{BCM}}\sqrt{\tilde{\chi}^2} = \sqrt{\frac{(A_{\text{MD}}^{\text{BCM5}} - A_{\text{MD}}^{\text{Renorm}})^2 + (A_{\text{MD}}^{\text{BCM6}} - A_{\text{MD}}^{\text{Renorm}})^2 + (A_{\text{MD}}^{\text{BCM8}} - A_{\text{MD}}^{\text{Renorm}})^2}{2}}. \quad (5.36)$$

Then divide it by n , the number of BCMs in Run 2, we have the systematic error as shown in Eq. 5.25:

$$\begin{aligned} \sigma'_{\text{syst}}(A_{\text{MD}}^{\text{Renorm}}) &= \frac{\sigma_{\text{BCM}}}{\sqrt{n}}\sqrt{\tilde{\chi}^2} \\ &= \sqrt{\frac{(A_{\text{MD}}^{\text{BCM5}} - A_{\text{MD}}^{\text{Renorm}})^2 + (A_{\text{MD}}^{\text{BCM6}} - A_{\text{MD}}^{\text{Renorm}})^2 + (A_{\text{MD}}^{\text{BCM8}} - A_{\text{MD}}^{\text{Renorm}})^2}{6}} \\ &= \sqrt{\frac{(-167.86 + 164.01)^2 + (-159.91 + 164.01)^2 + (-164.26 + 164.01)^2}{6}} \\ &= 2.30 \text{ ppb}. \end{aligned} \quad (5.37)$$

The systematic error calculated above with Eq. 5.25 includes the contribution from BCM resolution. We need to subtract BCM noise from it. The BCM resolution at quartet level is known to be ~ 50 ppm in Run 2, and we have 939 million quartets in Run 2. The BCM resolution for entire Run 2 is

$$\sigma_{\text{BCM}} = \frac{\sigma_{\text{BCM}}(\text{quartet})}{\sqrt{\text{number of quartets}}} = \frac{50 \text{ ppm}}{\sqrt{9.39 \times 10^8}} = 1.63 \text{ ppb}. \quad (5.38)$$

Alternatively, we could estimate the BCM noise based on BCM double differences between different BCMs, BCM5, 6 and 8. We assume in Run 2, these three BCMs have close noises

and we calculate the BCM noise this way

$$\begin{aligned}
\sigma_{\text{BCM}} &= \frac{1}{\sqrt{2}} \frac{\sigma_{\text{stat}}(\text{BCMDD56}) + \sigma_{\text{stat}}(\text{BCMDD58}) + \sigma_{\text{stat}}(\text{BCMDD68})}{3} \\
&= \frac{1}{\sqrt{2}} \frac{2.81 + 1.80 + 2.73}{3} = 1.73 \text{ ppb}.
\end{aligned}
\tag{5.39}$$

The BCM noises obtained from the two equations above are very close.

Then with the help of Eq. 5.30 we have the effective systematic error in Run 2:

$$\begin{aligned}
\sigma_{\text{syst}}(A_{\text{MD}}^{\text{Renorm}}) &= \sqrt{\sigma_{\text{syst}}'^2(A_{\text{MD}}^{\text{Renorm}}) - \frac{\sigma_{\text{BCM}}^2}{n}} \\
&= \sqrt{2.30^2 - \frac{1.73^2}{3}} \\
&= 2.07 \text{ ppb}.
\end{aligned}
\tag{5.40}$$

Chapter 6

Ditherless Data Recovery

This chapter summarizes ditherless data recovery, including the definition of the main detector sensitivities for the ditherless periods, calculation of the dithering statistical error and the comparison of Null and Physics asymmetries before and after the inclusion of ditherless data.

6.1 Background

During the experiment, beam dithering was performed constantly to help determine the main detector sensitivities to beam parameters for later analysis. Still, we have some data periods that don't have dithering slopes, which are "ditherless". They are ditherless for different reasons. Some slugs are due to insufficient healthy dithering patterns. Some slugs miss a good energy modulation pattern, etc.

6.1.1 Ditherless Data Coverage

Tab. 6.1 shows how much ditherless data we have in our data set. In Run 1 we have 9 out of 91 slugs that don't have dithering slopes. And in Run 2 we have 23 out of 182 slugs. By calculating the ratio between ditherless quartets and total quartets, we have the percentage

Table 6.1: Ditherless data coverage summary.

	Run 1	Run 2
Ditherless Slugs	9	23
Total Slugs	91	182
Ditherless Quartets	30901868	96655558
Total Quartets	449610032	939320843
Ditherless Percentage (%)	6.9	10.3

of ditherless data in our data set, which is 6.9% in Run 1 and 10.3% in Run 2.

Since the percentage of the ditherless data is on the order of 10%, they should be treated in a careful manner. We don't have dithering slopes to perform beam corrections on them. We could simply throw them away by losing 10% accuracy or we could figure out ways to save them.

6.1.2 Regression and Dithering Approaches

The ditherless slugs miss measured dithering slopes. We have two different approaches to perform beam corrections for these data. The first approach is regression slope calculation and the second approach is dithering slope interpolation or extrapolation.

The first approach is using regression slope to correct the main detector asymmetry. We have been using dithering instead of regression because dithering correction is proven to work better than regression [16][17]. Regression slope can be influenced by monitor noise and therefore it is not effective at correction to weak jitter directions. Work was done on the prediction of the "correct" regression slope [18] but it required more verification. Plus, it maybe be better to stick to one correction scheme, not a mixture of regression and dithering.

The second approach is to project the good dithering data to the ditherless data with the help of adjacent data periods that have measured dithering slopes. The details of this method will be discussed here.

6.2 Recovery Method

6.2.1 Ditherless Sensitivity Definition

For most of the ditherless slugs, we have dithering slopes for the previous slugs (smaller slug number) and the subsequent slugs (higher slug number). The change of the slope across the gap is often not statistical, which means the distance between the two ends represents a systematic “jump” of the slope. We use the average of the previous and subsequent slugs to fill the ditherless slug in the middle and use half of the distance between the two slopes as an error bar. This procedure is illustrated in Fig. 6.1.

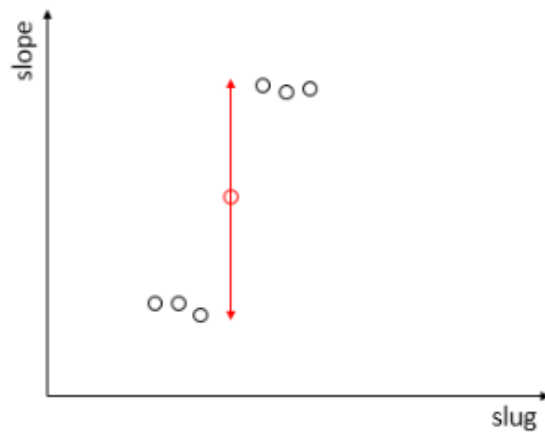


Figure 6.1: Ditherless slug with measured sensitivities on both sides.

This error bar shown in Fig. 6.1 is high enough to cover these scenarios: the “true” slope of unmeasured slug is consistent with the previous slug or the subsequent slug with a different beam tune, which are the two most probable cases. This is a simple procedure but it is also effective to cover the unknown nature for these ditherless data. The error bar is generous but it should and will be propagated into the final main detector asymmetry error to make sure these ditherless data can be safely included.

For the ditherless slug inbetween the “good” slugs, its “slope” is set to be the average of the left and right slugs:

$$S = \frac{S^{\text{left}} + S^{\text{right}}}{2}. \quad (6.1)$$

The error of the defined slope is set to be half of the change from left to right:

$$\sigma = \left| \frac{S^{\text{left}} - S^{\text{right}}}{2} \right|. \quad (6.2)$$

Eq. 6.1 and 6.2 are conceptual formulas. In application, first we make sure we use the same number of slugs on its left and right. For example, we use 5 slugs from the ditherless slug's left side and 5 slugs from its right. Then Eq. 6.1 becomes simply the average of all slugs that are involved:

$$S_m = \langle S_{mi} \rangle, \quad (6.3)$$

in which m can take 0-4, one of the five monitors and i takes all adjacent slugs, including both good slugs on the left and right in Fig. 6.1.

Not only do we need to calculate the error of the slope, to make sure the dithering correction error is properly propagated into the physics asymmetry error, we also need to calculate the slope error covariance for the ditherless slug:

$$\text{cov}(S_m S_n) = \langle (S_{mi} - S_m)(S_{ni} - S_n) \rangle, \quad (6.4)$$

in which m and n both take 0-4, five monitor slopes. $\text{cov}(S_m S_n)$ is the error covariance between monitor m and monitor n . The square roots of the diagonal elements are the error of the ditherless slope:

$$\sigma_m = \sqrt{\text{cov}(S_m S_m)}. \quad (6.5)$$

It can be proven that when the slopes of the left slugs are stable, the slopes of the right slugs are stable and the number of slopes on the left equal the number of slopes on the right, Eq. 6.5 and Eq. 6.2 are equivalent.

6.2.2 Further Details of Ditherless Sensitivity Calculation

Some details related to the treatment of the ditherless data:

- The slugs used for calculation are given equal weighting. The reason is that the statistical error bar of the dithering slopes is normally very small compared to the change of slope from slug to slug. So across the ditherless gap, if we used weighted average, it is highly likely the average of them would not lie in the middle, the “unbiased” position, and the slope variance would not equal half of the distance between the two sides. For example, the slugs on the left have small statistical error and the slugs on the right have relatively high statistical error (both of them are way less than the jump between the slopes). If we use the statistical error as the weighting, the average of the slopes is going to be closer to the slugs on the left and the slope variance is going to be smaller than half of the change between the slopes on both sides. Often we don’t know if the ditherless slug have a more similar beam tune condition to its previous slugs than the slugs happened afterwards.
- The number of good slugs used for calculation should vary depending on the situation. For the consecutive slugs, like the middle of Wien 9b, we could use more slugs to average things because the adjacent slugs are relatively stable on its side. For this situation, 10 slugs (5 on the left and 5 on the right) were used to fill the ditherless slugs. But for other region that is more sparse, the slugs on both sides don’t always have 5 or more slugs that have stable slopes. So for these slugs, 2 slugs were used for calculation, 1 on the left and 1 on the right. If not, the error bar of the filled slope sometimes is not high enough to represent the change of the slug gap due to the interference from other unstable slopes distant from current ditherless stand-alone slug.
- Some slugs don’t always have both dithering slugs on its left and right. For example, slug 42-45 in Wien 1 and slug 320 in Wien 10. In this case, Eq. 6.1 and 6.2 don’t apply but still Eq. 6.3, 6.4 and 6.5 can be used. 5 slugs were used for Wien 1 and 4 slugs for Wien 10 to calculate slope and slope error covariances. Since these ditherless

slugs only have “one end” of useful information, we have assumed its slope to be consistent with this end, or extrapolation. There are other ways to give these ditherless slugs higher error bar. For example, we could use all slugs in Wien 1 to estimate error covariances of slug 42-46 and all slugs in Wien 10 to fill slug 320.

6.2.3 Dithering Sensitivity Slug History

With the procedure provided in the previous sections, the dithering slopes for ditherless slugs are calculated and put together with other slugs that have measured dithering slopes.

First let’s look at energy slope in Fig. 6.2, which is dominated by energy modulation and stable through Run 1 and Run 2. The black points are those slugs with measured dithering slopes and the red points are the ditherless slugs.

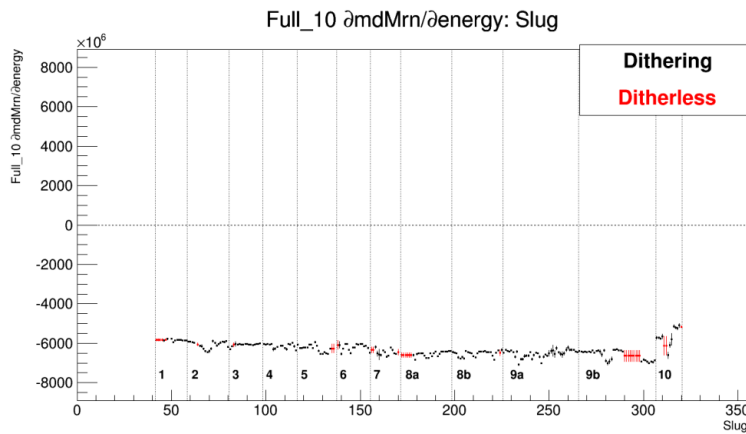


Figure 6.2: Main detector dithering sensitivity slug history for energy monitor.

From Fig. 6.2, we can see that the energy slope is pretty stable. The filled (red) slopes are approximately the same with other slugs. For the slugs around slug 290, the filled slopes have error bars that can cover the change of slopes from before slug 290 to after slug 300. The two slugs in the middle of Wien 10 have error bars that are also high enough to cover the instability of slopes. For the slugs 42–46 in Wien 1, the slopes are set consistent with the slugs after slug 46. For slug 320, the slope is taken to be consistent with the four slugs previous to it.

Now let's look at horizontal monitors, targetX and targetXSlope, the horizontal position and angle in Fig. 6.3 and 6.4. We can see that for slugs 290–300, we don't know where the slopes are for those ditherless slugs inbetween. They could be consistent with previous or subsequent slugs. Therefore, the error bar is chosen to be so high that it can cover both cases. For ditherless slugs 311 and 312 in Wien 10, the error bar is high enough to cover the change of slopes from slug 310 to 313.

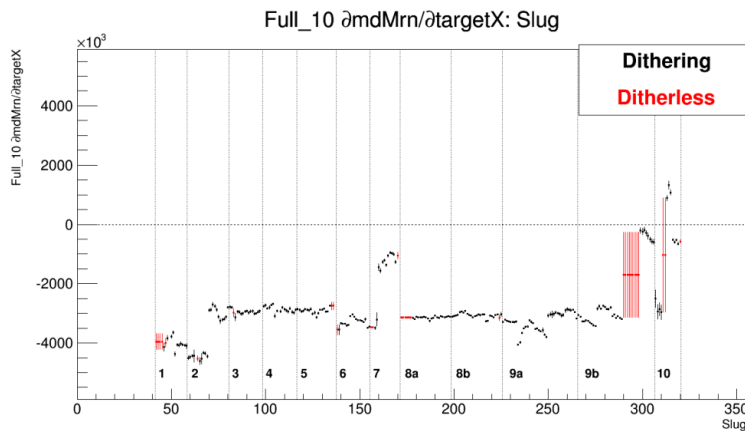


Figure 6.3: Main detector dithering sensitivity slug history for targetX monitor.

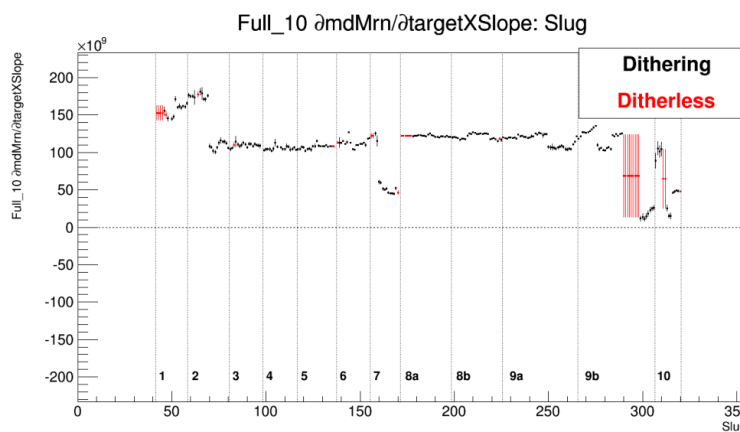


Figure 6.4: Main detector dithering sensitivity slug history for targetXSlope monitor.

Now let's look at monitors targetY and targetYSlope, which are vertical position and angle. Since we have used energy monitor in the horizontal direction, the Y slopes for main detector monopole are relatively small compared to horizontal ones. For Y direction, the

dithering and ditherless slopes are shown in Fig. 6.5 and 6.6.

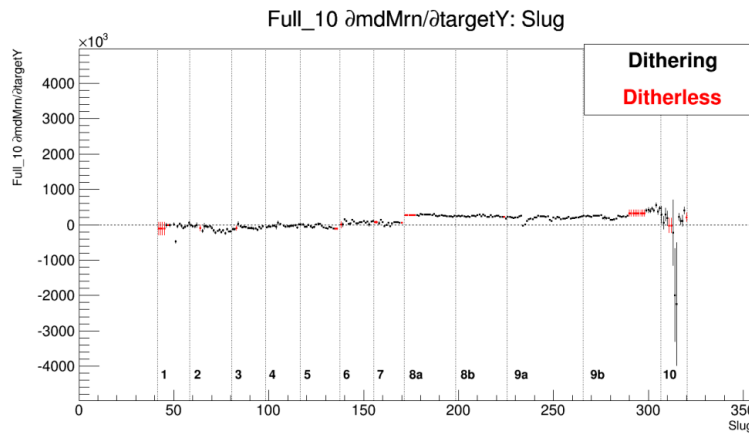


Figure 6.5: Main detector dithering sensitivity slug history for targetY monitor.

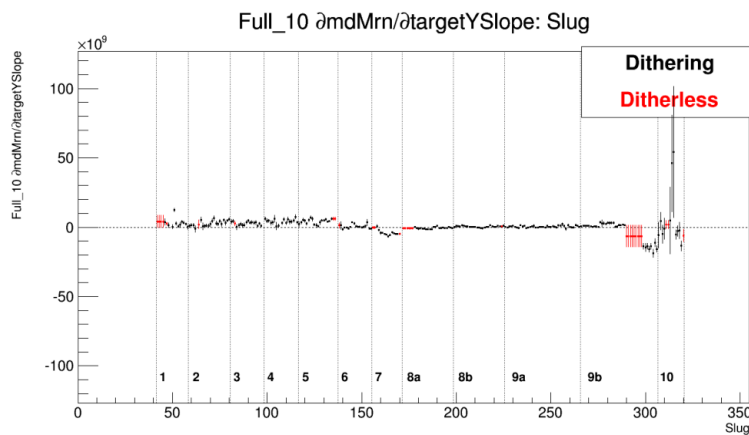


Figure 6.6: Main detector dithering sensitivity slug history for targetYSlope monitor.

In the Y direction, we have similar observations as shown in the X directions. For slug ~ 290 , the error bar can cover the systematic change of slopes. For the slugs in Wien 10, we can see that the statistical error for some of the slugs are very high. The value of the slope and its error still make the vertical dithering slopes in Wien 10 effectively small, or close to zero, like the rest of the slugs in Run 1 and Run 2. However, the high error bar here in Fig. 6.5 and 6.6, like the high error bar with ditherless slugs in X direction as shown in Fig. 6.3 and 6.4, can all be incorporated into statistical error of dithering correction and in the end combined with main detector asymmetry error. This problem shown here is covered.

6.3 Main Detector Asymmetry with Ditherless Data

In the previous sections, “dithering slopes” for ditherless slugs were defined. This enables us to calculate the main detector asymmetry with these ditherless data included. Here we compare the main detector asymmetries with and without these ditherless slugs.

IHWP+Spin Null, IHWP-only Null and Physics asymmetries are provided here.

6.3.1 Null Asymmetry

In Fig. 6.7, we have main detector IHWP+Spin Null asymmetries. Blue is for the slugs with measured dithering slopes. Red is the ditherless data only. And black in the middle is the two sets combined, which is our whole data set. Please note that in some Wiens, we could only have one ditherless slug so there is no Null asymmetry defined for that ditherless Wien, like the zero Null value in Wien 2, 3, 4, 6, 8b and 9a ditherless data set. Also for Wien 5, the ditherless slugs have very small statistics so the error bar is very high.

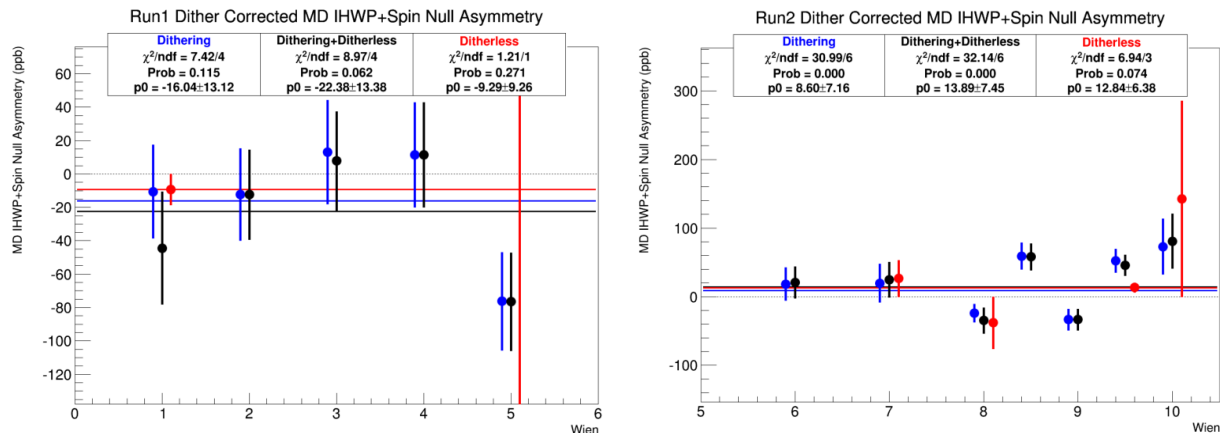


Figure 6.7: Main detector IHWP+Spin Null asymmetries.

From Fig. 6.7, we can tell that the Null asymmetry for ditherless data (red) is not very different from the dithering data (blue). For Wien 1, 5, 7, 8a and 10, the Null asymmetries agree within one sigma. We can also tell from the IHWP-only Null asymmetries shown in Fig. 6.8.

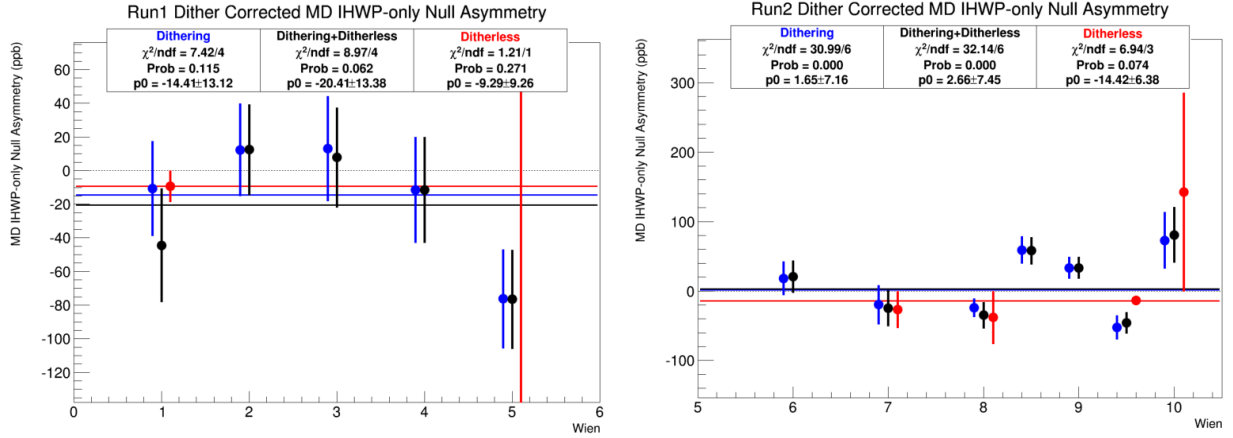


Figure 6.8: Main detector IHWP-only Null asymmetries.

6.3.2 Physics Asymmetry

The physics asymmetries of main detector are shown in Fig. 6.9. We can tell that for the majority of the Wiens, the dithering data and the ditherless data agree pretty well within one sigma, like Wien 2, 3, 5, 6, 7, 8b, 9b and 10. There are only two Wiens that show mismatch between red and blue data sets, which are Wien 1 and Wien 8a.

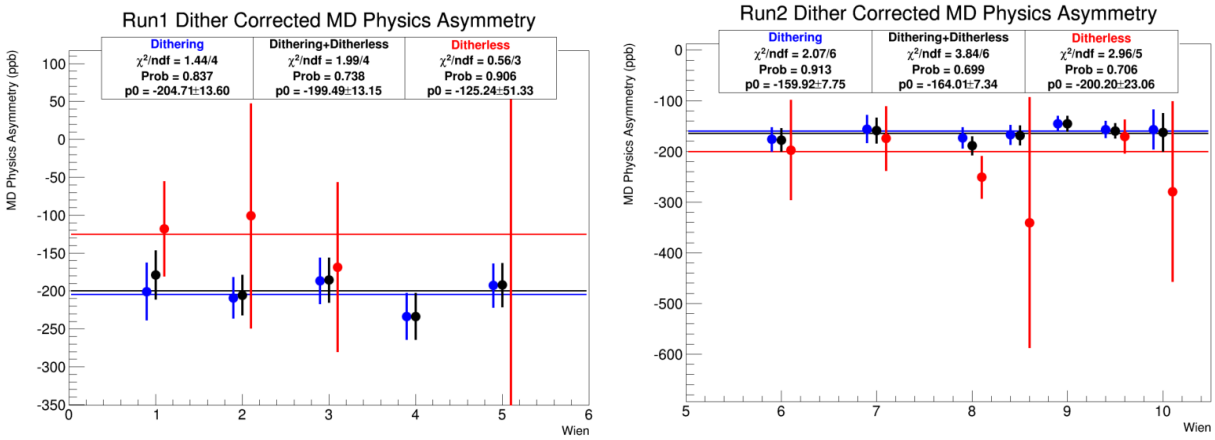


Figure 6.9: Main detector Physics asymmetries.

These two Wiens have their own special problems from other sources. Wien 1 asymmetry can be different for different beam current monitors [19] and Wien 8a asymmetry can differ from different beam correction schemes [20]. The observations from other aspects of asymmetry corrections can suggest the underlying systematic error that caused the

discrepancy between dithering and ditherless data in these two Wiens.

Table 6.2: Main detector Physics asymmetries.

Run	Data Set	Asymmetry (ppb)
1	Dithering	-204.71 ± 13.60
1	Dithering+Ditherless	-199.49 ± 13.15
1	Ditherless	-125.24 ± 51.33
2	Dithering	-159.92 ± 7.75
2	Dithering+Ditherless	-164.01 ± 7.34
2	Ditherless	-200.20 ± 23.06

In Tab. 6.2 we have the physics asymmetry values from different data sets. The discrepancies between dithering and ditherless data sets for Run 1 and Run 2 are

$$\text{Run 1, Dither Corrected: } A(\text{Dithering-Ditherless}) = 79.47 \pm 53.10 \text{ ppb}, \quad (6.6)$$

$$\text{Run 2, Dither Corrected: } A(\text{Dithering-Ditherless}) = 40.28 \pm 24.33 \text{ ppb}. \quad (6.7)$$

From Eq. 6.6 and 6.7, we can tell that the discrepancy is about 1–2 sigma for Run 1 and Run 2. This may seem to tell us that the dithering and ditherless don't quite agree. But the main detector asymmetry error here is statistical only. There are the systematic error terms, including the bcm systematics, beam correction systematics and BB correction error, etc. When these systematic errors are added¹, we have better agreement between the dithering and ditherless data. Besides, we can apply other corrections (like beamline background correction) to the physics asymmetry and see if the agreement can be further improved.

6.3.3 BB Corrected Physics Asymmetry

The discrepancy between dithering and ditherless data shown in Eq. 6.6 and 6.7 are from dither-corrected physics asymmetry. Here beamline background (BB) is applied as well to

¹The bcm, beam and BB correction systematic error combined can be as high as half of the main detector asymmetry statistical error. The inclusion of these systematics can typically increase the error by 10%.

test the dithering-ditherless consistency.

In Fig. 6.10, we have the main detector physics asymmetries for Run 1 and Run 2 with BB correction applied. We can see that in Run 1, the benefit from BB correction is not obvious but in Run 2, for example Wien 8a, the agreement between dithering (blue) and ditherless (red) is much better. The discrepancy in Wien 8a is about 1 sigma now, much better than what Fig. 6.9 showed without BB correction.

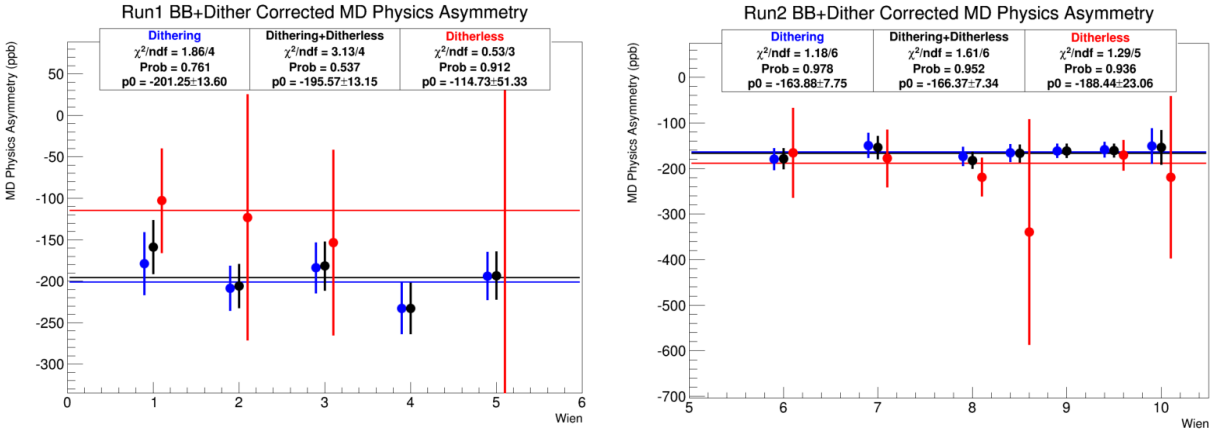


Figure 6.10: Main detector Physics asymmetries + BB correction.

Table 6.3: Main detector Physics asymmetries + BB correction.

Run	Data Set	Asymmetry (ppb)
1	Dithering	-201.25 ± 13.60
1	Dithering+Ditherless	-195.57 ± 13.15
1	Ditherless	-114.73 ± 51.33
2	Dithering	-163.88 ± 7.75
2	Dithering+Ditherless	-166.37 ± 7.34
2	Ditherless	-188.44 ± 23.06

In Tab. 6.3, we have the main detector asymmetry values with different data sets, dithering only, ditherless only and the complete set. The dithering-ditherless discrepancies after beam and BB corrections are

$$\text{Run 1, BB+Dither Corrected: } A(\text{Dithering-Ditherless}) = 86.52 \pm 53.10 \text{ ppb}, \quad (6.8)$$

$$\text{Run 2, BB+Dither Corrected: } A(\text{Dithering-Ditherless}) = 24.56 \pm 24.33 \text{ ppb} . \quad (6.9)$$

From Eq. 6.8, the discrepancy in Run 1, we can see the discrepancy is actually a few ppb larger than Eq. 6.6, before BB correction. But in Run 2, the dithering-ditherless discrepancy is greatly reduced from Eq. 6.7 to Eq. 6.9 after BB correction is applied. Now in Run 2, the discrepancy is only about one sigma.

6.4 Dithering Sensitivity Error

6.4.1 From Ditherless Slope Error to Main Detector Error

Since we have given the ditherless slope a high error (Fig. 6.1), the error of the slope for these ditherless slugs must propagate into the main detector asymmetry error. If this error term is small compared to main detector error, we can say that the uncertainty of the ditherless slope does not affect the final physics asymmetry by much. If the high error of the ditherless slope does not result in increase of main detector asymmetry error after the inclusion of ditherless data, we can say that the missing slope for these data really can't justify the "low quality" of ditherless data and there will be no reason to distinguish between the data that have measured slopes and the data that don't.

6.4.2 Beam Correction Statistical Error

Now let's turn to the definition of dithering statistical error. The high defined error of ditherless slope is analog to the statistical error of the dithering slopes, which means they can be treated the same way.

We have dithering correction defined as

$$A_{\text{beam}} = - \sum_{m=0}^4 S_m \cdot dm , \quad (6.10)$$

in which m takes any monitor from E, X, X', Y, Y'. S_m is the slope for monitor m and dm is the monitor difference.

Besides the systematic error previous discussed, here we focus on the statistical error part in this beam correction.

Taking the error of Eq. 6.10, we have

$$\Delta A_{\text{beam}} = \sqrt{\sum_{m=0}^4 \sum_{n=0}^4 \text{cov}(S_m S_n) dmdn + \sum_{m=0}^4 \sum_{n=0}^4 S_m S_n \text{cov}(dmdn)}, \quad (6.11)$$

in which $\text{cov}(S_m S_n)$ is the error covariance between the slopes for monitor m and n , like the definition of slope error covariance for the ditherless data in Eq. 6.4. Likewise, $\text{cov}(dmdn)$ is the error covariance between the monitors, or the resolution of the monitors. The monitors have intrinsic resolution, typically $1 \mu\text{m}$ for position monitors. Different monitors might have common mode noise so their resolution can be correlated. A typical example is the familiar targetX and targetXSlope monitors we are using. They have their own resolution but still their noises are correlated by definition assuming the original BPMs have relatively independent noises.

In Eq. 6.11, the statistical error of beam correction is composed of two parts, the part with slope error is ‘‘Sensitivity Error Term’’ and the part with monitor difference noise is ‘‘Monitor Noise Term’’. When we perform beam correction to main detector asymmetry, we have already propagated the monitor noise to main detector asymmetry width. So the ‘‘Monitor Noise Term’’ of beam correction should not be included again when we have the correct statistical error of main detector asymmetry to avoid double counting. Therefore, we are left with the ‘‘Sensitivity Error Term’’:

$$\Delta A_{\text{sens}} = \sqrt{\sum_{m=0}^4 \sum_{n=0}^4 \text{cov}(S_m S_n) dmdn}. \quad (6.12)$$

For good dithering slugs, since the error in slope comes from beam natural motion, the

dithering sensitivity error for dithering slugs should be considered statistical. But for ditherless slugs, since the slope error are defined and should be considered as boundaries instead of Gaussian distribution, the dithering sensitivity error for ditherless slug should be considered systematic. So when combining sensitivity error from different slugs, the statistical type error should be considered uncorrelated and the systematic type error should be considered correlated.

When averaging the slugs, we have the combined sensitivity error for the dithering+ditherless combined set

$$\Delta A_{\text{sens}}^{\text{Run}} = \sqrt{\sum_s w_s^2 (\Delta A_{\text{sens}}^{\text{Dithering}})_s^2 + \sum_r \sum_t w_r w_t (\Delta A_{\text{sens}}^{\text{Ditherless}})_r (\Delta A_{\text{sens}}^{\text{Ditherless}})_t}, \quad (6.13)$$

in which s takes the dithering slugs and r, t take ditherless slugs. The w is from main detector error weighting, normalized to 1. The first term in the quadrature is from the contribution of dithering slugs. The second term is from ditherless data, in which the systematic sensitivity errors from ditherless slugs are correlated.

For Run 1 and Run 2, the calculated Sensitivity Errors are

$$\text{Run 1: } \Delta A_{\text{sens}} = 0.07 \text{ ppb}, \quad (6.14)$$

$$\text{Run 2: } \Delta A_{\text{sens}} = 0.26 \text{ ppb}. \quad (6.15)$$

We have 0.07 ppb for Run 1 and 0.26 ppb for Run 2. These values are from data set with ditherless data included. Compared to the statistical error of main detector asymmetry 13.15 ppb for Run 1 and 7.34 ppb for Run 2, this sensitivity error term is very small.

With the comparison between dithering and ditherless data and the smallness of the sensitivity error term, we can include the ditherless data and increase our statistics. For Run 1, it is improved from 13.60 ppb to current 13.15 ppb and in Run 2, the original 7.75 ppb becomes 7.34 ppb when the ditherless data is included.

Chapter 7

Conclusion

7.1 The Asymmetry

The asymmetry results for Run 1 and Run 2 are

$$\text{Run 1 : } A_{\text{ep}} = -223.5 \pm 15.0(\text{stat}) \pm 10.1(\text{syst}) \text{ ppb ,}$$

$$\text{Run 2 : } A_{\text{ep}} = -227.2 \pm 8.3(\text{stat}) \pm 5.6(\text{syst}) \text{ ppb ,}$$

which are in excellent agreement with each other. The combined asymmetry is

$$A_{\text{ep}} = -226.5 \pm 7.3(\text{stat}) \pm 5.8(\text{syst}) \text{ ppb .}$$

The systematic error contributions are listed in Fig. 7.1, including A_{BCM} and A_{beam} (the beam Sensitivity Errors calculated in Ch. 6 are incorporated with A_{beam} error) calculated in this thesis. From Fig. 7.1, in Run 2, the fractional contribution from beam parameter related systematic errors is smaller than Run 1.

Quantity	Run 1 error (ppb)	Run 1 fractional	Run 2 error (ppb)	Run 2 fractional
BCM Normalization: A_{BCM}	5.1	25%	2.3	17%
Beamline Background: A_{BB}	5.1	25%	1.2	5%
Beam Asymmetries: A_{beam}	4.7	22%	1.2	5%
Rescattering bias: A_{bias}	3.4	11%	3.4	37%
Beam Polarization: P	2.2	5%	1.2	4%
Target windows: A_{b1}	1.9	4%	1.9	12%
Kinematics: R_{Q^2}	1.2	2%	1.3	5%
Total of others	2.5	6%	2.2	15%
Combined in quadrature	10.1		5.6	

Figure 7.1: Most significant systematic error contributions [2].

Method	Quantity	Value	Error
PVES fit	Q_{w}^{p}	0.0719	0.0045
	ρ_{s}	0.20	0.11
	μ_{s}	-0.19	0.14
	$G_{\text{A}}^{Z(T=1)}$	-0.64	0.30
PVES fit + APV	Q_{w}^{p}	0.0718	0.0044
	Q_{w}^{n}	-0.9808	0.0063
	$C_{1\text{u}}$	-0.1874	0.0022
	$C_{1\text{d}}$	0.3389	0.0025
	C_1 correlation	-0.9318	
PVES fit + LQCD	Q_{w}^{p}	0.0685	0.0038
Q_{weak} datum only	Q_{w}^{p}	0.0706	0.0047
Standard model	Q_{w}^{p}	0.0708	0.0003

Figure 7.2: Results for the weak charge of the proton [2].

7.2 The Weak Charge of the Proton

Based on the asymmetry result, the weak charge of the proton can be extracted with different methods (Fig. 7.2). The PVES database determined the weak charge to be 0.0719 ± 0.0045 (the intercept of the global fitting of PVES data including Q_{weak} at $Q^2 = 0$ shown in Fig. 7.3), which agrees well with the Standard Model.

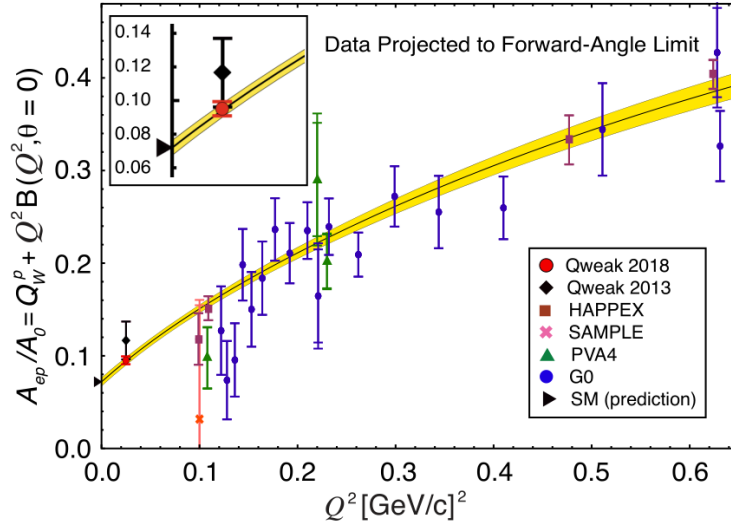


Figure 7.3: World PVES data fitting of reduced asymmetry versus Q^2 to determine the weak charge of the proton [2].

The Q_{weak} experiment has made the first direct measurement of the proton's weak charge. Fig. 7.4 gives C_{1d} vs C_{1u} showing the constraints from Q_{weak} and APV experiments.

The Q_{weak} experiment had also made the best measurement of the weak mixing angle at low energy, shown in Fig. 7.5.

For New lepton-quark PV physics at TeV scale shown in Fig. 7.6, at 95% confidence level, new physics is ruled out at 0.9 TeV.

The Q_{weak} experiment pushed existing boundaries on many fronts and provides scientific and technical developments for next generation of measurements. My methods developed in this thesis are being used for the on-line and off-line analysis of PREx and CREx and will be important for the MOLLER experiment.

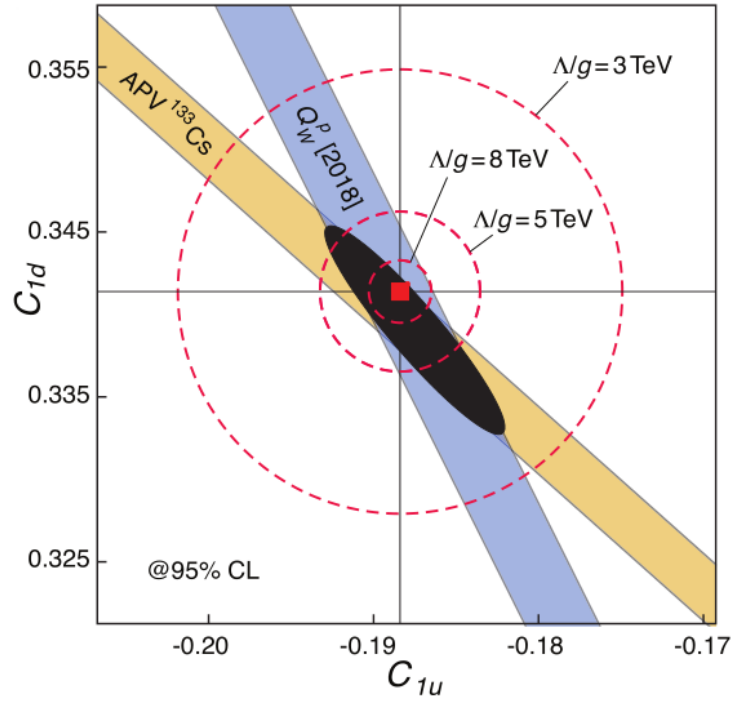


Figure 7.4: Constraints on coupling constants C_{1u} and C_{1d} [2].

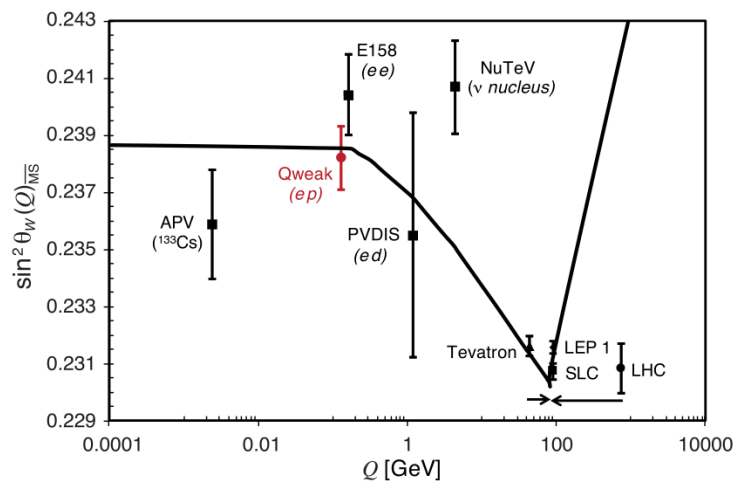


Figure 7.5: Running of weak mixing angle with previous measurements [2].

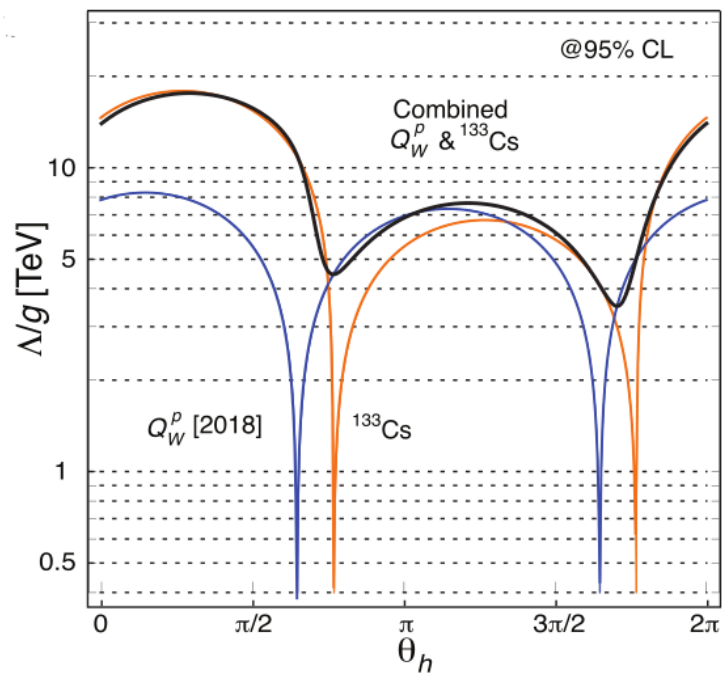
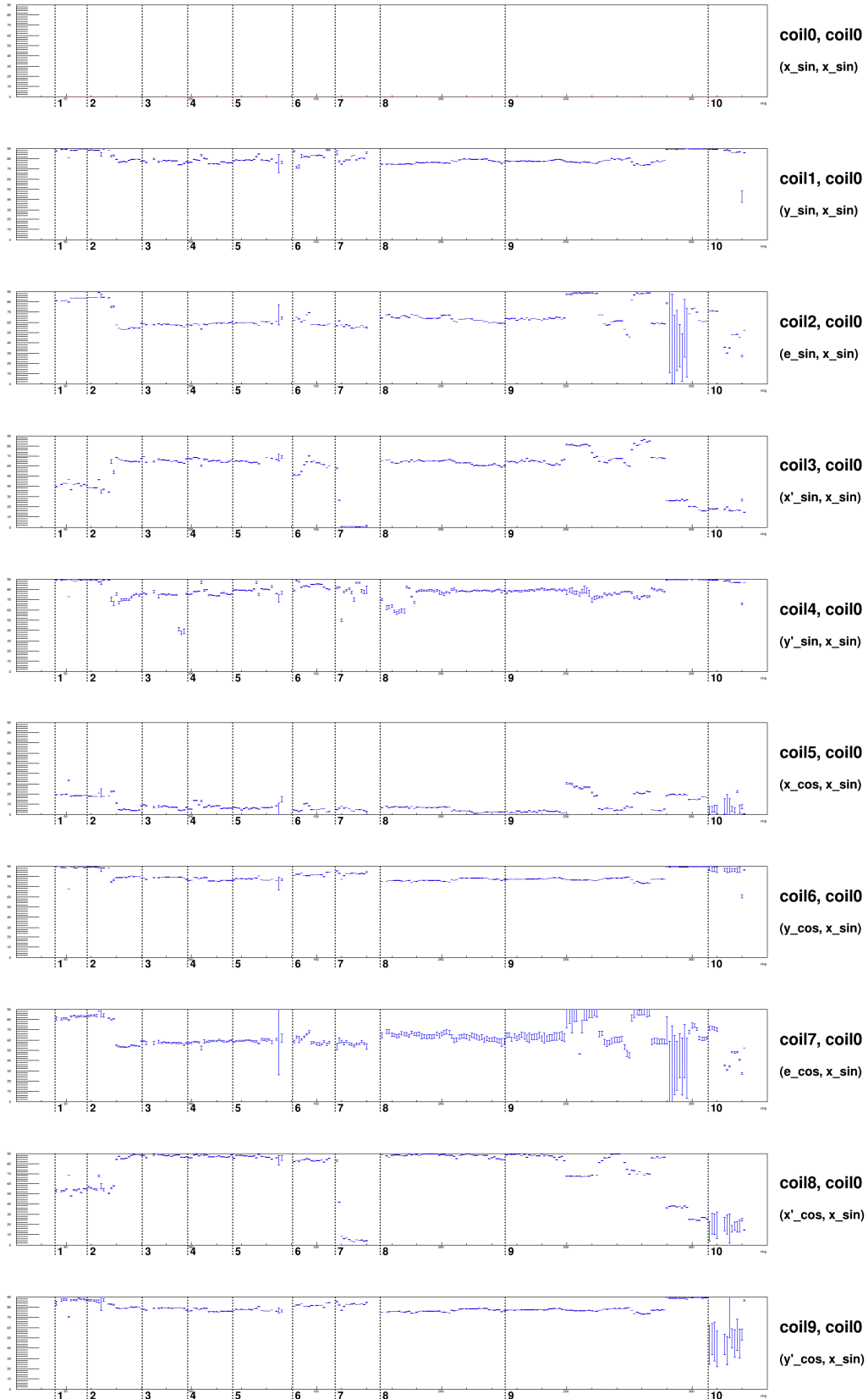


Figure 7.6: New physics limits vs quark flavor coupling [2].

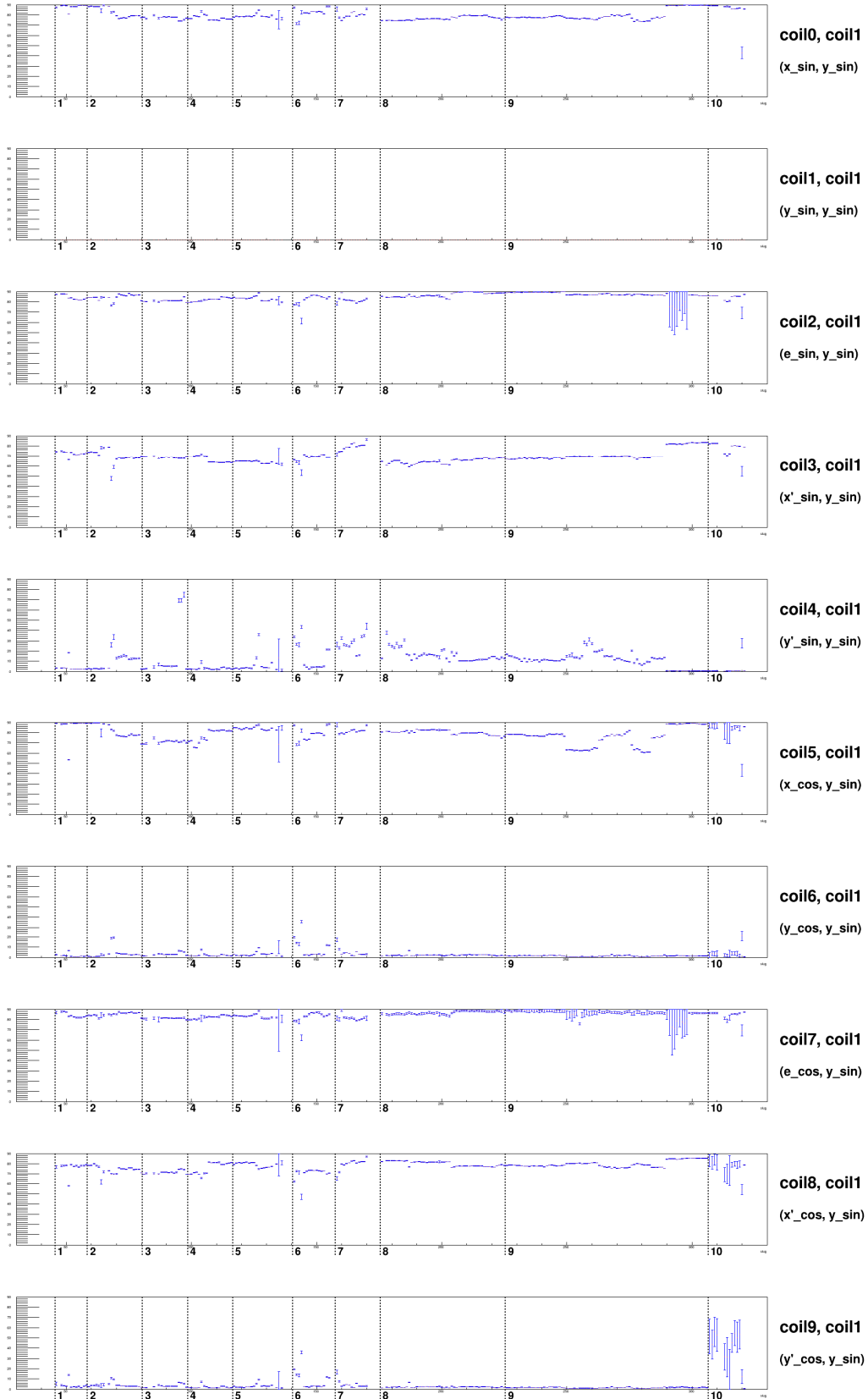
Appendix A

MCV Angle History

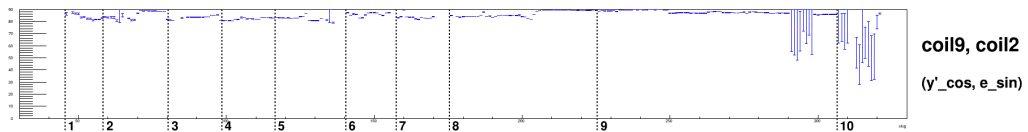
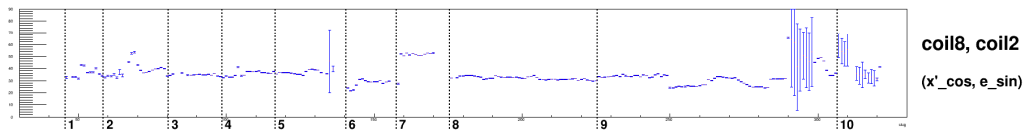
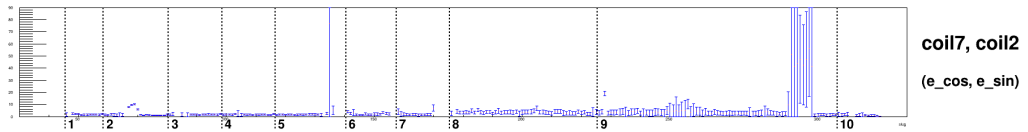
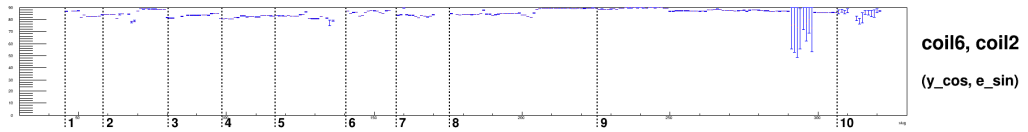
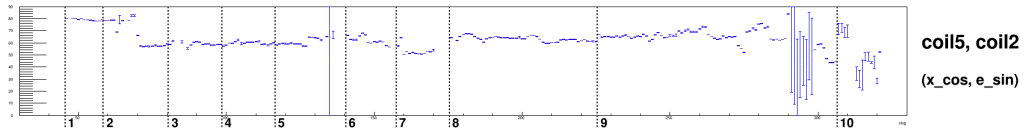
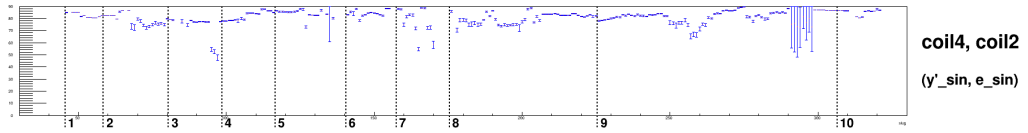
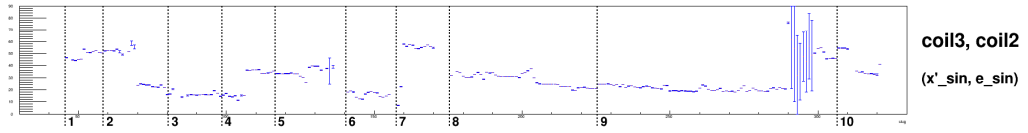
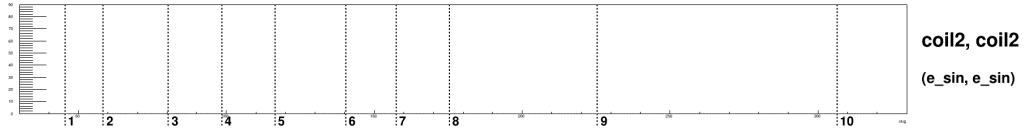
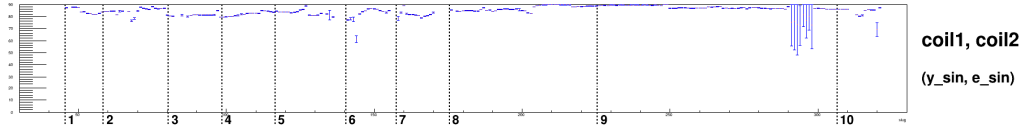
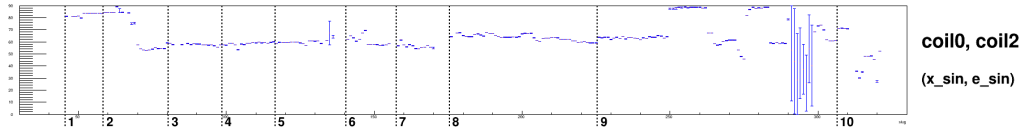
Angle between Pattern 0-9 and Pattern 0 : Slug



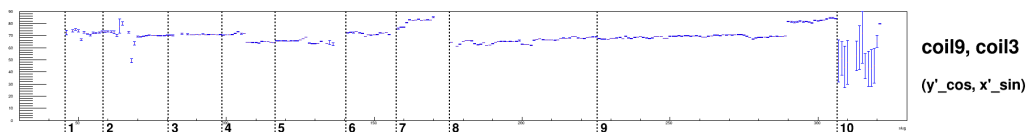
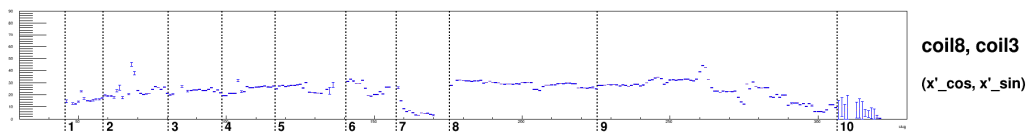
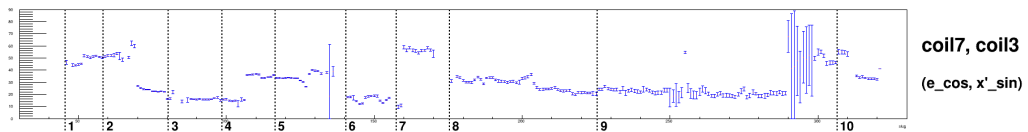
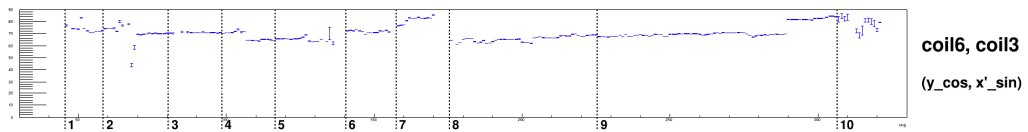
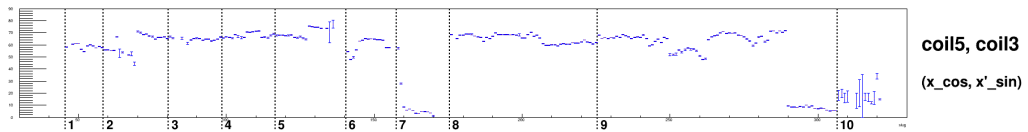
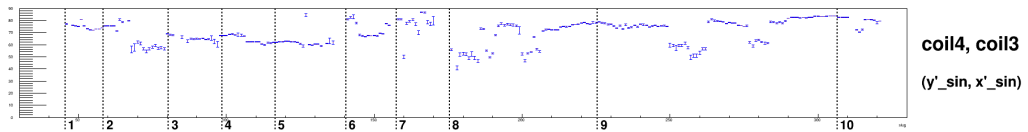
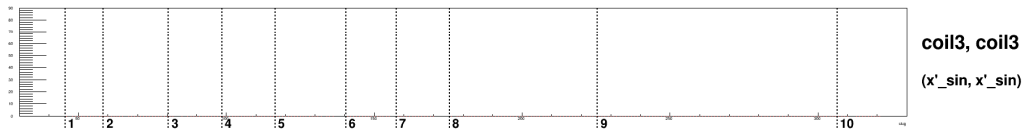
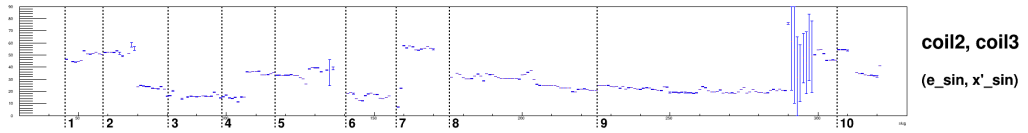
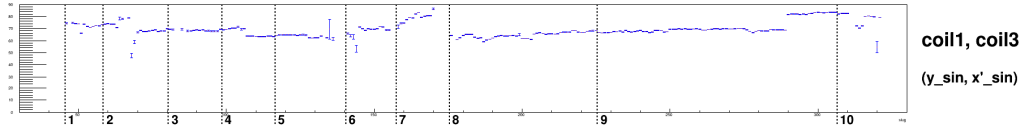
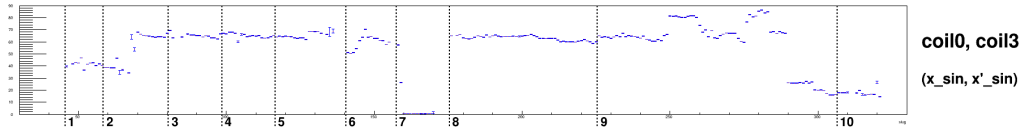
Angle between Pattern 0-9 and Pattern 1 : Slug



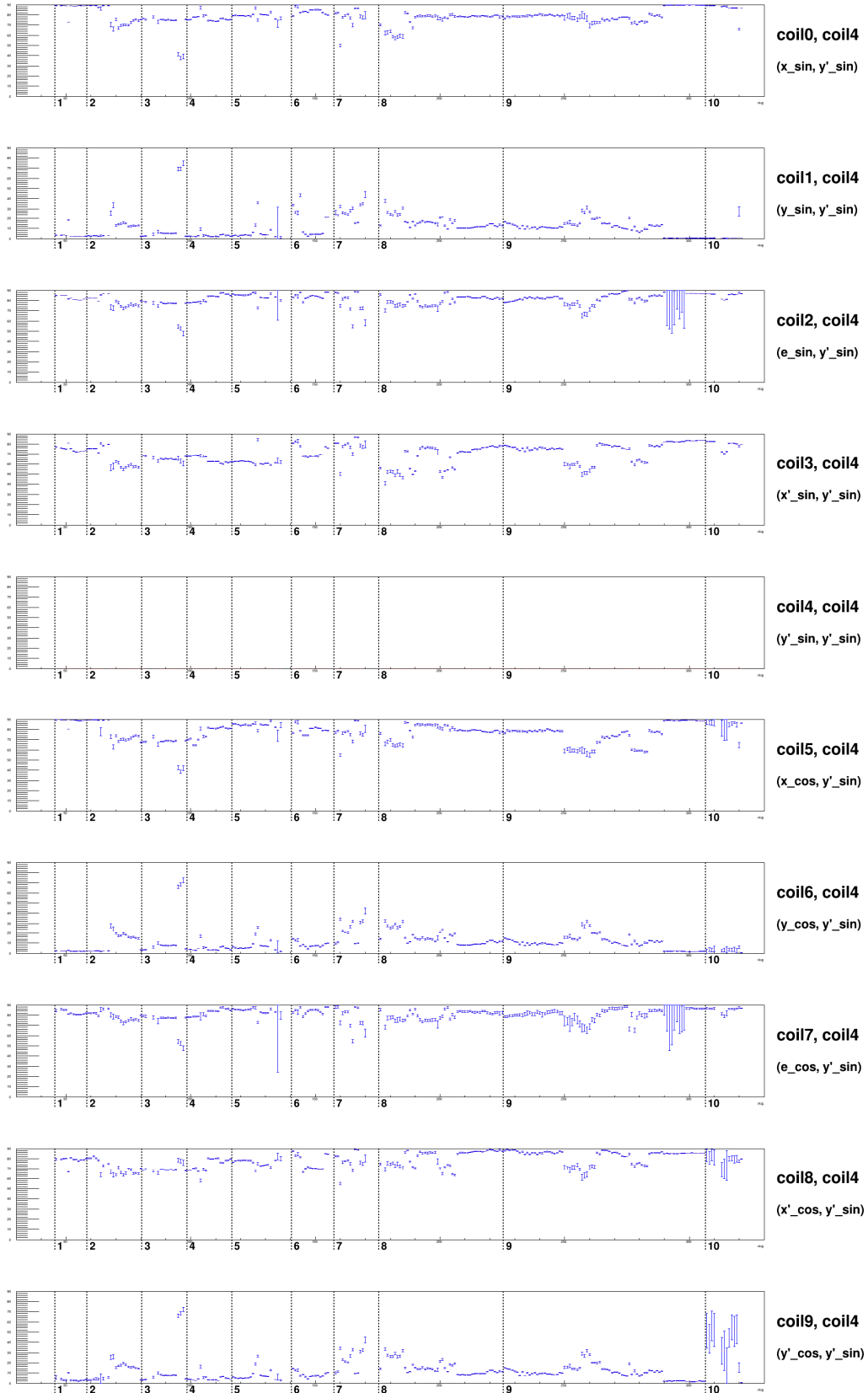
Angle between Pattern 0-9 and Pattern 2 : Slug



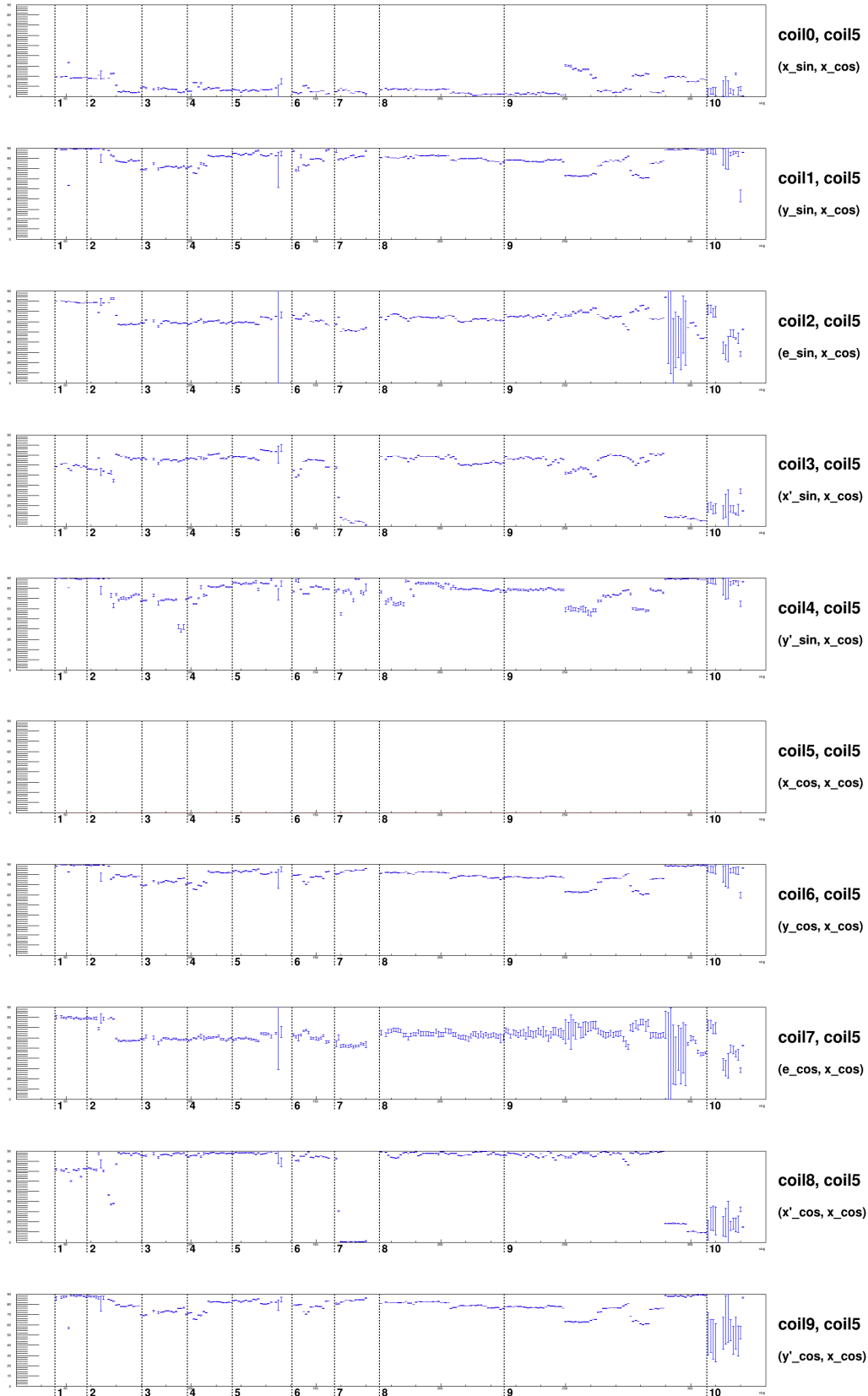
Angle between Pattern 0-9 and Pattern 3 : Slug



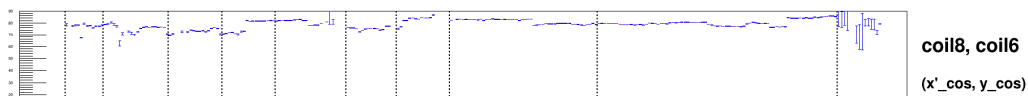
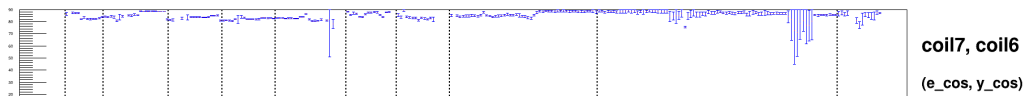
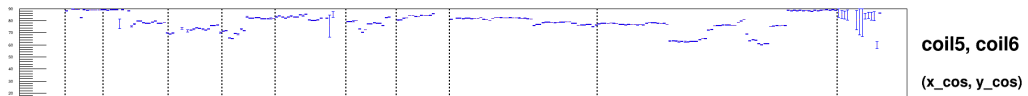
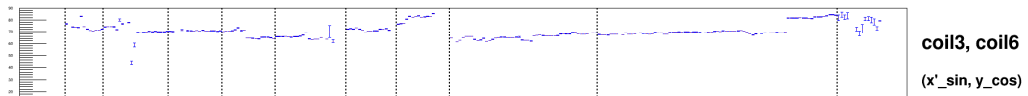
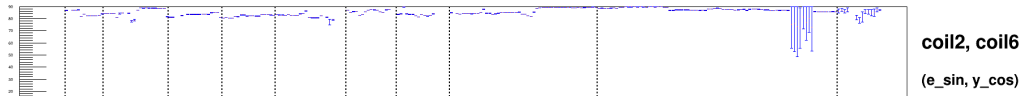
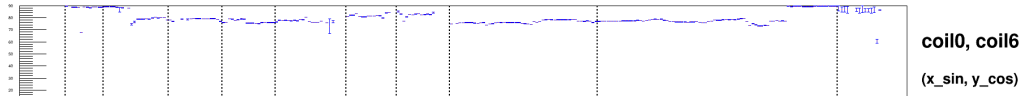
Angle between Pattern 0-9 and Pattern 4 : Slug



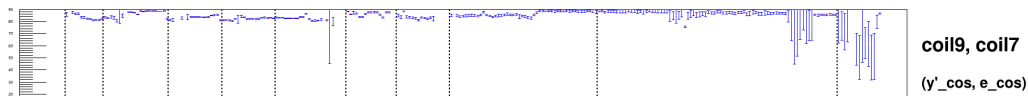
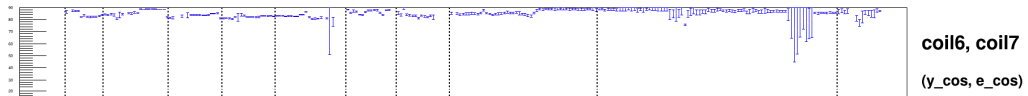
Angle between Pattern 0-9 and Pattern 5 : Slug



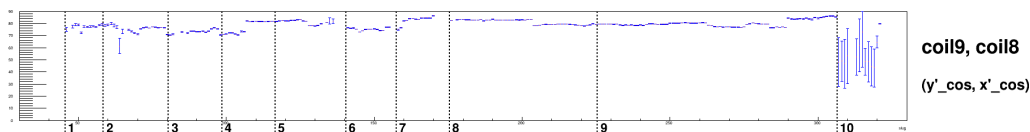
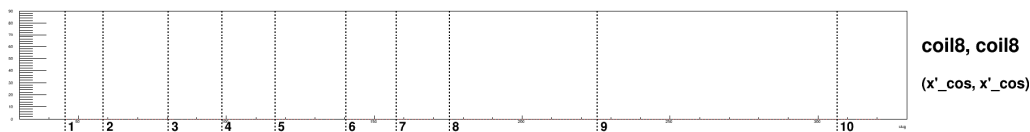
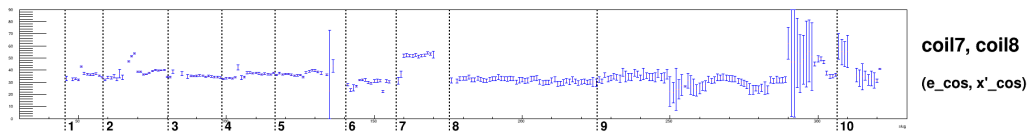
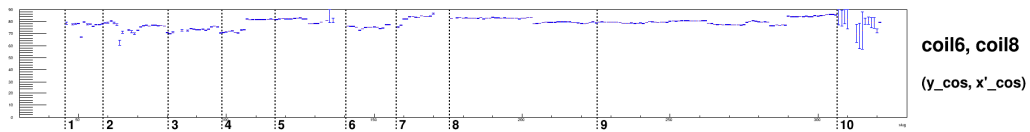
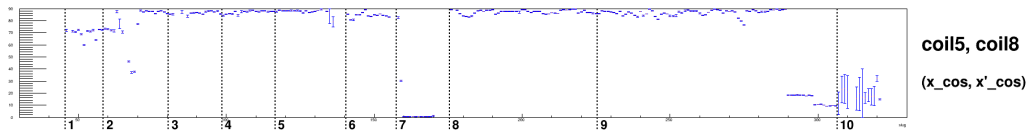
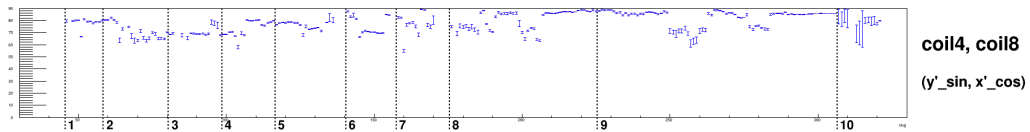
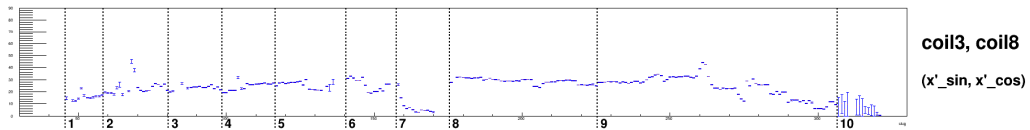
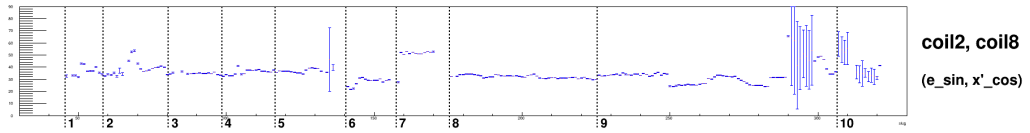
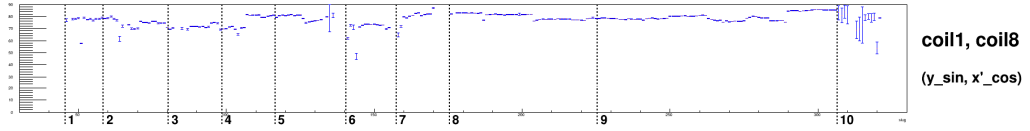
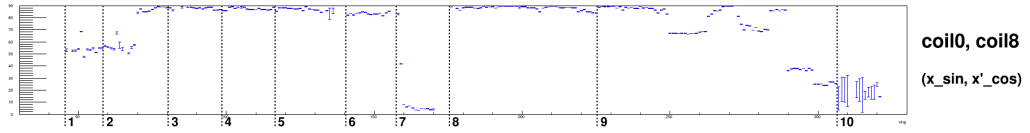
Angle between Pattern 0-9 and Pattern 6 : Slug



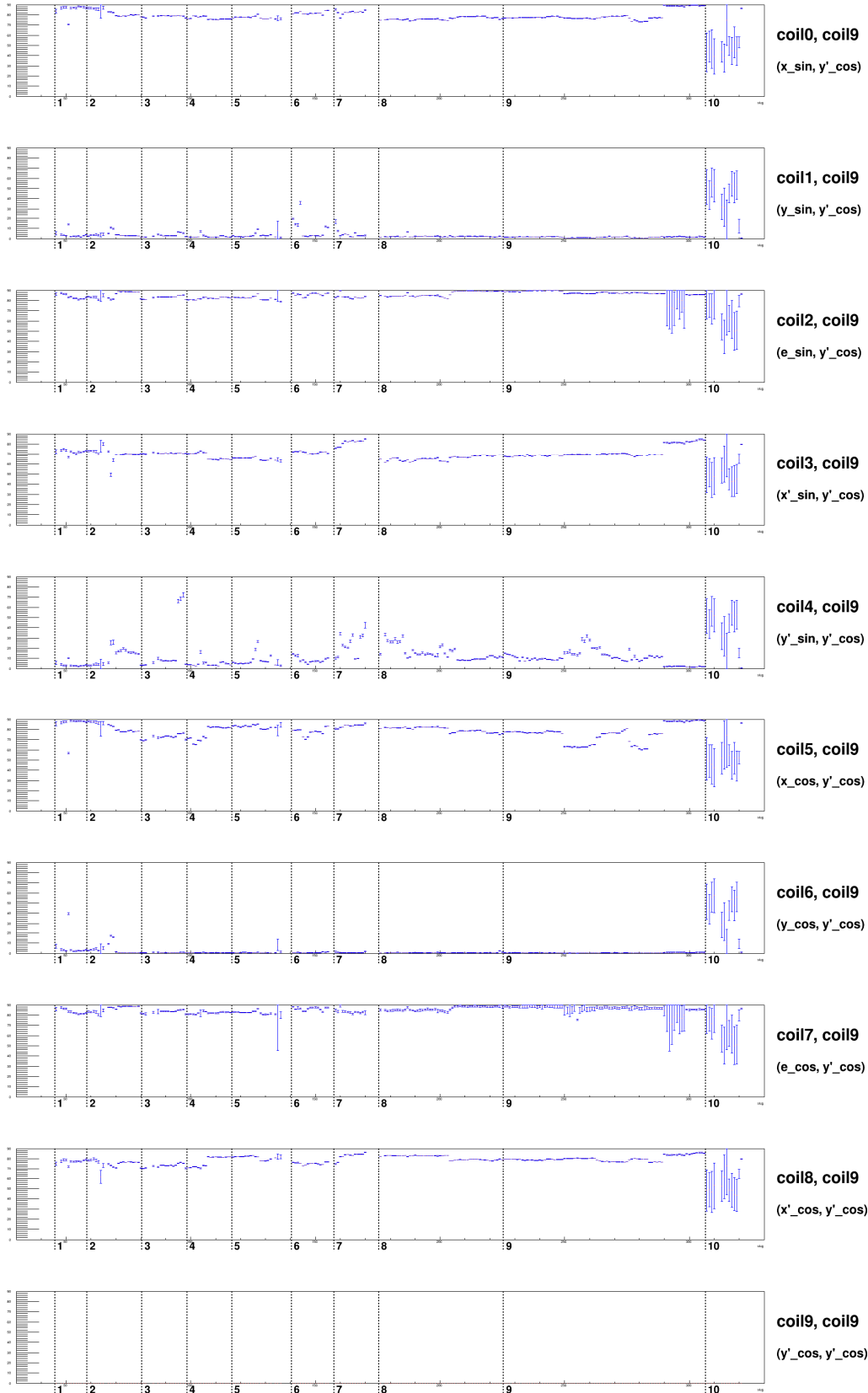
Angle between Pattern 0-9 and Pattern 7 : Slug



Angle between Pattern 0-9 and Pattern 8 : Slug



Angle between Pattern 0-9 and Pattern 9 : Slug



Bibliography

- [1] Peng Zang. Dither quality checking method. *Qweak Electronic Logbook*, 1224.
- [2] D. Androic *et al.* (Qweak Collaboration). Precision measurement of the weak charge of the proton. *Nature*, 557:207–211, 2018.
- [3] Online source Wikipedia by user MissMJ.
https://upload.wikimedia.org/wikipedia/commons/0/00/standard_model_of_elementary_particles.svg.
- [4] J.J. Kelly. Simple parametrization of nucleon form factors. *Physical Review C*, 70:068202, 2004.
- [5] D. Androic *et al.* (Qweak Collaboration). First determination of the weak charge of the proton. *Physical Review Letters*, 111:141803, 2013.
- [6] C.W. Leemann, D.R. Douglas, and G.A. Krafft. The continuous electron beam accelerator facility: CEBAF at the jefferson laboratory. *Annual Review of Nuclear and Particle Science*, 51(1):413–450, 2001.
- [7] T. Allison *et al.* (Qweak Collaboration). The qweak experimental apparatus. *Nuclear Instruments and Methods in Physics Research A*, 781:105–133, 2015.
- [8] J. M. Grames, J. F. Benesch, J. Clark, J. Hansknecht, R. Kazimi, D. Machie, M. Poelker, M. L. Stutzman, R. Suleiman, and Y. Zhang. Two wien filter spin flipper. *Proceedings of 2011 Particle Accelerator Conference*, pages 862–864, 2011.

- [9] M. Hauger, A. Honegger, J. Jourdan, G. Kubon, T. Petitjean, D. Rohe, I. Sick, G. Warren, H. Wöhrle, J. Zhao, R. Ent, J. Mitchell, D. Crabb, A. Tobias, M. Zeier, and B. Zihlmann. A high-precision polarimeter. *Nuclear Instruments and Methods in Physics Research Section A*, 462(3):382–392, 2001.
- [10] L. G. Levchuk. The intra-atomic motion of bound electrons as a possible source of the systematic error in electron beam polarization measurements by means of a møller polarimeter. *Nuclear Instruments and Methods in Physics Research A*, 345:496–499, 1994.
- [11] Peng Zang. Md asymmetries summary. *Qweak Document Database*, 2373.
- [12] Peng Zang. Renormalized main detector - correlation with current monitors. *Qweak Electronic Logbook*, 1556.
- [13] Peng Zang. Renormalized main detector - null and physics asymmetries. *Qweak Electronic Logbook*, 1558.
- [14] Peng Zang. Bcm double difference. *Qweak Electronic Logbook*, 1539.
- [15] Peng Zang. Correlation between different bcms. *Qweak Electronic Logbook*, 1559.
- [16] Peng Zang. Regression and dithering correction comparison. *Qweak Electronic Logbook*, 1454.
- [17] Peng Zang. Beam correction to beam position monitors. *Qweak Electronic Logbook*, 1483.
- [18] Peng Zang. Tentative quantization of regression and dithering discrepancy. *Qweak Electronic Logbook*, 1588.
- [19] Peng Zang. Bcm normalization in run1 and run2. *Qweak Document Database*, 2344.
- [20] Peng Zang. Beam correction summary. *Qweak Document Database*, 2376.

VITA

NAME OF AUTHOR: Peng Zang

PLACE OF BIRTH: China

EDUCATION:

B.S. in Physics, Shandong University (2008)

M.S. in Condensed Matter Physics, Beijing University of Technology (2011)

M.S. in Physics, Syracuse University (2015)

SELECTED PUBLICATIONS:

Parity-violating inelastic electron-proton scattering at low Q_2 above the resonance region,
Qweak Collaboration, Phys. Rev. C 101, 055503 (2020).

Precision measurement of the weak charge of the proton, the Jefferson Lab Qweak
Collaboration, Nature 557, 207–211 (2018).